Technische Universität München
Max-Planck-Institut für Astrophysik

Modeling delayed detonations of Chandrasekhar-mass white dwarfs

Franco Ciaraldi-Schoolmann

Vollständiger Abdruck der von der Fakultät für Physik der Technischen Universität München zur Erlangung des akademischen Grades eines

Doktors der Naturwissenschaften (Dr. rer. nat.)

genehmigten Dissertation.

Vorsitzender: Univ.-Prof. S. Bishop, Ph.D

Prüfer der Dissertation:

1. Univ.-Prof. Dr. F. K. Röpke
   Julius-Maximilians-Universität Würzburg
2. Univ.-Prof. Dr. H. Friedrich

Die Dissertation wurde am 16.05.2012 bei der Technischen Universität München eingereicht und durch die Fakultät für Physik am 17.09.2012 angenommen.

Contents

List of Figures

List of Tables

1

Motivation and objectives

About supernovae

Supernovae are very luminous and compared to usual astrophysical time scales very short-lived phenomena that are related to explosions of stellar objects. Due to observational limitations only a few progenitor stars have been detected before they explode. Thus, a supernova, which commonly constitutes a final phase in the stellar evolution, reveals that a star has existed at this location. The brightness of a supernova may rise to such an extent that its peak luminosity is of the same order of magnitude as its host galaxy (see Figure 1.1). Supernovae are responsible for galactic chemical evolution. The reason are the nucleosynthesis processes in the center of massive stars that lead to the production of heavy elements which are released during the supernova explosion (Burbidge et al., 1957).[1] In addition, the supernova breakout itself may lead to the production of heavy elements, since physical conditions for thermonuclear reaction processes in the explosion are achieved (e.g. Seeger et al., 1965; Arnett, 1971b; Woosley et al., 1973). It is also believed that star formation can be triggered by supernovae. The pressure wave released from a supernova may compress the surrounding interstellar medium, leading to a gravitational collapse in molecular clouds that eventually induces star formation (e.g. Preibisch & Zinnecker, 1999, 2001; Prialnik, 2000). In this sense, there is a cycle between the destructions and births of stars. Younger star generations, however, will consequently have a larger fraction of heavier elements (metallicity) that were produced in the nucleosynthesis processes in older stars. Moreover, a subclass of supernovae shows very homogeneous features that can be used for applications in cosmology (Kowal, 1968; Colgate, 1979). Investigations of these supernovae have led to the surprising conclusion that we are living in an accelerating expanding universe (Perlmutter et al., 1999; Riess et al., 1998, 2004).

[1] The famous work of Burbidge et al. (1957) is also called the B^2FH paper (named after the initials of the authors).

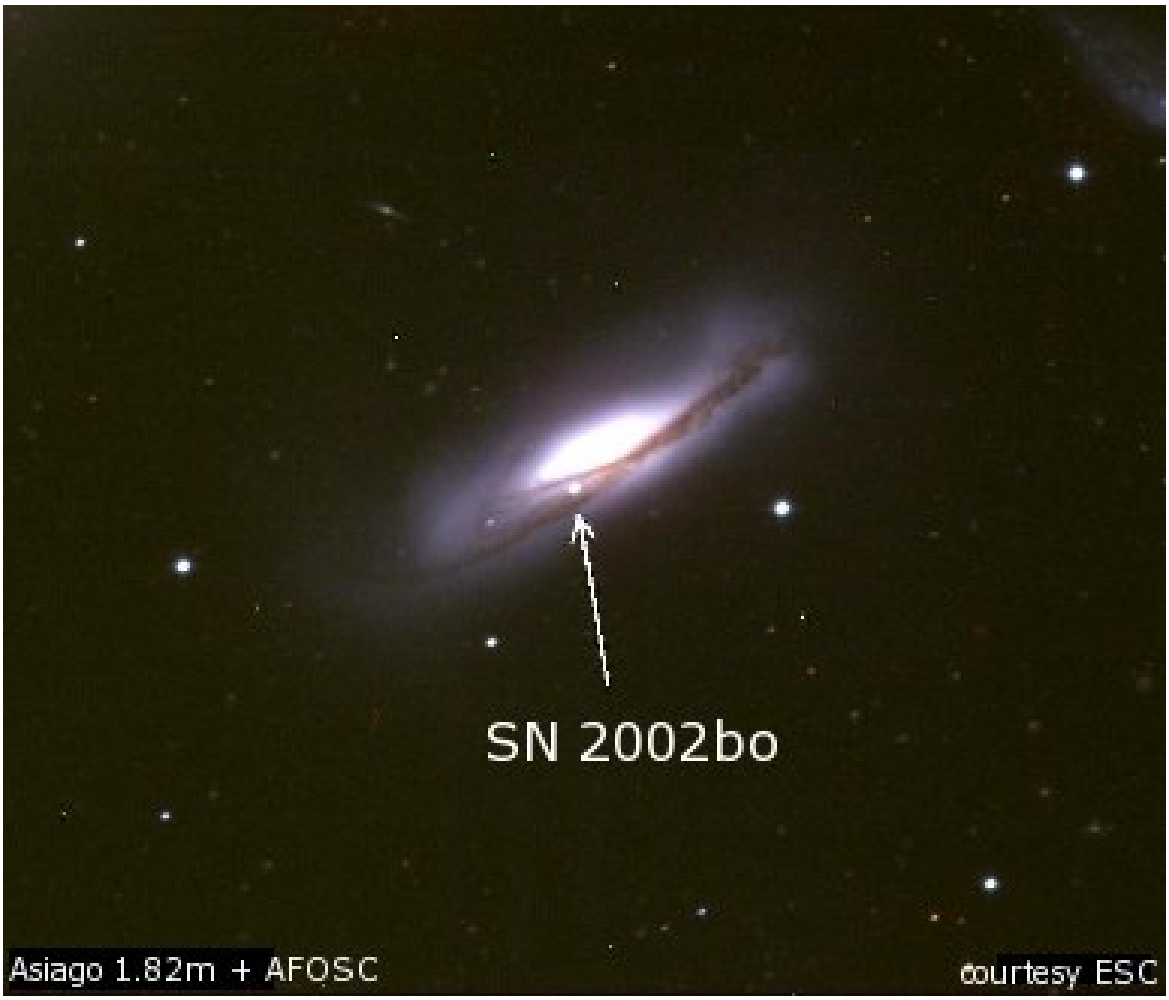

Fig. 1.1: The Type Ia supernova SN 2002bo, discovered in the spiral galaxy NGC 3190 in march 2002 (Benetti et al., 2004).

Historical Overview

In December 185 AD a *guest star* that suddenly appeared and slowly vanished was reported by Chinese authors in the *Hou Hanshu* (Zhao et al., 2006).[2] In April 1054 AD a *new star* in the sky was described in several sources (mostly again in Chinese documents) where we can observe the famous Crab Nebula today. In early modern Europe it was Tycho Brahe in 1572 and Johannes Kepler in 1604 who discovered *new stars*. Their publications about these observations led to a revolution in the universally accepted opinion of the sky. Fritz Zwicky and Walter Baade proposed in 1934 the term *Supernova* for these bright events (Baade & Zwicky, 1934; Zwicky, 1940). Zwicky was also the first who suggested in 1938 that supernovae are induced by a gravitational collapse. With Baade he pioneered the theory that supernovae may produce neutron stars (Zwicky, 1938). Due to a continuous increase in observations it was revealed that supernovae can have very different features. Therefore, they have been subdivided into two classes (Minkowski, 1941). Type I supernovae show no hydrogen in their spectra which is present in Type II supernovae. In contrast to Zwicky's theory, no neutron

[2]The history of the later Han Dynasty

star could be identified in many Type I supernovae.[3] Instead, lines of intermediate mass elements like silicon appeared in the spectra. Fred Hoyle and William Fowler proposed in 1960 that these events may result from thermonuclear explosions of *white dwarf stars* (Hoyle & Fowler, 1960). Therefore, these supernovae that are called *Type Ia supernovae (SNe Ia)* have a fundamentally different explosion mechanism than all other subclasses of supernovae. For the latter it is commonly believed that these explosions originate from the gravitational core collapse of massive stars.

SNe Ia seem to have remarkably homogeneous features. Charles Kowal was the first to use the homogeneity in the brightness of these objects to measure cosmological distances (Kowal, 1968). However, the improvements of observational methods and the associated increasing number of observed supernovae revealed that there are some variations in the spectra and light curves within the class of SNe Ia. Therefore, these events are further subdivided into *normal* and *peculiar* SNe Ia (Branch et al., 1993), where the latter may show pronounced anomalies in the spectra and light curves, so that they cannot be used for cosmological distance measurements anymore. However, also the normal SNe Ia show a certain degree of variations that affect the applicability to use them as cosmological distance indicators. It is therefore desirable to understand the observed variations on a physical basis. Since this issue remains unresolved to date, one tries to calibrate these variations with specific correlations between peak luminosities, spectral properties and light curve shapes. A particularly successful model is the Phillips relation that describes a correlation between the peak luminosity and the decline of the light curve in the first 15 days after approaching its maximum (Phillips, 1993). In 1999, investigations of the research groups HZT (High-z Supernova Search Team) and SCP (Supernova Cosmology Project) showed independently that the absolute brightnesses of SNe Ia in far away galaxies are dimmer than expected for a matter-dominated universe. Their results lead to the discovery that our universe currently undergoes an accelerating expansion (Perlmutter et al., 1999; Riess et al., 1998, 2004).[4] The reason of this acceleration may be explained by the existence of a dark energy, of which the properties are still controversially discussed (e.g. Huterer & Turner, 1999; Carroll, 2001; Caldwell et al., 1998, 2003).

The delayed detonation model of Chandrasekhar-mass white dwarfs

Since SNe Ia have attained a crucial importance for cosmology, we need to understand the physics of these objects. The biggest challenge in this context is to find a physically motivated model for SN Ia explosions that can reproduce the homogeneous features, but has still the capability of explaining the observed variations. In addition, a model has to account for the observed correlation between the brightness of an event and the age of the host stellar population (Gallagher et al., 2008) and it must predict the observed rate of SN Ia explosions (e.g. Ruiter et al., 2009). There is a high probability that not all SNe Ia can be described with a single scenario. To develop a reliable SN Ia model we need information about the progenitor system. In contrast to some core collapse supernovae, a progenitor system for a SN Ia explosion has not been identified yet, hence valuable knowledge of the origin of SNe Ia is not available directly. Therefore, information of these explosions can only be indirectly derived from the observed light curves and spectra. Several theoretical scenarios of the progenitor system and the explosion mechanism have been proposed from these observations. One popular progenitor system invokes the so-called *Chandrasekhar-mass explosion*

[3] There are also some Type II supernovae where no neutron star has been found so far (e.g. SN 1987A).

[4] S. Perlmutter, B. P. Schmidt and A. Riess received the Nobel Prize in Physics in 2011 for this discovery.

model. Characteristic for this model is that all white dwarfs have the same mass when they explode, which may explain the main homogeneous features. For the explosion mechanism in this model the *delayed detonation* scenario (Khokhlov, 1991a) is particularly successful in explaining several main features of SNe Ia. Here a thermonuclear burning front (commonly described as a *flame*) starts out as a subsonic *deflagration* that propagates through heat conduction processes. In the later explosion phase a physical mechanism leads to a *Deflagration-to-Detonation Transition (DDT)*, where the onset of a supersonic *detonation* affects the further explosion dynamics.

Objectives and organization of the thesis

Despite the success of the delayed detonation model, the physics of the DDT is not well understood. However, since the work of Khokhlov (1991a), many studies in this field have been carried out from which we can derive necessary constraints for DDTs in SNe Ia. These constraints are the starting point of this thesis. From the relevant quantities for a DDT we develop a new model that includes the physics of a DDT according to our current knowledge. This DDT model is implemented in a numerical hydrodynamic code and applied to three-dimensional large-scale simulations that follow the explosion of the whole white dwarf on the simulation grid. The main focus of the model are the properties of *turbulence*. Turbulence occurs due to different instabilities during the deflagration phase and may play a fundamental role in the mechanism that triggers a DDT. The DDT process is not resolved in our *full-star* simulations, so that the DDT quantities have to be modeled on unresolved scales in an appropriate way. The turbulent evolution depends strongly on the properties of the deflagration which in turn depend on the unknown ignition process of the deflagration flame. Therefore, different ignition scenarios of the deflagration have to be taken into account as an additional model parameter within the studies of DDTs. The main issues and questions on which this thesis focuses are given in the following:

1. An important basic question is whether the properties of turbulence at the deflagration flame are suitable for the occurrence of DDTs. The analysis of Röpke (2007) indicates that turbulence may be strong enough to trigger a DDT, but we intend to investigate this issue in more detail.

2. Since we perform numerical simulations we need to find out how the necessary physical constraints on delayed detonations can be treated in a numerical approach properly. The DDT process is not resolved in our studies, so that these constraints are implemented in a so-called *subgrid-scale (SGS) model*. What are the requirements to keep this DDT-SGS model robust and resolution-independent?

3. Can three-dimensional simulations of delayed detonations that use the new DDT-SGS model reproduce the observed variations in the brightness of normal SNe Ia? What are the effects of different ignition scenarios of the deflagration and the associated different evolutions of the turbulent deflagration on the DDT model? What are the immediate consequences for the dynamics of the ensuing detonation phase?

4. Most of the values of the DDT quantities are not well known and we cannot determine these values in our large-scale simulations. However, we intend to find out how the explosion brightness can be controlled with the DDT model. To what extent is a variation of the values of the DDT quantities or a different evolution of the deflagration the decisive parameter that determines the explosion brightness? Can we place

any constraints on DDT quantities, so that the obtained range of brightnesses in the simulations is largely consistent with the observed variations in the brightness of normal SNe Ia? Can we further derive any necessary constraints for DDTs to occur in deflagrations of white dwarfs generally?

To address these issues, the thesis is organized as follows: In Chapter 2 our current understanding of SNe Ia is discussed. The properties of turbulence in the deflagration phase and the known constraints on DDTs are described in Chapter 3. In Chapter 4 the hydrodynamic code LEAFS that is used to carry out the simulations of this work and the initial white dwarf model are explained. The implementation of the DDT model and the tests in simulations are described in Chapter 5 where we will address the issues (1) and (2). In Chapter 6 we tackle issue (3) where we apply the DDT model to different ignition setups of the deflagration and investigate the evolution of the explosions in simulations of pure deflagrations and delayed detonations. To address issue (4) a detailed parameter study of DDT simulations is performed, of which the results are discussed in Chapter 7. In Chapter 8 a summary of the thesis and an outlook of further applications and projects are given.

2
Type Ia Supernovae

In this chapter the current knowledge of SNe Ia and the derived models are described. Since the progenitor systems are not identified yet, theoretical models have been developed from observational results. In Section 2.1 we summarize the main observational properties of SNe Ia. The theoretical progenitor scenarios are given in Section 2.2. In Section 2.3 the explosion models are discussed.

2.1 Observational properties of Type Ia Supernovae

SNe Ia are classified by the absence of hydrogen and the presence of silicon lines in the early spectra. The observations reveal that apart from the homogeneous features there are also events that show a higher degree of anomalies in the light curves and spectra. Therefore, SNe Ia are subdivided into *normal* and *peculiar* SNe Ia (Branch et al., 1993). While in the beginning of this separation 83 - 89% appeared to be of normal type, the improved observations show that the fraction of peculiar SNe Ia is about 30% (Li et al., 2011).

2.1.1 Normal SNe Ia

Light curves

For a normal SN Ia there is a steep rise in the luminosity that approaches a maximum of about $M_{\mathrm{B}} \approx M_{\mathrm{V}} \approx -19.3\,\mathrm{mag}$[1] at about 20 days after the onset of the explosion (Riess et al., 1999; Hillebrandt & Niemeyer, 2000). The bolometric luminosity at this time is $L_{\mathrm{bol}} \approx 10^{43}\,\mathrm{erg\ s^{-1}}$ (Contardo et al., 2000). After maximum there is a steep decline of about 3 mag in the following 30 days. Normal SNe Ia obey the Phillips relation, hence for brighter explosions, a slower decay of the luminosity after the maximum of the light curve is observed (Phillips, 1993; Hamuy et al., 1996; Höflich et al., 1996; Phillips et al., 1999). The later evolution is characterized by a weak exponential decline with a rate of about 1 mag per month. Observations in the infrared show a second maximum that appears approximately 20 - 30 days after the first one (e.g. Suntzeff, 2003; Contardo et al., 2000). The overall

[1] B = blue band ($\approx 445\,\mathrm{nm}$), V = visible band ($\approx 550\,\mathrm{nm}$) (e.g. Johnson & Morgan, 1953)

release of kinetic energy is of the order of 10^{51} erg (e.g. Khokhlov et al., 1993). There is no appreciable emission of radio waves and X- and gamma rays.

Spectra

The spectra at the time of peak luminosity are dominated by blue-shifted lines of intermediate mass elements, such as SiII, MgII, CaII and OI. In particular, a deep absorption line at a wavelength of about 615 nm that is attributed to singly ionized silicon, is a characteristic feature for SN Ia spectra. Since the inner part of the star remains opaque at this time we see the chemical composition of the outer expanding envelope. The expansion velocities, determined from the Doppler shift of the blue-shifted spectral lines is of the order of 10^4 km s^{-1} (Filippenko, 1997). Two weeks after peak luminosity, the central part of the star becomes optically visible. The spectra show now FeII lines and the intermediate mass elements (except for CaII) have gone. About one month after peak luminosity the supernova enters the so-called nebular phase, where the outer layers become completely transparent for optical radiation. Now the spectra are dominated by forbidden FeII, FeIII, and CoIII lines (Axelrod, 1980). During the temporal evolution the Co lines lose intensity, while the intensity in the Fe lines grows.

Occurrence

While core collapse supernovae occur only in spiral and irregular galaxies, and here predominantly in spiral arms and HII regions, the SNe Ia are found in all types of galaxies. In spiral galaxies they are also less concentrated in spiral arms or in the vicinity of HII regions than core collapse supernovae. The rate of nearby SNe Ia is about 0.2 SNu[2] (Cappellaro et al., 1999). Mannucci et al. (2005) showed that SNe Ia occur more frequently in spiral and irregular galaxies than in elliptical galaxies.

Summary

From the observational properties one can conclude that the light curves of SNe Ia are powered by the decay chain $^{56}\mathrm{Ni} \rightarrow {}^{56}\mathrm{Co} \rightarrow {}^{56}\mathrm{Fe}$ (Truran et al., 1967; Colgate & McKee, 1969). The half-life of ^{56}Ni is approximately 6.1 days and of ^{56}Co 77.3 days. Before approaching peak luminosity the outer layers are so dense that due to high opacities the radiation from the ^{56}Ni decay can hardly escape. By approaching peak luminosity at about 20 days, most of the ^{56}Ni has already decayed to ^{56}Co, so that a significant part of the further decline of the light curve is determined by the ^{56}Co decay (Kuchner et al., 1994). From light curves and spectra we can estimate the amount of produced ^{56}Ni (Arnett, 1982; Arnett et al., 1985) which is in the range of approximately $0.4 \ldots 0.9\, M_\odot$[3] for normal SNe Ia (Contardo et al., 2000; Stritzinger et al., 2006; Mazzali et al., 2007). From the ^{56}Ni yield one can further find an explanation for the Phillips relation. Brighter SN Ia explosions produce more ^{56}Ni that also leads to an increase of the amount of iron group elements. The high densities of these elements causes high opacities that in turn broaden the light curve (Mazzali et al., 2007). It should be noted that a strong neutronization during the thermonuclear burning at high densities leads to an enhanced production of stable isotopes of the iron group (e.g. Seitenzahl et al., 2009b) that in turn affects the opacities and hence the light curve. This is why

[2] 1 SNu = 1 supernova per century per $10^{10}\, L_{B_\odot}$ (where $L_{B_\odot} \approx 5.2 \cdot 10^{32}$ erg s^{-1} is the solar luminosity in the B-band)

[3] $1 M_\odot$ = 1 solar mass $\approx 1.989 \cdot 10^{33}$ g

a relationship between the brightness of an explosion and the produced ^{56}Ni holds only up to a certain extent. For the second maximum seen in the infrared there are several theories, but it is most probable that it results from ionization processes of iron group elements in the outer ejecta (Kasen, 2006).

Since SNe Ia occur in all types of galaxies and stellar populations of very different ages, the exploding stellar objects cannot be short-living massive stars. Due to the absence of a compact remnant associated with the lack of radio waves and X- and gamma rays, neutron stars and black holes seem not to originate from SN Ia explosions. From these considerations it is generally believed that SNe Ia are the result of thermonuclear explosions of white dwarfs as proposed by Hoyle & Fowler in 1960.

2.1.2 Peculiar SNe Ia

1991T-like objects

1991T-like objects (Phillips et al., 1992) contribute at least 9% to all SNe Ia (Li et al., 2011). They are named after the prototype supernova SN 1991T and are characterized by a higher brightness than those of normal SNe Ia. The peak luminosity of these events is on average -19.6 mag and about $1\,M_\odot$ of ^{56}Ni is needed to power the light curve (Spyromilio et al., 1992; Mazzali et al., 1995). These supernovae also obey the Phillips relation, hence their light curves appear broader than those of normal SNe Ia. In the early spectra, neither SiII nor CaII lines are found (Phillips et al., 1992). In contrast, spectral lines of highly excited FeIII are identified (Filippenko et al., 1992b). In the later phase, the spectra tend to adjust gradually to that of normal SNe Ia (Phillips et al., 1992). These supernovae seem to produce more iron group and less intermediate mass elements than normal SNe Ia. They are predominantly found in spiral galaxies in regions of recent star formation.

Superluminous objects

Rarer but even brighter than the 1991T-like objects are the so-called *superluminous* events. They reach peak luminosities up to -20 mag (Yamanaka et al., 2009). The amount of ^{56}Ni needed to achieve such high luminosities is $1.2 \ldots 1.7\,M_\odot$ (Howell et al., 2006; Hicken et al., 2007; Silverman et al., 2011; Taubenberger et al., 2011). They have a very slow decline rate in the light curve which does not obey the Phillips relation anymore. Also the main homogeneous features that are found in the spectra of normal SNe Ia are lost. There is some evidence that superluminous events preferentially occur in regions of recent star formation (Silverman et al., 2011).

1991bg-like objects

1991bg-like objects (Filippenko et al., 1992a; Leibundgut et al., 1993) named after the prototypical supernova SN 1991bg, are faint events with peak luminosities in the range from -16.9 mag to -17.9 mag. They merely produce about $0.1\,M_\odot$ of ^{56}Ni (Mazzali et al., 1997). At least 15% of all SNe Ia seem to fall into this subclass (Li et al., 2011). However, the real number of these objects may be highly underestimated, since due to their low brightness an uncertain fraction of them may elude detection. The light curves show a rapid decline that does not obey the Phillips relation (e.g. Garnavich et al., 2004; Hicken et al., 2009). Characteristic for their spectra is the absence of the second maximum in the infrared. The spectra

show predominantly lines of intermediate mass elements and only weak lines of iron (Mazzali et al., 1997). There is a tendency for these objects to occur preferentially in elliptical galaxies in old stellar populations (Sullivan et al., 2006).

Summary

From the observations of peculiar SNe Ia, there is no direct conclusion whether the majority or at least some of them are just extreme outliers of normal SNe Ia, or if a part of these events must be considered as an independent class with an own progenitor system. It is remarkable that between the 1991bg-like objects and the normal SNe Ia there seems to be a gap in the ^{56}Ni yields of approximately $0.1 \ldots 0.4\,M_{\odot}$. In this range only a few events have been found so far, like SN 2005hk (see Phillips et al., 2007). The 1991bg-like objects seem to have similar light curve and spectral properties (Garnavich et al., 2004; Taubenberger et al., 2008) that are distinct from the normal SNe Ia. This may indicate that these objects have a progenitor system and/or an explosion mechanism that is different from those of normal SNe Ia. Also the superluminous events, where a large amount of ^{56}Ni has to be produced in the explosion process may not be easily explained with the same scenario that is favored for normal SNe Ia.

2.2 Progenitor systems

As described at the end of Section 2.1.1 it is believed that the cause of normal SNe Ia is a white dwarf that undergoes a thermonuclear explosion. A white dwarf is a stable object of high density where the pressure of the degenerate electron gas compensates for self-gravity. A spontaneous explosion seems improbable, so that an isolated white dwarf will stay in this equilibrium forever, where merely its temperature declines and density increases on very long time scales (e.g. Lesaffre et al., 2006). Therefore, it is believed that SNe Ia occur only in close binary systems, in which a companion star plays a crucial role in the evolution of the white dwarf toward its explosion. Due to mass accretion from the companion onto the white dwarf, the latter may become unstable until physical conditions are achieved that lead to a thermonuclear explosion (see Section 2.3).

White dwarfs can be composed of pure helium or a mixture of carbon/oxygen or oxygen/neon. The mass of helium white dwarfs is usually lower than $0.45\,M_{\odot}$ (Iben & Tutukov, 1985). Due to mass accretion the helium may ignite in which case the thermonuclear combustion produces solely iron group elements and no intermediate mass elements (Nomoto & Sugimoto, 1977; Woosley et al., 1986), inconsistent with observations. White dwarfs that are composed of oxygen and neon show in numerical simulations that they preferentially collapse to neutron stars (Saio & Nomoto, 1985; Nomoto & Kondo, 1991; Gutierrez et al., 1996). In addition, these white dwarfs are probably not numerous enough to come into question for SN Ia explosions (Livio & Truran, 1992). Therefore, carbon/oxygen white dwarfs seem to be the most appropriate candidates for SN Ia explosions. The physical properties and composition of the companion star, however, are highly uncertain. Depending on the type of the companion, different theoretical models have been proposed.

2.2.1 Single-degenerate scenario

In the *single-degenerate scenario* (Whelan & Iben, 1973; Nomoto, 1982; Iben & Tutukov, 1984) the companion is either a main sequence star, a helium star or a red giant. The distance

between both components is so close that the companion fills its Roche lobe, leading to a continuous mass transfer of hydrogen or helium from the companion onto the surface of the white dwarf. If the companion is a red giant the mass transfer may also occur by stellar winds.

Hydrogen-accreting white dwarf and the Chandrasekhar-mass explosion model

In the case of the accretion of hydrogen-rich material, the hydrogen burns at the surface of the white dwarf to helium first that further burns to carbon. In this way, the mass of the white dwarf increases slowly. There is an upper limit for the mass of a white dwarf at which the pressure of the degenerate electron gas cannot compensate for self-gravity anymore. This mass is called the *Chandrasekhar limit* M_{CH} (Chandrasekhar, 1931) which is approximately $M_{\mathrm{CH}} \approx 1.4\,M_{\odot}$ for a non-rotating white dwarf. For masses $M > M_{\mathrm{CH}}$ a gravitational collapse will turn the white dwarf into a neutron star. However, under certain circumstances the white dwarf may explode just before its mass has reached M_{CH}. When approaching M_{CH}, the central density increases rapidly above $10^9\,\mathrm{g\,cm^{-3}}$. The temperature becomes high enough for the carbon ignition, which marks the beginning of the so-called *simmering phase* (see Section 2.3.1). At the end of this phase, a thermonuclear runaway sets in that eventually leads to the explosion and destruction of the whole white dwarf. This model is called the *Chandrasekhar-mass explosion model*.

Since all white dwarfs have the same mass at the time of the explosion, this model can explain some of the homogeneous features of SN Ia light curves and spectra. The observed variations can be mainly explained by different ignition and explosion dynamics (see Section 2.3) which in turn partially depend on the carbon/oxygen ratio, metallicity and rotation of the white dwarf. The main weakness of the Chandrasekhar-mass explosion model is that depending on the initial mass and rotation of the binary system, there is only a small window for allowed accretion rates at which the additional mass has to be transferred onto the surface of the white dwarf. In the case of hydrogen transfer, Nomoto & Kondo (1991) give an accretion rate of $\sim 10^{-7}\,M_{\odot}$ per year. If the accretion rate is of this order, the accreted material can burn in a stable way to heavier elements at the surface of the white dwarf. The produced heat in this process slowly penetrates the interior of the white dwarf, so that its center is continuously heated up to a point where conditions for the carbon fusion are achieved just before M_{CH} is reached. If the mass transfer occurs too fast, carbon ignites at the surface, which will turn the white dwarf into an oxygen/neon white dwarf, eventually leading to a collapse to a neutron star. If the accretion rate is too slow a constant fusion of the material at the surface of the white dwarf is not possible for a longer time and some of the accreted material will be expelled as repeated novae breakouts.

The problem of the required accretion rates is related to the question of whether the Chandrasekhar-mass explosion model can explain the observed SN Ia rates. Following Ruiter et al. (2009) the observed SN Ia rates are several orders of magnitude higher than the expected rates from exploding hydrogen accreting Chandrasekhar-mass white dwarfs. Furthermore, it is expected that the nuclear hydrogen burning at the surface of the white dwarf will release detectable soft X-rays (Kahabka & van den Heuvel, 1997). The X-ray emissions of nearby elliptical galaxies, however, seem to be far too low to explain the observed SN Ia rates with exploding hydrogen accreting Chandrasekhar-mass white dwarfs (Gilfanov & Bogdán, 2010).

Another question is whether the hydrogen itself should be detectable during the supernova breakout. Since there are no hydrogen lines in SN Ia spectra one can conclude that the

amount of hydrogen in the system must be so low that it eludes direct detection. However, it is believed that when the ejecta of the exploding white dwarf collides with the companion star, some of the hydrogen rich material in the outer layer of the companion is stripped off and mixed into the ejecta (Marietta et al., 2000), which may have an effect on the spectra. Pakmor (2010) showed that only $0.01\,M_{\odot}$ of hydrogen rich material is stripped off from the companion by the impact and mixed into the ejecta, which is lower than the current detection limit. There is also the possibility that the amount of hydrogen of the system at the time where the supernova breaks out is only marginal. One can assume that apart from the mass growth the white dwarf also gains a substantial amount of angular momentum during the accretion process that may postpone the explosion (Di Stefano et al., 2011; Justham, 2011). During this delay, the companion star may exhaust its hydrogen-rich envelope and shrink to a certain degree, so that before approaching the explosion phase, the companion does not fill its Roche lobe anymore (Justham, 2011). When the white dwarf eventually explodes, the interaction between the ejecta and the shrunken companion is expected to be much lower.

Helium-accreting white dwarf and the sub-Chandrasekhar mass explosion model

In the case of helium accretion from a helium star (Woosley & Weaver, 1994), only the helium needs to be burned to carbon. There is only marginal X-ray emission, since the nuclear energy release of the fusion from helium to carbon is far lower than the fusion of hydrogen to helium. Hence, these systems would be more consistent with the observations of Gilfanov & Bogdán (2010), but the calculations of Ruiter et al. (2009) show that these systems seem to be not frequent enough to explain the observed rates of SNe Ia. In this scenario, however, there is the possibility that the white dwarf explodes at a time when its mass is far below M_{CH}. In this *sub-Chandrasekhar mass explosion model* the helium is not steadily burned, so that the white dwarf may be enveloped by a degenerate helium shell. If the mass of this shell grows large enough, it may become dynamically unstable leading to a detonation that spreads over the entire surface of the white dwarf. This in turn can trigger a second detonation in the center of the carbon/oxygen core due to the convergence of shock waves that originate from the detonation of the helium shell (Woosley & Weaver, 1994; Livne & Arnett, 1995).

To a certain extent, the sub-Chandrasekhar mass explosion model can also be applied to systems where initially hydrogen is accreted that burns to helium at the surface of the white dwarf (e.g. Cassisi et al., 1998; Piersanti et al., 1999, 2000). In contrast to the Chandrasekhar-mass explosion model, a far lower mass has to be accreted from the companion star until the explosion occurs, so that the sub-Chandrasekhar mass explosion model is more consistent with the observed SN Ia rates. Fink et al. (2007) showed that a helium shell of only $0.1\,M_{\odot}$ is already sufficient to trigger the carbon/oxygen detonation. Differences in the ^{56}Ni yields can be obtained from different masses and densities of the white dwarfs. In particular, Fink et al. (2010) and Sim et al. (2010) showed that the sub-Chandrasekhar mass explosion model can reproduce the whole observed variations in the brightness of normal SNe Ia. However, radiative transfer calculations by Kromer et al. (2010) for these models showed some discrepancies of the synthetic light curves and spectra with observations.

2.2.2 Double-degenerate scenario

In the *double-degenerate scenario* (Iben & Tutukov, 1984; Webbink, 1984) both components of the binary progenitor system are white dwarfs. In the beginning (when the formation of

the second white dwarf is completed) the distance between both white dwarfs is commonly so large that mass transfer is impossible. However, the system loses angular momentum due to emission of gravitational waves, leading to a continuous decrease in the distance between both components. When one of the white dwarfs fills its Roche lobe, mass transfer sets in, where the stability of the transfer depends strongly on the mass ratio of the white dwarfs. If one component is a helium white dwarf, a similar scenario as in the sub-Chandrasekhar mass explosion model may happen (Guillochon et al., 2010). If both components are carbon/oxygen white dwarfs (which we assume in the following) and if the total mass of the system exceeds M_{CH} the system may behave similarly to the Chandrasekhar-mass explosion model, but this has not been shown yet. However, this scenario is only possible if the mass difference of the white dwarfs is sufficiently large, which ensures a stable mass transfer. If this is not true, the less massive white dwarf will be disrupted due to tidal forces shortly after mass transfer sets in (Benz et al., 1990; Yoon et al., 2007; Motl et al., 2007; Lorén-Aguilar et al., 2009) and its material is accreted at such a high rate by the more massive white dwarf that the carbon ignites at its surface (Saio & Nomoto, 1998). This will turn the white dwarf into an oxygen/neon white dwarf that will further collapse to a neutron star.

However, during the merger of the white dwarfs conditions for a detonation may be achieved, so that this scenario may lead to a SN Ia explosion (Pakmor et al., 2010, 2011). Perhaps it is possible that during the merger process neither a detonation nor a conversion of the white dwarf into a neutron star happens, in which case the mass accretion continues. Due to conversion of angular momentum, the differential rotation of the white dwarf increases. In this way, the mass of the white dwarf can grow up to $2\,M_{\odot}$ (Yoon & Langer, 2004, 2005), where an ensuing explosion in the interior of the white dwarf may proceed similar as in the non-rotating Chandrasekhar-mass explosion model. However, as stated in Section 2.2.1 the white dwarf may have to spin-down to a certain degree in order to explode.

Since the total mass in a double degenerate merger may exceed M_{CH} to a large extent there are conjectures that the explosion of these *super-Chandrasekhar mass* objects may explain the observed superluminous events. But calculations of Pakmor (2010) show that within the most massive merger of two white dwarfs, the maximum mass of ^{56}Ni that can be obtained is approximately $1\,M_{\odot}$, insufficient to explain superluminous events.

The main advantage of the double-generate scenario is that it easily explains the absence of hydrogen lines in the spectra. Compared to the single-degenerate Chandrasekhar-mass explosion model, there are no strict limitations of the accretion rates, since the accreted material has not to be burned to heavier elements. In addition, from population synthesis calculations one can derive that the frequency at which these systems occur can explain the observed SN Ia rates better than any other progenitor system (Ruiter et al., 2009). The results of Pakmor et al. (2010) and Pakmor et al. (2011) indicate that during the merger of two carbon/oxygen white dwarfs with an individual mass of about $0.9\,M_{\odot}$ and a sufficient small mass difference, conditions for a detonation are reached. However, the produced ^{56}Ni yield in the simulations was only $0.1\,M_{\odot}$, i.e. far below the mass needed to explain the brightness of normal SNe Ia. It is possible that these models are capable of explaining the 1991bg-like objects, since apart from the produced amount of ^{56}Ni also other features like synthesized light curves and spectra seem to fit the observed properties of the 1991bg-like objects quite well (Pakmor et al., 2010, 2011). However, a very recent study indicates that more massive merger may produce a significant higher ^{56}Ni yield that is comparable with typical normal SNe Ia (Pakmor et al., 2012).

2.2.3 Summary

All described and according to our current knowledge all potential progenitor scenarios have individual strengths and weaknesses. It is likely that not all observed SNe Ia can be described with a single progenitor scenario. This work is based on the Chandrasekhar-mass explosion model. Despite the discrepancy of the predicted SN Ia rates, this model has had great success in reproducing some of the main observed features of normal SNe Ia. In the following, the ignition phase and theoretical explosion models of Chandrasekhar-mass white dwarfs are discussed.

2.3 Explosion models

2.3.1 Simmering phase and ignition

The main physical processes leading to the ignition and explosion of the white dwarf are highly uncertain. However, there is a widely accepted picture about the final phase directly prior to the ignition that will be summarized here. When the mass of the white dwarf approaches M_{CH}, its center is highly degenerate and thermodynamic conditions for the carbon ignition are reached (Nomoto, 1982), which marks the beginning of the so-called *simmering phase*. This phase can be subdivided coarsely into three stages. In the first stage, carbon burning occurs only at a low rate, where neutrino losses alone are able to carry away all of the produced nuclear energy (Arnett, 1971a; Nomoto et al., 1984; Woosley & Weaver, 1986; Winget et al., 2004). The nuclear energy release, however, depends strongly on the temperature, so that a low temperature increase leads to a large growth of the nuclear energy production rate. At some point, when the time scale for carbon fusion becomes shorter than the time scale for neutrino losses, convection sets in, where the nuclear energy excess is transported outward due to convective motions (Arnett, 1969, 1971a; Woosley & Weaver, 1986). This leads to a rapid growth of a convective core, which is also called the *carbon-flash phase* that may last for several hundred years. Within this phase the so-called URCA-process is of high importance (Gamow & Schoenberg, 1941; Paczyński, 1972; Barkat & Wheeler, 1990; Aparicio & Isern, 1993; Lesaffre et al., 2005; Podsiadlowski et al., 2008; Förster et al., 2010).[4] The concept of this process is based on the assumption that apart from ^{12}C and ^{16}O there are traces of other heavier elements in the white dwarf[5], of which ^{23}Ne and ^{23}Na play a major role here. In the vicinity of the center of the white dwarf it is energetically favorable for a ^{23}Na nucleus to turn into a ^{23}Ne nucleus by electron capture. Due to convection the ^{23}Ne nucleus ascends up to a place, where it becomes energetically favorable to emit an electron by β^-- decay. Hence, the ^{23}Ne nucleus converts back to a ^{23}Na nucleus that now descends back to the center of the star. The described cycle can be

[4] The process was first discussed by George Gamow and Mario Schoenberg in a casino named *Cassino da Urca* in Rio de Janeiro, where Gamow said to Schoenberg that "the energy disappears in the nucleus of the supernova as quickly as the money disappeared at that roulette table" (see also Nadyozhin (1995) and Haensel (1995) and references therein).

[5] These elements result mostly from the metallicity of the main sequence star from which the white dwarf evolved. However, due to the high densities in the central region of the white dwarf, additional neutronization effects may lead to a further increase of the metallicity in the simmering phase (Piro & Bildsten, 2008).

summarized by the two following reactions:

$$^{23}\mathrm{Na} + e^- \rightarrow {}^{23}\mathrm{Ne} + \nu, \tag{2.1}$$

$$^{23}\mathrm{Ne} \rightarrow {}^{23}\mathrm{Na} + e^- + \overline{\nu}. \tag{2.2}$$

We see that in every conversion of the nucleus an electron neutrino ν or an electron anti-neutrino $\overline{\nu}$ is emitted that is able to carry away energy without interaction with the stellar material. Therefore, the URCA-process constitutes an enhanced cooling mechanism of the central region in this phase that may delay the initiation of the explosion.

In the last stage of the simmering phase the time scale for carbon fusion becomes shorter than the time scale of convective circulations. At this point efficient cooling mechanisms do not exist any longer and the energy released from the carbon fusion cannot be transported away from the central region. In addition, the white dwarf is unable to expand and to cool, since due to the high degeneracy of the central area, the pressure is independent of the temperature. Eventually the center of the star is heated up rapidly leading to a thermonuclear runaway that marks the birth of a thermonuclear flame and the begin of the explosion.

There are several parameters, like the initial mass, the accretion history, as well as the cooling time of the white dwarf that determine the thermodynamic state in the interior of the star. Lesaffre et al. (2006) derive a possible range of central densities from less than 2×10^9 g cm^{-3} up to more than 5×10^9 g cm^{-3} at ignition time of the flame. One uncertainty in the evolution up to the ignition of the flame is the value of the screened ^{12}C - ^{12}C fusion rate (Itoh et al., 2003; Gasques et al., 2005, 2007; Jiang et al., 2007). However, it seems that the central density at ignition time depends only weakly on the exact value of this rate (Cooper et al., 2009; Iapichino & Lesaffre, 2010). While metallicity has a high impact on the brightness of the explosion (Timmes et al., 2003; Travaglio et al., 2005; Bravo et al., 2010), the central density at ignition time also show only a weak dependence on metallicity as well as the carbon/oxygen ratio (Lesaffre et al., 2006).

Remarkable efforts have been made to study the simmering phase in detail but there are no clear conclusions yet about the physical properties and the geometry of the ignition region (e.g. Garcia-Senz & Woosley, 1995; Höflich & Stein, 2002; Woosley et al., 2004; Kuhlen et al., 2006; Almgren et al., 2006; Piro & Bildsten, 2008; Piro & Chang, 2008; Zingale et al., 2009; Aspden et al., 2011; Nonaka et al., 2012). In numerical simulations that do not follow the pre-ignition evolution but start immediately at ignition time of the flame, a simple single ignition or multiple ignitions in the vicinity of the center (Plewa, 2007; Röpke et al., 2006, 2007a,b) or even time-dependent, stochastic ignitions (Schmidt & Niemeyer, 2006) are frequently used. Woosley et al. (2004) propose a multispot ignition scenario where the first ignition occurs at a distance of $150 - 200$ km off-center. The diameter of an individual ignition spot is expected to be of the order of a kilometer (Iapichino et al., 2006). Another more recent study of Nonaka et al. (2012) suggests a single off-center ignition within a radius of roughly 50 km.

As the ignition process, also the burning mode of the ignited flame is unknown. From combustion theory, however, it is known that the flame can propagate either as a *detonation* or as a *deflagration*.

2.3.2 Detonations

The first model to explain the explosion of a white dwarf whose mass is near the Chandrasekhar limit was proposed by Arnett (1969), where a detonation commences in the center

of the white dwarf. A detonation occurs when the ignition leads to a strong pressure gradient (commonly described as a shock) that propagates supersonically with respect to the sound speed in the unburned carbon/oxygen material. The shock leads to a compression and heating of the material up to a point where thermonuclear burning processes occur. Hence, the shock wave and the flame are linked with each other and move with the same speed through the white dwarf.

The one-dimensional model of Arnett (1969) showed that a detonation releases enough energy to gravitationally unbind the star. However, due to the supersonic flame speed the white dwarf cannot react with an expansion, so that the whole carbon/oxygen composition is burned at high densities to heavy iron group elements. This is inconsistent with the observed spectra, since the latter also show the presence of intermediate mass elements (see Section 2.1). Hence, pure detonations of Chandrasekhar-mass white dwarfs are ruled out as a viable scenario to explain SN Ia explosions.

2.3.3 Deflagrations

Apart from a shock-driven detonation the burning in a white dwarf may proceed by thermal conduction. The burning speed is far slower than the sound speed in the unburned material. This burning mode is called a *deflagration*.[6] While the flame propagates outward the white dwarf reacts with an expansion, where the degree of this expansion depends strongly on the nuclear energy release. Due to the expansion and the associated decline in the density, there is a point at which the carbon/oxygen mixture cannot be burned to iron group elements anymore, so that in the later explosion phase mainly intermediate mass elements are produced. Thus in contrast to a pure detonation, a deflagration can explain the observed intermediate mass elements (e.g. Nomoto et al., 1976, 1984).

An undisturbed deflagration of a white dwarf, however, would never be strong enough to explain the main observed features of SN Ia explosions. The flame would propagate so slowly that the burning ceases after a marginal fraction of the unburned material has been converted to heavier elements. Moreover, the energy release would be too low to overcome the gravitational binding energy of the white dwarf. However, as shown in Chapter 3, instabilities occur during the deflagration that cause turbulent motions. The burning processes are highly affected by the interaction with turbulence, leading to an acceleration of the flame and an increase of the flame surface area, which in turn enhances the energy release.

The results of numerical simulations of pure turbulent deflagrations show that the released energy is sufficient to unbind the white dwarf (Reinecke et al., 2002; Gamezo et al., 2003; Röpke et al., 2007a). However, it should be noted that the dynamics of the turbulent flame and the energy release in pure deflagrations crucially depend on the modeled ignition scenario of the flame. Compared to pure detonations, pure turbulent deflagrations explain the observed properties of SNe Ia much better. The main problem of pure deflagrations, however, is that there are regions of unburned material left behind the flame in the central part of the white dwarf. This would be visible in the late time spectra, which is not the case for normal SNe Ia (Khokhlov, 2000; Gamezo et al., 2003; Kozma et al., 2005). Moreover, even strong turbulent deflagrations produce usually no more than $0.4\,M_\odot$ of ^{56}Ni and also the energy release tends to be too low compared to observations (Gamezo et al., 2003; Röpke et al., 2007a). Therefore, pure deflagrations cannot account for the observed variations in the brightness of normal SNe Ia. They may, however, explain some peculiar events, such as

[6] Sometimes this burning mode is also simply described as *slow burning*.

the supernovae SN 2002cx and SN 2005hk (Jha et al., 2006; Phillips et al., 2007).

2.3.4 Delayed Detonations

The *delayed detonation* model, introduced by Khokhlov (1991a), can fix the major problems of both pure deflagrations and pure detonations. The idea is that the explosion starts out as a deflagration and in a later explosion phase, a physical mechanism leads to a *Deflagration-to-Detonation Transition (DDT)* (Blinnikov & Khokhlov, 1986, 1987; Khokhlov, 1991a; Khokhlov et al., 1997; Niemeyer & Woosley, 1997). Due to the onset of the detonation, the explosion dynamics are drastically changed. The unburned material that is left behind by the deflagration front may be reached and burned by the detonation. Hence, the amount of iron group and intermediate mass elements are increased due to the additional burning of the carbon/oxygen mixture. In summary, a chemical composition can be obtained in the delayed detonation model that is in good agreement with observations (Gamezo et al., 2005; Golombek & Niemeyer, 2005; Röpke & Niemeyer, 2007; Mazzali et al., 2007; Bravo & García-Senz, 2008; Kasen et al., 2009).

For the delayed detonation model, the strength of the deflagration is an important parameter that sets the brightness of the explosion. In general, weak deflagrations lead to a low expansion of the star, so that a delayed detonation can burn a significant part of the stellar material at high densities to ^{56}Ni. Conversely, in strong deflagrations where the star expands much further, most of the unburned material is at low densities, where a delayed detonation burns less material to ^{56}Ni. Depending on the strength of the deflagration which in turn depends strongly on the ignition properties of the deflagration flame, a broad range of ^{56}Ni yields can be obtained from delayed detonation models that is consistent with the observed variations in the brightness (e.g. Mazzali et al., 2007; Kasen et al., 2009).

The problem of the delayed detonation model is that the physics of DDTs is not well understood. A generally accepted picture of DDTs is that this process occurs in a mixed region of a specific size that is composed of hot burned and cold unburned material.[7] A sufficient mixing of both components in turn requires a certain turbulent intensity. Therefore, the properties of turbulence play an important role in this explosion scenario which is discussed in more detail in Section 3.3.3.

2.3.5 Explosion of differentially rotating white dwarfs

Differential rotation of the white dwarf can significantly affect the explosion characteristics. The mass of differentially rotating white dwarfs may grow as large as $2\,M_\odot$ (Yoon & Langer, 2004, 2005). Pure deflagrations of these super-Chandrasekhar-mass models show only a marginal burning and an aspherical flame propagation that is attributed to a centrifugal expansion and to anisotropic buoyancy and mixing effects (Pfannes et al., 2010b). In contrast, pure detonations lead to very bright explosions that are comparable with superluminous events (Pfannes et al., 2010a). The nuclear energy release, however, is here so high that the ejecta expands too fast compared to observations. In addition, also in pure detonations the explosion evolves highly anisotropic, leading to an aspherical structure of the ejecta that is observed preferentially for the faint 1991bg-like objects. In simulations of delayed detonations of differentially rotating white dwarfs Fink (2010) found similar results as for the pure detonations simulated by Pfannes et al. (2010a).

[7] A recent study of Poludnenko et al. (2011) also supports the idea that a DDT may happen in unconfined media.

2.3.6 Gravitationally confined detonation

In the *gravitationally confined detonation (GCD)* model (Plewa et al., 2004; Plewa, 2007; Townsley et al., 2007; Jordan et al., 2008; Meakin et al., 2009) a delayed detonation is triggered in the late deflagration phase, but the whole explosion dynamics are fundamentally different compared to the delayed detonation model described in Section 2.3.4. The GCD model is primarily based on a very weak deflagration that starts off-center in the form of one or a few bubbles that burn aspherically toward the surface of the white dwarf. Turbulence leads to an increase of the burning speed and the flame surface area. However, the overall energy release is far too low to unbind the star gravitationally and only a marginal fraction of the entire carbon/oxygen material is burned at the time when the flame breaks through the surface of the white dwarf. The strong surface gravity forces the burned material to sweep along the surface until it converges at the opposite side of the star. At this convergence point unburned material is compressed and heated, leading to conditions where carbon ignites. In this case, two jets may be formed, while an inwardly directed jet is susceptible for shear instabilities, where eventually conditions for a detonation are achieved (Meakin et al., 2009). Because of the massive amount of unburned material that additionally resides at high densities, the detonation burns most of the material to iron group elements, where commonly more than $1\,M_{\odot}$ of ^{56}Ni is synthesized (e.g. Meakin et al., 2009). Hence, the GCD model produces exclusively bright events, like the 1991T-like objects.

2.3.7 Pulsational delayed detonation and pulsational reverse detonation model

The *pulsational delayed detonation (PDD) model* is similar to the delayed detonation model, described in Section 2.3.4, but a DDT occurs after one or several pulsations of a gravitationally bound white dwarf (Ivanova et al., 1974; Khokhlov, 1991a). A variant is the *pulsational reverse detonation (PRD) model*, where a deflagration leads to an initial expansion of the white dwarf that becomes damped before the gravitation is overcome. During the recollapse a detonation sets in due to compression and heating in the center, after burned material from the deflagration has ascended while new unburned material has descended to the center of the star (Dunina-Barkovskaya et al., 2001; Bravo & García-Senz, 2005, 2006). Within the PRD model ^{56}Ni yields can be obtained that are consistent with normal SNe Ia (Bravo & García-Senz, 2006). However, synthesized spectra of PRD models show at the time of maximum brightness carbon lines and at late times a considerable amount of iron group elements in the outer layers that are inconsistent with the observations (Baron et al., 2008).

2.3.8 Summary

From the discussed explosion mechanisms in a Chandrasekhar-mass white dwarf, the delayed detonation model described in Section 2.3.4 is a preferred model that is capable of explaining several main features of normal SNe Ia. In particular, a recent study of Kasen et al. (2009) and Blondin et al. (2011) showed that apart from the obtained ^{56}Ni yields also synthetic light curves and some spectral properties seem to be in good agreement with observations. It is remarkable that the light curves seem to reproduce the Phillips relation quite well. The uncertainty of the physics of the DDT process remains a problem to date. One main subject on which this work focuses is the construction of a new model that includes the current knowledge of the physics of DDTs. As already described, turbulence in the deflagration plays a crucial role for the DDT, hence we need to understand the properties of turbulence in this burning phase first.

3

Turbulence and delayed detonations in SNe Ia

The burning processes in a deflagration of a white dwarf are accelerated by turbulence in such a way that the associated increase in the energy release may be sufficient to gravitationally unbind the star (e.g. Reinecke et al., 2002). However, for reasons described in Section 2.3.3 pure turbulent deflagrations cannot account for the observed variations of normal SNe Ia. Here turbulence again may point to a way out, since it is believed that strong turbulent velocity fluctuations constitute a necessary constraint for a delayed detonation (e.g. Woosley et al., 2009). In this chapter the properties of turbulence in the deflagration phase and its implications for the delayed detonation scenario are explained. Since the cause of turbulent motions is the occurrence of instabilities during the deflagration in a white dwarf, we first describe these instabilities in Section 3.1. In Section 3.2 the properties of turbulence itself are discussed. Finally, the delayed detonation model is described in detail in Section 3.3 that is based on our current knowledge and is a key part of this work. Since the burning speed of the deflagration flame is much slower than the sound speed in the unburned material of the white dwarf, we restrict all considerations of this burning phase to incompressible flows in the following.

3.1 Instabilities in deflagrations of white dwarfs

We consider a system that has the length L, a mean flow velocity V and the kinematic viscosity ν. The flow characteristic can be estimated by the dimensionless *Reynolds number* Re (Stokes, 1851; Reynolds, 1883)

$$Re = \frac{L \cdot V}{\nu}. \tag{3.1}$$

The Reynolds number is a measure of the ratio of inertial forces to viscous forces. For sufficiently low Re effective external perturbations are suppressed and damped due to viscous forces. The flow is characterized by a slow, regular and eddy-free motion that is called a *laminar flow*. With growing Re viscous forces become less efficient and the flow is more susceptible to external perturbations. The condition where a fluid becomes unstable to perturbations is given by a critical Reynolds number Re_{crit}. For $Re > Re_{\mathrm{crit}}$ occurring

perturbations are not damped anymore and they will grow without restrictions. In this case, the flow is characterized by an irregular and disordered motion with some pronounced vortex structures, which is called a *turbulent flow*. If Re_{crit} is known, equation (3.1) can be applied to get a first impression of the main flow characteristic for a given system. However, to determine under what conditions a flow becomes unstable to a certain instability an analysis of the instability is required, which is outlined in the following sections.

3.1.1 Stability analysis of incompressible flows

We consider an incompressible fluid with a constant kinematic viscosity ν and density ρ that is not exposed to external forces. Then the momentum balance reads

$$\frac{\partial \boldsymbol{v}}{\partial t} + (\boldsymbol{v} \cdot \nabla)\boldsymbol{v} = -\frac{\nabla p}{\rho} + \nu \Delta \boldsymbol{v} \tag{3.2}$$

with the incompressibility constraint

$$\nabla \cdot \boldsymbol{v} = 0, \tag{3.3}$$

where P and $\boldsymbol{v}$ denote the pressure and velocity. Equation (3.2) is the *incompressible Navier-Stokes equation* (Navier, 1823) that constitutes the equation of motion for an incompressible fluid (e.g. Landau & Lifschitz, 1991). In general, a fluid may become unstable against infinitesimal perturbations if $Re \approx Re_{\mathrm{crit}}$ (e.g. Landau & Lifschitz, 1991). Then the onset of an instability and Re_{crit} can be estimated with the following procedure. The stationary solution of the Navier-Stokes equation (3.2) is superimposed by a small non-stationary perturbation. For the resulting system of equations, an ansatz of the form $\exp(i\boldsymbol{k}\boldsymbol{x} + \omega t)$ is made. That way we obtain a dispersion relation $\omega(k)$ between the complex frequencies ω and the wave numbers k of the perturbation. If all possible $\omega(k)$ have only negative real parts, all perturbations will decay exponentially with time t and $Re < Re_{\mathrm{crit}}$ holds. For $Re = Re_{\mathrm{crit}}$ there is exactly one $\omega(k)$, of which the real part is zero. This limiting case is characterized by a varying behavior between a laminar and turbulent flow. If there is only a single $\omega(k)$ with a positive real part, the perturbation will grow unrestrictedly with t. Consequently the flow is unstable to this instability, and $Re > Re_{\mathrm{crit}}$ holds.

3.1.2 Instabilities of thermonuclear deflagration fronts

After the ignition, the deflagration flame propagates from the center outward toward the surface of the white dwarf. The stellar material that is traversed by the flame is thermonuclearly burned to heavier elements. The energy release and the reaction rate depend on the density and temperature as well as on the composition and the thermal conductivity of the material which is currently burned. As long as the exothermic reactions release enough heat to ignite the surrounding material the deflagration can spread further through the star.

The onset of certain instabilities may crucially affect the flame propagation. Hence, a stability analysis is important to understand the impact of these instabilities on the explosion dynamics in the deflagration. In the following, we first discuss the properties of laminar burning, in which instabilities are neglected. Then the most important instabilities are described that occur in the deflagration. All considerations of burning in this chapter are restricted to *premixed flames*, where it is assumed that all necessary reactants for the burning are available in the fuel mixture.

Laminar Burning

In laminar burning there is a balance between thermal diffusion and energy generation. The profile of the deflagration flame is composed a diffusion zone in which the *fuel* (here the carbon/oxygen composition) is heated up to its ignition temperature, and a reaction zone, in which the burning takes place (e.g. Mikhel'son, 1889). For the diffusion time scale $\tau_{\mathrm{diff}} \sim \delta^2/\kappa$ holds, where δ is the flame width and κ is the thermal diffusivity. For the nuclear burning time scale $\tau_{\mathrm{nuc}} \sim e/\dot{S}$ holds, where e is the specific energy and $\dot{S}$ the specific energy generation rate. Since in equilibrium $\tau_{\mathrm{diff}} = \tau_{\mathrm{nuc}}$, we find (Mikhel'son, 1889; Landau & Lifschitz, 1991)

$$\delta \approx \sqrt{\frac{\kappa e}{\dot{S}}}. \tag{3.4}$$

In the time τ_{nuc} the flame progresses the distance δ. With equation (3.4) the laminar burning speed $u_{\mathrm{lam}} = \delta/\tau_{\mathrm{nuc}}$ results to

$$u_{lam} \approx \sqrt{\frac{\kappa \dot{S}}{e}}. \tag{3.5}$$

The laminar burning constitutes an ideal case of an undisturbed deflagration that basically does not occur in SN Ia explosions. However, the velocity in equation (3.5) is a good estimate for the burning speed v_{flame} in the early deflagration phase. A more detailed study of laminar burning velocities was performed by Timmes & Woosley (1992). The authors applied a fit to numerically calculated values of u_{lam} in a carbon/oxygen white dwarf for a range of fuel densities ρ_{fuel} of $10^7\,\mathrm{g\,cm^{-3}} \leq \rho_{\mathrm{fuel}} \leq 10^{10}\,\mathrm{g\,cm^{-3}}$, where u_{lam} is then given by

$$u_{\mathrm{lam}} = 92.0 \times 10^5 \left(\frac{\rho_{\mathrm{fuel}}}{2 \times 10^9}\right)^{0.805} \left[\frac{X(^{12}\mathrm{C})}{0.5}\right]^{0.889} \mathrm{cm\ s^{-1}}. \tag{3.6}$$

Here $X(^{12}\mathrm{C})$ denotes the specific mass fraction of ^{12}C. The uncertainty of u_{lam} in equation (3.6) is approximately 10% (Timmes & Woosley, 1992). Typical values for u_{lam} and δ in the early explosion phase are $u_{\mathrm{lam}} \approx 10^7\,\mathrm{cm\ s^{-1}}$ and $\delta = 10^{-5}\,\mathrm{cm}$ (Timmes & Woosley, 1992). Therefore, the width of the flame is very thin compared to other characteristic length scales of the white dwarf. Full-star simulations that follow the explosion of the whole white dwarf are usually unable to resolve the flame width. This is why the flame is sometimes treated as a sharp discontinuity in these simulations.[1]

The Landau-Darrieus instability

The *Landau-Darrieus instability (LD instability)* is a pure hydrodynamic instability. Darrieus (1938) and Landau (1944) revealed surprisingly that planar laminar flames in the discontinuity approximation are generally unstable. The dispersion relation of this instability is given by (Landau & Lifschitz, 1991)

$$\omega(k)_{\mathrm{LD}} = k u_{\mathrm{lam}} \frac{\mu}{1+\mu}\left(\sqrt{1+\mu-\frac{1}{\mu}} - 1\right), \tag{3.7}$$

[1] During the deflagration the laminar flame becomes broader up to several centimeters (Timmes & Woosley, 1992). However, at this explosion phase the flame is already strongly affected by turbulence which may broaden the flame up to several kilometers (see Section 3.2.3). Hence, strictly speaking, a turbulently broadened flame cannot be considered as a sharp discontinuity anymore.

where $\mu = \rho_{\mathrm{fuel}}/\rho_{\mathrm{ash}}$ is the ratio of the density in the fuel to the *ash* (the burned material). Due to the high heat generation in the burning processes and the partial lifting of the electron degeneracy $\rho_{\mathrm{fuel}} > \rho_{\mathrm{ash}}$. Hence, $\Re(\omega(k)_{\mathrm{LD}}) > 0$ follows for all wave numbers, leading to an uninterrupted growth of the instability. In the vicinity of the center of the white dwarf, the high densities and the associated high degree of the electron degeneracy lead initially to the effect that the burned material can hardly expand, so that here $\mu \sim 1$. However, the density declines continuously from the center outward, which is further amplified by the expansion of the star during the deflagration. In summary, the outward propagating flame becomes more unstable during the explosion process. The growth of the perturbations, however, is limited by cusp formation in the nonlinear regime and the flame is stabilized in a cellular structure (Zel'Dovich, 1966; Röpke, 2003). Consequently, the flame is only deformed slightly and its surface is increased mildly. The burning speed remains almost unchanged. Therefore, the LD instability in deflagrations plays a subordinate role in the generation of turbulent motions.

The Rayleigh-Taylor instability

In the description of the LD instability we indicated that in the deflagration phase a stratification occurs, where denser unburned material lies on top of less dense burned material. Due to the gravitational field of the white dwarf a configuration develops in which the gradients of gravitational acceleration g and density show in antiparallel directions. This unstable configuration is called the *Rayleigh-Taylor instability (RT instability)*. The stability analysis shows that the dispersion relation of this instability is given by (e.g. Chandrasekhar, 1961)

$$\omega(k)_{\mathrm{RT}} = \sqrt{kg\frac{\rho_{\mathrm{fuel}} - \rho_{\mathrm{ash}}}{\rho_{\mathrm{fuel}} + \rho_{\mathrm{ash}}}} = \sqrt{kgAt} = \sqrt{kg_{\mathrm{eff}}}, \tag{3.8}$$

where $g_{\mathrm{eff}} = gAt$ is the effective gravitational acceleration and $At = (\rho_{\mathrm{fuel}} - \rho_{\mathrm{ash}})/(\rho_{\mathrm{fuel}} + \rho_{\mathrm{ash}})$ the Atwood number. In our case, we conclude from $\rho_{\mathrm{fuel}} > \rho_{\mathrm{ash}}$ directly that $\Re(\omega(k)_{\mathrm{RT}}) > 0$, hence the configuration is unstable for all wave numbers, leading to an unrestricted growth of perturbations. Characteristic for the RT instability is the development and merger of hot rising bubbles of burned material in the nonlinear regime. Conversely, unburned dense material descends and mixes with burned material in the interior of the star. Moreover, the flame front becomes highly deformed, leading to the formation of mushroom cap like structures, which occur predominantly at the parts of the flame that have propagated farthest toward the surface of the white dwarf.

In contrast to the LD instability, there is no effective stabilizing mechanism for the RT instability. However, the latter is only effective on large length scales and it evolves predominantly parallel to the direction of gravity. On small length scales the RT instability becomes suppressed due to the competition of the time scale of the growth rate of the perturbations with the nuclear burning time scale τ_{nuc}. One can derive a minimum length scale λ_{min} at which the flame front can be affected by the RT instability. This scale (sometimes called the *fire polishing length*) is given by (Timmes & Woosley, 1992)

$$\lambda_{\mathrm{min}} = \frac{4\pi u_{\mathrm{lam}}^2}{g_{\mathrm{eff}}}. \tag{3.9}$$

With decreasing density the width of the flame δ grows (see Timmes & Woosley, 1992), while the quantity λ_{min} decreases (e.g. Figure 1 in Zingale et al., 2005). Hence, in the course of the deflagration the RT instability can disturb the flame on smaller and smaller length scales.

The Kelvin-Helmholtz instability

For two fluids that are in contact and that move with different velocities tangentially to their boundary layer, shear instabilities may arise.[2]. The dispersion relation of this instability, also known as the *Kelvin-Helmholtz instability (KH instability)*, depends on the tangential relative velocity Δv of the fluids and is given by (e.g. Landau & Lifschitz, 1991)

$$\omega(k)_{\mathrm{KH}} = k\Delta v \frac{\sqrt{\rho_{\mathrm{fuel}}\rho_{\mathrm{ash}}}}{\rho_{\mathrm{fuel}} + \rho_{\mathrm{ash}}}. \tag{3.10}$$

We easily see that analogously to the LD- and RT instability $\Re(\omega(k)_{\mathrm{KH}}) > 0$ for all wave numbers. However, in deflagrations of SNe Ia, the KH instability appears only as a result of the RT instability, since the latter is responsible for the occurrence of boundary layers that may move with different tangential velocities along each other. Therefore, the KH instability acts as a secondary induced instability.

The KH instability leads to a rapid eddy generation in the vicinity of the tangential discontinuity in the nonlinear regime. It should be noted that effective shear flows may be able to suppress the stability mechanism of the LD instability (e.g. Niemeyer, 1995). However, it is not known to what extent the turbulent behavior of a flame may be partly the result of the suspension of the stabilizing mechanism for the LD instability through the KH instability.

3.1.3 Summary

All three described instabilities are characteristic for deflagrations in SNe Ia.[3] The outward propagating flame is substantially affected by the RT instability on the large length scales, leading to the formation of pronounced mushroom cap like structures at the flame front. In addition, secondary induced shear instabilities lead to a strong eddy generation along these highly deformed structures at the flame. The lack of sufficient stabilizing mechanisms for both the RT- and the KH instability in the deflagration leads to the generation of turbulent motions. We can estimate the flow characteristic in an exploding white dwarf with the Reynolds number. The typical size of a *Rayleigh-Taylor bubble* is of the order of $L \sim 10^7\,\mathrm{cm}$, while for the average flow velocity $V \sim 10^7\,\mathrm{cm\ s^{-1}}$ holds. The shear viscosity η is of the order of $10^9\,\mathrm{g\ cm^{-1}\ s^{-1}}$ (e.g. Nandkumar & Pethick, 1984), hence for a typical density of $10^9\,\mathrm{g\ cm^{-3}}$ we find for the kinematic viscosity $\nu = \eta/\rho \sim 1\,\mathrm{cm^2\ s^{-1}}$. Inserting these values in equation (3.1) we find a huge Reynolds number of $\sim 10^{14}$. Therefore, in an exploding white dwarf we may assume $Re \gg Re_{\mathrm{crit}}$. Such flows are commonly described as *fully developed turbulence*, of which the properties are investigated in the following.

3.2 Turbulence in SNe Ia

In this section the turbulent phenomena are explained that are triggered by the described instabilities in the preceding section. In general, there are several, partially mathematically

[2]Under the presence of a gravitational force that points in the direction normal to the contact interface one can derive that the flow is stable, if the ratio of the buoyancy force to the inertia force (this ratio is also called the Richardson number) is greater than 1/4 (Chandrasekhar, 1961).

[3]There are other instabilities, like the diffusive-thermal instability that, however, have no significant effects on the flame propagation, since $\Re(\omega(k)) < 0$.

sophisticated approaches to describe and investigate the properties of turbulence. For instance, a study of the Navier-Stokes equation (3.2) reveals that the chaotic and turbulent behavior of fluid motions arises from the nonlinear term $(\boldsymbol{v}\cdot\nabla)\boldsymbol{v}$. In three-dimensional objects (like a white dwarf) also turbulence has to be treated as a three-dimensional phenomenon (e.g. Mathieu & Scott, 2000). This is why all considerations and analyses of this work will be three-dimensional. Turbulence is also part of chaos theory and turbulent structures may have a fractal character on certain length scales. Due to its chaotic and unpredictable behavior, statistical methods play an important role in the analysis of turbulent flows. In particular, a statistical approach is useful in the case of $Re \gg Re_{\mathrm{crit}}$, which is valid for turbulent deflagrations of white dwarfs. Under this condition some important scaling relations of turbulent velocity fields can be derived without challenging mathematical considerations. A pioneering work in this field was performed by Andrei Nikolajewitsch Kolmogorov, who made major contributions in the probability theory of turbulence. He was able to find important relations between characteristic quantities of a given turbulent system and summarized them in his theory in the form of different hypotheses (Kolmogorov, 1941, 1991). The Kolmogorov theory is only valid for incompressible flows.

3.2.1 Isotropic turbulence

The hypotheses of Kolmogorov

Similar to Section 3.1 we consider a fully developed turbulent and incompressible flow with the kinematic viscosity ν. We define now L as the *integral length scale* on which turbulence is generated and η_{k} as the so-called *Kolmogorov length scale*, on which kinetic energy is dissipated. Under these conditions the hypotheses of Kolmogorov apply that are summarized in the following (see Pope, 2000; Frisch, 1995):

- *H1. Isotropy hypothesis:* At sufficiently high Reynolds numbers a turbulent flow behaves on small length scales $\ell \ll L$ statistically isotropic.
- *H2. First similarity hypothesis:* Under the condition of *H1* the statistical properties of turbulent flows on small length scales are explicitly given by the kinematic viscosity ν and the energy dissipation rate ϵ.
- *H3. Second similarity hypothesis:* Under the condition of *H1* the statistical properties of turbulent flows on a scale ℓ in the range of $\eta_{\mathrm{k}} \ll \ell \ll L$ are explicitly given by the energy dissipation rate ϵ and independent of the kinematic viscosity ν.

Consequences of the Kolmogorov hypotheses

From the Kolmogorov hypotheses several interesting consequences can be inferred. By *H1* the behavior of a turbulent flow on scales $\ell \ll L$ remains unaffected of possible anisotropic effects on large scales $\ell \sim L$. From a mathematical point of view this means that broken symmetries of the Navier-Stokes equation by boundary effects or effects on large scales are restored on smaller scales (Frisch, 1995). The specific kinetic energy $e_{\mathrm{kin}}(\ell)$ of a turbulent system is proportional to $v'^2(\ell)$, where $v'(\ell)$ are the *turbulent velocity fluctuations* on the scale ℓ. From *H3* it follows that the average energy dissipation rate $\langle\epsilon\rangle$ in the range of length scales $\eta_{\mathrm{k}} \ll \ell \ll L$, which is defined as the *inertial range*, is given by

$$\langle\epsilon\rangle = \frac{d}{dt}e_{\mathrm{kin}}(\ell) \sim \frac{v'^2(\ell)}{\ell/v'(\ell)} = \frac{v'^3(L)}{L} = \mathrm{const} \qquad \eta_{\mathrm{k}} \ll \ell \ll L. \tag{3.11}$$

Hence, $\langle\epsilon\rangle$ is a constant and scale-independent quantity in the Kolmogorov theory that is simply determined by the integral length scale and the velocity fluctuations on this scale. Strictly speaking, equation (3.11) does not describe a dissipation of kinetic energy, since $\langle\epsilon\rangle$ is by *H3* independent on ν in the inertial range. In fact, a transfer of kinetic energy from larger to smaller length scales in the form of an energy cascade (also known as the Richardson cascade (Richardson, 1922)[4]) occurs, without any interaction with viscous forces. In this context, $\langle\epsilon\rangle$ complies with a constant energy flow of $e_{\mathrm{kin}}(\ell)/\tau_{\mathrm{eddy}}(\ell)$, where $\tau_{\mathrm{eddy}}(\ell) = \ell/v'(\ell)$ is the so-called *eddy turnover time*. For fully developed turbulent flows a universal scaling behavior of $v'(\ell)$ in the inertial range can be found that is given by

$$v'(\ell) \sim \ell^{\alpha}, \tag{3.12}$$

where α is a characteristic scaling exponent. In the case of Kolmogorov's theory, we find with equation (3.11) directly

$$v'(\ell) \sim \ell^{1/3} \tag{3.13}$$

and we see $\alpha = 1/3$. Using this relation we can estimate the Kolmogorov length scale η_{k}. By *H2*, on this scale the viscosity ν leads to a dissipation of kinetic energy. With the turbulent Reynolds number $Re_{\mathrm{t}}(\ell) = \ell \cdot v'(\ell)/\nu$ we can write

$$Re_{\mathrm{t}}(\eta_{\mathrm{k}}) = \frac{\eta_{\mathrm{k}} \cdot v'(\eta_{\mathrm{k}})}{\nu} = \frac{\eta_{\mathrm{k}}^{4/3} \langle\epsilon\rangle^{1/3}}{\nu}, \tag{3.14}$$

where in the second step equation (3.11) was applied. From the scaling behavior in equation (3.13) it follows that $Re_{\mathrm{t}}(\ell)$ decreases for smaller length scales. Hence, it is allowed to set $Re_{\mathrm{t}}(\eta_{\mathrm{k}}) = 1$ and we eventually find

$$\eta_{\mathrm{k}} = \left(\frac{\nu^3}{\langle\epsilon\rangle}\right)^{1/4}. \tag{3.15}$$

With $\nu = 1\,\mathrm{cm}^2\,\mathrm{s}^{-1}$, $L = 10^7\,\mathrm{cm}$ and $v(L) = 10^7\,\mathrm{cm\,s}^{-1}$ (see Section 3.1.3) we find with equation (3.11) that η_{k} is of the order of $10^{-3}\,\mathrm{cm}$ only. This further implies $L/\eta_{\mathrm{k}} \sim 10^{10}$, hence to study all turbulent effects of deflagrations in SNe Ia, one has to take 10 orders of magnitude in length scales into account. In general, this estimate can also be made with the Reynolds number only. In analogy to equation (3.14) we can write

$$\frac{Re_{\mathrm{t}}(L)}{Re_{\mathrm{t}}(\eta_{\mathrm{k}})} = \frac{L^{4/3} \cdot \langle\epsilon\rangle^{1/3}}{\nu} \frac{\nu}{\eta_{\mathrm{k}}^{4/3} \langle\epsilon\rangle^{1/3}}. \tag{3.16}$$

With $Re_{\mathrm{t}}(L) = Re = 10^{14}$ (see Section 3.1.3) and $Re_{\mathrm{t}}(\eta_{\mathrm{k}}) = 1$ we find the useful relation (see also Landau & Lifschitz, 1991)

$$\frac{L}{\eta_{\mathrm{k}}} = Re^{3/4} \sim 10^{10}. \tag{3.17}$$

[4] L. F. Richardson originally summarized the interplay of large and small scales with the rhyming verse "Big whirls have little whirls that feed on their velocity, and little whirls have lesser whirls and so on to viscosity" (Richardson, 1922).

From equation (3.11) and (3.15) it follows that the energy dissipation ϵ_η on the Kolmogorov scale can be written as

$$\epsilon_\eta = \frac{v'(\eta_\mathrm{k})^3}{\eta_\mathrm{k}} = \frac{\nu^3}{\eta_\mathrm{k}^4}. \tag{3.18}$$

Using equation (3.15) the velocity $v'(\eta_\mathrm{k})$ and eddy turnover time $\tau_\mathrm{eddy}(\eta_\mathrm{k})$ on the scale η_k are given by

$$v'(\eta_\mathrm{k}) = (\eta_\mathrm{k} \cdot \epsilon_\eta)^{1/3} = (\nu \cdot \epsilon_\eta)^{1/4}, \tag{3.19}$$

$$\tau_\mathrm{eddy}(\eta_\mathrm{k}) = \frac{\eta}{v'(\eta_\mathrm{k})} = \left(\frac{\nu}{\epsilon_\eta}\right)^{1/2}. \tag{3.20}$$

Dynamics of turbulent eddies

With equation (3.11) we also can write for $v'(\ell)$

$$v'(\ell) = v'(L)\left(\frac{\ell}{L}\right)^{1/3}. \tag{3.21}$$

The time scale for the rotation of an eddy on the length scale ℓ can be derived with equation (3.13), where we find $\tau_\mathrm{eddy}(\ell) = \ell/v'(\ell) \propto \ell^{2/3}$. Using equation (3.21) it follows

$$\tau_\mathrm{eddy}(\ell) = \frac{\ell}{v'(\ell)} = \frac{L^{1/3}}{v'(L)}\ell^{2/3} = \tau_\mathrm{eddy}(L)\left(\frac{\ell}{L}\right)^{2/3}. \tag{3.22}$$

From this equation we see that for smaller length scales, the dynamical eddy turnover time decreases. Hence, turbulent structures can evolve faster on these scales. Here we find again that the effects that are dominating on large length scales $\ell \sim L$ have no significant influence on much smaller length scales, since structures on scales $\ell \ll L$ may have been evolved already by several dynamical time scales.

Turbulent eddies can be further considered as a transport and mixing mechanism. In this picture, two fluid elements in a turbulent flow that are separated by a distance ℓ can be brought together in a half eddy turnover time

$$\tau_{\mathrm{eddy}_{1/2}}(\ell) = 0.5 \cdot \ell/v'(\ell). \tag{3.23}$$

Hence, $\tau_{\mathrm{eddy}_{1/2}}(\ell)$ is the minimum required time for the mixing of two different fluids on the scale ℓ.

Energy spectra and velocity structure functions

The statistical analysis of the turbulent velocity field in a fluid is a crucial method to derive scaling and correlation properties on certain length scales of the turbulent flow. The major task of such a statistical study is to obtain scaling exponents that may reveal the properties of turbulence in the underlying fluid. Two commonly used methods will be presented in the following.

From equation (3.12) we find for the specific kinetic energy the relation $e_\mathrm{kin}(\ell) \sim \ell^{2\alpha}$. If we change from real to Fourier space $e_\mathrm{kin}(k) \sim k^{-2\alpha}$ holds. From here we can derive a scaling relation of the energy spectra $E(k)$ that is given by

$$E(k) = \frac{d}{dk}e_\mathrm{kin}(k) \sim k^{-2\alpha-1}. \tag{3.24}$$

In the case of Kolmogorov's theory, we find with $\alpha = 1/3$ directly $E^{\mathrm{Kol}} \sim k^{-5/3}$. This is the scaling relation of the *Kolmogorov energy spectrum* that is valid for isotropic and incompressible turbulence.

In the other method we first consider the absolute velocity difference $\partial v(\boldsymbol{r}, \boldsymbol{\ell})$ of two fluid elements, whose distance is $\ell = |\boldsymbol{\ell}|$, where $\boldsymbol{r}$ is a position vector of one of the fluid elements. We can write

$$\partial v(\boldsymbol{r}, \boldsymbol{\ell}) = |\boldsymbol{v}(\boldsymbol{r} + \boldsymbol{\ell}) - \boldsymbol{v}(\boldsymbol{r})|. \tag{3.25}$$

From here we can obtain correlation properties of the turbulent velocity field by averaging over a sufficient number of velocity differences of various fluid elements that have different distances ℓ. We define the *velocity structure function* S_{p} of the order p as

$$S_{\mathrm{p}}(\ell) \equiv \langle (\partial v(\boldsymbol{r}, \boldsymbol{\ell}))^p \rangle \sim \ell^{\zeta(p)}. \tag{3.26}$$

In the case of Kolmogorov's theory, the scaling exponent $\zeta(p)$ of the first order is $\zeta(1) = \alpha = 1/3$. For every successive order, $\zeta(p)$ increases by an additional $1/3$, so that in general $\zeta^{\mathrm{Kol}}(p) = \alpha \cdot p = p/3$ for isotropic and incompressible turbulence. The calculated scaling properties of the turbulent velocity field are more convincing the higher the orders that can be obtained from the analysis. However, to obtain reliable scaling exponents of very high order the calculation of structure functions may become computationally too expensive. From a statistical point of view one also needs a very large number of different point pairs over that can be averaged.

It should be noted that the isotropy of turbulence can be further investigated by splitting up the velocity field into different directions. An exploding white dwarf can be considered as a spherical system, so that the turbulent velocity field can be split up into a radial and an angular component (Ciaraldi-Schoolmann et al., 2009). For isotropic turbulence, the corresponding *radial* and *angular* structure functions are equal (see Figure 2 in Ciaraldi-Schoolmann et al. (2009)). If this is not the case, anisotropic effects in the turbulence have to be taken into account.

Anisotropic Turbulence

According to *H1*, anisotropic turbulence may occur on large length scales. In particular, the RT instability may cause anisotropic effects in the turbulent velocity field, since this instability evolves anisotropic itself, mainly in the direction parallel to gravity. Similar to the Kolmogorov theory we can find a specific scaling relation of the velocity field with the length for the RT instability which is given by (Davies & Taylor, 1950; Sharp, 1984)

$$v_{\mathrm{RT}} = B\sqrt{g_{\mathrm{eff}}\ell}, \tag{3.27}$$

where the constant B is approximately $1/2$. Hence, for turbulence that is driven by the RT instability, $v_{\mathrm{RT}} \propto \ell^{1/2}$ and thus $\alpha = 1/2$. Due to the different scaling properties we may expect a transition from Kolmogorov to RT instability driven turbulence on a certain length scale. Here Niemeyer & Woosley (1997) give an estimate for this length scale of

$$\ell_{\mathrm{Kol/RT}} \approx 10^6 \text{ cm}, \tag{3.28}$$

which separates the Kolmogorov turbulence on scales $\ell \lesssim \ell_{\mathrm{Kol/RT}}$ from the RT instability driven turbulence on scales $\ell \gtrsim \ell_{\mathrm{Kol/RT}}$. For considerations of radial velocity fluctuations

that always point in the direction parallel to gravity, the described transition was found by Ciaraldi-Schoolmann et al. (2009), where these calculations were based on an analysis of the properties of turbulence in predominantly burned material. In analogy to the Kolmogorov theory, we can derive useful scaling relations for the RT instability driven turbulence. With equation (3.27) it follows for the structure functions $S_\mathrm{p} \sim \ell^{p/2}$ with the scaling exponents $\zeta^\mathrm{RT}(p) = p/2$. For the energy spectrum we find with $\alpha = 1/2$ and equation (3.24) $E^\mathrm{RT}(k) \sim k^{-6/3}$.

Summary

On the largest length scale L, kinetic energy is injected into the turbulent flow that becomes apparent in the motion of the largest turbulent eddies. These eddies decay to smaller eddies that further decay into smaller vortex structures. In this way, kinetic energy is transferred due to a cascade process in the inertial range $\eta_\mathrm{k} \ll \ell \ll L$ from large to small length scales. This behavior is illustrated in Figure 3.1, where a sketch of the energy spectrum is shown. As long as turbulence is fully developed, incompressible and isotropic, the cascade process appears as a power law in the energy spectrum that is given by $E(k) \propto k^{-5/3}$. In the presence of the RT instability the anisotropy in the velocity field in the range of length scales $\ell_\mathrm{Kol/RT} \lesssim \ell \lesssim L$ may lead to a change in the scaling properties of the turbulent flow in the direction parallel to gravity. In this case, a power law of the form $E(k) \propto k^{-6/3}$ can be found (see also Figure 1 in Ciaraldi-Schoolmann et al., 2009). By approaching the Kolmogorov scale η_k kinetic energy is converted to internal energy in the form of small vortex structures due to effective viscous forces on these scales. The flow on these scales has a laminar character.

3.2.2 Intermittency

Most studies of turbulent velocity fields that are based on computations of velocity structure functions reveal that for sufficiently high orders $\zeta(p) < \alpha \cdot p$. This anomaly is attributed to the intermittent character of turbulent motions. An intermittent system has the ability and affinity to change spontaneously between a periodic and chaotic behavior. The system has regular and steady phases with approximate periodic time dependence that is superimposed by sudden unpredictable, irregular and chaotic phases (e.g. Frisch, 1995).

The underlying cause of intermittent turbulence is not well understood, hence there are several theoretical models that try to give a prescription for this phenomenon. Here, we briefly summarize a basic picture of intermittent turbulence that is described in more detail in Frisch (1995)(see also Frisch et al., 1978). A commonly used explanation for intermittency is the spatial inhomogeneity in the energy dissipation. Illustratively the *daughter* eddies that emerge from the *mother* eddy will fill less space, so that some part of the kinetic energy is not transferred, but already dissipated in the inertial range due to eddy decays. In addition, kinetic energy will not dissipate on the smallest scales in always exactly identical vortices, but in different vortex structures. The different amount of dissipated kinetic energy in these diverse structures in turn leads to a spatially inhomogeneous and intermittent distribution of the turbulent intensity. This behavior becomes apparent in the occurrence of spontaneously very high velocity fluctuations that may play an important role for the DDT in the delayed detonation model (see Section 3.3).

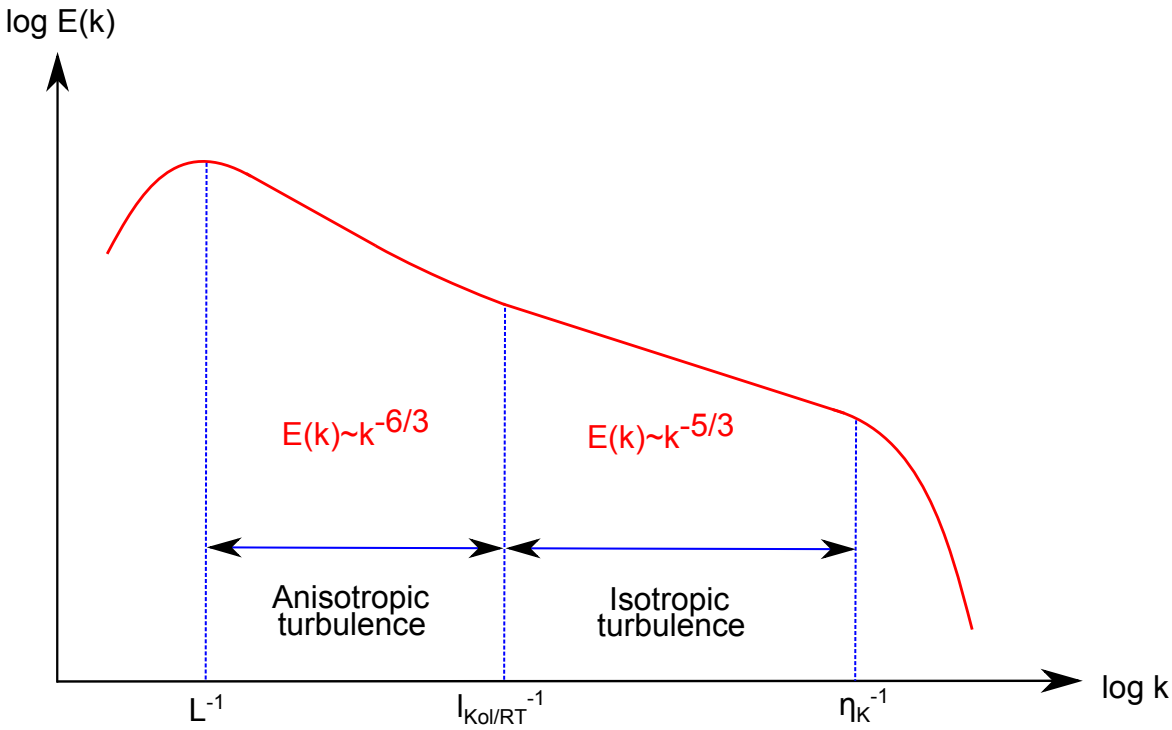

Fig. 3.1: Sketch of the turbulent energy spectrum that includes only radial velocity fluctuations under the presence of the RT instability.

3.2.3 Turbulent deflagration

The flamelet and distributed burning regime

After we discussed the properties of turbulence we can now describe the different phases of the deflagration of white dwarfs. With the ignition of the deflagration in the central area of the white dwarf, a thermonuclear flame is born that starts to propagate outward toward the surface due to heat conduction processes. In the very early stage, the characteristics of the flame are approximately given by laminar quantities, since instabilities have not evolved so far. Hence, for the burning speed $v_{\mathrm{flame}} \approx u_{\mathrm{lam}}$ holds.

During the deflagration the RT- and the KH instability appear, leading to turbulence production that in turn affects the flame propagation. There are different types of turbulent combustion that are usually summarized in a *regime diagram* (e.g. Abdel-Gayed et al., 1984, 1987; Borghi, 1985; Peters, 1986). Such a diagram is shown in Figure 3.2 in a slightly modified version of Peters (1999). The degree of interaction of turbulence with the flame can be estimated with a specific dimensionless number. The *Karlovitz number*

$$Ka = \frac{\tau_{\mathrm{nuc}}}{\tau_{\mathrm{eddy}}(\eta_{\mathrm{k}})} \tag{3.29}$$

measures the ratio of the burning time scale to the microscopic turbulent time scale of the flow. As long as $Ka < 1$, turbulence is not able to affect the internal flame structure. The interaction of the flame with turbulence on large scales is purely kinematic and the microphysical processes on small scales within the flame remain unaffected by turbulence. Illustratively the flame burns so fast through the large turbulent eddies that the latter cannot sufficiently rotate to modify the flame on scales $\ell \approx \delta$. This burning regime is the so-called

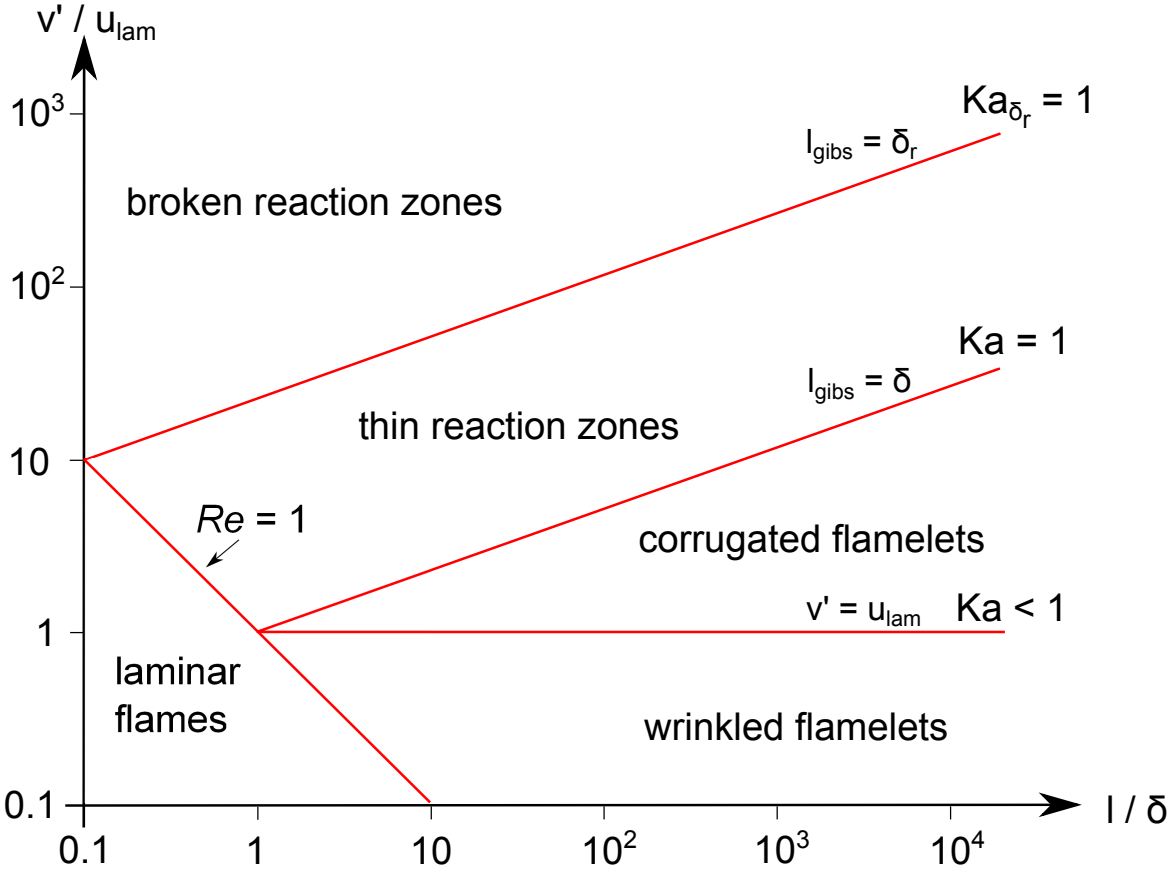

Fig. 3.2: Regime diagram for premixed turbulent combustion, based on Peters (1999).

flamelet regime which can be divided further into two sub-regimes. With increasing ℓ the velocity $v'(\ell)$ of the turbulent eddies grows (see equation (3.21)). As long as $v'(\ell) < u_{\rm lam}$ turbulence modifies the flame surface only marginally. This regime is called the *wrinkled flamelet regime*. On larger scales $\ell \gg \delta$, $v'(\ell)$ may become comparable to or higher than $u_{\rm lam}$. The regime with $Ka < 1$ and $v'(\ell) \gtrsim u_{\rm lam}$ is the so-called *corrugated flamelet regime* where turbulence significantly modifies the shape of the flame.

From equation (3.18) we find for the kinematic viscosity the relation

$$\nu = v'(\eta_{\rm k}) \cdot \eta_{\rm k}. \tag{3.30}$$

The *Schmidt number*

$$Sc = \frac{\nu}{D_i} \tag{3.31}$$

is defined as the ratio of viscous diffusivity to mass diffusivity D_i. Following Peters (2000) it seems useful for scaling purposes to assume equal diffusivities for all reactions. With a Schmidt number of unity it follows $\nu = D_i$ and the flame width and the kinematic viscosity can be written as (see Peters, 2000)

$$\delta = \frac{D_i}{u_{\rm lam}} = \frac{\nu}{u_{\rm lam}}, \tag{3.32}$$

$$\nu = \delta \cdot \ u_{\rm lam}. \tag{3.33}$$

Inserting equation (3.18) in (3.20) and using equation (3.33) for ν yields

$$\tau_{\mathrm{eddy}}(\eta_{\mathrm{k}}) = \left(\frac{\nu}{\epsilon_\eta}\right)^{1/2} = \left(\frac{\eta_{\mathrm{k}}^4}{\nu^2}\right)^{1/2} = \frac{\eta_{\mathrm{k}}^2}{u_{\mathrm{lam}} \cdot \delta}. \tag{3.34}$$

Then the Karlovitz number reads

$$Ka = \frac{\tau_{\mathrm{nuc}}}{\tau_{\mathrm{eddy}}(\eta_{\mathrm{k}})} = \frac{\delta}{u_{\mathrm{lam}}} \frac{u_{\mathrm{lam}} \cdot \delta}{\eta_{\mathrm{k}}^2} = \frac{\delta^2}{\eta_{\mathrm{k}}^2}. \tag{3.35}$$

Therefore, as long as $\eta_{\mathrm{k}} > \delta$ the flame resides in the flamelet regime. The transition between the burning regimes can also be described with the *Gibson scale* ℓ_{gibs} which is defined as the length scale at which $\tau_{\mathrm{eddy}}(\ell_{\mathrm{gibs}}) = \tau_{\mathrm{nuc}}$ and equivalently $v'(\ell_{\mathrm{gibs}}) = u_{\mathrm{lam}}$ holds (Peters, 2000). For $v'(\ell)$ and ℓ_{gibs} we conclude from the Kolmogorov theory with equation (3.21)

$$v'(\ell) = u_{\mathrm{lam}} \left(\frac{\ell}{l_{\mathrm{gibs}}}\right)^{1/3}, \tag{3.36}$$

$$\ell_{\mathrm{gibs}} = \ell \left(\frac{u_{lam}}{v'(\ell)}\right)^{3}. \tag{3.37}$$

For $\ell = \eta_{\mathrm{k}}$ we find with equation (3.18) and (3.33) for ℓ_{gibs}

$$\ell_{\mathrm{gibs}} = \eta_{\mathrm{k}} \left(\frac{u_{\mathrm{lam}}}{v'(\eta_{\mathrm{k}})}\right)^{3} = \frac{u_{\mathrm{lam}}^3}{\epsilon_\eta} = u_{\mathrm{lam}}^3 \cdot \frac{\eta_{\mathrm{k}}^4}{u_{\mathrm{lam}}^3 \cdot \delta^3} = \frac{\eta_{\mathrm{k}}^4}{\delta^3}. \tag{3.38}$$

Combining equation (3.35) with equation (3.38) yields another useful expression for the Karlovitz number:

$$Ka = \frac{\delta^2}{\eta_{\mathrm{k}}^2} = \frac{\delta^2}{\ell_{\mathrm{gibs}}^{1/2} \cdot \delta^{3/2}} = \left(\frac{\delta}{\ell_{\mathrm{gibs}}}\right)^{1/2}. \tag{3.39}$$

Hence, an equivalent condition for burning in the flamelet regime is $\ell_{\mathrm{gibs}} > \delta$.

For $Ka > 1$ (resp. $\ell_{\mathrm{gibs}} < \delta$), turbulence is strong enough to modify the internal flame structure and to distribute material within and around the flame. This is why this regime is called the *distributed burning regime*. As described in Section 3.1.2 the flame is composed of a diffusion and a reaction zone, while the latter may be much thinner than the former. Therefore, the flame enters the *thin reaction zone* regime first, where turbulence will only affect the diffusion zone which becomes broader, while the burning continues in the thinner reaction zone. Eventually turbulence becomes able to affect the internal flame structure on scales $\delta_{\mathrm{r}} < \delta$ where δ_{r} denotes the reaction zone thickness. This is the regime of *broken reaction zones*. We can replace δ with δ_{r} in equation (3.35) and use a modified Karlovitz number $Ka_{\delta_{\mathrm{r}}}$ which is given by

$$Ka_{\delta_{\mathrm{r}}} = \frac{\delta_{\mathrm{r}}^2}{\eta_{\mathrm{k}}^2} = Ka \frac{\delta_{\mathrm{r}}^2}{\delta^2}. \tag{3.40}$$

For $Ka_{\delta_{\mathrm{r}}} = 1$ and a typical width of the reaction zone of $\delta_{\mathrm{r}} \approx 0.1\,\delta$ we find $Ka \gtrsim 100$ in the regime of broken reaction zones (e.g. Peters, 1999).

Turbulent combustion and mixing in the deflagration phase

In the turbulent deflagration phase, the burning speed v_{flame} is not given by u_{lam} anymore, but by the turbulent velocity fluctuations $v'(\ell)$ that are much faster at the prevailing low densities. From equation (3.37) we see that ℓ_{gibs} scales with u_{lam} to the third power. Therefore, ℓ_{gibs} declines with decreasing fuel density (see equation (3.6) and Figure 2 in Niemeyer & Woosley (1997)). Since the density declines continuously in direction outward, which is additionally enhanced by the expansion of the star, ℓ_{gibs} falls steeply during the explosion. In summary, turbulence will affect the flame on an increasing range of length scales, leading to an acceleration and growth of the width δ of the flame with time.

For $\ell_{\mathrm{gibs}} \ll \delta$, τ_{nuc} is exclusively given by the fastest turbulent process that can transport unburned material to the flame. The time scale for this process is determined by $\tau_{\mathrm{eddy}}(\ell)$. The reason is that eddies in the vicinity of the flame are able to reach unburned material faster than the flame itself, and mix it in a time of the order of $\ell/v'(\ell)$ into the reaction zone. We follow the description of laminar burning in Section 3.1.2 but substitute now τ_{diff} by $\tau_{\mathrm{eddy}}(\ell)$. In equilibrium, $\tau_{\mathrm{nuc}} = \tau_{\mathrm{eddy}}(\ell)$ and we find (e.g. Damköhler, 1940; Niemeyer, 1995)

$$\tau_{\mathrm{nuc}} \sim \frac{\ell}{v'(\ell)}, \qquad \text{and} \qquad \delta(\ell) = \tau_{\mathrm{nuc}} \cdot v_{\mathrm{flame}}(\ell) \approx \ell, \tag{3.41}$$

where $v_{\mathrm{flame}}(\ell) = v'(\ell)$ was used. It is remarkable that for $\ell_{\mathrm{gibs}} \ll \delta$, the burning time scale τ_{nuc} is completely independent of the thermal diffusion. A further interesting consequence is that the flame width may grow as large as the turbulent integral scale. In this case, τ_{nuc} depends only on the largest turbulent velocities $v(L)$ and we easily find analogously to the equations (3.41) the relations $v_{\mathrm{flame}}(L) \approx v'(L)$, $\tau_{\mathrm{nuc}} \approx \tau_{\mathrm{eddy}}(L) \sim \frac{L}{v'(L)}$, and $\delta \approx L$. Under these conditions the behavior of the burning can be estimated with an additional dimensionless number. The turbulent *Damköhler number*

$$Da_{\mathrm{t}} = \frac{\tau_{\mathrm{eddy}}(L)}{\tau_{\mathrm{nuc}}} \tag{3.42}$$

measures the ratio of the macroscopic turbulent time scale of the flow to the burning time scale. Hence, the only difference between Ka and Da_{t} are the considered length scales of the turbulent flow.[5] The regime with $Da_{\mathrm{t}} < 1$ is called the *well-stirred reactor (WSR) regime* (Peters, 2000) and the regime with $Da_{\mathrm{t}} > 1$ is the *stirred flame (SF) regime* (Kerstein, 2001). Both regimes were studied in detail by Woosley et al. (2009) and Aspden et al. (2010) in the context of turbulent combustion in SN Ia explosions. In the WSR regime, $\delta > L$ holds. Since $\tau_{\mathrm{eddy}}(L) < \tau_{\mathrm{nuc}}$ the material at the flame is mixed before burned. The burning occurs on a well defined nuclear time scale (e.g. Woosley et al., 2009; Aspden et al., 2010). The SF regime constitutes a very complex regime of turbulent burning. Here turbulence on the integral scale cannot fully mix the material before it is burned by the flame. Consequently, there exists no well-defined nuclear time scale anymore (e.g. Woosley et al., 2009; Aspden et al., 2010).

Finally, in the late phase of the deflagration, the flame is propagated so far that at the prevailing low densities the thermonuclear combustion ceases. In this phase, no more energy is injected into the turbulent energy cascade on the scale L. The residual turbulent energy in the inertial range is dissipated on the smallest scales in a time of approximately $\tau_{\mathrm{eddy}}(L)$ and the energy cascade vanishes, leading to the freeze out of turbulent motions.

[5] Sometimes Da_{t} is not related to a fixed macroscopic scale in literature, hence $Da_{\mathrm{t}} \to Da_{\mathrm{t}}(l)$. With equation (3.29) we find $Da_{\mathrm{t}}(\eta_{\mathrm{k}}) = Ka^{-1}$.

3.2.4 Fractal description of the flame

In the inertial range $\eta_\mathrm{k} \ll \ell \ll L$, turbulent structures behave self-similar. Therefore, when the flame is deformed by turbulence, its structure may be similar to that of fractals (e.g. Gouldin, 1987; Kerstein, 1988; Woosley, 1990; Niemeyer, 1995). From a mathematical point of view, however, the flame is no ideal fractal, since deformations and curvatures of the flame are not sustained on very small length scales, which results particularly from the decrease of the interaction of turbulence with the flame. The range of length scales at which a fractal description of the flame seems appropriate is uncertain. It is generally agreed that the largest scale is the turbulent integral scale L (e.g. Gouldin, 1987; Kerstein, 1988; North & Santavicca, 1990). Peters (1986) and Kerstein (1988) propose that the smallest scale is ℓ_gibs while Gouldin (1987), North & Santavicca (1990) and Gülder (1991) argue that this scale should be η_k. We will follow here Peters (1986) and Kerstein (1988) and assume that within the range of length scales of $\ell_\mathrm{gibs} \ll \ell \ll L$ a fractal description of the flame can be applied. A fractal F can be defined as (Mandelbrot, 1983)

$$F \propto \ell^\beta, \tag{3.43}$$

where $\beta \in [0;1]$ is the fractal excess. The flame can be considered as an object whose two-dimensional extension scales in the three-dimensional space with the characteristic length scale ℓ to the power of β. The fractal dimension D is defined as

$$D = n - 1 + \beta, \tag{3.44}$$

where n is the integer dimension of the space the fractal is embedded in. In our case, $n = 3$ holds, hence $D \in [2;3]$.[6] We can use the scaling relations of $v'(\ell)$ to determine the fractal dimension of the flame theoretically. If the speed of the turbulent flame is interpreted in a geometrical way, so that $v'(\ell) \propto F$ holds (e.g. Woosley, 1990; Niemeyer, 1995; Niemeyer & Woosley, 1997), we find $v'(\ell) \propto \ell^\beta$. When comparing this relation with equation (3.13), we easily see $\beta = 1/3$ for the Kolmogorov theory. Using equation (3.44), the fractal dimension reads

$$D_\mathrm{Kol} = 2.33. \tag{3.45}$$

Following Sreenivasan (1991) and Kerstein (1991) the fractal dimension for intermittent turbulence can be written as

$$D_\mathrm{turb} = \frac{7}{3} + \frac{2}{3}(1 - D_{1/3}), \tag{3.46}$$

where $D_{1/3}$ is called the generalized dimension, of which the value was experimentally determined to 0.96, leading to $D_\mathrm{turb} = 2.36$ (Halsey et al., 1986; Sreenivasan, 1991). Finally, a fractal dimension for large length scales can be determined where the RT instability is the dominant process that drives the turbulent motions. With $v_\mathrm{RT} \propto \ell^{1/2}$ (see Section 3.2.1) we find

$$D_\mathrm{RT} = 2.5. \tag{3.47}$$

[6] In general, D is not uniquely defined. From an experimental point of view D can be derived, for instance, from the Hausdorff dimension, the self-similarity dimension or the box-counting dimension (e.g. Feder, 1988; Schroeder, 1991).

It should be noted that the mere existence of the LD instability leads to the effect that the flame has a fractal character (Blinnikov & Sasorov, 1996). However, compared to the RT- and KH instability the influence of the LD instability on the flame characteristics appears only marginal in the turbulent deflagration phase (see Section 3.1.2). But it has not been strictly shown yet (and it is probably hard to examine) whether and to what extent the fractal character of the flame in a turbulent deflagration is a result from effects of the LD instability.

3.3 Theory of Deflagration-to-Detonation Transitions

3.3.1 Introduction

As indicated in Section 2.3.4, the delayed detonation model can reproduce some of the main features of observed normal SNe Ia quite well. However, the mechanism that causes the transition from a subsonic deflagration to a supersonic detonation is unclear and discussed controversially. Even if some recent studies reveal that DDTs may happen in unconfined media (Poludnenko et al., 2011) we use here the concept of the so-called *Zeldovich gradient mechanism* (Zel'dovich et al., 1970) that is outlined in the following. We consider a region at the flame front of a specific size with a rather uniform temperature and fuel fraction. This can be translated to a spatial region that has a shallow gradient of induction times. In this region a spontaneous ignition of the fuel may occur, leading to a supersonic reaction wave. If the phase velocity of this wave matches a particular velocity (the so-called Chapman-Jouguet detonation velocity (Chapman, 1899; Jouguet, 1905)), the wave may transition into a detonation. Similar to the described detonation model in Section 2.3.2, the ignition will build up a shock in this case that propagates through the white dwarf (Khokhlov et al., 1997; Niemeyer & Woosley, 1997), where the compressed material is burned thermonuclearly to heavier elements.

The gradient mechanism was first applied to SNe Ia by Blinnikov & Khokhlov (1986, 1987) and Khokhlov (1991a) and further investigated by Khokhlov (1991b), Khokhlov et al. (1997) and Niemeyer & Woosley (1997). The results of their analyses show that the described induction time gradient only occurs by a sufficient mixing of hot burned and cold unburned material. This mixing in turn requires a strong interaction of turbulence with the flame, hence the properties of turbulence in the deflagration phase are crucial for a DDT. Too intense turbulence can also cause local fluctuations in the temperature and chemical composition that may prevent the formation of sufficiently shallow induction time gradients, particularly in the flamelet regime (Niemeyer, 1999; Niemeyer et al., 1999).

The major challenge for the investigation of DDTs in SNe Ia is that this process occurs on microphysical length scales that are not resolved in full-star simulations which follow the explosion of the whole white dwarf. Therefore, it is difficult to study the microphysical properties of DDTs and its implications for the overall SN Ia explosion simultaneously. This is why DDTs are analyzed separately in small-scale simulations which are able to take the microphysics into account. However, in these studies the problem arises that the conditions at which DDTs occur are determined by the dynamics on the large scales.

On the other hand, for large-scale simulations the question arises, how DDTs can be modeled properly. Most of the developed DDT models so far include only one parameter (Arnett & Livne, 1994a; Khokhlov et al., 1997; Höflich et al., 1998; Livne, 1999; Gamezo et al., 2005; Bravo & García-Senz, 2008; Townsley et al., 2009; Jackson et al., 2010; Krueger et al., 2010), commonly a certain critical fuel density ρ_{crit} that has to be reached by the

flame in order to trigger the DDT. The choice of ρ_{crit} has a major impact on the produced ^{56}Ni masses, and hence on the brightness of the explosion. It was found that values of the order of $\rho_{\mathrm{crit}} \approx 10^7\,\mathrm{g\,cm^{-3}}$ may produce ^{56}Ni yields that are consistent with observations (e.g. Höflich, 1995; Höflich et al., 1998; Domínguez et al., 2001). At these densities the deflagration is already close to extinction.

The problem of these one-parameter models is the fact that the mixing process of burned an unburned material is given by turbulent quantities and not by a (sometimes arbitrarily chosen) critical fuel density. If no further constraints are set in these models, a DDT will always occur, since the simple constraint $\rho_{\mathrm{fuel}} < \rho_{\mathrm{crit}}$ at the flame will practically always be met during the deflagration. In specific deflagrations, however, the presence of relatively weak turbulence may lead to an insufficient mixing of the burned and unburned material, so that DDTs will in reality not occur. Finally, the constraint $\rho_{\mathrm{fuel}} < \rho_{\mathrm{crit}}$ will usually be met first by the parts of the flame that are propagated farthest toward the surface of the white dwarf. These parts are the *heads* of the mushroom cap like structures that occur due to the influence of the RT instability. As shown later, turbulence is here significantly weaker than alongside of these structures where strong shear instabilities occur.

From these considerations we argue that a criterion for a DDT should be based on turbulent quantities. One necessary constraint for the DDT is the burning in the distributed burning regime (Niemeyer & Woosley, 1997). This criterion has been applied to two- and three-dimensional simulations by Golombek & Niemeyer (2005) and Röpke & Niemeyer (2007). In general, the two relevant quantities δ and ℓ_{gibs} for this criterion are not resolved and have therefore to be modeled somehow in order to evaluate where distributed burning sets in (see Section 3.2.3). However, based on the turbulence driving mechanism, Niemeyer & Woosley (1997) and Niemeyer & Kerstein (1997) derived an upper threshold value for the fuel density for distributed burning. In this context, the density is an important parameter after all, since it can be qualitatively used to assess of whether the flame has already entered the distributed burning regime (e.g. Niemeyer & Woosley, 1997). As shown in the following, there are additional constraints for a DDT within this burning regime that also concerns the fuel density.

3.3.2 Constraints on DDTs

Turbulence

For a detailed study of DDTs it is inevitable to analyze the microphysical nature of turbulent flames in white dwarfs. Such studies were carried out extensively by Lisewski et al. (2000), Aspden et al. (2008) and Woosley et al. (2009). Although their analyses provide no evidence for DDTs, we can derive necessary constraints from these studies. The most important constraint for a DDT is the occurrence of particularly high velocity fluctuations at the flame. Here the question arises, of whether turbulence remains strong enough for a DDT in the phase where the deflagration is close to extinction. The RT instability in the late deflagration phase becomes weaker until the expansion of the star will freeze out all turbulent motions (Khokhlov, 1995). From microphysical studies, Lisewski et al. (2000) argue that the turbulent velocity fluctuations must be of the order of $10^8\,\mathrm{cm\,s^{-1}}$ for a DDT, which is already $20 - 25\%$ of the sound speed in the unburned material of the white dwarf. Röpke (2007) found in numerical simulations of SNe Ia that these high velocity fluctuations, although rare, may indeed occur at the flame. From a statistical point of view we can translate this to a non-vanishing probability of finding these fluctuations. In addition, the study of Röpke

(2007) was performed for some instants of time only. Hence, the occurrence of one or a few of these fluctuations at the flame during the entire late deflagration phase may reach a high probability. Recent studies of Woosley et al. (2009) show also that velocity fluctuations of the order of 0.5×10^8 cm s^{-1} maybe already sufficient to trigger a DDT.

The average velocity fluctuations at the flame in the turbulent deflagration phase are approximately 10^7 cm s^{-1} (e.g. Figure 1 in Röpke, 2007)). Turbulent velocity fluctuations of 0.5×10^8 cm s^{-1} or even 10^8 cm s^{-1} are therefore statistically expected to occur much rarer. The occurrence of these high velocity fluctuations can only be explained by intermittency, of which the properties may be crucial for a DDT (Pan et al., 2008). Weak intermittency in predominantly burned material of the white dwarf was found by Schmidt et al. (2010). This analysis was based on the computation and fitting of characteristic scaling exponents of the turbulent velocity field that were obtained from the calculation of velocity structure functions up to the sixth order, using the data of a highly resolved deflagration model (Ciaraldi-Schoolmann et al., 2009; Röpke et al., 2007a). The fact that Röpke (2007) also found high velocity fluctuations in the same model may indicate that intermittency is also present at the flame. But the analysis of Röpke (2007) has never been intended to study intermittency in detail, hence some uncertainties about the origin of these high velocity fluctuations remain. Anyway, we conclude that a certain degree of intermittency in turbulence at the flame is necessary for a DDT to occur.

Fuel fraction and fuel density

The sole fact that high velocity fluctuations exist somewhere at the flame is not sufficient for a DDT to occur. It is also important that these fluctuations are predominantly located in the unburned material within the mixed region. The minimum amount of fuel $X_{\mathrm{fuel}}^{\mathrm{DDT}}$ that is required for the ignition and development of a self-sustained propagating detonation wave depends on many quantities, such as the fuel density ρ_{fuel}, the chemical composition of the local material as well as the fuel temperature (Arnett & Livne, 1994b; Khokhlov et al., 1997; Seitenzahl et al., 2009a). In general, the ignition in a region that contains a too low amount of fuel cannot build up the required shock strength for the detonation. Due to the described dependencies, there is no general value for $X_{\mathrm{fuel}}^{\mathrm{DDT}}$ for triggering a DDT. A detailed analysis in this context is given in Seitenzahl et al. (2009a) for instance.

To estimate a value for ρ_{fuel} for a DDT, we first ensure that burning takes place in the distributed burning regime. Here Niemeyer & Woosley (1997) found that this condition is approached for densities lower than 3×10^7 g cm^{-3}. But there are further constraints for detonations in the distributed burning regime. As long as a balance between turbulent mixing and burning exists, DDTs may be prevented (Woosley, 2007). This balance is disturbed when the flame width δ approaches the integral scale L, where the unsteady nature of the burning becomes important. The condition $\delta \simeq L$ is met, when $Da_{\mathrm{t}} = 1$ (see Section 3.2.3), which is therefore an additionally necessary constraint for a DDT in the distributed burning regime (Woosley, 2007).[7] For this case, Woosley (2007) derived a density range of $\rho_{\mathrm{fuel}} = (0.5 \ldots 1.5) \times 10^7$ g cm^{-3} at which DDTs are expected to occur. It should be noted that Woosley (2007) assumes $L \approx 10$ km, which is of the same order of magnitude as $\ell_{\mathrm{Kol/RT}}$ (see Section 3.2.1). In the analysis of Ciaraldi-Schoolmann et al. (2009), L seems to be larger, since kinetic energy is injected into the cascade on larger length scales, similar to the case

[7] Woosley et al. (2009) further argue that DDTs can only occur in the SF regime, where $Da_{\mathrm{t}} \gtrsim 1$. However, there is no clear conclusion yet at which value of Da_{t} DDTs are most probable. According to Woosley et al. (2009) DDTs are expected for $Da_{\mathrm{t}} \sim 1 \ldots 10$.

shown in Figure 3.1. However, at $\ell_{\mathrm{Kol/RT}}$ the isotropy in the turbulence is broken, hence in the context of the study of Woosley (2007) we may define $L_{\mathrm{Kol}} = \ell_{\mathrm{Kol/RT}}$ as the integral length scale for isotropic turbulence (see also discussion in Schmidt et al., 2010). Whether or not $Da_{\mathrm{t}} \gtrsim 1$ holds for the burning processes in the case of $L_{\mathrm{Kol}} \lesssim \delta \lesssim L$ under the influence of an anisotropic turbulent velocity field is not known. However, as shown later, we have to take into account the different scaling properties of the turbulent velocity field for length scales smaller and larger than $\ell_{\mathrm{Kol/RT}}$ for a modeling approach for DDTs.

Critical size and mixing of the DDT region

Finally, a region that meets the described constraints for the quantities $v'(\ell)$, $X_{\mathrm{fuel}}^{\mathrm{DDT}}$ and ρ_{fuel} has to exceed a critical length scale ℓ_{crit} for a DDT (e.g. Khokhlov et al., 1997; Niemeyer & Woosley, 1997; Dursi & Timmes, 2006; Seitenzahl et al., 2009a) that is approximately 10^6 cm (e.g. Khokhlov et al., 1997; Seitenzahl et al., 2009a). As shown later, the size of this region has to be derived from the flame geometry, hence the fractal dimension of the flame becomes important.

In Section 3.2.1 we introduced with the half eddy turnover time $\tau_{\mathrm{eddy}_{1/2}}(\ell) = 0.5 \cdot \ell / v'(\ell)$ (equation (3.23)) a time scale which constitutes the minimum required time for the mixing of two different fluids (like the fuel and ash in a DDT region) on the scale ℓ. However, as outlined in the following the eddy turnover time depends on the degree of anisotropy and intermittency in the turbulent motions that are both not considered in equation (3.23). For isotropic turbulence equation (3.22) holds. To account for anisotropic effects on certain length scales the exponent of 2/3 in equation (3.22) has to be modified accordingly on these scales, which consequently affects the eddy turnover time. Moreover, for the study of DDTs we restrict the considerations to high turbulent velocity fluctuations that are mainly attributed to intermittency. When we fully exclude the average velocity fluctuations that occur far more frequently and obey well-defined statistical properties (see Section 3.2.1), the picture of a steady and undisturbed energy cascade with a well-defined scaling relation breaks down. This becomes even more obvious, when we consider that the high velocity fluctuations may originate from inhomogeneous energy dissipation rates on different length scales due to intermittency in the turbulent motions (see Section 3.2.2). The eddy turnover time in equation (3.22) relies on a constant energy dissipation rate in the inertial range. Therefore, the real eddy turnover time in a region with very high turbulent velocity fluctuations may significantly deviate from the estimated value for $\tau_{\mathrm{eddy}_{1/2}}(\ell)$ with equation (3.23). As shown later in Section 5.2 both the degree of anisotropy and intermittency in the vicinity of the flame are difficult to estimate and not well known. In the following, we neglect the influences of anisotropy and intermittency on the eddy turnover time and assume an undisturbed mixing of the fuel and ash on the scale ℓ_{crit}. Then we can estimate the time for the mixing process with equation (3.23), where we assume that the fuel and ash can be mixed by a turbulent eddy of size ℓ_{crit} in a time of

$$\tau_{\mathrm{eddy}_{1/2}}(\ell_{\mathrm{crit}}) = 0.5 \cdot \ell_{\mathrm{crit}} / v'(\ell_{\mathrm{crit}}). \tag{3.48}$$

With $\ell_{\mathrm{crit}} = 10^6\,\mathrm{cm}$ and $v'(\ell_{\mathrm{crit}}) = 10^8\,\mathrm{cm\,s^{-1}}$ (Lisewski et al., 2000) it follows $\tau_{\mathrm{eddy}_{1/2}}(\ell_{\mathrm{crit}}) = 0.5 \times 10^{-2}\,\mathrm{s}$. With $v'(\ell_{\mathrm{crit}}) = 0.5 \times 10^8\,\mathrm{cm\,s^{-1}}$ (Woosley et al., 2009) we find $\tau_{\mathrm{eddy}_{1/2}}(\ell_{\mathrm{crit}}) = 1.0 \times 10^{-2}\,\mathrm{s}$, respectively. If eventually a region that meets the above-mentioned constraints exceeds ℓ_{crit} for at least $\tau_{\mathrm{eddy}_{1/2}}(\ell_{\mathrm{crit}})$, DDTs may occur.

3.3.3 Summary

From the described constraints for a DDT it becomes obvious that a one-parameter criterion is not capable of accounting for the detailed physics of the DDT process, even if such models may lead to results that are consistent with observations. However, the latter has not been strictly shown yet for multi-dimensional models. In two- and three-dimensional models DDTs occur more frequently and the explosions become brighter than in one-dimensional models. As a consequence, the threshold value of a relevant quantity for a DDT criterion (such as ρ_{crit} for instance) has to be accordingly adjusted in dependence of the dimensionality in order to obtain the observed explosion brightnesses. In this way, it may become very hard to reproduce the observed faint events of normal SNe Ia in three-dimensional simulations. In this work, a new DDT model is introduced and applied exclusively to three-dimensional simulations, where the model is motivated by the described necessary constraints for a DDT to occur. The following quantities have to be taken into account for the physics of a DDT (in the following referred to as *DDT quantities*):

- Turbulent velocity fluctuations $v'(\ell)$ and the turbulent driving mechanism (Kolmogorov or RT instability) at the flame
- Minimum amount of fuel $X_{\mathrm{fuel}}^{\mathrm{DDT}}$ and fuel density ρ_{fuel} at the flame
- Fractal dimension D of the flame
- The size of the flame surface area and the DDT region
- The half eddy turnover time $\tau_{\mathrm{eddy}_{1/2}}(\ell_{\mathrm{crit}})$

In general, a conclusive evidence for DDTs requires resolving the microphysical properties of the DDT. As already described, the length scales where this process is expected to occur are too small to be resolved in multidimensional full-star simulations. Therefore, we do not address the question of whether or not DDTs occur here from a microphysical point of view. Instead, we assume that they occur and devise a model to implement them into large-scale SN Ia simulations taking into account all known constraints on the microphysical mechanism.

4

Numerical simulations of Type Ia supernova explosions

The physical processes of an exploding white dwarf are very complex and constitute a major challenge for numerical modeling. In particular, the hydrodynamic equations, including the reaction equations of the thermonuclear burning in partially relativistic degenerate gases of very high densities have to be taken into account. These equations are commonly implemented in numerical hydrodynamic codes that run on supercomputers, sometimes for several weeks or months. Despite the continuous improvements of numerical codes and the performance of supercomputers it will probably never be possible to resolve all relevant length scales of SN Ia explosions in full-star simulations. These length scales span a range of approximately 12 orders of magnitudes, if we assume that a typical white dwarf has a radius of 2000 km (which may additionally expand in a deflagration) and the Kolmogorov length scale is smaller than a millimeter (see Section 3.2.1). Since physical processes occur on unresolved length scales which determine the explosion dynamics, a corresponding modeling approach is required. Several numerical methods have been developed in this context, including the *large eddy simulations (LES)*. In LES the largest turbulent structures are resolved on the grid scale or above. Physical processes in smaller irresolvable turbulent structures are modeled with a *subgrid-scale (SGS) turbulence model*. In this work, a hydrodynamic code is used which complies with some basic concepts of LES. The main features of this code are outlined in Section 4.1. The standard setup of the performed simulations that includes the initial white dwarf model is described in Section 4.2.

4.1 LEAFS

For this work, the hydrodynamic code LEAFS (**LE**velset based **A**strophysical **F**lame **S**imulations) is used. LEAFS is a descendant of the PROMETHEUS code which has been developed by Fryxell et al. (1989) (see also Reinecke, 2001). In this work, the code is used to perform three-dimensional full-star simulations of delayed detonations of Chandrasekhar-mass white dwarfs. In the following, the main features of LEAFS are discussed. For a detailed description of the code we refer to Reinecke (2001). The SGS model is outlined

separately in Section 5.2, where it is tested with respect to the implementation of the DDT model.

4.1.1 Flame propagation via level set method

The numerical code uses two nested co-moving simulation grids (Röpke, 2005; Röpke et al., 2006). While an outer inhomogeneous grid follows the expansion of the whole white dwarf, the flame is tracked with an inner homogeneous Cartesian grid. Throughout this work it is understood that $\Delta(t)$ belongs to the time-dependent resolution of the inner expanding grid. The flame width δ is very thin compared to the size of the white dwarf and treated as a sharp discontinuity. This holds for both deflagration and detonation flames. For propagating flames in white dwarfs in the discontinuity approach, the *level set method* has been proven useful (Osher & Sethian, 1988; Smiljanovski et al., 1997; Reinecke et al., 1999). Here the geometry $\Gamma(t)$ of the flame front in a three-dimensional simulation is given by a two-dimensional hyper surface. As shown later, this relation can be used to estimate the fractal dimension of the deflagration flame. $\Gamma(t)$ is additionally associated with the zero point of a scalar distance function $G(\boldsymbol{r}, t)$, where in burned material $G(\boldsymbol{r}, t) > 0$ and in unburned material $G(\boldsymbol{r}, t) < 0$ holds. Therefore, for grid cells near the flame we find $|G(\boldsymbol{r}, t)| < \Delta(t)$. The propagation of the flame is determined by the temporal evolution of $G(\boldsymbol{r}, t)$. Here, we have to take into account that the flame is advected by the fluid motion and it propagates normal to the flame surface due to burning. The time evolution of $G(\boldsymbol{r}, t)$ is given by (see Reinecke et al., 1999)

$$\frac{\partial G}{\partial t} = -(\boldsymbol{v}_\mathrm{u} + v_{\mathrm{flame_u}}\boldsymbol{n})(-\boldsymbol{n}|\nabla G|) = (\boldsymbol{v}_\mathrm{u} \cdot \boldsymbol{n} + v_{\mathrm{flame_u}})|\nabla G|, \tag{4.1}$$

where $\boldsymbol{v}_\mathrm{u}$, $v_{\mathrm{flame_u}}$ and $\boldsymbol{n}$ denote the velocity of the fluid in the fuel, the burning speed with respect to the unburned material and the normal vector to the flame front that points toward the unburned material, respectively.

4.1.2 The effective burning speed of the deflagration flame

In the very early deflagration phase the flame propagation is laminar, hence v_flame equals approximately the laminar burning speed u_lam which is given by equation (3.6). In the turbulent deflagration phase a correct determination of v_flame requires to resolve all the wrinkles and curvatures of the flame front. But in our large-scale simulations these turbulent flame structures are not fully resolved and the flame surface is smoothed artificially. However, the burning speed can be estimated by assigning an *effective turbulent flame speed* $v_\mathrm{t}(\ell)$ to the smoothed flame and relating this quantity to the laminar burning speed u_lam and the turbulent velocity fluctuations $v'(\ell)$. Following Pocheau (1994) $v_\mathrm{t}(\ell)$ is given by

$$v_\mathrm{t}(\Delta(t)) = u_\mathrm{lam}\sqrt{1 + \frac{4}{3}\left(\frac{v'(\Delta(t))}{u_\mathrm{lam}}\right)^2}, \tag{4.2}$$

where we used $\ell = \Delta(t)$. The turbulent velocity fluctuations $v'(\Delta(t))$ are provided by a turbulence SGS model, of which the properties are discussed extensively in Schmidt et al. (2006a,b).

4.1.3 Hydrodynamics and equation of state

White dwarfs are self-gravitating degenerate gas masses that are in hydrostatic equilibrium. For a complete physical description of these objects, one needs the hydrodynamic conservation laws for mass, momentum and energy and a thermodynamic equation of state (EOS) for the degenerate material. In addition, for the SN Ia problem the properties of thermonuclear burning and the participating chemical species and reactions have to be included. The resulting system of coupled partial differential equations are called the *reactive Euler equations*. With gravitation as external force, these equations are given by (e.g Röpke & Schmidt (2009)):

- mass conservation

$$\frac{\partial \rho}{\partial t} = -\nabla \cdot (\rho \boldsymbol{v}), \tag{4.3}$$

- momentum balance

$$\frac{\partial \rho \boldsymbol{v}}{\partial t} = -\nabla \cdot (\rho \boldsymbol{v}\boldsymbol{v}) - \nabla p - \rho \nabla \phi, \tag{4.4}$$

- species balance

$$\frac{\partial \rho X_i}{\partial t} = -\nabla \cdot (\rho X_i \boldsymbol{v}) + \rho \omega_{X_i} \qquad i = 1...\mathrm{N}, \tag{4.5}$$

- energy balance

$$\frac{\partial \rho e_{\mathrm{tot}}}{\partial t} = -\nabla \cdot (\rho e_{\mathrm{tot}} \boldsymbol{v}) - \nabla(\rho \boldsymbol{v}) - \rho \boldsymbol{v} \cdot (\nabla \phi) + \rho S, \tag{4.6}$$

with

$$\omega_{X_i} = \omega_{X_i}(\rho, T, X_i), \tag{4.7}$$
$$p = f_{\mathrm{EOS}}(\rho, e_{\mathrm{int}}, X_i), \tag{4.8}$$
$$T = f_{\mathrm{EOS}}(\rho, e_{\mathrm{int}}, X_i), \tag{4.9}$$
$$S = S(\omega_{X_i}), \tag{4.10}$$
$$\Delta \phi = 4\pi G \rho. \tag{4.11}$$

In these equations is ρ the mass density, $\boldsymbol{v}$ the velocity, p the pressure, ϕ the gravitational potential, X_i the specific mass fraction of the i-th chemical species, ω_{X_i} a corresponding reaction rate, e_{tot} the specific total energy, e_{int} the specific internal energy, f_{EOS} an appropriate EOS, T the temperature, S a source term for the energy release due to the reactions and G the gravitational constant. The EOS of white dwarf matter that determines the pressure and energy, consists of the non-relativistic ion gas, the electron gas that may be both degenerate and relativistic, the thermal photon gas, as well as a contribution from the generation of electron-positron pairs. For the individual components, the pressure and energy density e

are given by (see Cox, 1968; Shapiro & Teukolsky, 1983)

$$p_{\mathrm{ion}} = \rho R T \sum_i \frac{X_i}{M_i}, \tag{4.12}$$

$$p_{\mathrm{e^-}} = \frac{16\pi\sqrt{2}}{3h^3} m_{\mathrm{e}}^3 c^5 \beta^{\frac{3}{2}} \left[F_{\frac{3}{2}}(\eta,\beta) + \frac{1}{2}\beta F_{\frac{5}{2}}(\eta,\beta) \right], \tag{4.13}$$

$$p_{\mathrm{photon}} = \frac{4}{3c}\sigma_{\mathrm{B}} T^4, \tag{4.14}$$

$$p_{\mathrm{e^-+e^+}} = \frac{16\pi\sqrt{2}}{3h^3} m_{\mathrm{e}}^3 c^5 \beta^{\frac{3}{2}} \left[\tilde{F}_{\frac{3}{2}}(\eta,\beta) + \frac{1}{2}\beta \tilde{F}_{\frac{5}{2}}(\eta,\beta) \right], \tag{4.15}$$

$$e_{\mathrm{ion}} = 3/2 p_{\mathrm{ion}}, \tag{4.16}$$

$$e_{\mathrm{e^-}} = \frac{8\pi\sqrt{2}}{h^3} m_{\mathrm{e}}^4 c^5 \beta^{\frac{5}{2}} \left[F_{\frac{3}{2}}(\eta,\beta) + \beta F_{\frac{5}{2}}(\eta,\beta) \right], \tag{4.17}$$

$$e_{\mathrm{photon}} = 3 p_{\mathrm{photon}}, \tag{4.18}$$

$$e_{\mathrm{e^-+e^+}} = \frac{8\pi\sqrt{2}}{h^3} m_{\mathrm{e}}^4 c^5 \beta^{\frac{5}{2}} \left[\tilde{F}_{\frac{3}{2}}(\eta,\beta) + \beta \tilde{F}_{\frac{5}{2}}(\eta,\beta) \right], \tag{4.19}$$

where R is the gas constant, M_i the molar mass of the i-th chemical species, h the Planck constant, m_{e} the electron mass, c the speed of light, σ_{B} the Stefan-Boltzmann constant and F_{k} and $\tilde{F}_{\mathrm{k}}$ are the relativistic Fermi integrals defined as

$$F_{\mathrm{k}}(\eta,\beta) = \int_0^\infty \frac{x^{\mathrm{k}} \left(1 + \frac{1}{2}\beta x\right)^{\frac{1}{2}}}{e^{-\eta+x}+1} dx \qquad \mathrm{k} > -1, \tag{4.20}$$

$$\tilde{F}_{\mathrm{k}}(\eta,\beta) = F_{\mathrm{k}}(\eta,\beta) + F_{\mathrm{k}}\left(-\eta - \frac{2}{\beta}, \beta\right). \tag{4.21}$$

The parameters η and β are further given by

$$\eta = \frac{E_{\mathrm{F}}}{k_{\mathrm{B}} T} \qquad \text{and} \qquad \beta = \frac{k_{\mathrm{B}} T}{m_{\mathrm{e}} c^2}, \tag{4.22}$$

where E_{F} is the Fermi energy and k_{B} the Boltzmann constant. η and β are a measure for the degree of the degeneracy and the influence of relativistic effects, respectively. In the dense center of the white dwarf E_{F} is high enough that relativistic effects become important. During the explosion process the degeneracy is partially lifted in the burned material due to the high temperature increase.

The reactive Euler equations are treated numerically in a finite volume approach (Fryxell et al., 1989) by the use of the Piecewise Parabolic Method (PPM) of Colella & Woodward (1984). Since the Fermi integrals in the EOS are computationally too expensive to be calculated during a simulation time step directly, the corresponding values are obtained from a prior calculated table with bilinear interpolation.

4.1.4 Nuclear reaction processes

The complete nuclear reaction network to burn a carbon/oxygen mixture to iron group elements includes more than 3000 reactions and hundreds of isotopes (e.g. Hix & Thielemann,

1996; Burbidge et al., 1957). The use of such a sophisticated network in hydrodynamic simulations would require a significant amount of computational resources. In LEAFS, only a few effective reactions and chemical species are taken into account.

Depending on the density where burning currently takes place, the material is converted to heavier elements: For sufficiently high densities, the material is mainly burned to a mixture of ^{56}Ni and α-particles in *nuclear statistical equilibrium (NSE)*. In this case, at each time step the fractions of ^{56}Ni and α-particles are adapted to the current thermodynamic conditions of the white dwarf. Burning to NSE increases the overall fraction of iron group elements (IGE) that is approximated by one representative. With decreasing density, the reaction already ends with the production of intermediate mass elements (IME), of which the overall fraction is also given by one representative. For lower densities, only ^{12}C can still burn to ^{16}O until at even lower densities no thermonuclear reactions occur anymore.

The required fuel densities to burn the carbon/oxygen composition to heavier elements, additionally strongly depend on the burning mode. In the case of a shock-driven detonation, fuel at relatively low densities can be still sufficiently compressed to be burned, which does not hold for deflagrations. In Figure 4.1 the obtained mass fractions of the chemical species that are used in LEAFS are shown as function of the fuel density for a deflagration and a detonation (see also Fink et al., 2010), where the fuel is assumed to be consisted of carbon and oxygen in equal amounts by mass.

The described simplified reaction network consumes only marginal computational resources in the hydrodynamic simulation and leads already to a good estimate for the energy release during the burning (or equivalently for the source term S). However, we are also able to obtain mass fractions of individual elements and isotopes by performing a post processing step with tracer particles that are implemented in LEAFS. The tracer act as artificial particles that are passively advected by the flow, whereby they collect certain information along their trajectories during the SN Ia simulation (see Travaglio et al., 2004; Seitenzahl et al., 2010a,b).

4.2 The initial white dwarf model

The initial model of the white dwarf that is set up in the numerical simulation includes some parameters, of which the values are not well known (see Section 2.3.1). In particular at ignition time, the central density ρ_c and temperature T_c, the chemical composition (metallicity and carbon/oxygen ratio) of the white dwarf, as well as the physical properties of the ignition region from which the flame evolves are highly uncertain. Furthermore, the rotation of the star can be included in which case the white dwarf may also have a higher initial mass than M_{CH} (see Section 2.3.5).

4.2.1 The standard initial conditions of the white dwarf

In the following, the standard setup of the initial white dwarf model is described that is frequently used in the simulations of this work. We assume isothermal, cold and non-rotating Chandrasekhar-mass white dwarfs in hydrostatic equilibrium with $\rho_c = 2.9 \times 10^9$ g cm^{-3} and $T_c = 5 \times 10^5$ K. The chemical composition is 50% ^{12}C and 50% ^{16}O which is distributed homogeneously throughout the star. The electron fraction Y_e of a given composition can be

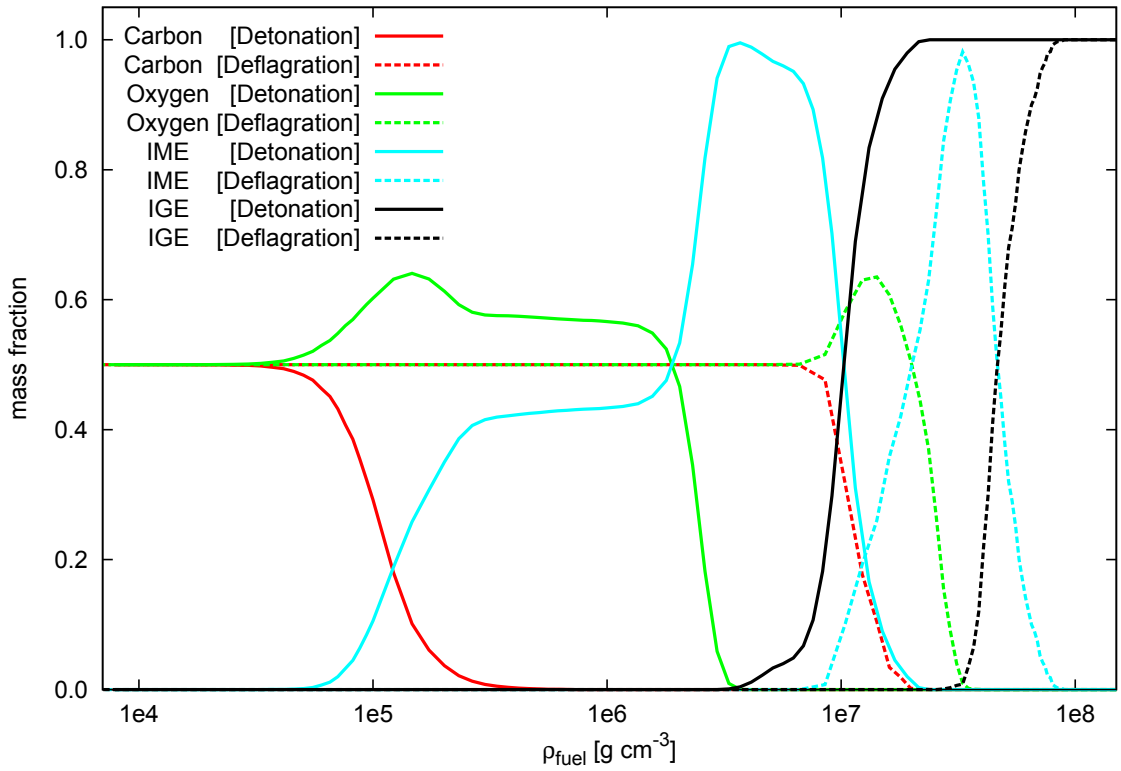

Fig. 4.1: Mass fractions of chemical species from thermonuclear burning as function of the fuel density ρ_{fuel} in detonations (Fink et al., 2010) (solid lines) and deflagrations (dashed lines).

defined as

$$Y_{\mathrm{e}} = \sum_i X_i \frac{P_i}{A_i}, \tag{4.23}$$

where X_i, P_i and A_i denote the specific mass fraction, the proton number and the nucleon number of the i-th chemical species in the composition, respectively. Hence, for $X(^{12}\mathrm{C}) = X(^{16}\mathrm{O}) = 0.5$ we find $Y_{\mathrm{e}} = 0.5$. The initial chemical composition is fixed in the current implementation of the code. However, we can take a certain metallicity of the white dwarf into account by determining Y_{e} with a slightly different chemical composition. In our case, we replace a certain amount of the carbon/oxygen mixture with ^{22}Ne and adjust the value of Y_{e} accordingly. We assume that the progenitor star of the white dwarf has solar metallicity, which corresponds to a ^{22}Ne mass fraction of about $X(^{22}\mathrm{Ne}) = 0.025$.[1] With

[1] $X(^{22}\mathrm{Ne}) = 0.025$ has been used by Nomoto et al. (1984) in a famous deflagration model (called *W7*). We outline here, how $X(^{22}\mathrm{Ne})$ can be estimated roughly under the assumption of solar metallicity. The metallicity Z can be defined as the mass ratio of chemical species with a proton number of $P \geq 3$ to the overall chemical species. For the Sun, Anders & Grevesse (1989) give a value of $Z \approx 0.020$, while Asplund et al. (2005) propose a far lower metallicity of $Z \approx 0.012$. Here we make a compromise and simply take the average, which yields $Z = 0.016$. We further assume that most of the metals (isotopes with $P \geq 3$) are found within the CNO cycle in which continuously ^{14}N is produced. Thereby the metallicity stays approximately constant. During the ensuing helium burning phase ^{22}Ne is synthesized from ^{14}N by two captures of α-particles and a subsequent β^+- decay. As a result the metallicity now increases up to $A(^{22}\mathrm{Ne})/A(^{14}\mathrm{N}) \cdot Z \approx 0.025$ (Seitenzahl, 2012).

$X(^{12}\mathrm{C}) = X(^{16}\mathrm{O}) = 0.5 - (0.5 \cdot 0.025) = 0.4875$ we find with equation (4.23)

$$Y_\mathrm{e} = 0.4875 \cdot \frac{6}{12} + 0.4875 \cdot \frac{8}{16} + 0.025 \cdot \frac{10}{22} = 0.49886 \tag{4.24}$$

which is our standard value for Y_e of the initial white dwarf model.

4.2.2 The ignition geometry of the deflagration

The main difference in the models in most of the performed simulations of this work is the ignition geometry of the deflagration. As indicated in Section 2.3.1 there are no clear conclusions about the location(s) and size(s) of the ignition region(s). Therefore, the ignition geometries in our models are not directly motivated by physical assumptions, but constructed in a way to obtain different evolutions of the deflagration flame. As pointed out in Section 2.3.4 for the delayed detonation scenario the strength of the deflagration plays an important role for the brightness of the explosion. It is known that off-center ignitions of the deflagration flame yield mainly weak deflagrations (e.g. Röpke et al., 2007b). Here an ensuing detonation commonly leads to bright explosions only (e.g. Meakin et al., 2009). Therefore, for the delayed detonation scenario centrally ignited deflagration flames are required if the delayed detonation scenario should account for the whole observed variations in the brightness of normal SNe Ia. For our ignition models we follow Plewa (2007), Röpke et al. (2006) and Röpke et al. (2007a,b) and perform single and multiple spot ignitions in the vicinity of the center of the white dwarf. In Table 4.1 the ten standard ignition models with specific values of the parameters of the ignition geometry are summarized. These models are frequently used in the following studies.

The primary parameter of the ignition geometry is the number of spherical ignition kernels N_k from which the deflagration flame evolves. This parameter sets mainly the strength of the deflagration (Röpke et al., 2006) which in turn determines the energy release and hence the expansion rate of the white dwarf. Two additional parameters are the radius r_k of the kernels and the minimum distance d_k that the center of these kernels have to maintain.

For each ignition geometry exclusively one uniform value for r_k and d_k is chosen. The radius of an individual kernel in multiple spot ignition scenarios may be of the order of 10^5 cm (e.g. Woosley et al., 2004; Iapichino et al., 2006). This value is below our initial grid resolution and we use $r_\mathrm{k} = 10^6$ cm. The value of d_k is chosen arbitrarily. Since we use a constant value for r_k for all ten standard models, the parameter d_k can be seen as a measure of how fast the flame kernels become merged in the explosion. This in turn has an effect on the occurrence of different kinks and bends at the flame that are the seeds for instabilities to arise. We note that for large N_k, $d_\mathrm{k} < r_\mathrm{k}$, indicating that kernels may partially overlap, so that instabilities may arise quickly after the onset of the explosion. The effect of a variation of r_k and d_k within an ignition geometry on the simulation results is investigated in Section 7.2.3.

For all ignition geometries, the kernels are placed spherically symmetric in the central region of the white dwarf. They are mostly concentrated in the vicinity of the center, while their number declines outward, following a Gaussian distribution. A fixed cutoff R is set, which defines the maximum distance for the ignition kernels from the center of the white dwarf. We use $R = 2.5 \cdot \sigma$, where σ is the variance of the Gaussian distribution. σ is chosen in a way that we obtain (except for Model I) values for R that agree with the study of Woosley et al. (2004). However, there is no physical consensus on how the ignition kernels should be distributed generally. For ignition geometries with small N_k we note that the arrangement of

the kernels cannot be considered as a real Gaussian distribution anymore. In particular, for $N_\mathrm{k} = 1$ (Model I), where $R = \sigma$, the setup can be described as a simple *off-center* ignition scenario. A further special ignition model is Model X that is based on a configuration used in a highly resolved simulation of a pure deflagration, performed by Röpke et al. (2007a). By the generation of this setup also $R = \sigma$ holds. Furthermore, individual ignition kernels are removed and newly arranged, until a very compact and dense initial flame configuration of high spherical symmetry is obtained.

In Figure 4.2 we show the ignition geometries from Table 4.1, except for the single spot off-center of Model I. In the figures an isosurface is drawn that corresponds to a density of $2.2 \times 10^9\,\mathrm{g\,cm^{-3}}$ which is about $2.5 \times 10^7\,\mathrm{cm}$ away from the center of the white dwarf. For the generation of the ignition geometries, a Monte-Carlo based program is used that produces the ignition setups from the input of the required parameters in the form of a table that includes the position and the uniform size of ignition kernels. It should be noted that in general for a chosen set of parameters for an ignition setup, more than one realization is possible which are different in the spatial distribution of the ignition kernels.

In this work, a detailed parameter study is performed, where a large number of additional ignition geometries of the deflagration is used, of which the parameters are summarized in Table 4.2. Some setups may appear twice in Table 4.2 or equal a standard setup of Table 4.1. Here another realization of the corresponding setup was chosen.

Model	N_k	σ [10^7 cm]	r_k [10^6 cm]	d_k [10^6 cm]
I	1	0.36	1.00	-
II	3	0.50	1.00	3.00
III	5	0.60	1.00	1.00
IV	10	0.60	1.00	1.00
V	20	0.60	1.00	0.60
VI	40	0.60	1.00	1.00
VII	100	0.60	1.00	0.30
VIII	200	0.75	1.00	0.30
IX	1600	1.00	1.00	0.05
X	1600	1.80	1.00	0.05

Table 4.1: Setups of the ten standard ignition geometries of the deflagration flame.

Model	N_k	σ [10^7 cm]	r_k [10^6 cm]	d_k [10^6 cm]	Model	N_k	σ [10^7 cm]	r_k [10^6 cm]	d_k [10^6 cm]
1	5	0.60	1.00	1.00	**19**	200	0.75	1.00	0.10
2	30	0.60	1.00	1.00	**20**	200	0.75	1.00	0.34
3	40	0.60	1.00	1.00	**21**	200	2.00	1.00	0.50
4	50	0.60	1.00	0.80	**22**	250	0.80	1.00	0.23
5	60	0.40	1.00	0.40	**23**	300	0.80	1.00	0.23
6	60	0.40	1.00	0.40	**24**	350	0.90	1.00	0.20
7	80	0.60	1.00	0.50	**25**	400	1.00	1.00	0.10
8	125	0.60	1.00	0.40	**26**	500	1.00	1.00	0.17
9	150	0.60	1.00	0.35	**27**	600	1.00	1.00	0.13
10	175	0.60	1.00	0.30	**28**	700	1.00	1.00	0.12
11	200	0.75	1.00	0.30	**29**	800	1.00	1.00	0.08
12	200	0.66	1.00	0.30	**30**	900	1.00	1.00	0.08
13	200	1.00	1.00	0.30	**31**	1000	1.00	1.00	0.07
14	200	1.50	1.00	0.30	**32**	1200	1.00	1.00	0.06
15	200	2.00	1.00	0.30	**33**	1400	1.00	1.00	0.05
16	200	3.00	1.00	0.30	**34**	1600	1.00	1.00	0.05
17	200	0.75	0.50	0.30	**35**	3000	1.40	1.00	0.03
18	200	0.75	1.10	0.30	**36**	5000	1.60	1.00	0.02

Table 4.2: Setups of the ignition geometries of the deflagration flame for the parameter study in Chapter 7.

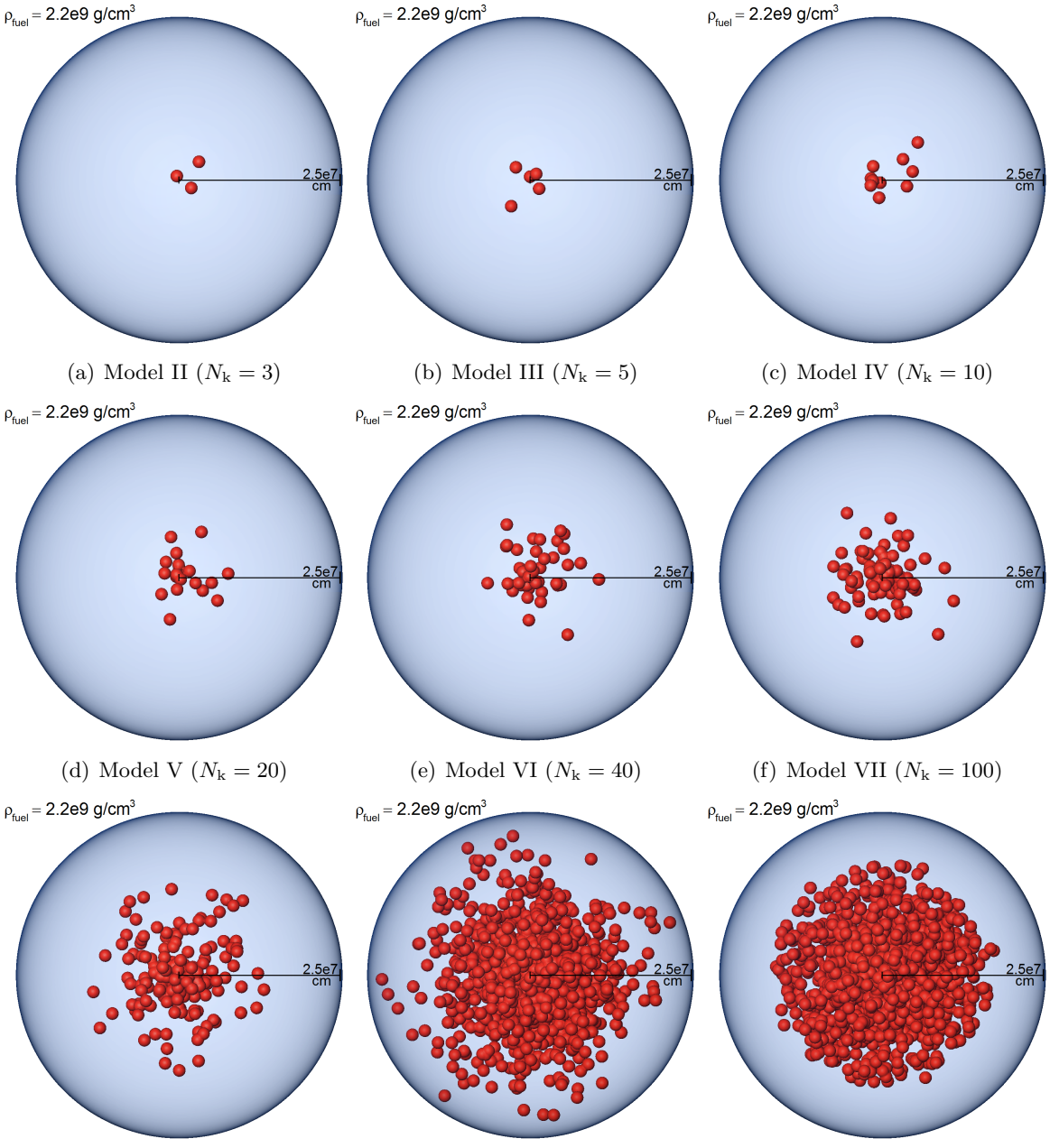

(a) Model II ($N_\mathrm{k} = 3$) (b) Model III ($N_\mathrm{k} = 5$) (c) Model IV ($N_\mathrm{k} = 10$)

(d) Model V ($N_\mathrm{k} = 20$) (e) Model VI ($N_\mathrm{k} = 40$) (f) Model VII ($N_\mathrm{k} = 100$)

(g) Model VIII ($N_\mathrm{k} = 200$) (h) Model IX ($N_\mathrm{k} = 1600$) (i) Model X ($N_\mathrm{k} = 1600$)

Fig. 4.2: Ignition geometries of the deflagration of Model II - Model X. Shown are the arranged ignition kernels (red spheres) and a transparent blue isosurface where $\rho_\mathrm{fuel} = 2.2 \times 10^9$ g cm^{-3}. The distance from the center of the white dwarf where $\rho_\mathrm{c} = 2.9 \times 10^9$ g cm^{-3} to this isosurface is approximately 2.5×10^7 cm. Only in Model IX, some ignition kernels may approach this distance. Model X obviously has a very compact and dense arrangement of the ignition kernels, resulting in a setup of high spherical symmetry.

5 Modeling delayed detonations

To resolve a DDT region that has a length of $\ell_{\text{crit}} \approx 10^6\,\text{cm}$ we need at least 1024^3 grid cells in LEAFS. The microphysical processes within a DDT region occur on much smaller scales that cannot be resolved in our full-star simulations. With the currently available computational resources, simulations with 1024^3 grid cells are already very expensive and take a significant amount of time. This work, however, is designed to run many simulations in order to perform detailed parameter studies, which is motivated by the fact that most of the values of the DDT quantities that are summarized in Section 3.3.3 are not well known. Therefore, many low resolved simulations with 256^3 grid cells are performed in which the length of the grid cells $\Delta(t)$ is larger than ℓ_{crit} during the entire late deflagration phase. For the implementation of a DDT model in LEAFS this means that an appropriate SGS approach is required to model the DDT quantities on unresolved scales. In this chapter the construction and the tests of this DDT-SGS model (in the following simply referred to as DDT model) are described. In Section 5.1 we first determine the flame surface area that meets certain constraints for a DDT. The already existing SGS model in LEAFS that calculates the turbulent velocity fluctuations $v'(\ell)$ in the deflagration phase is tested in Section 5.2 where we explicitly evaluate, whether this model is capable of modeling the important high velocity fluctuations for a DDT properly. In Section 5.3 we formulate the DDT model and the criterion for DDTs. The resolution dependence of the DDT model is tested in Section 5.4. Here we are also able to derive a value for the fractal dimension of the flame. Section 5.5 gives a summary of the DDT model.

5.1 Determination of the flame surface area

First we determine the grid cells that meet the necessary constraints for a DDT. To capture all regions at the flame we take into account only grid cells where $|G(\boldsymbol{r}, t)| < \Delta(t)$ (see Section 4.1.1). Furthermore, as stated in Section 3.3.2 a specific amount of fuel $X_{\text{fuel}}^{\text{DDT}}$, a certain fuel density ρ_{fuel} and high velocity fluctuations $v'(\ell)$ at the flame are required for a DDT. Here the question arises how these constraints can be implemented in a model in which a DDT region is not resolved. A further complication is that the flame is treated as a sharp discontinuity that prevents us to determine values of physical quantities at the

flame precisely. Hence, the value of $X_{\text{fuel}}^{\text{DDT}}$, ρ_{fuel} and $v'(\ell)$, as well as the mixing processes within a DDT region at the flame cannot be determined directly. We also have to take into account that due to the grid discretization the flame can be found in all possible regions within a grid cell. The values of the physical quantities of a grid cell represent the physical properties at the flame best, when the flame approximately splits the grid cell into two parts of equal size. Therefore, we will perform a preselection of the grid cells in which the flame propagates on average through their centers. We note that in principle DDTs may occur at all suitable places at the deflagration flame that meet the necessary DDT constraints, regardless of whether the flame propagates through the central part of a grid cell or whether a grid cell is hardly intersected by the flame. The latter will be skipped in our analysis, since this cell mainly represents the physical properties in ash or fuel regions. The preselection of grid cells implies that a certain fraction of the deflagration flame that may meet the necessary DDT constraints is not taken into account in our study. In the context of the DDT model, this will eventually lead to an underestimate of the occurrence of DDTs. However, as shown later the flame surface area that meets the DDT constraints is not the only (and often not the most important) quantity that is relevant for the DDT criterion. In the following, we describe the method, how our study can be restricted to grid cells that seem appropriate for a DDT.

5.1.1 Constraints on the fuel fraction in the grid cells

We define the fuel fraction X_{fuel} in a grid cell as the fraction of the carbon/oxygen composition to the overall chemical species, hence $X_{\text{fuel}} \in [0;1]$. In the performed simulations a value of X_{fuel} is always given for the entire grid cell, of which the length is larger than ℓ_{crit}. Hence, for the implementation of a DDT model the analysis should be restricted to the vicinity of the flame on a sub scale $\ell_{\text{crit}} < \Delta(t)$.

For grid cells with $X_{\text{fuel}} \approx 0$ and $X_{\text{fuel}} \approx 1$ (these cells are not or hardly intersected by the flame) we mainly analyze the physical properties of ash and fuel regions that are far away from the flame and therefore inappropriate for the DDT model. To estimate the physical properties at the flame we employ with $X_{\text{fuel}}^{\text{min}}$ and $X_{\text{fuel}}^{\text{max}}$ two free parameters for the minimum and maximum fuel fraction and take for the analysis only grid cells into account in which $X_{\text{fuel}}^{\text{min}} \leq X_{\text{fuel}} \leq X_{\text{fuel}}^{\text{max}}$. For now we set $X_{\text{fuel}}^{\text{min}} = 1/3$ and $X_{\text{fuel}}^{\text{max}} = 2/3$ but these threshold values are varied later in the following studies to analyze the influence of a variation of these parameters on the simulation results. The average fuel fraction in the grid cells is expected to be $\overline{X}_{\text{fuel}} = 1/2 \cdot (X_{\text{fuel}}^{\text{min}} + X_{\text{fuel}}^{\text{max}}) = 1/2$. This also holds if no restrictions on X_{fuel} would have been set but now we find that the flame (resp. the level set) propagates on average through the central part of the grid cells. Under these conditions, we argue that a DDT region should also be localized in the central part within a grid cell, since at this place there is an enhanced probability that both fuel and ash are found on a sub scale ℓ_{crit}, while in other places there will be mostly pure fuel or ash.

From the viewpoint of DDTs that occur in the centers of grid cells we note that in most cases where $X_{\text{fuel}} > X_{\text{fuel}}^{\text{max}}$, there is pure fuel on a sub scale ℓ_{crit} in the center of the corresponding grid cell, whereas for $X_{\text{fuel}} < X_{\text{fuel}}^{\text{min}}$ there will be most often exclusively burned material. In both cases, a DDT in the center of the corresponding grid cell is unlikely to occur, since the distance between the flame and the DDT region is too large. At some local places, however, strong turbulence may deform the flame in a way that the value of X_{fuel} on a sub scale ℓ_{crit} in the center of the grid cells can be still quite high or low, even if the frequency at which these cells occur is significantly reduced due to the introduced restrictions

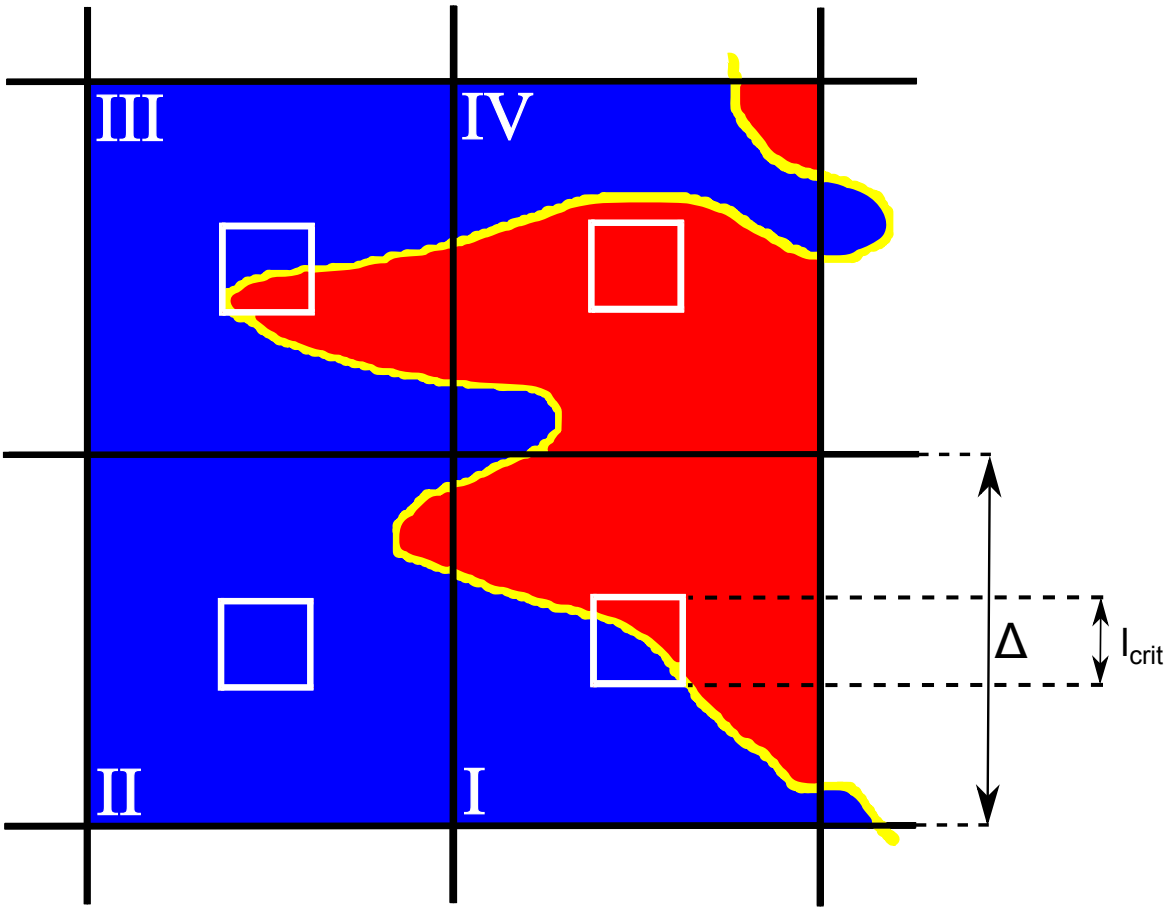

Fig. 5.1: Sketch to illustrate the effect of the restrictions on X_{fuel} in the case of $\Delta(t) \approx 4 \cdot \ell_{\mathrm{crit}}$ in two-dimensional view. In the center of the grid cells a square with the edge length of ℓ_{crit} is shown in white. Within the cells, the fuel is shown in blue and the ash in red, where both components are separated by the flame that is shown as a yellow curve. In grid cell I the flame propagates through the center and since $X_{\mathrm{fuel}}^{\mathrm{min}} \leq X_{\mathrm{fuel}} \leq X_{\mathrm{fuel}}^{\mathrm{max}}$ this cell obeys the constraint concerning X_{fuel} in our approach. In grid cell II the flame misses the center and in addition $X_{\mathrm{fuel}} > X_{\mathrm{fuel}}^{\mathrm{max}}$. Consequently this cell is not taken into account for further considerations. The inaccuracy of the described method is illustrated in the grid cells III and IV. In the former, the flame propagates through the center and there may be in addition sufficient fuel for a DDT on the sub scale ℓ_{crit}, but since $X_{\mathrm{fuel}} > X_{\mathrm{fuel}}^{\mathrm{max}}$, this cell is skipped in our study. In the latter, the fuel fraction is in the range of $X_{\mathrm{fuel}}^{\mathrm{min}} \leq X_{\mathrm{fuel}} \leq X_{\mathrm{fuel}}^{\mathrm{max}}$ so that this cell will not be skipped. However, the flame misses the center of the cell. We note that in particular the cases in the grid cells III and IV only appear if the flame propagates in a strong unusual serpentine like way through the grid cells. In reality the curvatures of turbulent flames are less pronounced in the level set approach in LEAFS than in the shown sketch here (see for instance Figure 6.15).

on X_{fuel}. This behavior is illustrated in Figure 5.1.

We further find that due to the various curvatures of the flame and the implemented co-moving grid technique, $\overline{X}_{\mathrm{fuel}}$ deviates from 1/2 to a certain degree. In addition, the value of $\overline{X}_{\mathrm{fuel}}$ varies for different ignition models of the deflagration. Both effects are shown in Figure 5.2 where $\overline{X}_{\mathrm{fuel}}$, determined from all grid cells with $|G(\boldsymbol{r}, t)| < \Delta(t)$ is plotted as function of simulation time t for five ignition models of Table 4.1 that give rise to different

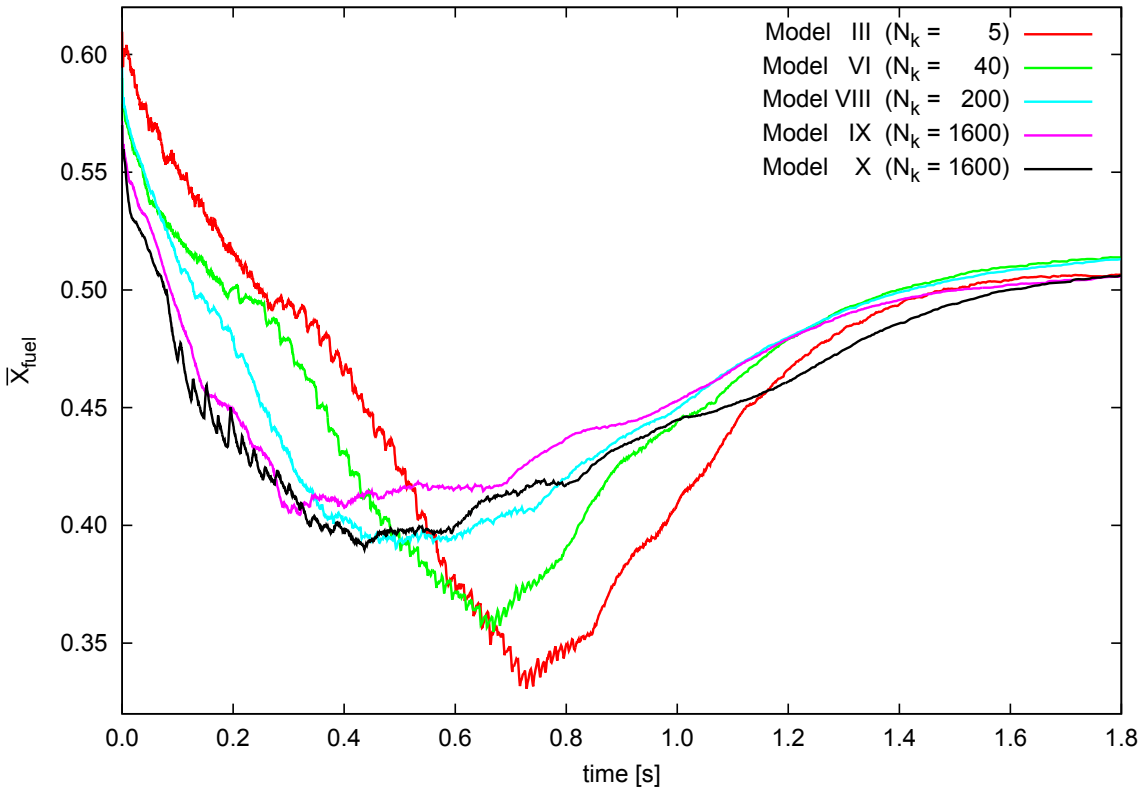

Fig. 5.2: Average fuel fractions in the grid cells at the flame as function of simulation time t for five ignition models of the deflagration of Table 4.1.

strengths of the deflagration. The resolution of the simulations of these pure deflagrations was 256^3 grid cells. We see that $\overline{X}_{\text{fuel}}$ initially declines below 1/2 for all models, indicating that in the DDT model preferentially grid cells are captured that have less than 50% of fuel. Only in the very late deflagration phase where no more DDTs occur $\overline{X}_{\text{fuel}}$ approaches 1/2.

If we increase the resolution, but let the threshold values for $X_{\text{fuel}}^{\text{min}}$ and $X_{\text{fuel}}^{\text{max}}$ constant, the number of grid cells that have a low or a high fraction of fuel on a sub scale ℓ_{crit} in the center is further reduced. A similar result can be achieved by placing more stringent constraints on X_{fuel}, where a higher value for $X_{\text{fuel}}^{\text{min}}$ always implies a lower value for $X_{\text{fuel}}^{\text{max}}$, since the flame should cross on average the central part of the grid cells. Here the problem arises that for the application of the DDT model, a certain number of grid cells is required, so that much more stringent constraints on X_{fuel} than $X_{\text{fuel}}^{\text{min}} = 1/3$ and $X_{\text{fuel}}^{\text{max}} = 2/3$ are hardly possible for simulations with 256^3 grid cells.

We can summarize that there is no accurate way to determine the physical properties of DDT regions at the flame precisely. The main reasons are that these regions are not resolved and that the flame is treated as a sharp discontinuity. However, with two parameters $X_{\text{fuel}}^{\text{min}}$ and $X_{\text{fuel}}^{\text{max}}$ we can restrict the analysis to the vicinity of the flame and additionally ensure that there is on average some fuel for a DDT. We emphasize that $X_{\text{fuel}}^{\text{min}}$ and $X_{\text{fuel}}^{\text{max}}$ are not in any way related to the required fuel fraction $X_{\text{fuel}}^{\text{DDT}}$ for a DDT (see Section 3.3.2). The lack of a sufficiently accurate modeling approach for $X_{\text{fuel}}^{\text{DDT}}$ on scales $\ell_{\text{crit}} < \Delta(t)$ prevents us to judge whether there is indeed enough fuel for a DDT. This is also why we cannot take into account that $X_{\text{fuel}}^{\text{DDT}}$ additionally depends on various other quantities as outlined

in Section 3.3.2.

5.1.2 Constraints on the fuel density in the grid cells

The second constraint a grid cell has to meet is that the flame in this cell is in the distributed burning regime. Furthermore, the constraints for detonations in this burning regime, described by Woosley (2007) and Woosley et al. (2009) have to be taken into account. In analogy to the quantity X_{fuel}, we define two threshold values $\rho_{\mathrm{fuel}}^{\mathrm{min}}$ and $\rho_{\mathrm{fuel}}^{\mathrm{max}}$ as the minimum and maximum fuel density and take only grid cells into account where $\rho_{\mathrm{fuel}}^{\mathrm{min}} \leq \rho_{\mathrm{fuel}} \leq \rho_{\mathrm{fuel}}^{\mathrm{max}}$. For now, we follow Woosley (2007) and use $\rho_{\mathrm{fuel}}^{\mathrm{min}} = 0.5 \times 10^7$ g cm^{-3} and $\rho_{\mathrm{fuel}}^{\mathrm{max}} = 1.5 \times 10^7$ g cm^{-3}. Similar to X_{fuel}, these threshold values will be varied later, since the allowed range of ρ_{fuel} with the above values seems to be quite large.

5.1.3 The flame surface area

We define the number of all grid cells that are located in the vicinity of the flame (hence the cells in which $|G(\boldsymbol{r}, t)| < \Delta(t)$) at the time t as $N_{\mathrm{flame}}(t)$ and the grid cells that additionally obey the DDT constraints concerning X_{fuel} and ρ_{fuel} as $N_{\mathrm{flame}}^{*}(t)$. In the same context, we define the entire flame surface area as $A_{\mathrm{flame}}(t)$ and the part of the flame that additionally meets the DDT constraints as $A_{\mathrm{flame}}^{*}(t)$, respectively. In general, $N_{\mathrm{flame}}^{*}(t) \ll N_{\mathrm{flame}}(t)$ and hence $A_{\mathrm{flame}}^{*}(t) \ll A_{\mathrm{flame}}(t)$. To estimate the flame surface area we have to relate the quantities $\Delta(t)$ and $N_{\mathrm{flame}}(t)$ to $A_{\mathrm{flame}}(t)$. Here we assume that due to the nature of turbulence, the flame in the deflagration phase can be considered as a fractal object that has a fractal dimension D. As indicated in Section 3.2.4 the fractal description of turbulent flames is only an approximation, since the wrinkled and folded flame structures become smoother on smaller length scales, which is not valid for a fractal. However, for fully developed turbulence we expect that in the range of length scales $\ell_{\mathrm{gibs}} \ll \ell \ll L$ a fractal description can be applied to the flame (Peters, 1986; Kerstein, 1988). In our analysis we may assume that due to the co-moving grid technique (see Section 4.1.1) and the fact that ℓ_{gibs} decreases significantly during the explosion (see Section 3.2.3), $\ell_{\mathrm{gibs}} < \Delta(t)$ for the late turbulent deflagration phase, where we may expect DDTs. However, it is uncertain, whether at the same time $\Delta(t) < L$ holds. With $L = L_{\mathrm{Kol}} \approx 10\,\mathrm{km}$ (see Section 3.3.2) we always find $\Delta(t) > L$ for the late deflagration phase, hence the entire inertial range of isotropic turbulence is not resolved. Following Ciaraldi-Schoolmann et al. (2009) L is much larger, where for length scales larger than 10 km the angular velocity fluctuations still obey the Kolmogorov scaling, whereas the radial velocity fluctuations follow a scaling law of the RT instability (see Section 3.2.1). As described in Section 3.2.4 different scaling behaviors of the turbulent velocity field have an effect on the fractal dimension of the flame. In the case of $\Delta(t) < L$ we further have to take into account that due to the grid expansion the range of length scales $\ell_{\mathrm{gibs}} \ll \ell \ll L$ that can be resolved on the grid scale continuously decreases until eventually $\Delta(t) > L$ (even for high values of L). These uncertainties and problems prevent us to perform detailed considerations and studies (such as in Gouldin (1987), Kerstein (1988) and North & Santavicca (1990) for instance). Instead, we will use a more general method to determine the fractal dimension of the flame and compare our results with the expected values for D that are indicated in Section 3.2.4. As described in Section 4.1.1 the turbulent flame is numerically treated as a sharp discontinuity which propagates as a thin interface through the grid cells. Since this holds for all chosen grid resolutions we assume that the flame surface behaves self-similar for different resolved length scales and that the quantity

$A_{\mathrm{flame}}(t)$ is resolution-independent. Then we can calculate the self-similarity dimension that is defined as (e.g. Feder, 1988; Schroeder, 1991)

$$D = \frac{\log N}{\log \epsilon}, \tag{5.1}$$

where N is the number of self-similar pieces and ϵ the reduction or zoom factor. For our purposes we need the number of grid cells $N_{\mathrm{flame}_1}(t)$ and $N_{\mathrm{flame}_2}(t)$ from two simulations with different resolutions $\Delta_1(t)$ and $\Delta_2(t)$ that are performed with the same initial white dwarf model. Then D is given by

$$D = \frac{\log(N_{\mathrm{flame}_2}(t)/N_{\mathrm{flame}_1}(t))}{\log(\Delta_1(t)/\Delta_2(t))}. \tag{5.2}$$

From here it follows

$$N_{\mathrm{flame}_1}(t) \cdot (\Delta_1(t))^D = N_{\mathrm{flame}_2}(t) \cdot (\Delta_2(t))^D \tag{5.3}$$

and since $A_{\mathrm{flame}}(t)$ should be equal for both simulations we identify

$$A_{\mathrm{flame}}(t) = N_{\mathrm{flame}}(t) \cdot (\Delta(t))^D \tag{5.4}$$

as the flame surface area (see also Sreenivasan, 1991; Niemeyer, 1995). The calculation of D will be performed together with a resolution study of the DDT model in Section 5.4. If D is determined, $A^*_{\mathrm{flame}}(t)$ can be calculated with $N^*_{\mathrm{flame}}(t)$ and D by applying equation (5.4).[1]

5.2 Testing the turbulence SGS model for DDTs

For the construction of a DDT model that is based on the properties of high turbulent velocity fluctuations, the already implemented SGS model that calculates the turbulence in the deflagration phase has to be tested. This SGS model was developed by Schmidt et al. (2006a,b) and has been applied to numerical simulations of pure turbulent deflagrations in white dwarfs (e.g. Röpke et al., 2007a). Röpke (2007) found that the SGS model generates some velocity fluctuations at the flame that maybe sufficiently high for a DDT. However, it was not explicitly tested, whether these high velocity fluctuations reveal the intermittent behavior in turbulence or whether they constitute an artifact of turbulence modeling. For the delayed detonation scenario that relies on the existence of high velocity fluctuations, a correct modeling of turbulence, which also includes the intermittent behavior, may be decisive for the success of this explosion scenario. Therefore, in this section we perform some test calculations in order to assess, whether the SGS model can be used for the construction of a DDT model. For a detailed description of the SGS model we refer to the work of Schmidt et al. (2006a,b) and Schmidt (2004).

The most important quantity that we need from the SGS model are the turbulent velocity fluctuations, where the model returns a value of $v'(\ell)$ on the time-dependent grid scale $\Delta(t)$. Since we need a value of $v'(\ell_{\mathrm{crit}})$ on the fixed length scale ℓ_{crit}, we have to investigate how to rescale $v'(\Delta(t))$ to $v'(\ell_{\mathrm{crit}})$.

[1] Here it is assumed that both the entire flame as well as the region of the flame that meets the DDT constraints have the same fractal dimension. Due to $N^*_{\mathrm{flame}}(t) \ll N_{\mathrm{flame}}(t)$ there are not enough data to derive a reliable value of D for $A^*_{\mathrm{flame}}(t)$ directly.

For testing the SGS model we will exclusively use the simulation data of pure deflagrations with different resolutions of the model described in Röpke et al. (2007a) which is a variant of Model X and is referred to as Model X* in the following. Model X* that has been originally performed with 1024^3 grid cells uses a finer resolved ignition geometry with $r_\mathrm{k} = 2.6 \times 10^5$ cm and $d_\mathrm{k} = 5.2 \times 10^4$ cm. The properties of turbulence in burned regions of this deflagration model were extensively analyzed by Ciaraldi-Schoolmann et al. (2009) and Schmidt et al. (2010), which enables us to compare our results with these studies.

5.2.1 About probability density functions and histograms

To judge whether the SGS model is capable of reproducing the high velocity fluctuations at the flame correctly, we first have to find out how often these fluctuations occur. One commonly used statistical method is the calculation of a *probability density function (PDF)*. The probability $P(a \leq X \leq b)$ that a random variable X takes on a value between a and b is given by

$$P(a \leq X \leq b) = \int_a^b f(x)\ dx, \tag{5.5}$$

where $f(x)$ is the PDF of the random variable X. The PDF is normalized by

$$\int_{-\infty}^{\infty} f(x)\ dx = 1. \tag{5.6}$$

By definition a PDF constitutes a continuous function but in most cases only discrete data are available. Then the probability density can be estimated by sampling and sorting the data into *bins* and constructing histograms. We define the *relative frequency density* as

$$h(x_i) = \frac{1}{\Delta x} \cdot \frac{\text{Number of data points in the } i\text{-th bin}}{\text{Total number of data}}, \tag{5.7}$$

which constitutes the ratio of the number of data points in the i-th bin to the total number of data, normalized to the bin width Δx.[2] The normalization of the histogram is then given analogously to equation (5.6) by

$$\sum_i \left(h(x)_i \cdot \Delta x\right) = \sum_i \frac{\text{Number of data points in the } i\text{-th bin}}{\text{Total number of data}} = 1. \tag{5.8}$$

After a histogram is constructed, a continuous function can be used to fit the histogram. The fit then constitutes an approximated PDF of the random variable.

Usually the data in histograms are presented by rectangles, but in our case this would be somewhat impractical. The width of the rectangles (resp. the bin width Δx) in the histograms is so narrow that these rectangles are replaced by a simple data point which is located at the half width of the corresponding rectangle. These data points are sometimes additionally connected with lines.

[2] Here a constant bin width is assumed that holds within each constructed histrogram in our studies.

5.2.2 Testing the SGS model in reproducing the high velocity fluctuations

Röpke (2007) calculated histograms of $v'(\ell)$ at the flame that contain the data of the SGS model and used an empirical function to fit the data. The result shows clearly a slow decline of the histogram toward higher velocity fluctuations. Therefore, there may be still a low probability of the occurrence of velocity fluctuations that are high enough for a DDT. It is not clear, however, whether the found slow decline of $v'(\ell)$ in the histogram appears due to high intermittent turbulence or whether it is an artifact of turbulence modeling. To investigate this we developed an algorithm that derives the turbulent velocity fluctuations from the resolved velocity field of the hydrodynamic flow. This allows us to compare the histogram that contains the data of the resolved fluctuations with the histogram that contains the values $v'(\ell)$ of the SGS model.

Estimating the resolved velocity fluctuations on the grid scale

The resolved velocity field $\boldsymbol{v}(\boldsymbol{r})$ of the hydrodynamic flow is a superposition of the turbulent velocity fluctuations and the bulk expansion of the white dwarf, where the latter contribution points in radial direction. We have to subtract the bulk expansion from $\boldsymbol{v}(\boldsymbol{r})$ to obtain the pure fluctuating part $\boldsymbol{v}_{\mathrm{turb}}(\boldsymbol{r})$. This procedure is described in Ciaraldi-Schoolmann et al. (2009). To compare $v_{\mathrm{turb}}(\boldsymbol{r}) = |\boldsymbol{v}_{\mathrm{turb}}|(\boldsymbol{r})$ with $v'(\ell)$ we have to take into account that the SGS model returns a value on the scale $\Delta(t)$, so that the quantity $v_{\mathrm{turb}}(\boldsymbol{r})$ has to be considered on the scale $\Delta(t)$ as well. To ensure this we use a routine that is similar to the computation of structure functions (see Section 3.2.1). Here, however, we choose a constant length scale of $\ell = |\boldsymbol{\ell}| = \Delta(t)$, hence the routine is based on the computation of averaged absolute velocity differences $\overline{|v_{\mathrm{turb}}(\Delta(t))|}$ of neighboring grid cells. Using a Monte-Carlo based algorithm, a random grid cell and N adjacent cells are selected. Then $\overline{|v_{\mathrm{turb}}(\Delta(t))|}$ is given by

$$\overline{|v_{\mathrm{turb}}(\Delta(t))|} = \frac{1}{N}\sum_{i=1}^{N} |v_{\mathrm{turb}}(\boldsymbol{r}) - v_{\mathrm{turb}_i}(\boldsymbol{r}+\boldsymbol{\ell})|, \tag{5.9}$$

where $v_{\mathrm{turb}}(\boldsymbol{r})$ is the velocity fluctuation in the selected grid cell and $v_{\mathrm{turb_i}}(\boldsymbol{r}+\boldsymbol{\ell})$ is the velocity fluctuation in the i-th of the N adjacent grid cell. In our three-dimensional analysis the number of all adjacent grid cells is $N = 6$.[3] However, as shown in the following, not all of these cells are always taken into account.

We further extend this analysis by performing the calculation with a fixed length scale of $\ell = 4 \cdot \Delta(t)$. For comparison with the result from the SGS model, we have to rescale the values of $v'(\ell)$ from $v'(\Delta(t))$ to $v'(4 \cdot \Delta(t))$. Following equation (3.12) the rescaling can be performed with

$$v'(4 \cdot \Delta(t)) = v'(\Delta(t)) \cdot \frac{(4 \cdot \Delta(t))^{\alpha}}{\Delta(t)^{\alpha}} = 4^{\alpha} \cdot v'(\Delta(t)). \tag{5.10}$$

For sufficiently small length scales the scaling of the turbulent velocity field is given by the Kolmogorov theory (see Section 3.2.1), where $\alpha = 1/3$ and hence $v'(4 \cdot \Delta(t)) = 4^{1/3} \cdot v'(\Delta(t))$. With increasing length scales the turbulent velocity field becomes anisotropic, where in the direction parallel to gravity a scaling behavior for RT instability driven turbulence is observed (Ciaraldi-Schoolmann et al., 2009). In this case, $\alpha = 1/2$ and hence $v'(4 \cdot \Delta(t)) = 2 \cdot v'(\Delta(t))$.

[3] The computational domain is far away from the edge of the simulation grid.

The computation is performed for data in burned regions and for the data $N_{\text{flame}}(t)$ in the vicinity of the flame. For burned regions, $G(\boldsymbol{r}, t) \geq \Delta(t)$ holds for the randomly selected grid cell as well as for the N cells that are used for the calculation of $\overline{|v_{\text{turb}}(\Delta(t))|}$ (equation (5.9)). This applies to both cases $\ell = \Delta(t)$ and $\ell = 4 \cdot \Delta(t)$. All grid cells are far away from the flame and $N = 6$ always holds.

For regions at the flame, $|G(\boldsymbol{r}, t)| < \Delta(t)$ holds for the randomly selected grid cell but this is frequently not automatically true for adjacent grid cells and particularly for the more distant cells in the case of $\ell = 4 \cdot \Delta(t)$. Here we exclude all grid cells with $X_{\text{fuel}} > 0.5$ for the calculation of $\overline{|v_{\text{turb}}(\Delta(t))|}$ (equation (5.9)). Therefore, we ensure that only grid cells are taken into account that are located either at the flame or in burned regions (in which $X_{\text{fuel}} \approx 0$). As a consequence, we frequently find here for the number of grid cells that are used for the calculation of $\overline{|v_{\text{turb}}(\Delta(t))|}$, $N < 6$. The routine is always applied to a total number of 10^6 different randomly selected grid cells, where for a larger number we find no change in the results anymore. After the calculation, a histogram of $\overline{|v_{\text{turb}}(\Delta(t))|}$ is constructed.

Comparison of the histograms of $\overline{|v_{\text{turb}}(\Delta(t))|}$ and $v'(\Delta(t))$

In the Figures 5.3 and 5.4 the histograms of $\overline{|v_{\text{turb}}(\Delta(t))|}$ and $v'(\Delta(t))$ that contain the data in burned regions and in the vicinity of the flame are shown, where for the performed simulation a resolution of 512^3 grid cells was used. The simulation time is $t \approx 0.8\,\text{s}$ corresponding to the late deflagration phase, where turbulence is strong and therefore affects the structure and propagation of the flame significantly. In the case of $\ell = \Delta(t)$ no scaling procedure has to be performed for the SGS model, while for $\ell = 4 \cdot \Delta(t)$ the results of both rescaling operations – Kolmogorov- and RT instability driven turbulence – are shown in the plots.

In all figures we see a qualitative agreement of the histograms, where the histogram of $\overline{|v_{\text{turb}}(\Delta(t))|}$ shows a stronger scatter than the SGS model. The main reason lies in the algorithm for determining $\overline{|v_{\text{turb}}(\Delta(t))|}$ that is based on averaging over a few (maximum six) grid cells only leading to a poor statistic. This becomes particularly apparent for high velocity values in the half-logarithmic plot. However, we see a slow decline in all plots at the right side of the histogram of $\overline{|v_{\text{turb}}(\Delta(t))|}$ that is in an adequate agreement with the histogram of $v'(\Delta(t))$. This is a first hint that the found high velocity fluctuations of the SGS model are no artifact of turbulence modeling but may reveal the intermittent behavior of turbulence.

For the length scale $\ell = 4 \cdot \Delta(t)$ we unfortunately cannot obtain any conclusion, of whether the behavior of the velocity fluctuations can be explained by either the Kolmogorov theory or the influence of the RT instability. While the maximum of the histograms seems to fit better with the Kolmogorov theory, the high velocity fluctuations seen in the half-logarithmic plots fit better with a scaling behavior of the RT instability.

In Figure 5.5 we show a comparison of the resolved velocity fluctuations $\overline{|v_{\text{turb}}(\Delta(t))|}$ for both length scales $\ell = \Delta(t)$ and $\ell = 4 \cdot \Delta(t)$ with the data $N_{\text{flame}}(t)$. Apart from the fact that the probability of finding high velocity fluctuations is obviously higher for the length scale $\ell = 4 \cdot \Delta(t)$, we see a similar slope of the right part of both histograms toward higher velocity fluctuations. This result is not trivially expected, since in the case of $\ell = 4 \cdot \Delta(t)$ a major part of the grid cells are not located in the vicinity of the flame but in the burned material. Even if the resolved velocity fluctuations show a strong scatter the agreement of the slopes of both curves indicates that the occurrence of high velocity fluctuations at the flame and in burned regions near the flame may be similar. This behavior will be further

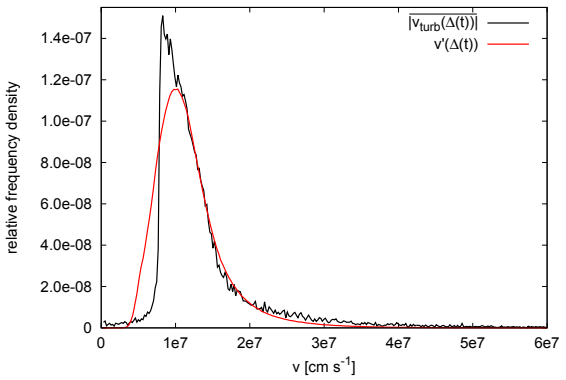

(a) $\ell = \Delta(t)$, Burned region

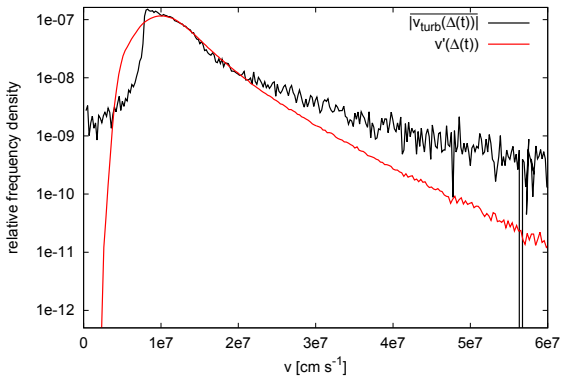

(b) $\ell = \Delta(t)$, Burned region

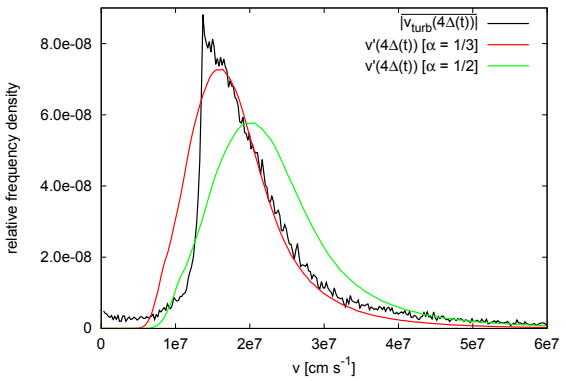

(c) $\ell = 4 \cdot \Delta(t)$, Burned region

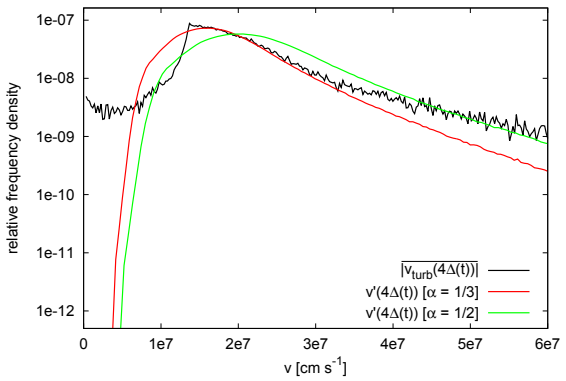

(d) $\ell = 4 \cdot \Delta(t)$, Burned region

Fig. 5.3: Histograms of $\overline{|v_{\mathrm{turb}}(\ell)|}$ and $v'(\ell)$ for the fixed length scales $\ell = \Delta(t)$ and $\ell = 4 \cdot \Delta(t)$ in burned regions at $t \approx 0.8\,\mathrm{s}$.

investigated with the data of the SGS model in Section 5.2.4.

Conclusions and comparison with other studies

Since we found in burned regions as well as at the flame front a slow decline in the histogram of $v'(\Delta(t))$ toward high velocity fluctuations that can be additionally reproduced from the resolved velocity field, it is very likely that the SGS model does not calculate artificially high velocity fluctuations, but can reproduce the intermittent behavior in turbulence. This preliminary conclusion, however, should be further reinforced by an appropriate intermittency model that can explain the occurrence of the found high velocity fluctuations. For burned regions, a detailed analysis of intermittency was performed by Schmidt et al. (2010), where the same SGS model was used in the simulation. Here an intermittency model of Kolmogorov (1962) and Oboukhov (1962) was applied that assumes that the turbulent velocity profile follows a log-normal distribution. The result indicates weaker intermittency than predicted by the Kolmogorov-Oboukhov model. In contrast, the analysis of Röpke (2007) revealed that the slow decline in the histogram that contains the data of the SGS model at the flame cannot be explained by a log-normal fit, since the latter declines faster toward higher velocity fluctuations than the histogram of $v'(\ell)$. Hence, the results of Röpke (2007)

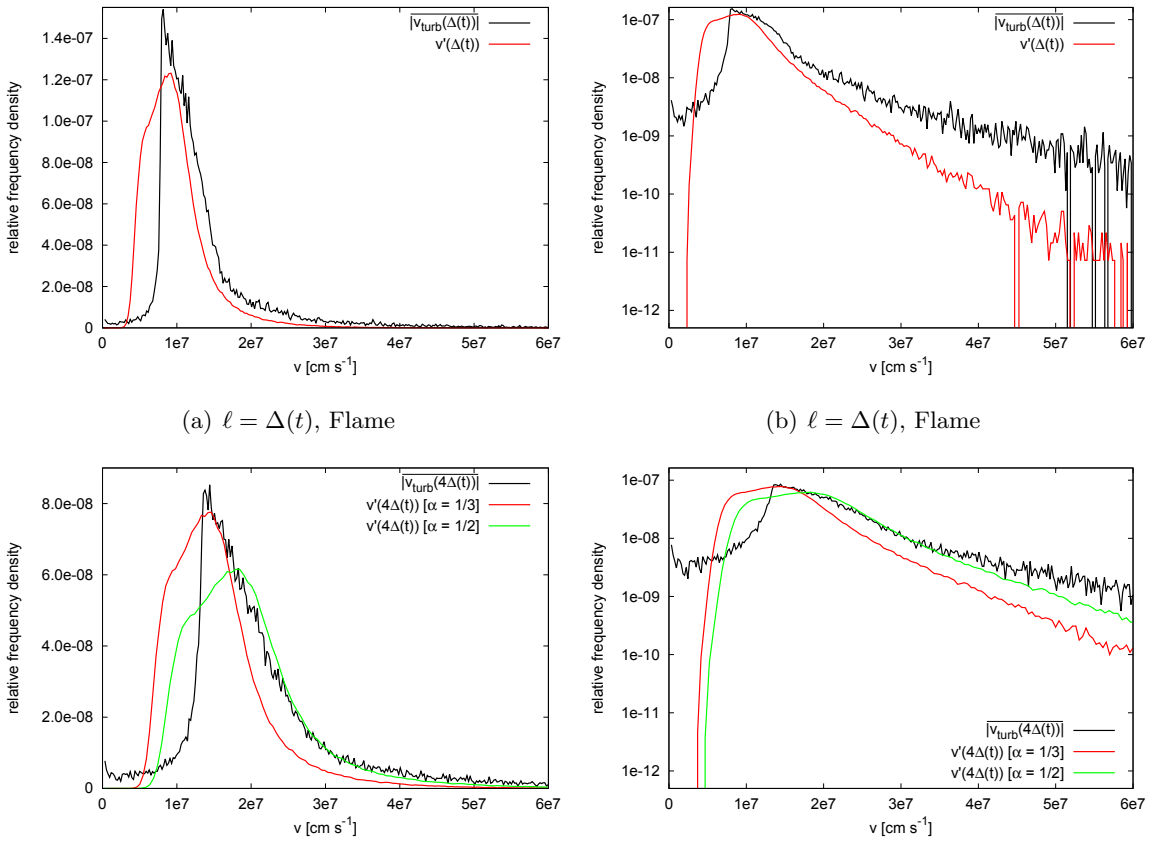

(a) $\ell = \Delta(t)$, Flame

(b) $\ell = \Delta(t)$, Flame

(c) $\ell = 4 \cdot \Delta(t)$, Flame

(d) $\ell = 4 \cdot \Delta(t)$, Flame

Fig. 5.4: Histograms of $\overline{|v_{\mathrm{turb}}(\ell)|}$ and $v'(\ell)$ for the fixed length scales $\ell = \Delta(t)$ and $\ell = 4 \cdot \Delta(t)$ in the vicinity of the flame at $t \approx 0.8\,\mathrm{s}$.

and Schmidt et al. (2010) are different. Since an incorrect modeling of turbulence seems unlikely according to the analysis presented above, a possible explanation is that intermittency at the flame is much stronger than in burned regions (see also the discussion in Schmidt et al., 2010). Unfortunately we cannot perform a detailed analysis of intermittency such as in Schmidt et al. (2010) which was based on fitting of characteristic scaling exponents that were obtained from the computation of structure functions up to the sixth order. The data for this computation must be available within a simply connected region, where a chosen pair of points has to be connected by a straight (uninterrupted) line.[4] For this reason, it is impossible to compute structure functions at a highly wrinkled and folded flame.[5] However, as shown later in Section 5.2.4 we are at least able to qualitatively estimate the difference in the degree of intermittency at the flame and in burned regions by comparing the shape of the slow decline toward high velocity fluctuations of the corresponding histograms of $v'(\ell_{\mathrm{crit}})$.

[4] In an exploding white dwarf for instance the computation can be performed inside a sphere, whose surface is approximately at the flame and whose center coincides with the center of the white dwarf (see Ciaraldi-Schoolmann et al., 2009).

[5] From a statistical point of view we argue that a reliable analysis of intermittency requires scaling exponents up to significant high orders. Unless increasing the resolution of the simulation up to non-realizable high values, the number of grid cells at the flame in full-star simulations is far too small to obtain these high-order scaling exponents.

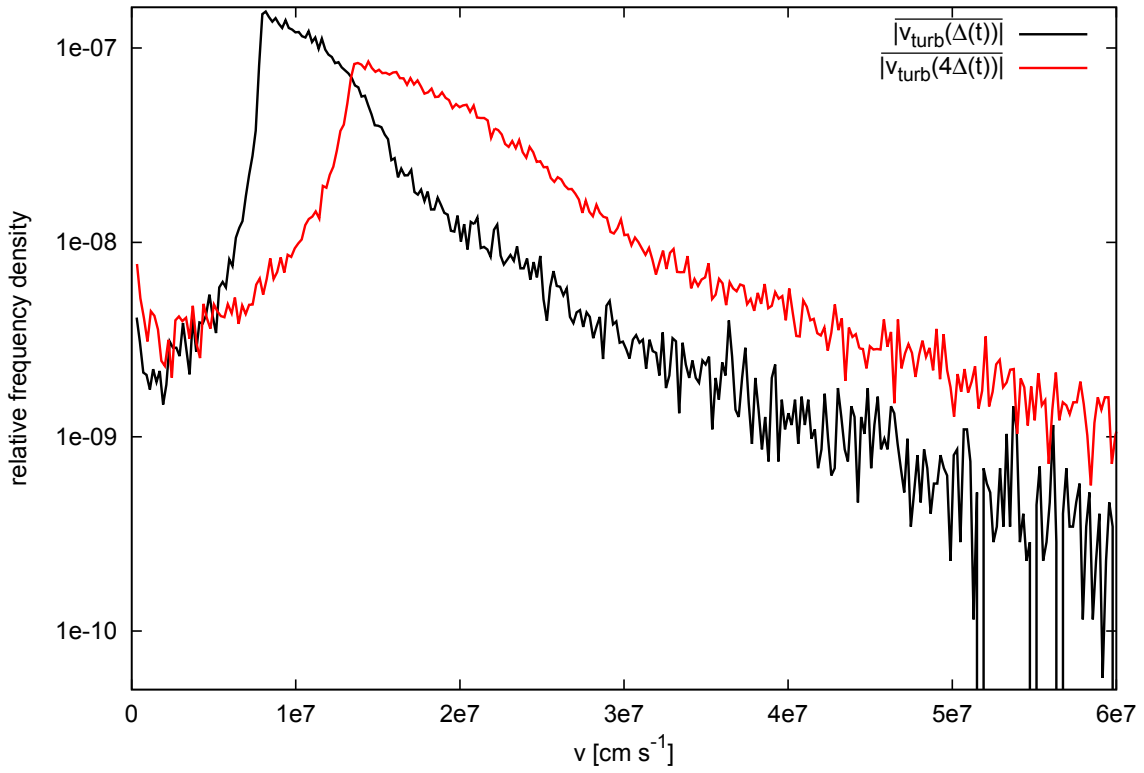

Fig. 5.5: Comparison of the histograms of the resolved velocity fluctuations $\widetilde{|v_{\mathrm{turb}}(\Delta(t))|}$ for both length scales $\ell = \Delta(t)$ and $\ell = 4 \cdot \Delta(t)$ in the vicinity of the flame.

5.2.3 Rescaling of the velocity fluctuations

Compared to the quantities X_{fuel} and ρ_{fuel} the turbulent velocity fluctuations can be modeled on unresolved scales more appropriately, since we expect that the turbulent velocity field obeys defined scaling relations in the intertial range (see 3.2.1). For the DDT model we have to rescale $v'(\Delta(t))$ to $v'(\ell_{\mathrm{crit}})$ at each time step. In analogy to equation (5.10), $v'(\ell_{\mathrm{crit}})$ is given by

$$v'(\ell_{\mathrm{crit}}) = v'(\Delta(t)) \cdot (\ell_{\mathrm{crit}}/\Delta(t))^{\alpha}\,, \tag{5.11}$$

where α is the rescaling exponent that depends on the properties of the turbulent velocity field. As discussed in Section 3.2.1 the transition length scale $\ell_{\mathrm{Kol/RT}}$ between the Kolmogorov turbulence and the large-scale RT instability driven turbulence is approximately 10^6 cm (Niemeyer & Woosley, 1997; Ciaraldi-Schoolmann et al., 2009). Hence, at first glance $\alpha = 1/2$ seems to be always the right exponent, since $\ell_{\mathrm{Kol/RT}}$ is of the same order of magnitude as ℓ_{crit} and in our performed simulations $\ell_{\mathrm{crit}} < \Delta(t)$. The calculations of Ciaraldi-Schoolmann et al. (2009), however, have been performed in predominantly burned material. For the DDT model a corresponding scaling behavior at the flame is needed that cannot be easily obtained for the reasons described in the preceding section. But there is a specific method to estimate the degree of anisotropy in turbulence at the flame qualitatively. Following Zingale et al. (2005) contours of the turbulent velocity field in Fourier space can be constructed. Here Zingale et al. (2005) and Ciaraldi-Schoolmann et al. (2009) showed

that turbulence at the flame becomes anisotropic with lower wave numbers. Hence, we may speculate that the properties of the isotropy in turbulence at the flame and in burned regions are similar.

There is, however, no clear conclusion on how anisotropy in turbulence at the flame affects the scaling properties of the turbulent velocity field (that are unknown at the flame anyway). Finally, we argue that the considerations described above include all turbulent velocity fluctuations but for the DDT model we need only the properties of the rarer high fluctuations. In this context, it is of high importance to find out where the high fluctuations are exactly located. As shown later, the strongest turbulent motions are found at trailing edges along the Rayleigh-Taylor mushroom cap like structures and in small crevices between them, where strong shear instabilities occur. The scaling behavior of an intermittent turbulent velocity field in these regions at the flame is not known.

From the described aspects so far it remains uncertain which scaling law has to be applied to rescale $v'(\Delta(t))$ to $v'(\ell_{\mathrm{crit}})$. In addition, we found in Figure 5.4 no clear evidence of whether turbulence at the flame on the considered length scales $\Delta(t)$ and $4{\cdot}\Delta(t)$ agrees better with the Kolmogorov theory or a RT instability driven turbulence. It is confirmed in most performed studies, however, that at least on small length scales turbulence complies with the Kolmogorov theory (e.g. Zingale et al., 2005; Röpke et al., 2007a; Ciaraldi-Schoolmann et al., 2009). In this work, we will also assume Kolmogorov turbulence for all length scales. However, in the following we estimate the uncertainty if the effects of the RT instability have to be taken into account. With equation (5.11) the error $c_{\mathrm{Kol/RT}}$ that results from the difference between the scaling behavior for Kolmogorov turbulence and the RT instability is given by

$$c_{\mathrm{Kol/RT}} = \frac{(\Delta(t)/\ell_{\mathrm{crit}})^{1/2}}{(\Delta(t)/\ell_{\mathrm{crit}})^{1/3}} = (\Delta(t)/\ell_{\mathrm{crit}})^{1/6}\,. \tag{5.12}$$

This means that in LEAFS simulations with very high resolutions of 1024^3 grid cells where $\Delta(t) \approx \ell_{\mathrm{crit}}$, the error becomes negligible. In the performed studies, however, simulations with 256^3 and 512^3 grid cells are performed. Here in the late deflagration phase at the time where DDTs are expected to occur, the length of the grid cells is $\Delta(t) \approx 4 \times 10^6\,\mathrm{cm}$ for simulations with 256^3 grid cells and $\Delta(t) \approx 2 \times 10^6\,\mathrm{cm}$ for the higher resolved simulations, leading to uncertainties of 26% and 12%, respectively. To check to what extent these deviations affect the rescaled values of the high velocity fluctuations at the flame we compare the histograms of $v'(\ell_{\mathrm{crit}})$ with both rescaling exponents $\alpha = 1/3$ and $\alpha = 1/2$. With respect to the implementation of a DDT model, we take now only grid cells into account that meet the DDT constraints, hence the data $N^*_{\mathrm{flame}}(t)$ is used for the construction of the histogram (see Section 5.1.3). The histograms are shown in Figure 5.6 at $t \approx 0.9\,\mathrm{s}$ and we see particularly in the lower resolved simulation a slight deviation between both histograms.

5.2.4 Fitting the high velocity fluctuations of the histogram

In numerical simulations of deflagration models Röpke (2007) found that the high velocity fluctuations in the histogram cannot be reproduced by a Gaussian- or a log-normal fit, since these distributions fall off steeper here than $v'(\ell_{\mathrm{crit}})$. Since a detailed analysis of intermittency at the flame cannot be performed easily, we compare the histogram of $v'(\ell_{\mathrm{crit}})$ that contains the data in burned regions with the histogram that contains the data $N^*_{\mathrm{flame}}(t)$. In Figure 5.7 both histograms are shown at $t \approx 0.9\,\mathrm{s}$. We find a clear difference between the

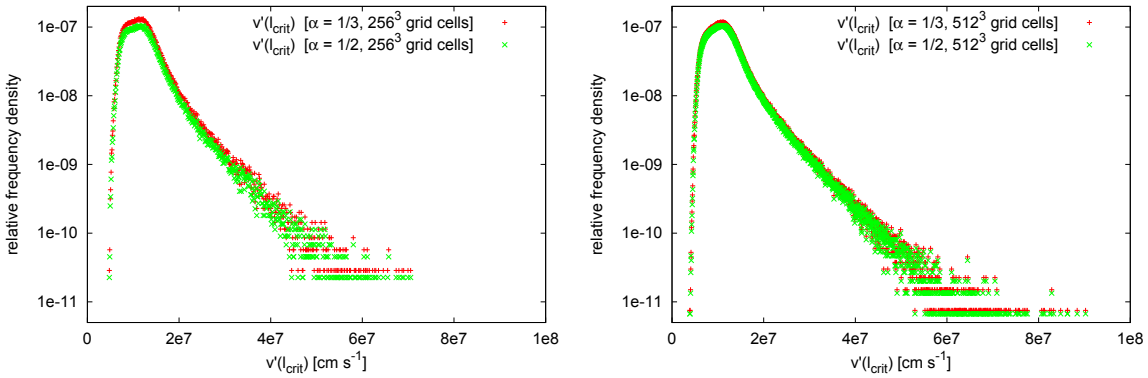

(a) Simulation with 256^3 grid cells

(b) Simulation with 512^3 grid cells

Fig. 5.6: Comparison of the histograms of $v'(\ell_{\text{crit}})$ at the flame with a resolution of (a) 256^3 and (b) 512^3 grid cells with a rescaling exponent of $\alpha = 1/3$ (Kolmogorov) and $\alpha = 1/2$ (RT instability) at $t \approx 0.9\,\text{s}$.

histograms after the maximum toward high velocity fluctuations. In the half-logarithmic plot we see for the histogram of $v'(\ell_{\text{crit}})$ that contains the data in burned regions an almost linear slope after the maximum, while the histogram that contains the data $N^*_{\text{flame}}(t)$ shows here a significantly stronger positive curvature. This result is a further evidence that intermittency at the flame is stronger than in the ash. However, the value of the most probable velocity fluctuation (the maximum of the histogram) and also the probability of finding high velocity fluctuations (the right part of the histogram) are higher in burned regions. We also show in Figure 5.7 a histogram of $v'(\ell_{\text{crit}})$ that contains the data in unburned regions where we see only marginal velocity fluctuations.

In our study we obviously find in Figure 5.7 high velocity fluctuations in burned regions, while in the study of Schmidt et al. (2010) only weak intermittency was found in these regions. We emphasize that further investigations are required to determine what may cause a possible difference in the results of both studies. It would be desirable to apply a fit that corresponds to the intermittency model of Kolmogorov (1962) and Oboukhov (1962) to our histogram of $v'(\ell_{\text{crit}})$ that contains the data in burned regions. This would eventually enable us to compare our results with the results of Schmidt et al. (2010). Unfortunately, this is not possible, since for this comparison we need again a sufficiently large set of scaling exponents that requires a more detailed analysis, where our data are insufficient (see Section 5.2.2).

We cannot rule out completely that the difference between the histograms that contain the data in burned regions and the data at the flame are a result from an effect of flame modeling, which may lead here to a different decline in the histograms of $v'(\ell_{\text{crit}})$ toward high velocity fluctuations. However, this cannot be analyzed easily, since that would require either a detailed analysis of intermittency at the flame or one has to compare histograms of $v'(\ell_{\text{crit}})$ at the flame that are constructed from data of different flame models. On the other hand the question arises, whether a flame modeling effect would also appear in the curves of the resolved velocity fluctuations in Figure 5.5. Here we found that the decline of the histograms of $v'(\ell_{\text{crit}})$ toward high velocity fluctuations at the flame and in burned regions near the flame seem to be similar. However, due to the large scatter of the resolved velocity fluctuations some uncertainties remain.

To obtain a clearer picture, it would also be desirable to find a distribution function that

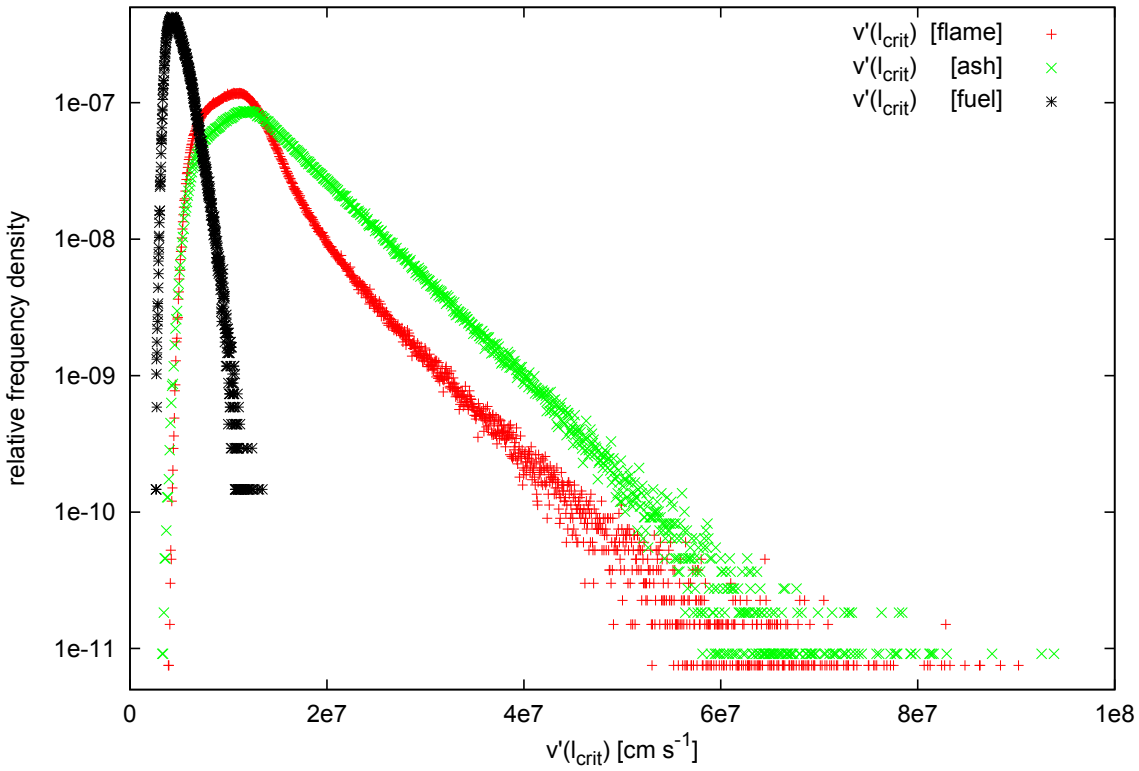

Fig. 5.7: Histograms of $v'(\ell_{\text{crit}})$ constructed from the data in burned regions ($G(\boldsymbol{r},t) \geq \Delta(t)$), from the data $N^*_{\text{flame}}(t)$ at the flame ($|G(\boldsymbol{r},t)| < \Delta(t)$), as well as from the data in unburned regions ($G(\boldsymbol{r},t) \leq -\Delta(t)$) at $t \approx 0.9\,\text{s}$.

is supported by the theory of intermittency and that is capable of explaining the found high velocity fluctuations at the flame. Since this distribution function is unknown, we have to find an empirical fit function that reproduces the right part of the histogram of $v'(\ell_{\text{crit}})$. Here we follow the suggestion of Röpke (2007) and use a three-parameter geometric fit function of the form

$$f(v'(\ell_{\text{crit}})) = \exp\left(a_1 v'(\ell_{\text{crit}})^{a_2} + a_3\right), \tag{5.13}$$

where $f(v'(\ell_{\text{crit}}))$ constitutes an approximated probability density function of $v'(\ell_{\text{crit}})$ (see Section 5.2.1) and a_1, a_2 and a_3 are fit parameters. The probability of finding velocity fluctuations of at least $v'(\ell_{\text{crit}})$ is given by the integration of this equation (see Section 5.3.1, equation (5.14)).

Remarks on the implementation of the fit

Since the rare high velocity fluctuations are crucial for the DDT, we will focus on the data of the histogram of $v'(\ell_{\text{crit}})$ that lies to the right of the maximum. There is, however, no consensus on which value of $v'(\ell_{\text{crit}})$ in the histogram is the most appropriate starting point. But we may expect that the higher $v'(\ell_{\text{crit}})$ (and hence the further away the data are located from the maximum toward higher velocity fluctuations) the more can these fluctuations be attributed to intermittency.

To restrict the fit to the right part of the histogram of $v'(\ell_{\mathrm{crit}})$, we first determine its maximum. If we start the fit right away at this maximum the fit will not converge. The reason is that the histogram of $v'(\ell_{\mathrm{crit}})$ that contains the data $N^*_{\mathrm{flame}}(t)$ has a turning point after the maximum (see Figure 5.7) that cannot be fitted with equation (5.13). In addition, it is questionable to use the most probable value of the velocity fluctuations as a starting point, since as described above the corresponding velocities here may probably not be attributed to intermittent turbulence. Therefore, we arbitrarily varied the starting point of the fit and checked at which value a fit seems to be most appropriate.

We outline that a further complication is involved here by the fact that due to the nature of turbulence, the values of the velocity fluctuations are not predictable. This of course holds also for the histogram of $v'(\ell_{\mathrm{crit}})$ and here particularly for the right slow decline toward high velocity fluctuations. Hence, there will be no uniform ideal starting point for the fit for different time steps in the simulation. However, in the late deflagration phase where turbulence is fully developed and where DDTs are expected to occur, there is some kind of a typical histogram profile as shown in Figure 5.7 for instance.

From many convergence tests for the fit we find that an appropriate starting point is twice the velocity value, at which the histogram is maximal. From the fit with this starting point, the initial values a_1, a_2 and a_3 were determined that lead to a reliable convergence. In the simulation then, the first histogram of $v'(\ell_{\mathrm{crit}})$ and the fit are calculated when a sufficient number of grid cells $N^*_{\mathrm{flame}}(t)$ are available. From there on the histogram and the fit are calculated at each time step, provided that sufficient data are available. When convergence is achieved in the fit, the obtained values for the fit parameters are just the new initial values for the fit in the next time step, where $N^*_{\mathrm{flame}}(t)$ is sufficiently large again. This procedure leads to a fast and reliable convergence of the fit during this phase in the simulation, as long as the profile of the histogram of $v'(\ell_{\mathrm{crit}})$ changes smoothly.

5.2.5 Resolution study of the high velocity fluctuations of the histogram

As a final test of the SGS model, we analyze whether the decline in the histogram of $v'(\ell_{\mathrm{crit}})$ toward high velocity fluctuations and the applied fit are resolution-dependent. Here we use the data $N^*_{\mathrm{flame}}(t)$ at $t \approx 0.9\,\mathrm{s}$ from the simulations that are performed with a resolution of 256^3 and 512^3 grid cells. Unfortunately other resolutions cannot be taken into account. Higher resolutions are not possible due to limitations of computational resources, while the histogram and the fit cannot be calculated for lower resolutions due to insufficient data. Therefore, the resolution dependence of the histogram and the fit can only be estimated roughly. The results are shown in Figure 5.8 where we see a very good agreement of the histograms and the corresponding fits. However, for the lower resolved case we find a larger scatter for given values of $v'(\ell_{\mathrm{crit}})$ in the histogram and an earlier cutoff of the slow decline toward high velocity fluctuations. For the latter, which can also be seen when comparing both panels of Figure 5.6, we emphasize that this behavior indicates by no means that the probability of the occurrence of high velocity fluctuations at the flame in higher resolved simulations is higher. The described effect occurs due to the fact that there are much less grid cells that meet the DDT constraints in lower resolved simulations, leading to a smaller number of grid cells that have high velocity fluctuations. In our implementation, the less data in lower resolved simulations means a coarser binning of the histogram of $v'(\ell_{\mathrm{crit}})$. This explains the smaller horizontal scatter toward the right end of the histogram and the absence of data at high values of $v'(\ell_{\mathrm{crit}})$ for lower resolved simulations. In the case shown here, these effects have an insignificant impact on the fit. However, for very low resolved simulations

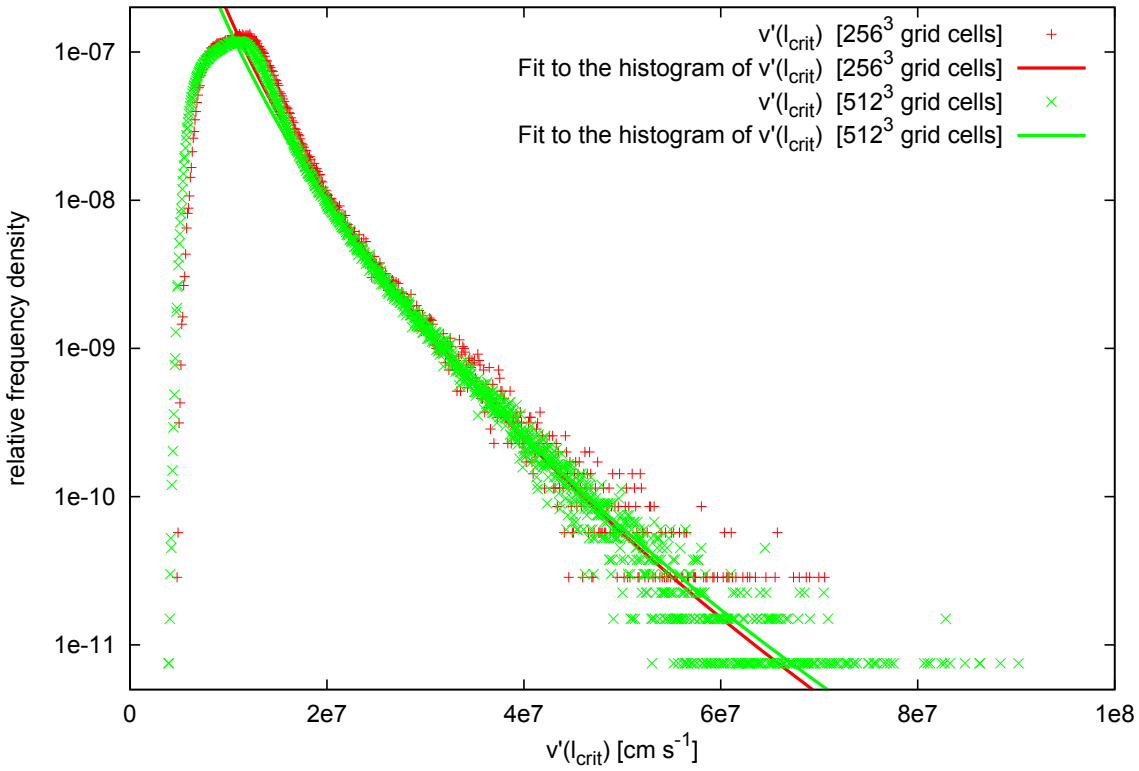

Fig. 5.8: Histograms of $v'(\ell_{\text{crit}})$ at the flame and the corresponding fits (equation 5.13) for different resolutions at $t \approx 0.9\,\text{s}$.

the binning may become so coarse that the fit may deviate to a certain degree or even fail to converge. That is why the histogram of $v'(\ell_{\text{crit}})$ and the fit are only calculated, when $N^*_{\text{flame}}(t)$ is sufficiently large, which implies that the DDT model cannot be applied to very low resolved simulations (see Section 5.3.3).

In Section 5.1.1 we introduced with $X^{\text{min}}_{\text{fuel}} = 1/3$ and $X^{\text{max}}_{\text{fuel}} = 2/3$ two threshold values for the allowed fuel fractions in the grid cells in order to restrict our analysis to the vicinity of the flame. The largely resolution independence of the histogram of $v'(\ell_{\text{crit}})$ and the fit in Figure 5.8 shows that these restrictions have no significant effect on the results obtained for different resolutions. In the following, we will further estimate the influence of different allowed ranges for X_{fuel} and ρ_{fuel} on the histogram of $v'(\ell_{\text{crit}})$.

5.2.6 The impact of different fuel fractions and fuel densities in the grid cells on the histogram of $v'(\ell_{\text{crit}})$

In this section we investigate roughly to what extent the probability of finding high velocity fluctuations depends on different allowed ranges for X_{fuel} and ρ_{fuel} in the grid cells. Using the data $N_{\text{flame}}(t)$ we place constraints on ρ_{fuel} and X_{fuel} separately and construct and compare the resulting histograms of $v'(\ell_{\text{crit}})$. For X_{fuel} we use the two ranges $0.2 \leq X_{\text{fuel}} \leq 0.8$ and $1/3 \leq X_{\text{fuel}} \leq 2/3$. For ρ_{fuel} we simply use the part of the flame with $\rho_{\text{fuel}} \geq 10^7\,\text{g cm}^{-3}$ and $\rho_{\text{fuel}} < 10^7\,\text{g cm}^{-3}$. We use for this analysis the data of the simulation with 512^3 grid cells at $t \approx 0.8\,\text{s}$ which is the same snapshot as used in Section 5.2.2 (but note that we use here

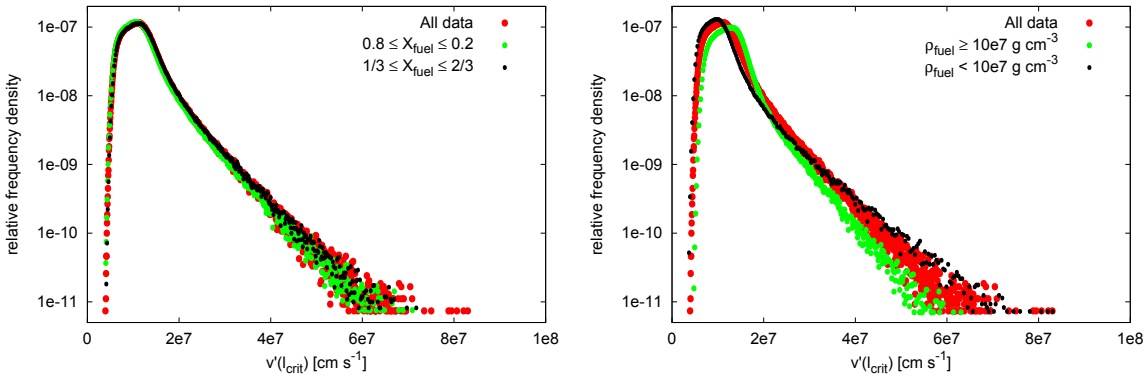

(a) Histograms of $v'(\ell_{\text{crit}})$ for different restrictions on the quantity X_{fuel}.

(b) Histograms of $v'(\ell_{\text{crit}})$ for different restrictions on the quantity ρ_{fuel}.

Fig. 5.9: The influence of restrictions on the quantities X_{fuel} and ρ_{fuel} on the histogram of $v'(\ell_{\text{crit}})$.

the rescaled velocity fluctuations $v'(\ell_{\text{crit}})$ and not $v'(\Delta(t))$).

The results are shown in Figure 5.9 together with the obtained histogram of $v'(\ell_{\text{crit}})$ which contains the total data $N_{\text{flame}}(t)$. We see in Figure 5.9(a) that the histograms for different allowed ranges for X_{fuel} are very similar. Therefore, the restrictions on the fuel fraction in the grid cells do not lead to large deviations of the probability of finding high velocity fluctuations.

In contrast to X_{fuel}, we see in Figure 5.9(b) for different ranges of allowed fuel densities a clear deviation of the histograms. We find the slowest decline of the histogram toward high velocity fluctuations for fuel densities of $\rho_{\text{fuel}} < 10^7\,\text{g cm}^{-3}$. For fuel densities of $\rho_{\text{fuel}} \geq 10^7\,\text{g cm}^{-3}$ the histogram falls off even steeper toward high velocity fluctuations than the histogram that contains the total data $N_{\text{flame}}(t)$ (where all densities at the flame are taken into account). On the other hand, we find for higher densities that the maximum of the histogram is located at higher velocity fluctuations. Therefore, we may assume that turbulence is on average stronger at higher densities, but the intermittency in turbulence that leads to the occurrence of particularly high velocity fluctuations becomes more evident at lower densities.

5.2.7 The impact of different fuel fractions in the grid cells on the rescaled velocity fluctuations

As described in Section 5.1.1 the discontinuity approach of the flame prevents us to determine the physical properties (such as $v'(\ell_{\text{crit}})$) at the flame precisely. However, for grid cells with $|G(\boldsymbol{r},t)| < \Delta(t)$ and $X_{\text{fuel}} \approx 0.5$ the flame propagates frequently through the center of these cells. Hence, the values of the physical quantities in these cells represent an estimation of the physical conditions at the flame.

With the rescaled velocity fluctuations $v'(\ell_{\text{crit}})$ we estimate to what extent the values of these velocity fluctuations depend on the fuel fraction X_{fuel} in the grid cells. For this study we use $N_{\text{flame}}(t)$, hence all cells with $|G(\boldsymbol{r},t)| < \Delta(t)$ are taken into account. The analysis is performed for four different ignition models from Table 4.1 that give rise to different strengths of the deflagration. These models are simulated with a resolution of 256^3 grid cells. The results are shown in Figure 5.10 where the average values of $v'(\ell_{\text{crit}})$ in the grid cells $N_{\text{flame}}(t)$

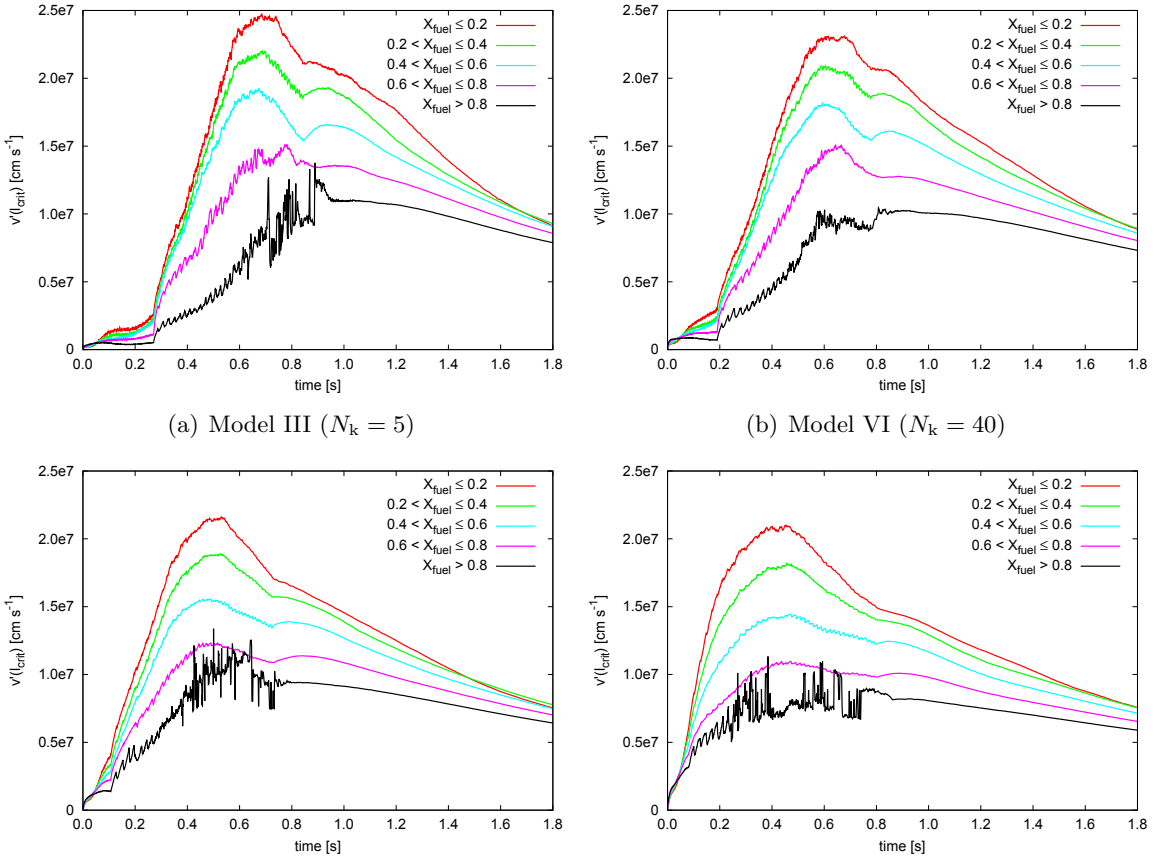

(a) Model III ($N_\mathrm{k} = 5$)

(b) Model VI ($N_\mathrm{k} = 40$)

(c) Model VIII ($N_\mathrm{k} = 200$)

(d) Model X* ($N_\mathrm{k} = 1600$)

Fig. 5.10: Average rescaled velocity fluctuations $v'(\ell_\mathrm{crit})$ in the grid cells $N_\mathrm{flame}(t)$ that are found within a specific interval of the fuel fraction X_fuel in the grid cells as function of time for four ignition models of the deflagration (see Table 4.1). The rescaled turbulent velocity fluctuations become higher with decreasing X_fuel.

that are found within a specific interval of the fuel fraction X_fuel in the grid cells is plotted as function of time. Obviously the grid cells that contain a large fraction of fuel have only low velocity fluctuations, while turbulence seems to be much stronger in burned regions. This result is consistent with the histograms of $v'(\ell_\mathrm{crit})$ in Figure 5.7. We further see in Figure 5.10 a first indication that weak deflagrations (models with small N_k) may generate higher velocity fluctuations at the flame (compare the blue curves where $0.4 < X_\mathrm{fuel} \leq 0.6$). This behavior is investigated in more detail in Chapter 6.

5.3 Determination of the DDT criterion

5.3.1 The probability of finding high velocity fluctuations

The function (5.13) that is used to fit and extrapolate the histogram of $v'(\ell_\mathrm{crit})$ that contains the data $N^*_\mathrm{flame}(t)$ constitutes an approximated PDF of $v'(\ell_\mathrm{crit})$ (see Section 5.2.1). Therefore, we can determine the probability $P(v'(\ell_\mathrm{crit}) \geq v'_\mathrm{crit})(t)$ of finding velocity fluctuations $v'(\ell_\mathrm{crit})$ on the scale ℓ_crit of at least v'_crit at the flame that meets the DDT constraints concerning

X_{fuel} and ρ_{fuel} by integration (see equation (5.5)) which yields (Röpke, 2007)

$$P(v'(\ell_{\mathrm{crit}}) \geq v'_{\mathrm{crit}})(t) = \int_{v'_{\mathrm{crit}}}^{\infty} f(v'(\ell_{\mathrm{crit}}))\, dv'(\ell_{\mathrm{crit}}) = \frac{\exp(a_3)\Gamma(1/a_2, -a_1(v'_{\mathrm{crit}})^{a_2})}{a_2(-a_1)^{1/a_2}}, \quad (5.14)$$

where Γ is the upper incomplete gamma function. For v'_{crit} we follow Lisewski et al. (2000) and use $v'_{\mathrm{crit}} = 10^8\,\mathrm{cm\ s^{-1}}$ but this threshold value will be varied later in a parameter study in Chapter 7. Equation (5.14) is calculated at each time step when the fit to the histogram of $v'(\ell_{\mathrm{crit}})$ was successful. In this case, the parameters a_1, a_2 and a_3 found from the fit have to be inserted.

5.3.2 The potential detonation area and the DDT criterion

In Section 5.1.3 we defined $A^*_{\mathrm{flame}}(t)$ as the part of the flame that meets the DDT constraints concerning the fuel fraction X_{fuel} and the fuel density ρ_{fuel}. In the preceding section we derived separately the probability of finding velocity fluctuations of at least v'_{crit} at this restricted flame front. We can now define

$$A_{\mathrm{det}}(t) = A^*_{\mathrm{flame}}(t) \cdot P(v'(\ell_{\mathrm{crit}}) \geq v'_{\mathrm{crit}})(t) \quad (5.15)$$

as the fraction of the flame surface area that is capable of performing a DDT (see also Röpke, 2007). This quantity which we call the *potential detonation area* in the following has to be compared with the critical size of DDT regions. Here we face the problem that the dimension and geometry of DDT regions are not known. Despite the fractal properties of turbulent structures (such as the flame) we will assume here at first that DDT regions have a smooth surface area. We define the *critical flame surface area* required for a DDT as

$$A_{\mathrm{crit}} = \ell^2_{\mathrm{crit}} = 10^{12}\,\mathrm{cm}^2. \quad (5.16)$$

If during the simulation $A_{\mathrm{det}}(t) \geq A_{\mathrm{crit}}$ occurs it is checked, whether this condition holds for $\tau_{\mathrm{eddy}_{1/2}}(\ell_{\mathrm{crit}})$. This is the DDT criterion in our DDT model. For $\tau_{\mathrm{eddy}_{1/2}}(\ell_{\mathrm{crit}})$ we will use $0.5 \times 10^{-2}\,\mathrm{s}$ (see Section 3.3.2) but this threshold value will be varied later in a parameter study in Chapter 7. If the criterion is finally met detonations are initialized. We note that both quantities $A^*_{\mathrm{flame}}(t)$ and particularly $P(v'(\ell_{\mathrm{crit}}) \geq v'_{\mathrm{crit}})(t)$ in $A_{\mathrm{det}}(t)$ may vary strongly within $\tau_{\mathrm{eddy}_{1/2}}(\ell_{\mathrm{crit}})$.

The main problem of the proposed DDT model is that it does not make a statement of whether there exits indeed a compact region of the size A_{crit}. The histogram of $v'(\ell_{\mathrm{crit}})$ (and hence the probability $P(v'(\ell_{\mathrm{crit}}) \geq v'_{\mathrm{crit}})(t)$) and the quantity $A^*_{\mathrm{flame}}(t)$ are determined from all grid cells at the flame that meet the DDT constraints. Thus, we get no information about the physical properties of localized structures, since the DDT model contains mainly global quantities. This also holds for $\tau_{\mathrm{eddy}_{1/2}}(\ell_{\mathrm{crit}})$ where we also use one uniform value for the DDT criterion.

For the above-mentioned reasons it further follows that there are no clear conclusions at which specific places at the flame detonations have to be initialized. Four different scenarios have been considered and tested and shall be outlined here:

1. The DDT occurs in a single grid cell of $N^*_{\mathrm{flame}}(t)$ in which $v'(\ell_{\mathrm{crit}})$ is maximal. This scenario takes into account the importance of the high velocity fluctuations and the

improbability that the constraints for a DDT are met simultaneously at different places. It is, however, unclear whether in the grid cell where $v'(\ell_{\text{crit}})$ is maximal that the other conditions for a DDT are most suitable.

2. The DDT occurs in all grid cells of $N^*_{\text{flame}}(t)$ independently of $v'(\ell_{\text{crit}})$, hence all grid cells are taken into account that meet the DDT constraints concerning X_{fuel} and ρ_{fuel}. The probability $P(v'(\ell_{\text{crit}}) \geq v'_{\text{crit}})(t)$ may be sufficiently high to meet the DDT criterion, but the histogram of $v'(\ell_{\text{crit}})$ with the underlying data $N^*_{\text{flame}}(t)$ shows clearly that most of the values of $v'(\ell_{\text{crit}})$ are not found at the slow decline of the right part of the histogram that contains the important high velocity fluctuations. In this context, we remember that the fit to the histogram of $v'(\ell_{\text{crit}})$ starts approximately at the beginning of this decline, from which $P(v'(\ell_{\text{crit}}) \geq v'_{\text{crit}})(t)$ is eventually calculated. In summary, the velocity fluctuations in the grid cells $N^*_{\text{flame}}(t)$ are mostly too low for a DDT.

3. The DDT occurs in all grid cells of $N^*_{\text{flame}}(t)$ in which $v'(\ell_{\text{crit}}) \geq v'_{\text{crit}}$. This approach seems reasonable, since v'_{crit} is defined as the minimum required velocity fluctuation for a DDT. In contrast to scenario (2), only grid cells are taken into account that represent the slow decline of the right part of the histogram of $v'(\ell_{\text{crit}})$. As stated in Section 5.2.5, however, grid cells with $v'(\ell_{\text{crit}}) \geq v'_{\text{crit}}$ are not necessarily found in the simulation. Those cells are more likely to occur in simulations with higher resolutions, leading to a resolution depending effect of the DDT model. In an extreme case, it is possible that v'_{crit} is not found in a single grid cell in low resolved simulations, so that with this approach no DDTs occur in the entire simulation.

4. The DDT occurs in a number of grid cells of $N^*_{\text{flame}}(t)$ that is equivalent to the ratio of the potential detonation area $A_{\text{det}}(t)$ to the critical flame surface area A_{crit}. This approach can be considered as a measure, to what extent the DDT criterion is met. Since $A_{\text{det}}(t)$ may significantly grow within $\tau_{\text{eddy}_{1/2}}(\ell_{\text{crit}})$ DDTs will commonly occur in several grid cells. However, in this approach we still have to choose in which cells detonations should be initialized. We follow scenario (1) and initialize the first detonation in the cell with the highest value of $v'(\ell_{\text{crit}})$. If $A_{\text{det}}(t)/A_{\text{crit}} \geq 2$ the cell with the second highest value of $v'(\ell_{\text{crit}})$ is selected for a DDT and so on, until the number of initialized detonations equals the ratio $A_{\text{det}}(t)/A_{\text{crit}}$. Similar to scenario (3) we capture here only grid cells that make up the slow decline of the right part of the histogram of $v'(\ell_{\text{crit}})$, but a further advantage of this scenario is that DDTs will definitely occur, when the criterion is met.

As described in Section 3.3.2 high velocity fluctuations are crucial for a DDT, hence we exclude that scenario (2) is from a physical point of view a suitable approach for the delayed detonation model. For reasons of the resolution dependence and the uncertainty that high values of $v'(\ell_{\text{crit}})$ are indeed found in the grid cells, scenario (3) is inappropriate for a SGS model for DDTs. Since the DDT criterion constitutes a global criterion it is highly uncertain, which is the most suitable location to perform a DDT. This uncertainty concerns scenario (1), but also to a certain extent scenario (4). In the latter case, however, DDTs may occur in many grid cells, hence local considerations where DDTs are most suitable are far less important. Together with the fact that scenario (4) evaluates to what extent the criterion is met, we will exclusively use this scenario in the analyses of this work. The number of DDTs

F_{DDT} at a time t_{DDT} when the DDT criterion is met is then given by

$$F_{\mathrm{DDT}} = \frac{A_{\mathrm{det}}(t = t_{\mathrm{DDT}})}{A_{\mathrm{crit}}}. \tag{5.17}$$

The value of F_{DDT} is always rounded to the next smaller integer. In the simulation, detonations are set artificially by initializing a second level set at the DDT locations. The minimum time between two DDTs is given by $\tau_{\mathrm{eddy}_{1/2}}(\ell_{\mathrm{crit}})$, since the time measurement for $A_{\mathrm{det}}(t) \geq A_{\mathrm{crit}}$ is reset when the DDT criterion is met. The same holds if the condition $A_{\mathrm{det}}(t) < A_{\mathrm{crit}}$ occurs, before $\tau_{\mathrm{eddy}_{1/2}}(\ell_{\mathrm{crit}})$ is reached.

5.3.3 Remarks on the DDT model

Remarks on the time step

From the view of the performed hydrodynamic simulations, the inclusion of $\tau_{\mathrm{eddy}_{1/2}}(\ell_{\mathrm{crit}})$ is also important to keep the DDT model resolution-independent. The reason is that the time step in the hydrodynamic simulation is determined by the Courant-Friedrichs-Lewy (CFL) criterion that sets the maximally possible time step Δt_{CFL} to ensure the numerical stability of the solution of the Euler equations (Courant & Friedrichs, 1948) (see also Reinecke, 2001). Due to the smaller size of the grid cells, the maximal time step of higher resolved simulations is shorter than for lower resolved ones. Hence, to approach a certain time (for instance the time where DDTs are expected to occur), a higher resolved simulation needs more time steps. Since the DDT criterion is evaluated each time step, this simulation becomes an enhanced chance for a successful DDT due to the more attempts to meet the DDT criterion, if no time-dependent quantity like $\tau_{\mathrm{eddy}_{1/2}}(\ell_{\mathrm{crit}})$ is included.

Remarks on the required resolution for the application of the DDT model

As already indicated in Section 5.2.5, to construct and fit the histogram of $v'(\ell_{\mathrm{crit}})$ a sufficient large number of grid cells $N^*_{\mathrm{flame}}(t)$ is required. The quantity $N^*_{\mathrm{flame}}(t)$ depends on the resolution and on the restrictiveness of the DDT criterion. Therefore, in lowly resolved simulations in combination with a very restrictive DDT criterion, the calculation of the histogram of $v'(\ell_{\mathrm{crit}})$ and the fit may be either impossible for the entire simulation or only possible in a particularly late phase when the number of $N^*_{\mathrm{flame}}(t)$ becomes eventually large enough. In the latter case, an additional problem may arise due to the fact that the length of the grid cells $\Delta(t)$ becomes very large. Here we find very large values of $A^*_{\mathrm{flame}}(t)$ at the time, when the histogram and fit calculation is initialized. This in turn may lead to the effect that the first value of the potential detonation area $A_{\mathrm{det}}(t)$ that is also determined for the first time when the histogram of $v'(\ell_{\mathrm{crit}})$ and the fit can be calculated, may already exceed A_{crit}. In this case, the application of the DDT model becomes questionable, since here A_{crit} may already be exceeded by $A_{\mathrm{det}}(t)$ at an earlier time step, which is not possible to evaluate, since due to the lack of sufficient data $P(v'(\ell_{\mathrm{crit}}) \geq v'_{\mathrm{crit}})(t)$ could not be calculated.

For resolutions with less than 256^3 grid cells these problems occur frequently, where in most cases no DDTs occur due to the lack of sufficient data to construct and fit the histogram of $v'(\ell_{\mathrm{crit}})$. Moreover, in these simulations Δt_{CFL} may become comparable to $\tau_{\mathrm{eddy}_{1/2}}(\ell_{\mathrm{crit}})$ that lead to a resolution dependence of the DDT model. With a resolution of 256^3 grid cells, the above-described problems only occurred in the case of a few simulations that show a very small flame surface area, so that $N_{\mathrm{flame}}(t)$ is particularly low. Here a too restrictive DDT criterion may lead in addition to very low values of $N^*_{\mathrm{flame}}(t)$ that is insufficient to

construct and fit the histogram of $v'(\ell_{\mathrm{crit}})$. These simulations, however, constitute only a minor fraction of the overall performed simulations and we conclude that for simulations with a resolution of at least 256^3 grid cells the DDT model can be applied.

Remarks on the resolution-dependent quantities of the DDT model

Since the occurrence of high velocity fluctuations in the grid cells depends on the resolution (see Section 5.2.5) the locations where detonations are initialized are also resolution-dependent. We further note that for given DDT constraints, the minimum number of grid cells $N^*_{\mathrm{flame}}(t)$ that are required to construct and fit the histogram of $v'(\ell_{\mathrm{crit}})$ is reached earlier in higher resolved simulations. This, however, would only be significant if for a given ignition model and DDT criterion the condition $A_{\mathrm{det}}(t) \geq A_{\mathrm{crit}}$ in combination with a successful DDT occurs in a higher resolved simulation, before the histogram of $v'(\ell_{\mathrm{crit}})$ and the fit can be calculated in a lower resolved one. In this work, this effect has never been observed. A further resolution-depending quantity is the size of the grid cells in which DDTs occur. However, it is most likely that the dynamics of the detonations do not depend on the size of the grid cells in which they are initialized.

5.4 Determination of the fractal dimension of the flame and resolution test in one full-star model

To investigate the resolution dependence of the implemented DDT model, we apply it to the Model X* (resp. the model described in Röpke et al. (2007a)) and perform two simulations of pure deflagrations with a resolution of 256^3 and 512^3 grid cells.[6] In the preceding sections we set specific threshold values for the DDT quantities that are used in the following test simulations and that shall be summarized here: $X^{\mathrm{min}}_{\mathrm{fuel}} = 1/3$, $X^{\mathrm{max}}_{\mathrm{fuel}} = 2/3$, $\rho^{\mathrm{min}}_{\mathrm{fuel}} = 0.5 \times 10^7\,\mathrm{g\,cm^{-3}}$, $\rho^{\mathrm{max}}_{\mathrm{fuel}} = 1.5 \times 10^7\,\mathrm{g\,cm^{-3}}$, $v'_{\mathrm{crit}} = 10^8\,\mathrm{cm\,s^{-1}}$, $A_{\mathrm{crit}} = 10^{12}\,\mathrm{cm^2}$ and $\tau_{\mathrm{eddy}} = 0.5 \times 10^{-2}\,\mathrm{s}$. One parameter which was left undetermined is the fractal dimension D of the flame that has to be calculated from the resolution study itself.

5.4.1 The fractal dimension of the flame

In Figure 5.11(a) $N_{\mathrm{flame}}(t)$ is shown as function of time. The black curve is the result of the simulation with 256^3 grid cells and the red curve is the result of the higher resolved one. All other curves belong to theoretically expected curves for the higher resolved simulation that are determined by assuming a specific fractal dimension of the flame. These curves can be calculated from the obtained values of $N_{\mathrm{flame}_1}(t)$ and the known resolutions $\Delta_1(t)$ and $\Delta_2(t)$. Then a value of D has to be specified and equation (5.3) applied. It follows that $N_{\mathrm{flame}_2}(t)$ is given by

$$N_{\mathrm{flame}_2}(t) = N_{\mathrm{flame}_1}(t) \cdot (\Delta_1(t)/\Delta_2(t))^D. \tag{5.18}$$

We see in Figure 5.11(a) that the curves with $D = 2$ and $D = 3$ are obviously inconsistent with the result of the higher resolved simulation. Hence the fractal character of the flame is

[6] These simulations were in reality performed as delayed detonations in order to apply the implemented DDT model. However, we left out the initialization of the detonations when the DDT criterion was met, since this study concerns only the resolution dependence of the DDT model. The properties of the detonation phase and its feedback on the DDT model will be investigated in Chapter 6.

verified. In Figure 5.11(b), the fractal dimension, calculated with equation (5.2) is plotted as function of time where we see a clear variation of D during the explosion. A necessary constraint for DDTs is that the flame resides in a certain range of fuel densities. At the time $t \approx 0.8\,\mathrm{s}$, the first grid cells approach the upper density threshold of $1.5 \times 10^7\,\mathrm{g\,cm^{-3}}$, where we find $D \approx 2.5$. However, DDTs occur at later times when more grid cells are in the necessary density range of $0.5 \times 10^7\,\mathrm{g\,cm^{-3}} \leq \rho_{\mathrm{fuel}} \leq 1.5 \times 10^7\,\mathrm{g\,cm^{-3}}$. Here we find $D < 2.5$. Taking into account the intermittency in turbulence we will use a constant value of 2.36 for D in our studies (see Section 3.2.4). In Figure 5.11(c), the flame surface area $A^*_{\mathrm{flame}}(t)$ calculated with equation (5.4) with $D = 2.36$ is shown as function of time for both simulations and we see there is a very good agreement of the curves. For comparison we show in Figure 5.11(d) $A^*_{\mathrm{flame}}(t)$ with $D = 2$ where we see that $A^*_{\mathrm{flame}}(t)$ is larger for the higher resolved simulation.

Remarks on the fractal dimension

We have to outline some issues concerning the determination of the fractal dimension of the flame. At first we see that the choice of a constant fractal dimension is obviously a crude approximation, since we see in Figure 5.11(b) that D declines continuously from 2.5 to almost 2.3 in the late explosion phase until $t \approx 1.2\,\mathrm{s}$. In addition, one may expect a different curve shape of D for models with a different evolution of the turbulent deflagration. Hence, D should be determined for each DDT simulation where the flame evolves from a different ignition setup of the deflagration. Since in this work many different ignition models of the deflagration flame are used, this cannot be performed. Only for Model III and Model VIII (see Table 4.1) that are frequently used in the following studies, D has been calculated. The results are shown together with Model X* in Figure 5.12. All three models have very different ignition geometries (see Table 4.1) and as shown later in Chapter 6, they have very different evolutions of the turbulent deflagration. Nevertheless, we see qualitatively a good agreement of the curves. A probable reason is the fact that turbulence in the deflagration of SNe Ia obeys well defined statistical properties (see Section 3.2.4). Hence, a significant deviation of D for different deflagrations may be unlikely but cannot be ruled out completely.

The biggest problem, however, is the uncertainty that we cannot fully ensure whether the data at the flame from the chosen resolutions are sufficient to determine a reliable value for D. If for instance D would be calculated from Model X* from simulations with resolutions of 512^3 and 1024^3 grid cells, the result for D may be different, indicating that a convergence of D is obtained at even higher resolutions only. Therefore, a logical approach to determine a reliable value of D would be to perform a resolution study first, until D does not change anymore. This, however, cannot be performed, since the currently available computational resources prevent simulations with LEAFS with very high resolutions.

Obviously, there are some uncertainties in the determination of the quantity D. But there is also the possibility that the found curve shape of D can be explained by physical properties. The curves in Figure 5.12 are certainly not capable of describing the behavior of turbulence and its impact on the flame in detail. They may, however, indicate that there are several mechanisms and instabilities that drive the turbulent motions in the vicinity of the flame. This assumption is reinforced by the fact that the found values of $D \approx [2.3 \ldots 2.5]$ are expected for different instabilities and turbulence driving mechanisms (see Section 3.2.4). We emphasize, however, that we used a more simplified method to estimate the fractal dimension of the flame than in most of the other studies in which the values of $D \approx [2.3 \ldots 2.5]$ were derived (see Section 3.2.4 and 5.1.3).

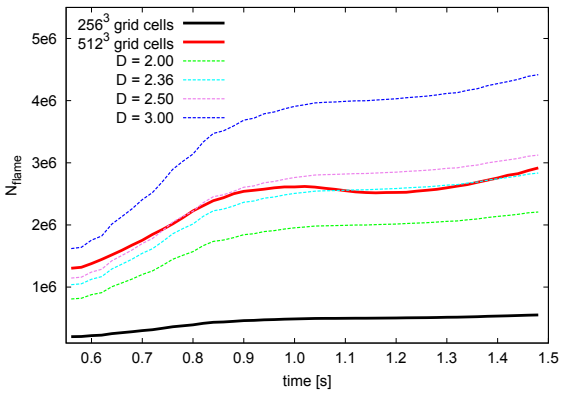

(a) Number of all grid cells at the flame as function of time for different resolutions (black and red curve). In addition, theoretical curves for the higher resolved simulation are shown where a specific fractal dimension of the flame is assumed.

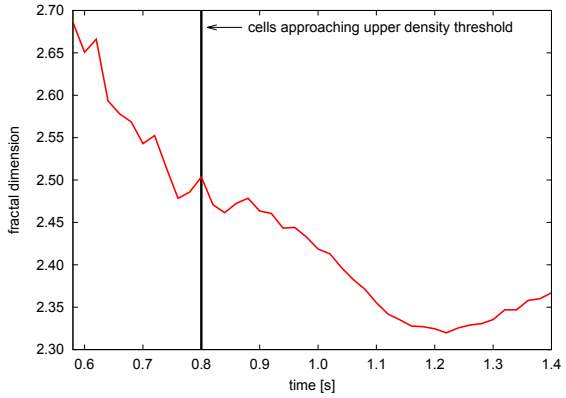

(b) Fractal dimension of the flame as function of time for Model X*.

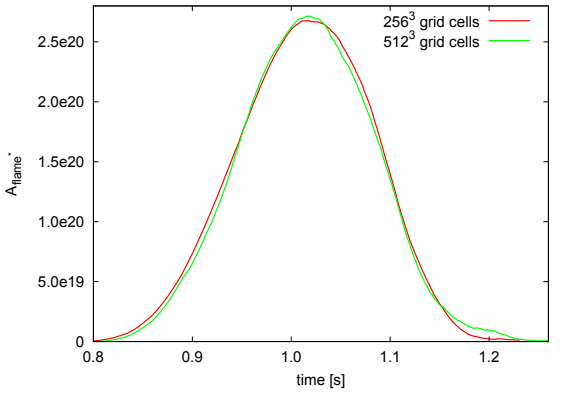

(c) Flame surface area $A^*_{\text{flame}}(t)$ as function of time for different resolutions with $D = 2.36$.

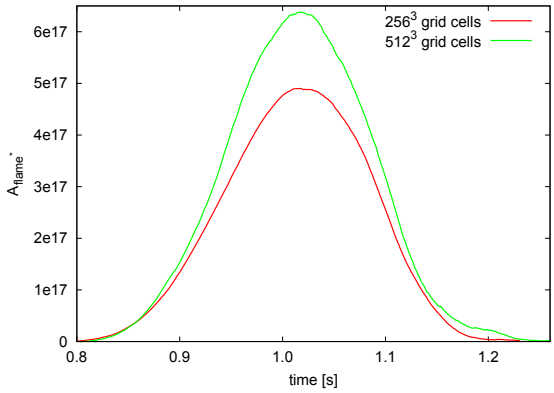

(d) Flame surface area $A^*_{\text{flame}}(t)$ as function of time for different resolutions with $D = 2$.

Fig. 5.11: Analysis of the fractal dimension of the flame. (a) The number of grid cells found at the flame indicates that the flame has a fractal character. (b) The fractal dimension is a time-dependent quantity that falls below 2.5 when the first grid cells approach $\rho^{\max}_{\text{fuel}}$. (c/d) The flame surface area $A^*_{\text{flame}}(t)$ with $D = 2.36$ shows a good agreement for both resolutions, while with $D = 2$, $A^*_{\text{flame}}(t)$ appears larger for the higher resolved simulation.

Even if the described uncertainties in the quantity D should not be neglected completely, it seems that the chosen value of $D = 2.36$ is appropriate for the DDT model, since the curve shapes of $A^*_{\text{flame}}(t)$ for both resolutions in Figure 5.11(c) and also the temporal evolution of D in different deflagrations in Figure 5.12 are in good agreement (see also Chapter 6.2.2).

5.4.2 The probability of finding high velocity fluctuations

The probability $P(v'(\ell_{\text{crit}}) \geq 10^8\,\text{cm s}^{-1})(t)$ of finding velocity fluctuations $v'(\ell_{\text{crit}})$ on the scale ℓ_{crit} of at least $10^8\,\text{cm s}^{-1}$ is shown as function of time in Figure 5.13(a) for both simulations. Since there is only a slight resolution dependence of the flame evolution in the deflagration and the calculated histograms of $v'(\ell_{\text{crit}})$ and the fits, both curves are in a very good agreement. We see that the quantity $P(v'(\ell_{\text{crit}}) \geq 10^8\,\text{cm s}^{-1})(t)$ has the first

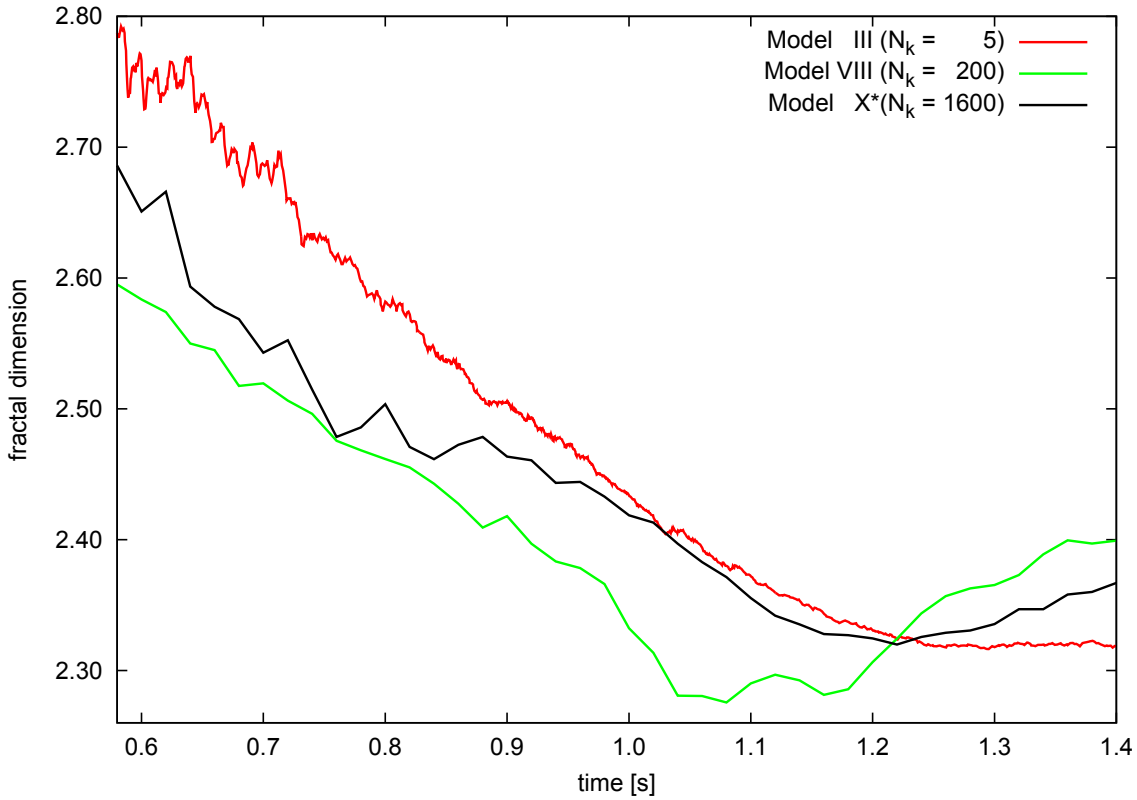

Fig. 5.12: Fractal dimension of the flame as function of time for three ignition models of the deflagration. The fractal dimension behaves similar even for very different strengths of the deflagration.

noticeable value at $t \approx 0.83\,\mathrm{s}$ and becomes marginal for times later than $t \approx 1.15\,\mathrm{s}$. The highest values are found between 0.95 and 1.00 seconds. At these times the intermittent character in the turbulence becomes most evident.

5.4.3 The potential detonation area

The quantity $A_{\mathrm{det}}(t)$ is shown as function of time in Figure 5.13(b) for both simulations. Since both quantities, $A^*_{\mathrm{flame}}(t)$ and $P(v'(\ell_{\mathrm{crit}}) \geq 10^8\,\mathrm{cm\ s^{-1}})(t)$ have been proven resolution independent, $A_{\mathrm{det}}(t)$ will follow this trend, which can be definitely seen in Figure 5.13. In particular, we see that the shape of the curves of $P(v'(\ell_{\mathrm{crit}}) \geq 10^8\,\mathrm{cm\ s^{-1}})(t)$ and $A_{\mathrm{det}}(t)$ are very similar over a long time interval. We can identify in $A_{\mathrm{det}}(t)$ the strong variations of the quantity $P(v'(\ell_{\mathrm{crit}}) \geq 10^8\,\mathrm{cm\ s^{-1}})(t)$. This indicates that the relative change in the quantity $A^*_{\mathrm{flame}}(t)$ for a given specific time interval like $\tau_{\mathrm{eddy}_{1/2}}(\ell_{\mathrm{crit}})$ is very low compared to $P(v'(\ell_{\mathrm{crit}}) \geq 10^8\,\mathrm{cm\ s^{-1}})(t)$.

For this resolution study we have chosen a critical flame surface area of $A_{\mathrm{crit}} = 10^{12}\,\mathrm{cm}^2$. We see in Figure 5.13(b) that this threshold is exceeded by $A_{\mathrm{det}}(t)$. Therefore, in the context of the delayed detonation scenario we expect DDTs, when $A_{\mathrm{det}}(t) \geq A_{\mathrm{crit}}$ for at least $\tau_{\mathrm{eddy}_{1/2}}(\ell_{\mathrm{crit}})$. This constraint is indeed fulfilled, where the time $t^{\mathrm{1st}}_{\mathrm{DDT}}$ of the first DDT is approximately 0.92 s for both simulations. This time is additionally marked in Figure 5.13(b) at the curve of $A_{\mathrm{det}}(t)$. In the simulation with 256^3 grid cells we obtain a

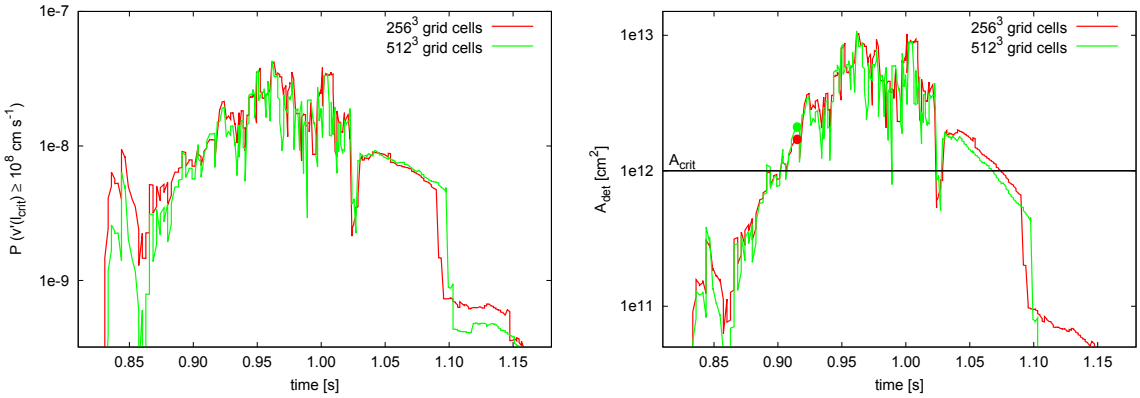

(a) (b)

Fig. 5.13: (a) The probability $P(v'(\ell_{\text{crit}}) \geq 10^8\,\text{cm s}^{-1})(t)$ of finding velocity fluctuations of at least $10^8\,\text{cm s}^{-1}$ and (b) the size of the potential detonation area $A_{\text{det}}(t)$ as function of time. For most of the time between 0.90 and 1.07 seconds $A_{\text{det}}(t) \geq A_{\text{crit}}$. The DDT criterion is met for the first time at $t \approx 0.92\,\text{s}$ for both simulations (see dot on the corresponding curve of $A_{\text{det}}(t)$).

value of $A_{\text{det}}(t = t^{\text{1st}}_{\text{DDT}}) \approx 1.72 \times 10^{12}\,\text{cm}^2$. Therefore, it follows $F_{\text{DDT}} = 1$. In the higher resolved simulation we find $A_{\text{det}}(t = t^{\text{1st}}_{\text{DDT}}) \approx 2.12 \times 10^{12}\,\text{cm}^2$, hence a DDT occurs here already in two grid cells.

In the delayed detonation scenario, the further evolution of the explosion for times $t > t^{\text{1st}}_{\text{DDT}}$ depends on whether the DDT criterion stays fulfilled, so that new DDTs may occur at later times. In the performed simulations, this is true, since $A_{\text{det}}(t) \geq A_{\text{crit}}$ for most of the time between approximately 0.90 and 1.07 seconds. There are, however, some interruptions, where in a time step $A_{\text{det}}(t) < A_{\text{crit}}$, before $\tau_{\text{eddy}_{1/2}}(\ell_{\text{crit}})$ is reached that prevent a few DDTs. In the simulation with 256^3 grid cells we find $F_{\text{DDT}} = 10$ and for the higher resolved simulation $F_{\text{DDT}} = 12$ at the maximum of $A_{\text{det}}(t)$ that is reached by both simulations at approximately $t \approx 0.96\,\text{s}$. The last DDT occurs at $t \approx 1.06\,\text{s}$ in a single grid cell in both simulations.

5.5 Conclusions for the DDT model

We developed and tested a new DDT model for the delayed detonation scenario in SN Ia explosions. Based on a SGS approach, specific ranges and threshold values of the DDT quantities have been selected that are according to our current knowledge consistent with the physical conditions and constraints for DDTs. Our DDT model can be summarized as follows: At first a sufficient number of grid cells at the flame must have a specific fuel fraction and a certain fuel density. Using a fractal description of the flame we determine a suitable flame surface area for DDTs from the number and size of these grid cells. Second, we calculate the probability of finding sufficiently high velocity fluctuations for a DDT at this flame surface area. This is accomplished by applying a fit to the histogram of the rescaled turbulent velocity fluctuations in the above-mentioned grid cells and integrating the obtained approximated probability density function. Afterwards we calculate the product of this probability and the suitable flame surface area for DDTs. This way we obtain a potential detonation area that has to be compared with a critical flame surface area that is required for a DDT to occur. Finally the potential detonation area has to exceed the critical flame

surface area for at least a half eddy turnover time in order to become sufficiently mixed. If all these conditions are met detonations are initialized in those grid cells, where the highest velocity fluctuations are found at the suitable flame surface area for DDTs. The number of DDTs equals the ratio of the potential detonation area to the critical flame surface area.

We showed that the DDT model is largely resolution-independent, which is a crucial feature, since most of the DDT quantities, such as the turbulent velocity fluctuations $v'(\ell_{\mathrm{crit}})$ on the critical length scale ℓ_{crit} and the DDT region(s) are not resolved. In the deflagration model of Röpke et al. (2007a) that has been used in the resolution study, the DDT criterion was met, indicating that according to the implemented DDT model the necessary conditions for DDTs in the turbulent deflagration were suitable.

A weakness of the DDT criterion is that it constitutes a global criterion, since most of the DDT quantities return no information about the physical properties of localized regions. Therefore, there is no clear conclusion of whether there is a spatially connected region that exceeds the critical flame surface area A_{crit}. In this context, we also face the problem of where to initialize detonations when the DDT criterion is met. In reality DDTs would occur in local structures at the flame, where the physical properties of these structures are given by local quantities (like $v'(\ell_{\mathrm{crit}})$). We also initialize detonations in local regions (resp. in specific grid cells) that have local quantities, but we use in our DDT model global quantities. In summary, we perform some kind of a translation from global quantities (such as $P(v'(\ell_{\mathrm{crit}}) \geq 10^8\,\mathrm{cm\ s^{-1}})(t)$) to local quantities (such as $v'(\ell_{\mathrm{crit}})$). This translation is a flaw in our modeling approach, since when the global DDT criterion is met, there is no evidence that there is indeed a localized region, which is capable of performing a DDT.

In addition, most of the values of the DDT quantities are not well known and are kept constant or in a constant range in the DDT model. Moreover, some of these quantities depend on each other but these dependencies cannot be modeled on unresolved scales within our chosen approach consistently. However, we can perform a detailed systematical parameter study in order to evaluate to what extent a change of the threshold values of the DDT quantities lead to a change of the simulation results (for instance of the obtained ^{56}Ni yield of the explosion). The results of such a parameter study give further insights in the necessary constraints for a DDT, since the outcome of the corresponding simulations has to match the observational properties (provided that the underlying supernova model is correct). Since the DDT model has been proven independent of resolution, this model can be applied reliably in simulations of delayed detonations even with a resolution of 256^3 grid cells only. Therefore, the computational demand is relatively low, so that a parameter study can cover a sufficiently wide range in the change of the threshold values of the DDT quantities to draw some conclusions for the delayed detonation scenario. Before we describe this parameter study, we will first study the features of the DDT model in more detail, by applying it with two sets of parameters for the DDT criterion to the ten ignition models of Table 4.1. Here we can estimate the range of brightnesses that can be obtained with the DDT model and the chosen DDT criteria. In addition, we are interested in the impact of the different evolutions of the deflagration in the models on the capability of meeting the DDT criterion. Finally we analyze the dynamics of detonations which were not initialized in the resolution study.

6

Application of the delayed detonation model in SN Ia simulations

In Section 5.4 we applied the DDT model with fixed parameters to a specific deflagration model, where we found that the DDT criterion was met. However, the occurrence of DDTs in a single arbitrary deflagration model with a fixed DDT criterion is no proof that the necessary constraints for DDTs are commonly met in SN Ia explosions. Apart from the uncertainties of these constraints, the properties of the turbulent deflagration have a crucial impact on the occurrence of DDTs. The evolution of the deflagration in turn depends strongly on the modeled ignition scenario of the deflagration flame. As described in Section 2.3.1 many properties of the ignition process of the deflagration are unclear, including the geometry and size of the ignition region(s) from which the deflagration flame emerges. For the delayed detonation model it is therefore of high importance to study the evolution of the turbulent deflagration from different ignition scenarios of the deflagration flame first in order to evaluate to what extent these different evolutions may favor the occurrence of DDTs.

In the following study, the DDT model is applied to the ten ignition models of the deflagration shown in Table 4.1. We perform simulations with resolutions of 256^3 and 512^3 grid cells of delayed detonations and also of pure deflagrations to investigate the difference in these explosion scenarios in more detail. For the DDT criterion we choose two different parameter sets for the threshold values of the DDT quantities, where we apply one set to the lower resolved simulations and the other set that constitutes a more restrictive DDT criterion to the higher resolved simulations. The DDT model is active in all simulations but in the case of pure deflagrations no detonations are initialized when the DDT criterion is met.

This chapter is organized as follows. In Section 6.1 we first describe the setup of the simulations and explain why we choose simultaneously different DDT criteria and resolutions. In Section 6.2 we follow the evolution of the deflagrations and delayed detonations in detail. Here we are mainly interested in the impact of different evolutions of the deflagration phase on the capability of meeting the DDT criterion. Furthermore, we will analyze the explosion phase beyond the onset of DDTs and investigate the change in the mass fractions of chemical

species due to the additional burning of the fuel after detonations are initialized. The results of the studies are discussed in Section 6.3 which will focus on the behavior of the DDT model in the different simulations and the implications for DDTs in SNe Ia. A summary of this study is given in Section 6.4.

6.1 Setup of the simulations

The initial white dwarf model is described in Section 4.2, where also details of the ignition models of the deflagration are shown (see Table 4.1 and Figure 4.2). The two parameter sets for the DDT criteria of this study are summarized in Table 6.1. We use for parameter set I a resolution of 512^3 grid cells (in the following referred to as *Study I*) and for parameter set II a resolution of 256^3 grid cells only (in the following referred to as *Study II*). For both DDT criteria we use $v'_{\mathrm{crit}} = 1.0 \times 10^8\,\mathrm{cm\ s^{-1}}$ and $\tau_{\mathrm{eddy}_{1/2}}(\ell_{\mathrm{crit}}) = 0.5 \times 10^{-2}\,\mathrm{s}$. The allowed ranges for X_{fuel} and ρ_{fuel} are more restrictive for Study I. Due to the higher resolution, however, there will be a significantly larger number of grid cells $N^*_{\mathrm{flame}}(t)$ that may be capable of meeting these more stringent DDT constraints (see also Section 5.3.3). This in turn ensures the calculation of the histogram of $v'(\ell_{\mathrm{crit}})$ and the application of the fit. As mentioned in Section 5.3.2, the geometry and the dimension of a DDT region is unknown and we assumed a smooth surface with $A_{\mathrm{crit}} = \ell^2_{\mathrm{crit}} = 10^{12}\,\mathrm{cm}^2$ so far. If the DDT region, however, has similar fractal properties as the flame, then $A_{\mathrm{crit}} = \ell^D_{\mathrm{crit}}$ may hold. In this analysis we use this threshold with $D = 2.36$ for Study I, so that the criterion becomes much more stringent. The parameter set for Study II equals the parameter set used in the resolution study in Section 5.4 except we choose here a much narrower allowed range of fuel densities. We use simultaneously different resolutions and DDT criteria in the two studies for the following reasons:

- We showed in Section 5.4 in a specific deflagration model that the flame surface area $A_{\mathrm{flame}}(t)$ is largely resolution-independent, provided that we assign a fractal dimension of $D = 2.36$ to the flame (see Figure 5.11(c)). We further found that the temporal evolution of D is similar for different strengths of the deflagration (see Figure 5.12) but we did not estimate a value of D for different deflagrations. Therefore, we will check in the following study whether a fractal dimension of $D = 2.36$ is appropriate for the ten ignition models of Table 4.1. This can be accomplished by calculating the flame surface area $A_{\mathrm{flame}}(t)$ (equation (5.4)) with $D = 2.36$ for all pure deflagrations and comparing the results obtained from different resolutions.

- In contrast to $A_{\mathrm{flame}}(t)$, the number of grid cells at the flame $N_{\mathrm{flame}}(t)$ and the subset of these grid cells $N^*_{\mathrm{flame}}(t)$ that meet the DDT constraints concerning the quantities ρ_{fuel} and X_{fuel} depend strongly on the resolution. $N^*_{\mathrm{flame}}(t)$ obviously further depends on the restrictiveness of the DDT criterion (see Section 5.3.3). Moreover, the quantity $N^*_{\mathrm{flame}}(t)$ represents the total number of grid cells where detonations can be initialized. When the criterion is met, DDTs occur in F_{DDT} grid cells of $N^*_{\mathrm{flame}}(t)$ (see Section 5.3.2). In Study II we expect higher values of F_{DDT}, since the DDT criterion is less restrictive than in Study I. On the other hand, $N^*_{\mathrm{flame}}(t)$ is far lower in Study II due to the lower resolution. In summary, we expect very different numbers, times and distributions of DDT regions in both studies which enables us to investigate to what extent these differences affect the subsequent detonation phase and eventually the explosion brightness.

- The evolution of the explosion toward the first DDT (and also to a certain extent beyond this time) is largely resolution-independent (see Section 5.4 and Figure 5.13). Taking this into account we can analyze to what extent the two different sets of DDT parameters affect the capability of the ignition models of meeting the DDT criterion. We can for instance analyze how the largely resolution-independent quantities $A^*_{\mathrm{flame}}(t)$ and $P(v'(\ell_{\mathrm{crit}}) \geq v'_{\mathrm{crit}})(t)$ vary for the two DDT criteria.

Study	Resolution	$X^{\mathrm{min}}_{\mathrm{fuel}} \leq X_{\mathrm{fuel}} \leq X^{\mathrm{max}}_{\mathrm{fuel}}$	$\rho^{\mathrm{min}}_{\mathrm{fuel}} \leq \rho_{\mathrm{fuel}} \leq \rho^{\mathrm{max}}_{\mathrm{fuel}}$	A_{crit}
I	512^3 grid cells	$0.4 \leq X_{\mathrm{fuel}} \leq 0.6$	$[6 \leq \rho_{\mathrm{fuel}} \leq 7] \times 10^6$ g cm^{-3}	ℓ^D_{crit}
II	256^3 grid cells	$1/3 \leq X_{\mathrm{fuel}} \leq 2/3$	$[6 \leq \rho_{\mathrm{fuel}} \leq 8] \times 10^6$ g cm^{-3}	ℓ^2_{crit}

Table 6.1: The two parameter sets of the DDT criterion for Study I and Study II.

6.2 The evolution of deflagrations and delayed detonations

6.2.1 The strength and gravitational binding of pure deflagrations

In Figure 6.1 the nuclear energy release E_{nuc} is shown as function of time for the simulated pure deflagrations of all models. We see a faster growth rate of E_{nuc} for models with larger N_{k} that implies a faster growth rate of the flame surface area. Hence, our assumption that N_{k} sets mainly the strength of the deflagration is justified (see also Röpke et al., 2006). There is, however, a saturation effect for models with $N_{\mathrm{k}} \geq 200$ in the late explosion phase that can be seen in the right panels of Figure 6.1 in both studies.

In weak deflagrations that evolve from a few ignition kernels the energy release may be so low that the gravitational binding energy of the white dwarf cannot be overcome. In this case, we find that the radial velocity $v_{\mathrm{rad}}(r) = \boldsymbol{v} \cdot \boldsymbol{e_r}$ in the grid cells that have a small distance r to the center of the white dwarf cannot reach the required escape velocity. Therefore, due to effective gravitational forces some of the stellar material experiences an acceleration toward the center of the exploding star. For strong deflagrations in contrast, a significant part of the stellar material may reach the stage of free (homologous) expansion in the late explosion phase, where $v_{\mathrm{rad}}(r) \propto r$.

In the following, we consider a very late phase of the explosion, after the deflagration has ceased. We define E_{kin}, E_{int} and E_{grav} as the kinetic, internal and gravitational energy, respectively. The stellar material in the grid cells in which $E_{\mathrm{kin}} + E_{\mathrm{int}} + E_{\mathrm{grav}} < 0$ remains gravitationally bound. The corresponding regions of the white dwarf will after an initial slight expansion start to collapse, where all these regions will unite to a compact object. In this way, we obtain a remnant of high density that contains a bound mass M_{b} with a relatively small radius r_{b}.[1] The other part of the exploding star that contains a certain mass M_{u} of unbound material will continue to expand, where for the distance r_{u} of the outer expanding ejecta to the center $r_{\mathrm{u}} \gg r_{\mathrm{b}}$ holds. For sufficiently strong deflagrations the system is completely unbound, hence $M_{\mathrm{b}} = 0$ and $M_{\mathrm{u}} = M_{\mathrm{CH}}$. We will choose in this analysis the data of the lower resolved simulations of pure deflagrations and analyze the time $t = 100\,\mathrm{s}$ only unless stated otherwise.

[1] We note that this remnant cannot be a neutron star, since the latter is only formed when $M_{\mathrm{b}} > M_{\mathrm{CH}}$ which is in practice never the case in our Chandrasekhar-mass explosion model.

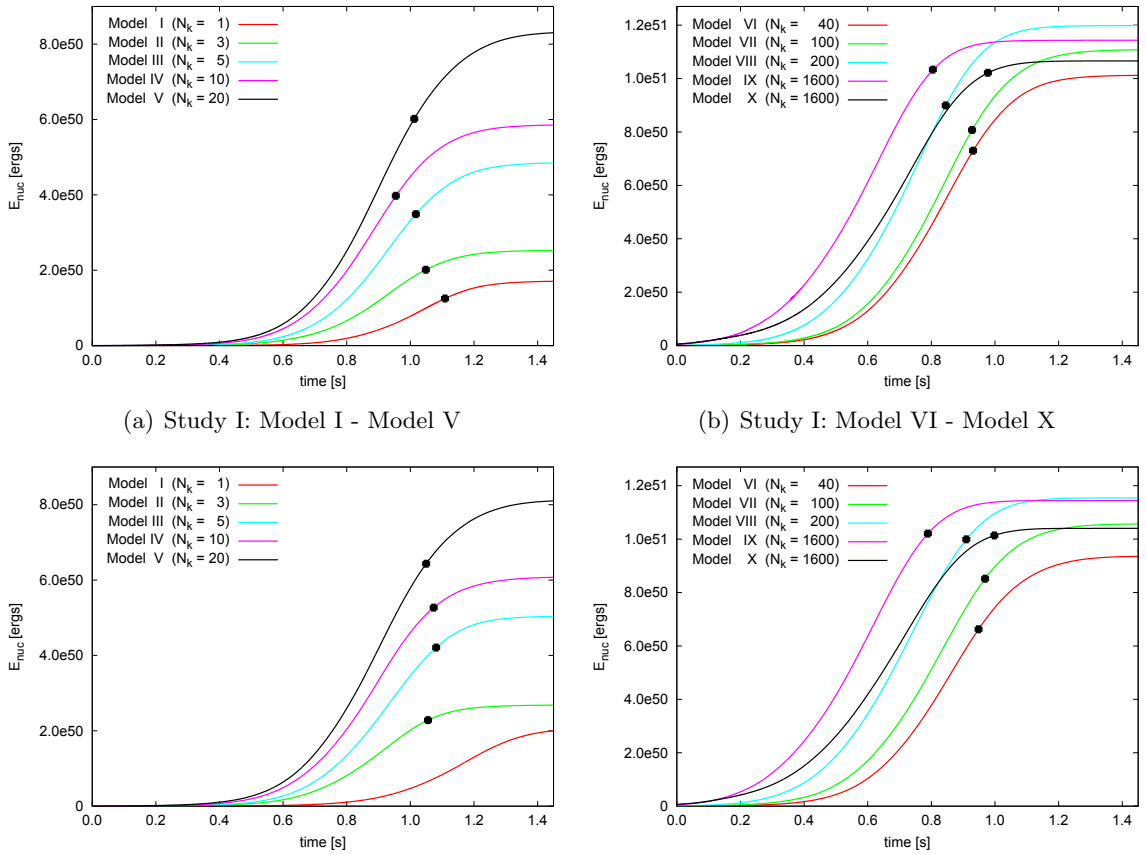

(a) Study I: Model I - Model V

(b) Study I: Model VI - Model X

(c) Study II: Model I - Model V

(d) Study II: Model VI - Model X

Fig. 6.1: Nuclear energy release E_{nuc} as function of time in the simulations of pure deflagrations. The first time where the DDT criterion is met is marked with a black dot.

In the upper panels of Figure 6.2 the masses M_{b} and M_{u} are shown in units of solar masses $M_{\odot}$ as function of the distance r to the center of the white dwarf. We see clearly that at large r, M_{b} is significantly larger for weak deflagrations. For $N_{\mathrm{k}} \geq 200$ we find $M_{\mathrm{u}} \approx M_{\mathrm{CH}}$. In the lower panels of Figure 6.2 a cross section of the density through the x-y plane through the center of the white dwarf is shown as function of r. Here we have to outline that due to the considered late time, the outer layers of the white dwarf have expanded so far that in combination with the co-moving grid technique, the central area is only resolved coarsely, even for simulations with high resolutions. Here, a resolution-depending effect occurs, where the central density in higher resolved simulations is higher. This behavior is illustrated in Figure 6.3(a) for Model II. Due to this resolution-depending effect, the real density in the central region of the white dwarf cannot be determined precisely. However, we can observe, whether there is a steep rise in the density in the grid cells in the vicinity of the center of the white dwarf. For these rough considerations the data of the lower resolved simulations are sufficient. In the lower panels of Figure 6.2 we see clearly that the weaker the deflagration the higher the density in the central area, where the density declines strongly with increasing r. In agreement with the considerations of the bound masses, we see that for models with $N_{\mathrm{k}} \geq 200$ there is no appreciable rise in the density in the vicinity of the center. The density profile here simply follows the expected behavior of a spherically free expansion of an object

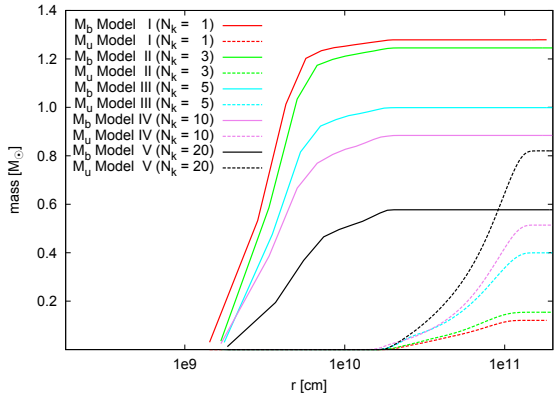

(a) M_b and M_u for weak deflagrations.

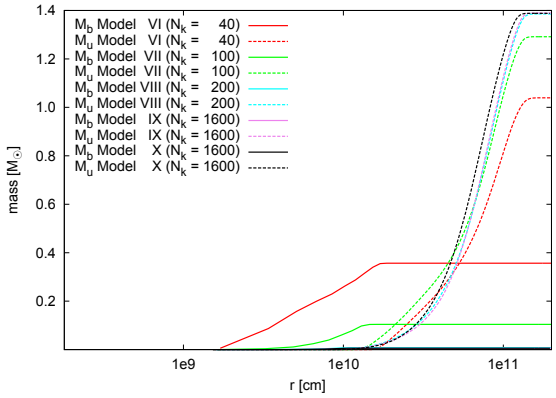

(b) M_b and M_u for strong deflagrations.

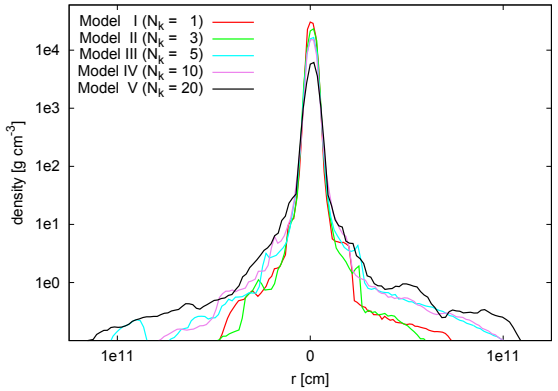

(c) Density profile for weak deflagrations.

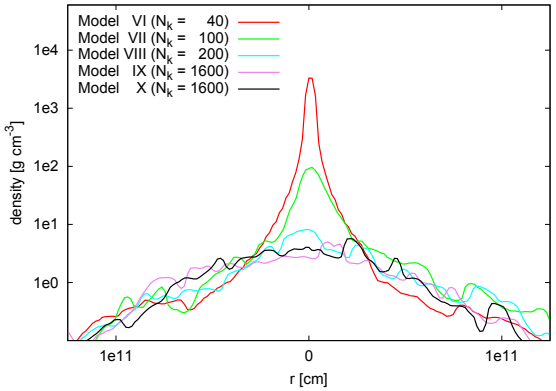

(d) Density profile for strong deflagrations.

Fig. 6.2: (a/b) Bound masses M_b and unbound masses M_u as function of the distance r to the center of the white dwarf for weak and strong deflagrations. (c/d) A cross section of the density through the x-y plane through the center of the white dwarf as function of r for weak and strong deflagrations.

that dilutes in direction outward.

In Figure 6.3(b) the average radial velocity $\bar{v}_\mathrm{rad}(r)$ of Model II and Model X are shown as function of $r/\Delta(t)$, for different instants of time. Here $\Delta(t)$ refers to the grid resolution of the corresponding simulation.[2] We see in the temporal evolution of Model II that for earlier times, greater negative values of $\bar{v}_\mathrm{rad}(r)$ are obtained for small distances r. At these distances the gravitation forces the stellar material to fall back toward the center of the exploding star with a velocity of approximately $\bar{v}_\mathrm{rad}(r)$. At later times this effect becomes weaker and the curves flatten out for small distances, so that $\bar{v}_\mathrm{rad}(r) \approx 0$. With larger distances the curve shapes of Model II become similar to the curves of Model X. For the latter we obtain a linear slope of the curves for the times shown in the figure, which reflects the behavior of a free expansion. We note that for large r we reach the outer inhomogeneous part of the grid (see Section 4.1.1), where $\Delta(t)$ becomes a function of r itself. However, all curves in Figure 6.3(b) show the behavior $v_\mathrm{rad}(r) \propto r$ already at a certain distance (Model II) or for all distances (Model X) on the homogeneous inner grid, which consequently holds for larger r. Therefore,

[2]The normalization of r onto the time-dependent grid resolution $\Delta(t)$ of the corresponding simulation is done to account for the different grid expansions in the simulations at different instants of time.

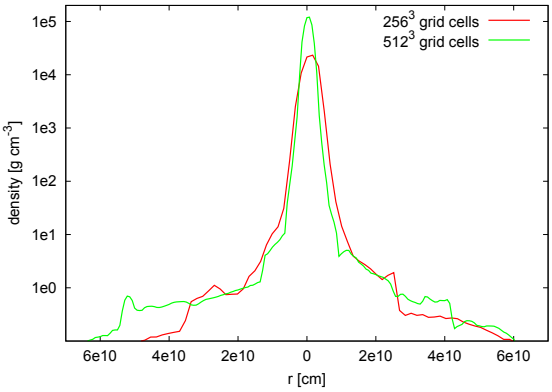

(a) Density profiles of Model II using a resolution of 256^3 and 512^3 grid cells.

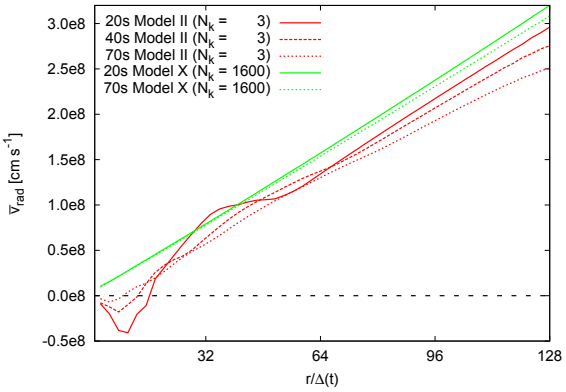

(b) Average radial velocities $\bar{v}_{\rm rad}(r)$ of Model II and Model X.

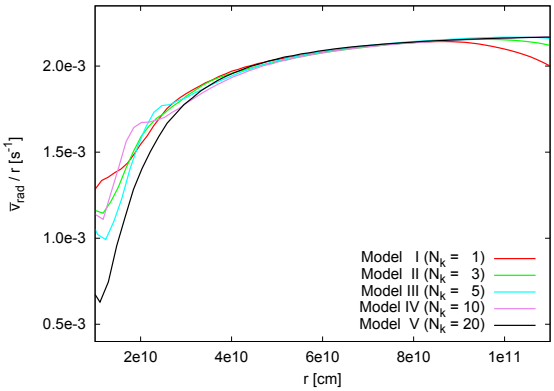

(c) $\bar{v}_{\rm rad}(r)/r$ as function of r for weak deflagrations.

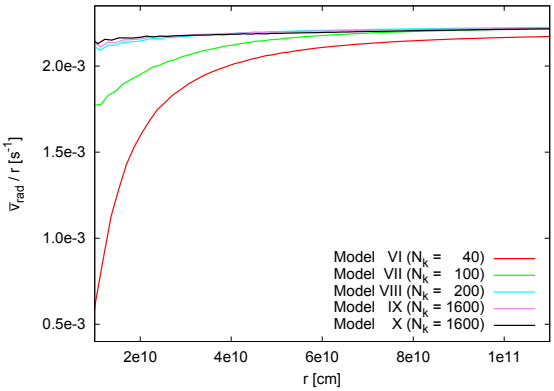

(d) $\bar{v}_{\rm rad}(r)/r$ as function of r for strong deflagrations.

Fig. 6.3: (a) Resolution dependence of the central density at $t = 100\,\mathrm{s}$ of Model II. (b) Comparison of the average radial velocities $\bar{v}_{\rm rad}(r)$ as function of $r/\Delta(t)$ of Model II and Model X for different instants of time. (c/d) The ratio of the average radial velocity $\bar{v}_{\rm rad}(r)$ to r as function of r for weak and strong deflagrations.

the entire inhomogeneous grid simply follows the free expansion of the outer layers of the white dwarf. This is why a transition effect in Figure 6.3(b) between both parts of the grid is not expected (and indeed not observed) with the above-described normalization.

In the lower panels of Figure 6.3 the ratio of $\bar{v}_{\rm rad}(r)$ to r as function of r is shown. Since for a free expansion $\bar{v}_{\rm rad}(r)/r = \mathrm{const}$, the corresponding curve will appear as a line parallel to the abscissa. We find in agreement with the previous considerations that this behavior is most dominating in strong deflagrations with $N_{\rm k} \geq 200$. For these models the curves are almost indistinguishable, which results from the fact that pure deflagrations of models in which the white dwarf becomes completely unbound have similar expansion velocities.

6.2.2 The turbulent energy and the flame surface area

The overall turbulent energy $E_{\rm turb}$ on unresolved scales (the so-called *subgrid-scale energy*) is shown as function of time in Figure 6.4. We note that $E_{\rm turb}$ is determined by the generation of turbulent energy but also by the expansion of the grid. With increasing $\Delta(t)$ more turbulent motions fall below the grid resolution and the amount of turbulent energy on unresolved

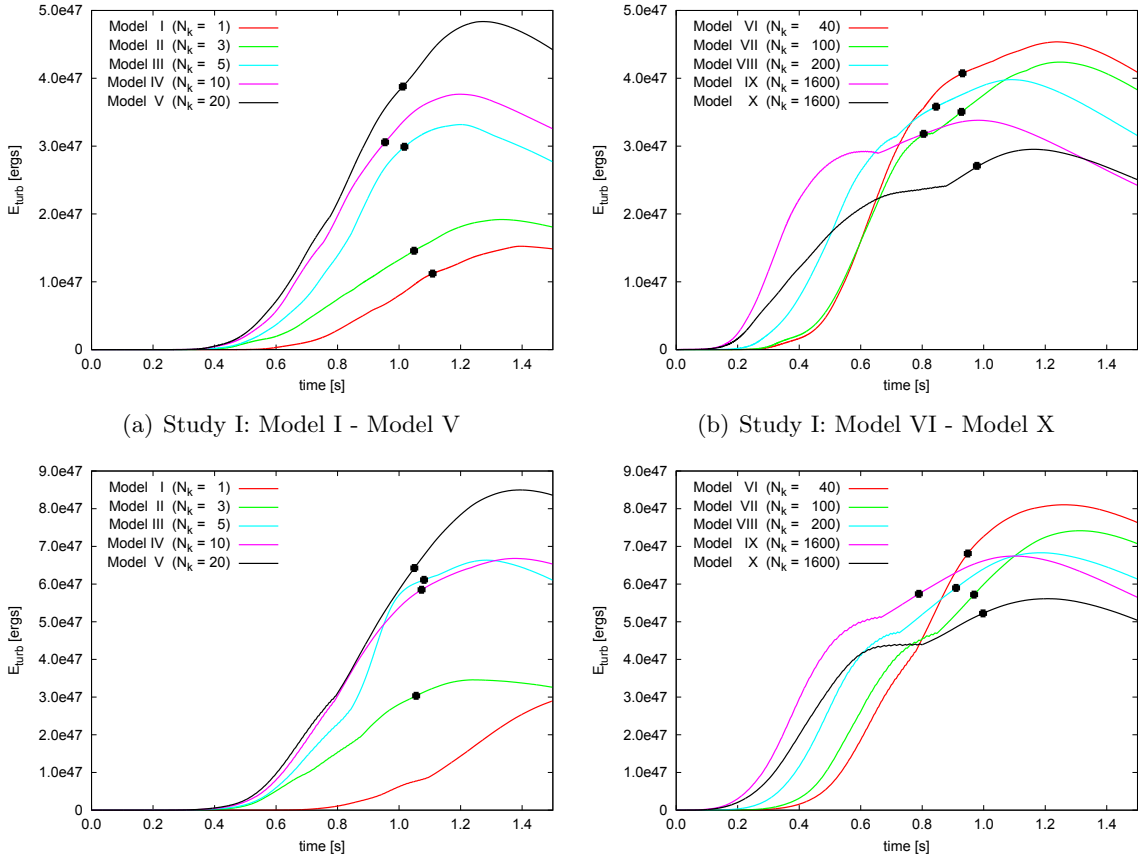

(a) Study I: Model I - Model V

(b) Study I: Model VI - Model X

(c) Study II: Model I - Model V

(d) Study II: Model VI - Model X

Fig. 6.4: Turbulent subgrid-scale energy E_{turb} as function of time in the simulations of pure deflagrations. The first time where the DDT criterion is met is marked with a black dot.

scales consequently increases. For the same reason we find in the higher resolved simulations of Study I lower values of E_{turb}.[3] We see in Figure 6.4 that in the early explosion phase E_{turb} is higher for stronger deflagrations. For models with $N_{\mathrm{k}} \leq 20$ the faster growth rate of E_{turb} is associated with a larger maximum of this quantity (see left panels of Figure 6.4). In contrast to these weak deflagrations, we find for models with $N_{\mathrm{k}} > 20$ that the initially

[3] To estimate the turbulent energy on a certain fixed length scale, such as ℓ_{crit}, one could rescale this energy from $\Delta(t)$ to ℓ_{crit}. This is similar to the rescaling procedure of the velocity fluctuations from $v'(\Delta(t))$ to $v'(\ell_{\mathrm{crit}})$ (equation (5.11)). However, in Section 5.2.3 we argued that there are some uncertainties in the rescaling of the velocity field. In the case of the turbulent energy, these uncertainties become even larger, since the latter scales with $v'(\Delta(t))^2$. Therefore, we do not consider the turbulent energy on a fixed unresolved length scale. We further note that E_{turb} represents the turbulent energy in the whole exploding white dwarf but for the DDT model we are mainly interested in the turbulent velocity fluctuations in the vicinity of the flame only. This is why Figure 5.10 is more important than Figure 6.4 for our study. Since the former shows the rescaled velocity fluctuations $v'(\ell_{\mathrm{crit}})$ (and not $v'(\Delta(t))$), different grid expansions play no role here.

When we assume that turbulence at the flame is similar to turbulence in all other regions of the white dwarf (particularly in ash regions) we can indirectly see the effect of the different grid expansion for several models by comparing Figure 6.4 with Figure 5.10. For instance, we see in Figure 5.10(d) in Model X that turbulence seems to *freeze out* far more rapidly than one would probably expect from Figure 6.4. Obviously the grid expands very fast in this model.

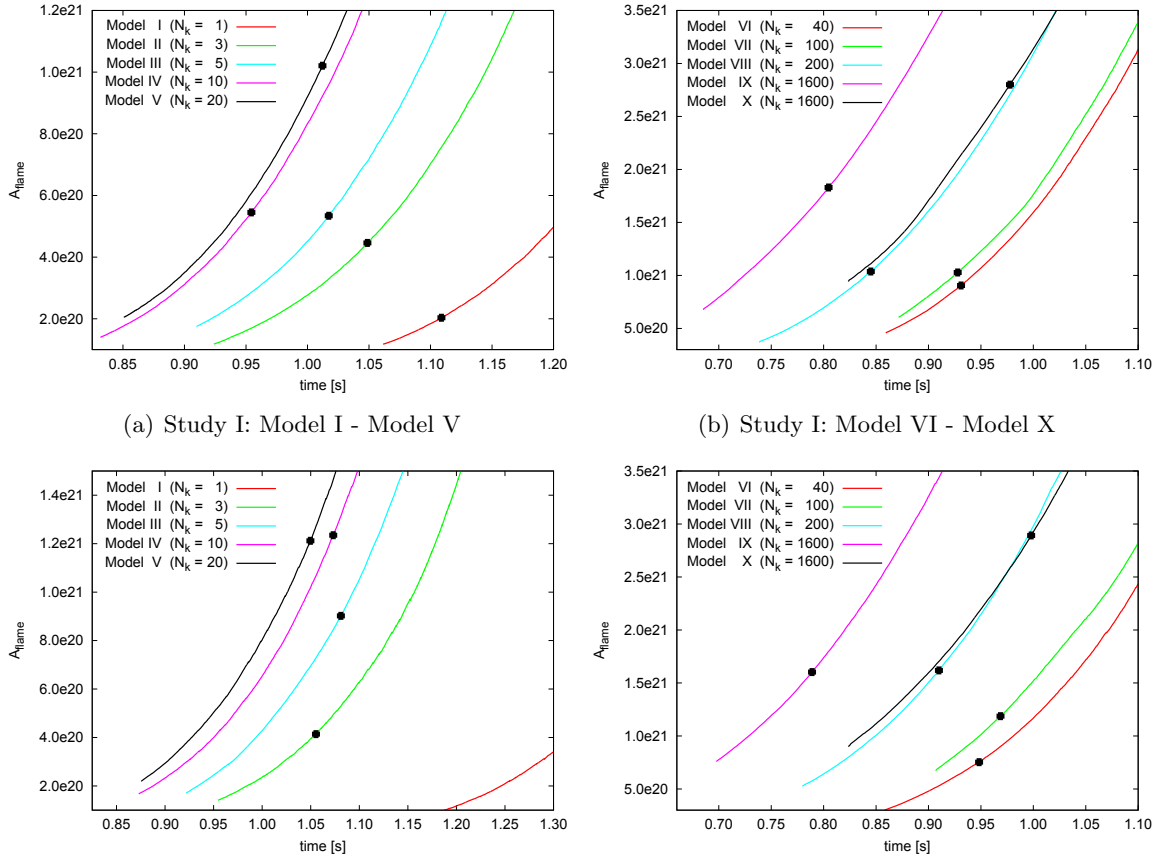

(a) Study I: Model I - Model V

(b) Study I: Model VI - Model X

(c) Study II: Model I - Model V

(d) Study II: Model VI - Model X

Fig. 6.5: Flame surface area $A_{\mathrm{flame}}(t)$ as function of time in the simulations of pure deflagrations. The first time where the DDT criterion is met is marked with a black dot.

faster growth rate of E_{turb} is outrun by models with smaller N_{k} in the late deflagration phase (see right panels of Figure 6.4).

In Figure 6.5 the flame surface area $A_{\mathrm{flame}}(t)$ (calculated with equation (5.4)) is shown as function of time from the time step on where the first grid cells at the flame approach the upper density threshold $\rho_{\mathrm{fuel}}^{\mathrm{max}}$. Except for Model X there is a clear trend that this threshold is reached earlier by the flame for stronger deflagrations. This behavior can be understood with the quantity E_{nuc} in Figure 6.1. Models with large E_{nuc} show an early large expansion of the white dwarf that in turn results in a fast decline of ρ_{fuel}. If we compare the slopes of the curves in Figure 6.5 we further find a faster growth rate of $A_{\mathrm{flame}}(t)$ with time for stronger deflagrations, which is mainly related to a faster expansion of the grid. Remarkable is the good agreement of $A_{\mathrm{flame}}(t)$ for equal models that are simulated in Study I and Study II with different resolutions (compare the upper with the lower panels of Figure 6.5). This indicates once more that the choice of a fractal dimension of $D = 2.36$ of the flame seems to be appropriate. An exception, however, is Model I that shows a very slow growth rate of $A_{\mathrm{flame}}(t)$ in Study II. We find that this model has a relatively small number of grid cells at the flame in both studies. Furthermore, a certain resolution dependence can be generally expected for models with $N_{\mathrm{k}} = 1$, since in a deflagration that evolves from a single spherical ignition kernel, there are no defined seeds for instabilities to arise. Due to buoyancy effects,

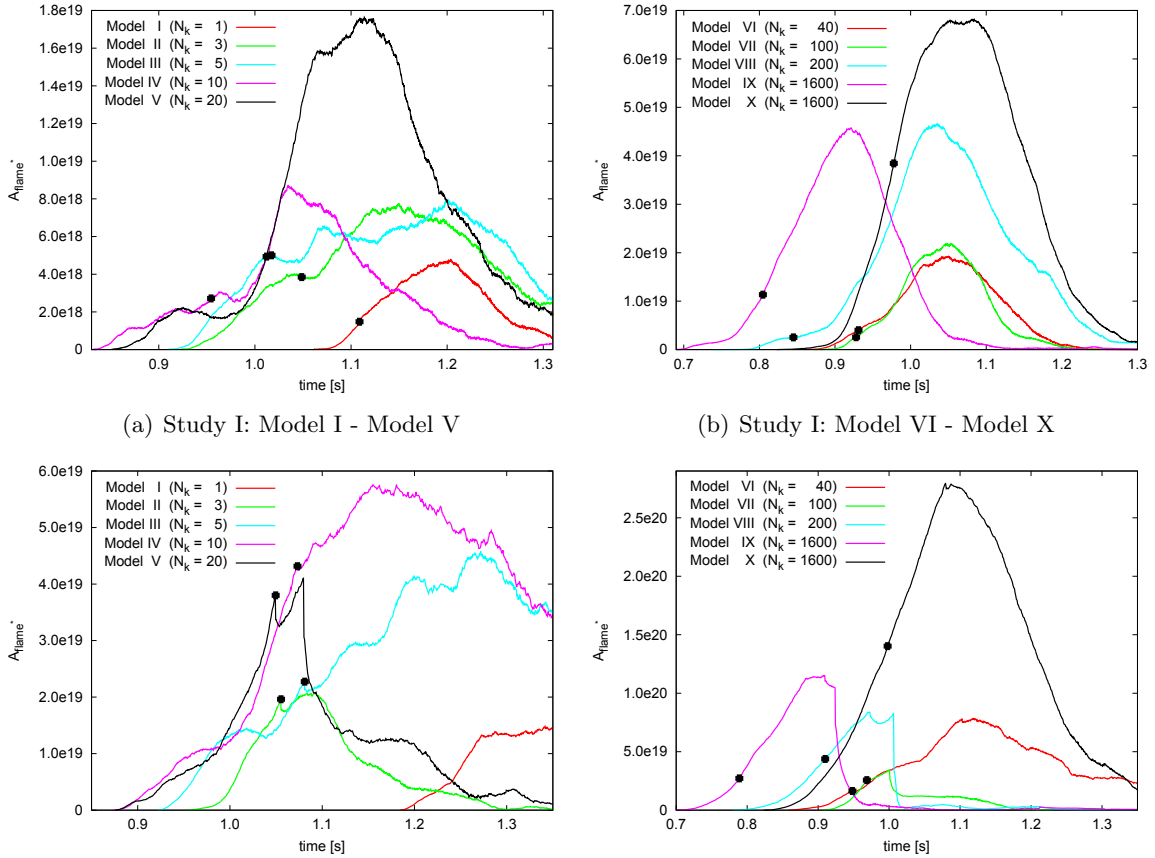

(a) Study I: Model I - Model V

(b) Study I: Model VI - Model X

(c) Study II: Model I - Model V

(d) Study II: Model VI - Model X

Fig. 6.6: The part of the flame surface area $A^*_{\text{flame}}(t)$ that meets the DDT constraints concerning the quantities ρ_{fuel} and X_{fuel} as function of time in the simulations of delayed detonations. The time $t^{\text{1st}}_{\text{DDT}}$ of the first DDT is marked with a black dot.

a deflagration bubble rises and at some point numerical noise in the simulation leads to instabilities at this bubble until we obtain the usual picture of a turbulent disturbed flame. The numerical noise in turn depends on the grid discretization (and hence on the resolution of the simulation).

In Figure 6.6 the flame surface area $A^*_{\text{flame}}(t)$ (calculated with equation (5.4) with $N^*_{\text{flame}}(t)$ instead of $N_{\text{flame}}(t)$) is shown as function of time. In contrast to the previous considerations in this study, these are the results of the simulated delayed detonations, in which detonations are initialized when the DDT criterion is met. Since $A_{\text{flame}}(t)$ is larger for stronger deflagrations, the quantity $A^*_{\text{flame}}(t)$ has also the tendency to be larger in the corresponding models, since there is a larger flame surface area that may additionally meet the necessary constraints concerning ρ_{fuel} and X_{fuel}. However, we have to take into account that a strong aspherical flame propagation can lead to the effect that there may be always only a small part of the entire flame surface area that can meet the constraint for ρ_{fuel} at the same time, leading on average to lower values of $A^*_{\text{flame}}(t)$. As shown later the flame evolves more asymmetric in our models that show a weaker deflagration. In Study II the values of $A^*_{\text{flame}}(t)$ of the models are significantly higher than in Study I, which results from a larger part of the flame that meets the larger allowed ranges of X_{fuel} and ρ_{fuel}. However, we also find in Study II

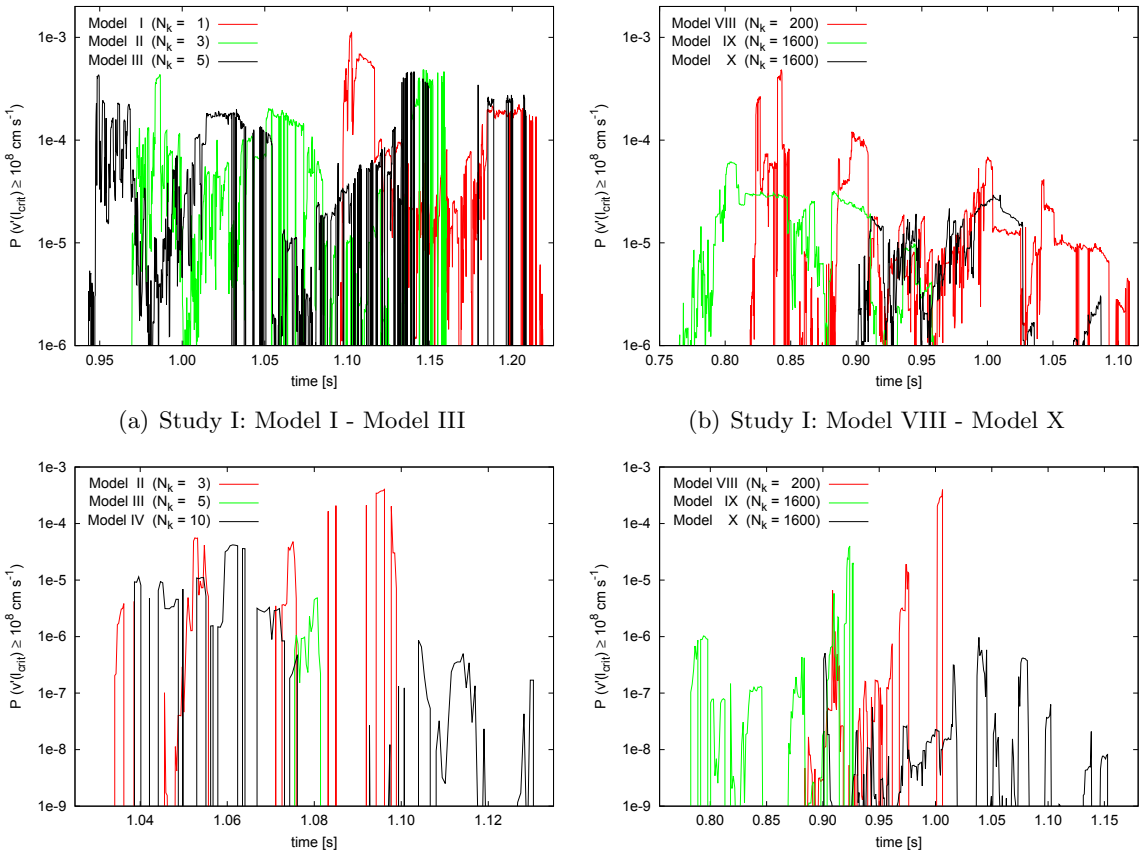

(a) Study I: Model I - Model III

(b) Study I: Model VIII - Model X

(c) Study II: Model II - Model IV

(d) Study II: Model VIII - Model X

Fig. 6.7: The probability $P(v'(\ell_{\mathrm{crit}}) \geq 10^8\,\mathrm{cm\ s^{-1}})(t)$ of finding velocity fluctuations $v'(\ell_{\mathrm{crit}})$ on the scale ℓ_{crit} of at least $10^8\,\mathrm{cm\ s^{-1}}$ at the flame as function of time for weak deflagrations (left panels) and strong deflagrations (right panels) for both studies.

that $N^*_{\mathrm{flame}}(t)$ is too small in Model I to construct and fit a reliable histogram of $v'(\ell_{\mathrm{crit}})$ in the entire simulation. Therefore the DDT model could not be applied here.

6.2.3 The behavior of the DDT model in different deflagrations

In Figure 6.7 the probability $P(v'(\ell_{\mathrm{crit}}) \geq 10^8\,\mathrm{cm\ s^{-1}})(t)$ (equation (5.14)) is shown as function of time for weak ($N_{\mathrm{k}} \leq 10$) and strong deflagrations ($N_{\mathrm{k}} \geq 200$).[4] We obtain as a surprising result that the probability of finding velocity fluctuations $v'(\ell_{\mathrm{crit}})$ on the scale ℓ_{crit} of at least $10^8\,\mathrm{cm\ s^{-1}}$ at the flame is higher for weak deflagrations. In addition, it seems that for weak deflagrations the quantity $P(v'(\ell_{\mathrm{crit}}) \geq 10^8\,\mathrm{cm\ s^{-1}})(t)$ varies much stronger with time that becomes apparent in sharp maxima and narrow widths of the curves in the left panels of Figure 6.7.

In Figure 6.8 the quantity $A_{\mathrm{det}}(t)$ (equation (5.15)) is shown as function of time together with the threshold value of A_{crit}. There is obviously no clear conclusion, of whether A_{crit} is reached easier for specific models. The reason lies in a compensation effect that is based on the described behavior of the quantities $A^*_{\mathrm{flame}}(t)$ and $P(v'(\ell_{\mathrm{crit}}) \geq 10^8\,\mathrm{cm\ s^{-1}})(t)$. Weak

[4] Since no values are available for Model I in Study II the analysis begins with Model II for this study.

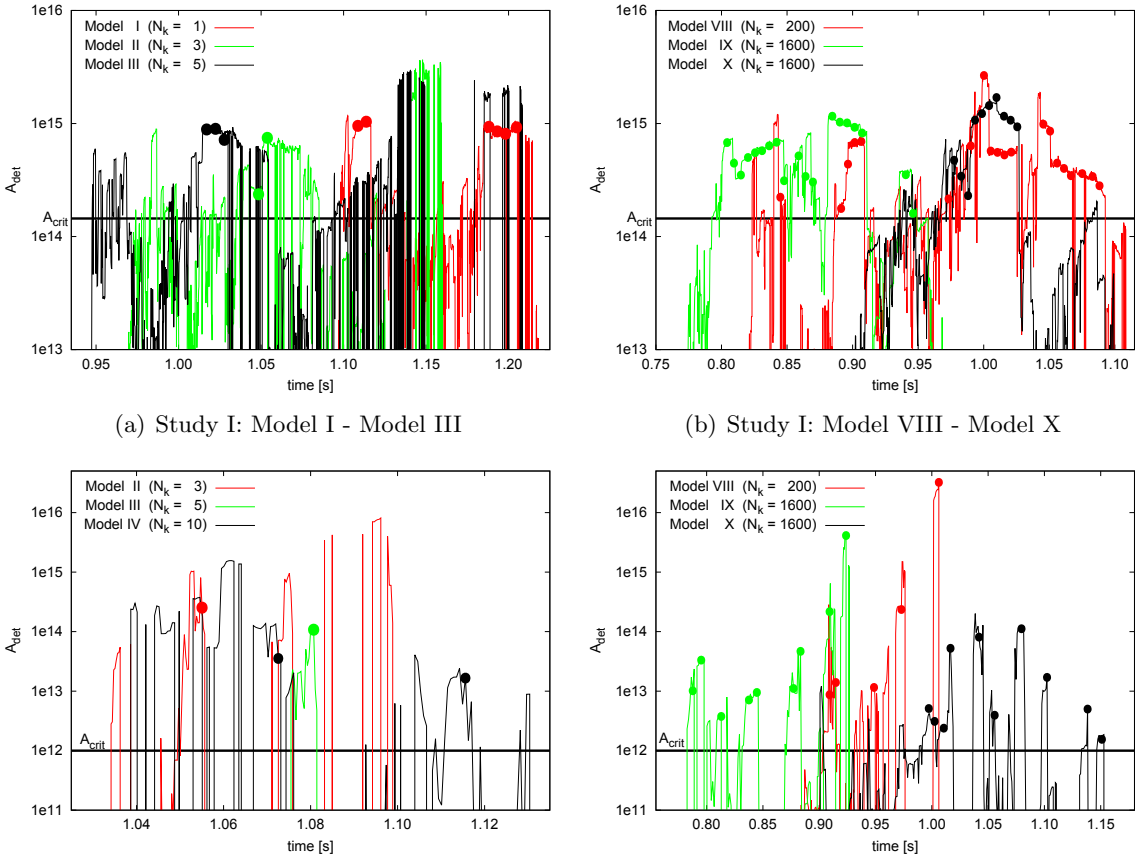

(a) Study I: Model I - Model III

(b) Study I: Model VIII - Model X

(c) Study II: Model II - Model IV

(d) Study II: Model VIII - Model X

Fig. 6.8: The potential detonation area $A_{\text{det}}(t)$ as function of time for weak deflagrations (left panels) and strong deflagrations (right panels) for both studies. The times t_{DDT} where DDTs occur are marked with dots.

deflagrations have higher values of $P(v'(\ell_{\text{crit}}) \geq 10^8\,\text{cm s}^{-1})(t)$ but lower values of $A^*_{\text{flame}}(t)$, hence there are higher velocity fluctuations located in a relatively small flame surface area that meets the DDT constraints concerning the quantities X_{fuel} and ρ_{fuel}. The opposite holds for strong deflagrations, where lower velocity fluctuations are located in a significantly larger flame surface area that meets the DDT constraints. In Figure 6.9 the ratio of $A_{\text{det}}(t)$ to $A_{\text{flame}}(t)$ is shown as function of time. There is a clear tendency that this ratio is higher for weak deflagrations. This indicates that for weak deflagrations, the strong turbulence and the small flame surface area lead to the effect that on average a significant part of the entire flame is capable of performing a DDT.

In Figure 6.8 we see that $A_{\text{det}}(t) \geq A_{\text{crit}}$, hence DDTs occur if this conditions holds for at least $\tau_{\text{eddy}_{1/2}}(\ell_{\text{crit}})$. In Figure 6.10 the measured time $t_{(A_{\text{det}}(t) \geq A_{\text{crit}})}$ for which the condition $A_{\text{det}}(t) \geq A_{\text{crit}}$ holds is shown as function of time together with the threshold value of $\tau_{\text{eddy}_{1/2}}(\ell_{\text{crit}})$. Since $t_{(A_{\text{det}}(t) \geq A_{\text{crit}})} \geq \tau_{\text{eddy}_{1/2}}(\ell_{\text{crit}})$, DDTs occur in all models. The total number of time steps $N_{\text{t}_{\text{DDT}}}$ where DDTs occur is given by the number how often the quantity $t_{(A_{\text{det}}(t) \geq A_{\text{crit}})}$ crosses the threshold value $\tau_{\text{eddy}_{1/2}}(\ell_{\text{crit}})$, approaching from the lower part of the curve. The number of DDTs F_{DDT} that occur at the time t_{DDT} when $t_{(A_{\text{det}}(t) \geq A_{\text{crit}})} \geq \tau_{\text{eddy}_{1/2}}(\ell_{\text{crit}})$ is given by the current ratio of $A_{\text{det}}(t = t_{\text{DDT}})$ to A_{crit} (see Section 5.3.2).

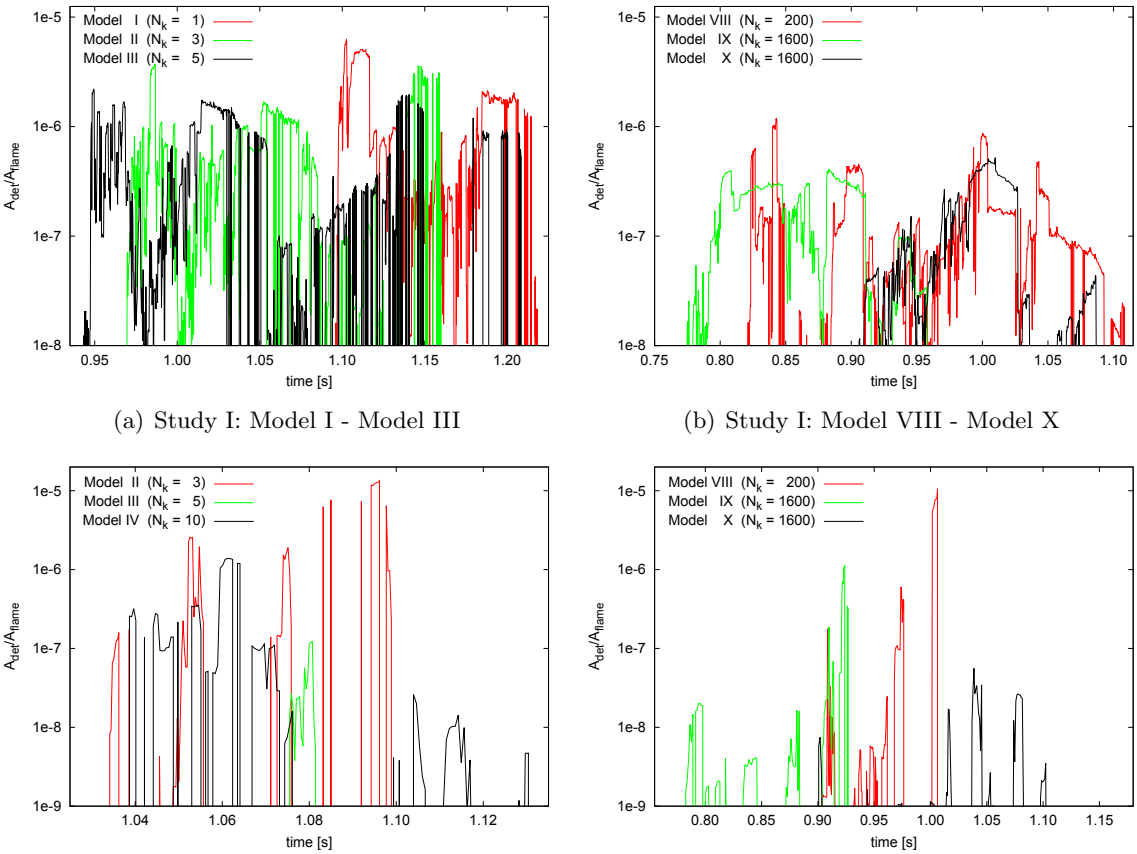

(a) Study I: Model I - Model III

(b) Study I: Model VIII - Model X

(c) Study II: Model II - Model IV

(d) Study II: Model VIII - Model X

Fig. 6.9: The ratio of the potential detonation area $A_{\mathrm{det}}(t)$ to the entire flame surface area $A_{\mathrm{flame}}(t)$ as function of time for weak deflagrations (left panels) and strong deflagrations (right panels) for both studies.

At each time when $t_{(A_{\mathrm{det}}(t) \geq A_{\mathrm{crit}})} \geq \tau_{\mathrm{eddy}_{1/2}}(\ell_{\mathrm{crit}})$ the time measurement $t_{(A_{\mathrm{det}}(t) \geq A_{\mathrm{crit}})}$ is reset. The condition $A_{\mathrm{det}}(t) \geq A_{\mathrm{crit}}$ will still hold in most cases, so that the quantity $t_{(A_{\mathrm{det}}(t) \geq A_{\mathrm{crit}})}$ immediately begins to rise again, causing eventually a further DDT provided that the constraint $t_{(A_{\mathrm{det}}(t) \geq A_{\mathrm{crit}})} \geq \tau_{\mathrm{eddy}_{1/2}}(\ell_{\mathrm{crit}})$ can be met again. This procedure may repeat several times, leading to certain oscillations of the quantity $t_{(A_{\mathrm{det}}(t) \geq A_{\mathrm{crit}})}$, which can be seen for instance in Figure 6.10(b).

In Figure 6.8 the times t_{DDT} are additionally marked with dots at the curves of $A_{\mathrm{det}}(t)$. We find in most cases that DDTs occur when $A_{\mathrm{det}}(t)$ has local maxima. From the Figures 6.8 and 6.10 we derive the trend that $N_{\mathrm{t_{DDT}}}$ is larger for stronger deflagrations, but for models with very large N_{k} in Study I, $N_{\mathrm{t_{DDT}}}$ decreases again. In Figure 6.10 we see some values of $t_{(A_{\mathrm{det}}(t) \geq A_{\mathrm{crit}})}$ that may exceed $\tau_{\mathrm{eddy}_{1/2}}(\ell_{\mathrm{crit}})$ to a certain degree. The reason is that particularly for the lower resolved simulations of Study II, the simulation time steps become only about one order of magnitude shorter than $\tau_{\mathrm{eddy}_{1/2}}(\ell_{\mathrm{crit}})$ (see Section 5.3.3).

6.2.4 The onset of DDTs and the evolution of detonations

The ignition geometries of the deflagration of the models are shown in Figure 4.2. Except for Model I, the spherical flame kernels burn their way outward through the stellar material

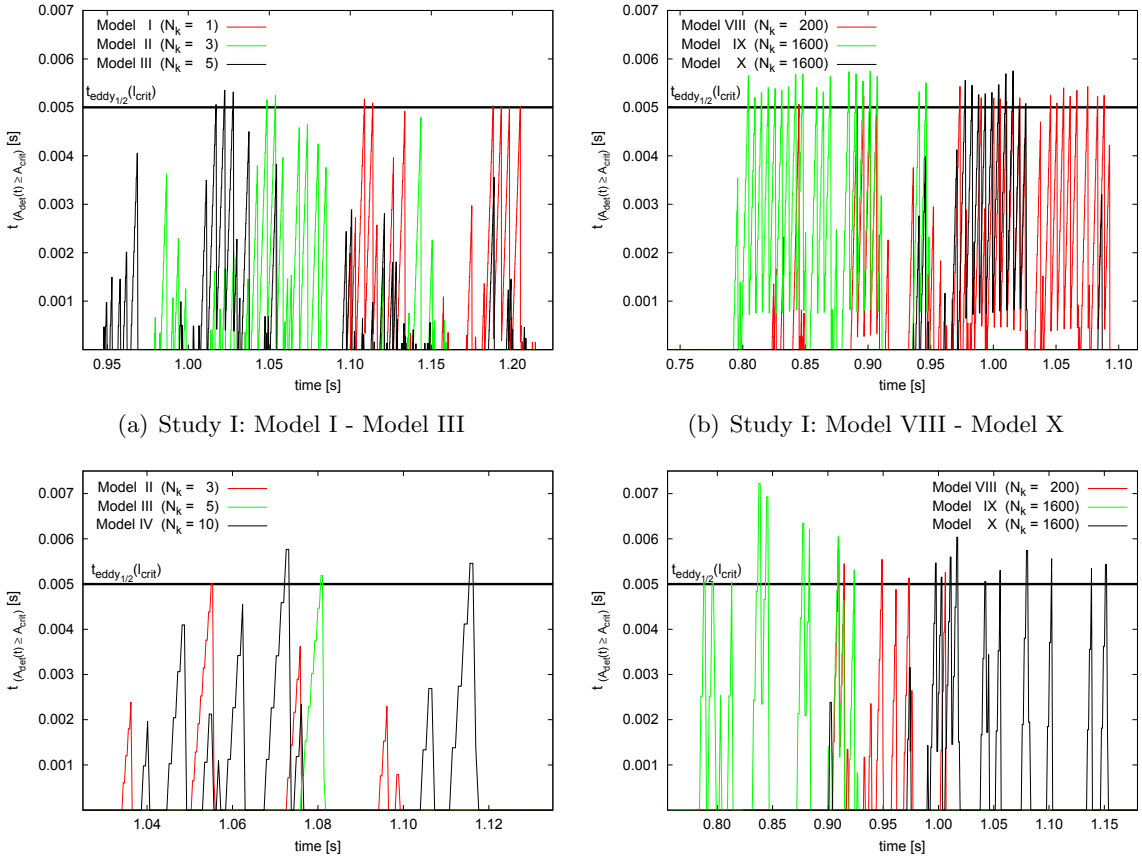

(a) Study I: Model I - Model III

(b) Study I: Model VIII - Model X

(c) Study II: Model II - Model IV

(d) Study II: Model VIII - Model X

Fig. 6.10: The measured time $t_{(A_{\mathrm{det}}(t) \geq A_{\mathrm{crit}})}$ for $A_{\mathrm{det}}(t) \geq A_{\mathrm{crit}}$ as function of time for weak deflagrations (left panels) and strong deflagrations (right panels) for both studies. At each time when $t_{(A_{\mathrm{det}}(t) \geq A_{\mathrm{crit}})} \geq \tau_{\mathrm{eddy}_{1/2}}(\ell_{\mathrm{crit}})$ detonations are initialized and the time measurement $t_{(A_{\mathrm{det}}(t) \geq A_{\mathrm{crit}})}$ is reset (see also Section 5.3.1).

and come in contact with other propagating flame kernels until they all merge into a single large deflagration front that moves toward the surface of the white dwarf. The larger N_{k} the faster is the merger process of the flame kernels in our ten standard ignition models (see discussion in Section 4.2.2). In Model I in contrast, a single deflagration bubble rises asymmetrically and burns only a marginal fraction of the fuel of the white dwarf to heavier elements.

In the Figures 6.11 and 6.12 the onset of the first DDTs and the evolution of the detonations are shown for Model III, Model VII and Model X of Study I and for Model II, Model VIII and Model X of Study II, respectively. The propagation of the deflagration and detonation fronts are each represented by a corresponding level set (see Section 4.1.1). In the Figures 6.11(a-c) and 6.12(a-c) the time $t_{\mathrm{DDT}}^{\mathrm{1st}}$ of the first DDT is shown, where the initialized detonations (resp. the DDT regions) are encircled at the deflagration flame. The latter is visualized in a transparent blue to obtain a clear view.[5] There are some interesting features

[5] We note that there is only a slight resolution dependence of the deflagration phase and the deflagration flame in Model X in the Figures 6.11(c) and 6.12(c) appears only different due to another viewing angle in order to present the DDT regions clearer.

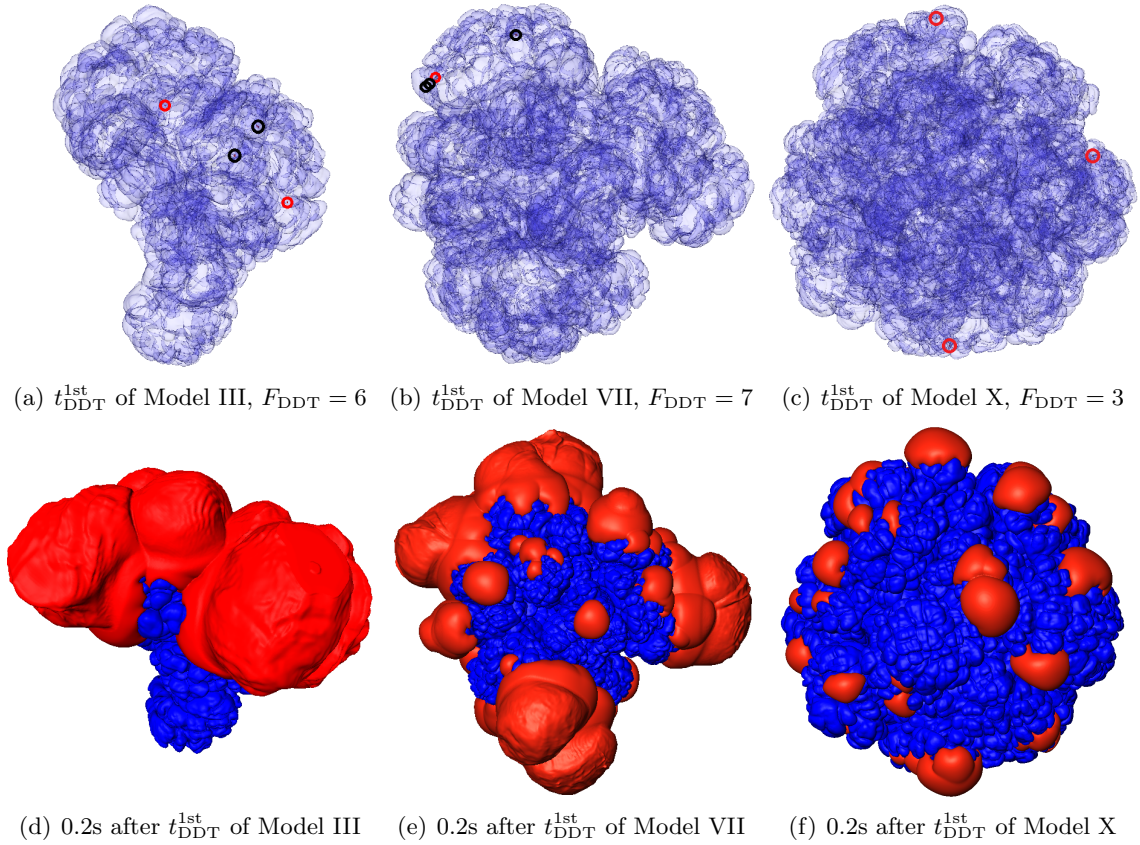

(a) $t^{\mathrm{1st}}_{\mathrm{DDT}}$ of Model III, $F_{\mathrm{DDT}} = 6$ (b) $t^{\mathrm{1st}}_{\mathrm{DDT}}$ of Model VII, $F_{\mathrm{DDT}} = 7$ (c) $t^{\mathrm{1st}}_{\mathrm{DDT}}$ of Model X, $F_{\mathrm{DDT}} = 3$

(d) 0.2s after $t^{\mathrm{1st}}_{\mathrm{DDT}}$ of Model III (e) 0.2s after $t^{\mathrm{1st}}_{\mathrm{DDT}}$ of Model VII (f) 0.2s after $t^{\mathrm{1st}}_{\mathrm{DDT}}$ of Model X

Fig. 6.11: Delayed detonations in Model III, Model VII and Model X of Study I (not to scale). Shown are the deflagration level set (blue) and the detonation level set (red). (a-c) The time $t^{\mathrm{1st}}_{\mathrm{DDT}}$ of the first DDT. Initialized detonations at the deflagration flame are encircled in red (DDT in a single grid cell) or black (DDTs in multiple connected grid cells). (d-f) 0.2 seconds after the first DDT. Several detonation fronts evolve from the DDT spots and burn the surrounding fuel to heavier elements.

that can be seen from these figures. First we observe an asymmetric flame propagation of the weak deflagrations in Model II and Model III. In addition, we find that the DDT regions are mostly not located on top of the mushroom cap like structures that occur due to the influence of the RT instability, but in trailing edges and crevices between these structures where the KH instability dominates the turbulent motions. Finally, we see that DDTs occur frequently in regions that are composed of more connected grid cells. Such regions are found, for instance, at the time $t^{\mathrm{1st}}_{\mathrm{DDT}}$ in the shown models III and VII of Study I, as well as in all models of Study II. In the Figures 6.11(a-c) and 6.12(a-c) these DDT regions are marked with black circles, while DDTs in single grid cells are marked with red circles.

In the Figures 6.11(d-f) and 6.12(d-f) the time 0.2 seconds after $t^{\mathrm{1st}}_{\mathrm{DDT}}$ is shown. Here the detonation fronts are visualized in red and the deflagration fronts in opaque blue. Except for Model II in Study II of the shown models, additional DDTs at other places at the deflagration flame have occurred up to this time, since the DDT criterion stays fulfilled for most of the time (see Figure 6.8) and because $\tau_{\mathrm{eddy}_{1/2}}(\ell_{\mathrm{crit}}) \gg 0.2\,\mathrm{s}$.

Similar to the ignition of the deflagration, the detonation fronts evolve from single DDT regions and come in contact with each other. The collisions and the merger of detonation

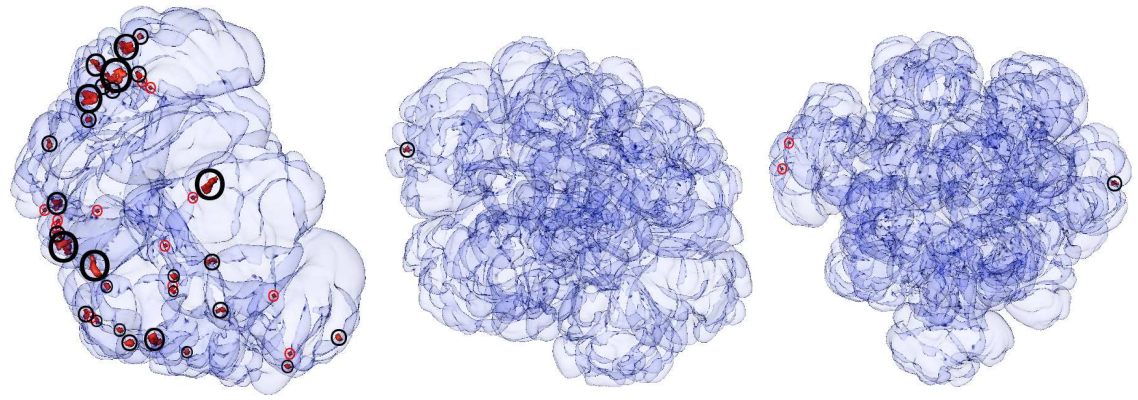

(a) $t_{\mathrm{DDT}}^{\mathrm{1st}}$ of Model II, $F_{\mathrm{DDT}} = 257$ (b) $t_{\mathrm{DDT}}^{\mathrm{1st}}$ of Model VIII, $F_{\mathrm{DDT}} = 8$ (c) $t_{\mathrm{DDT}}^{\mathrm{1st}}$ of Model X, $F_{\mathrm{DDT}} = 5$

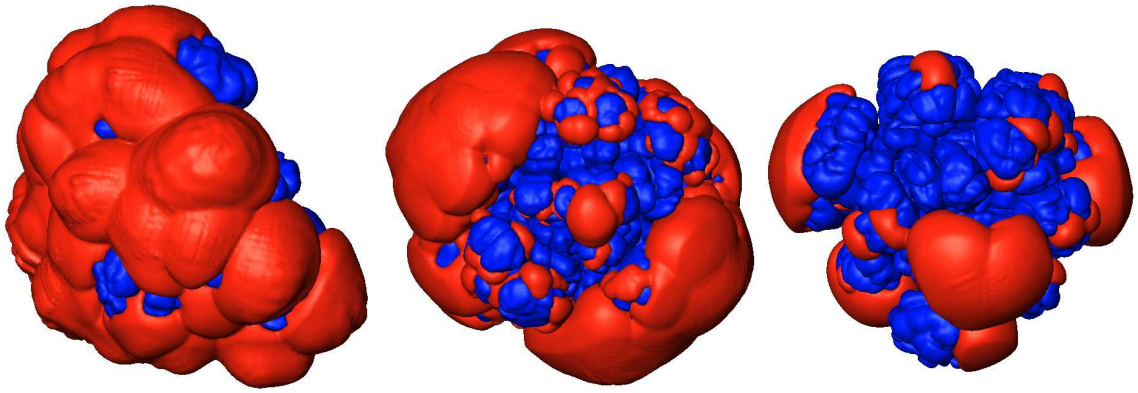

(d) 0.2s after $t_{\mathrm{DDT}}^{\mathrm{1st}}$ of Model II (e) 0.2s after $t_{\mathrm{DDT}}^{\mathrm{1st}}$ of Model VIII (f) 0.2s after $t_{\mathrm{DDT}}^{\mathrm{1st}}$ of Model X

Fig. 6.12: Delayed detonations in Model II, Model VIII and Model X of Study II (not to scale). Shown are the deflagration level set (blue) and the detonation level set (red). (a-c) The time $t_{\mathrm{DDT}}^{\mathrm{1st}}$ of the first DDT. Initialized detonations at the deflagration flame are encircled in red (DDT in a single grid cell) or black (DDTs in multiple connected grid cells). (d-f) 0.2 seconds after the first DDT. Several detonation fronts evolve from the DDT spots and burn the surrounding fuel to heavier elements.

fronts happen very fast, in particular for weak deflagrations. In the shown Model II and Model III the detonations have been advanced so far that a single detonation front has almost enclosed the entire deflagration flame. From a physical point of view this indicates that detonations burn in a very short time a lot of the remaining fuel to heavier elements. In Model VII and Model VIII we can still identify some isolated detonation fronts. Finally, for Model X where the expansion of the star at $t_{\mathrm{DDT}}^{\mathrm{1st}}$ is large, the impact of the detonations on the explosion dynamics is relatively weak in both studies. Here, there are many detonation fronts that propagate along the surface of the deflagration flame at low densities. Hence, the additional burning due to detonations is much lower than in the other models.

6.2.5 Obtained masses of chemical species

In the Figures 6.13 and 6.14 the obtained masses of the chemical species that are treated in LEAFS (see Section 4.1.4) are shown as function of time for simulations of delayed detonations for six models of both studies. The times t_{DDT} where DDTs occur are marked with

vertical lines. The masses of the chemical species of all simulations are also summarized in the Tables 6.2 and 6.3, where for the pure deflagrations only the results of the higher resolved simulations are shown. Within the simulations of delayed detonations the highest ^{56}Ni yield is obtained in Study I in Model I with $\approx 1.168\,M_\odot$ and in Study II in Model II with $\approx 1.130\,M_\odot$, respectively. In both studies, the lowest ^{56}Ni yield is obtained in Model X with $\approx 0.423\,M_\odot$ for Study I and $\approx 0.397\,M_\odot$ for Study II, respectively. Therefore, in both studies we obtain a range of brightnesses that is in good agreement with the studies of Contardo et al. (2000), Stritzinger et al. (2006) and Mazzali et al. (2007) (see also Section 2.1.1). However, the maximum in the ^{56}Ni yield in our case is slightly higher than expected for normal SNe Ia. Within the simulations of pure deflagrations, the highest ^{56}Ni yield is obtained in Model VIII with $\approx 0.463\,M_\odot$. Hence, with pure deflagrations we obtain mainly faint events. Model I produces less than $0.1\,M_\odot$ of ^{56}Ni in the pure deflagration. Due to the marginal burning the energy release is so low that a significant part of the star remains gravitationally bound (see Figure 6.2(a)).

Model	IGE $[M_\odot]$	^{56}Ni $[M_\odot]$	IME $[M_\odot]$	^{12}C $[M_\odot]$	^{16}O $[M_\odot]$	^{56}Ni/IGE
I	0.092	0.074	0.019	0.639	0.650	0.804
II	0.141	0.105	0.055	0.577	0.627	0.745
III	0.273	0.210	0.041	0.531	0.555	0.769
IV	0.326	0.246	0.052	0.497	0.526	0.755
V	0.461	0.341	0.078	0.410	0.452	0.740
VI	0.568	0.408	0.087	0.350	0.397	0.718
VII	0.619	0.439	0.098	0.315	0.369	0.709
VIII	0.678	0.463	0.096	0.288	0.339	0.683
IX	0.648	0.415	0.090	0.307	0.356	0.640
X	0.593	0.369	0.096	0.328	0.384	0.622

Table 6.2: Obtained yields of total iron group elements (IGE), ^{56}Ni, intermediate mass elements (IME), ^{12}C and ^{16}O after 100 seconds in the simulations of pure deflagrations for the ten ignition models of Table 4.1 using a resolution of 512^3 grid cells.

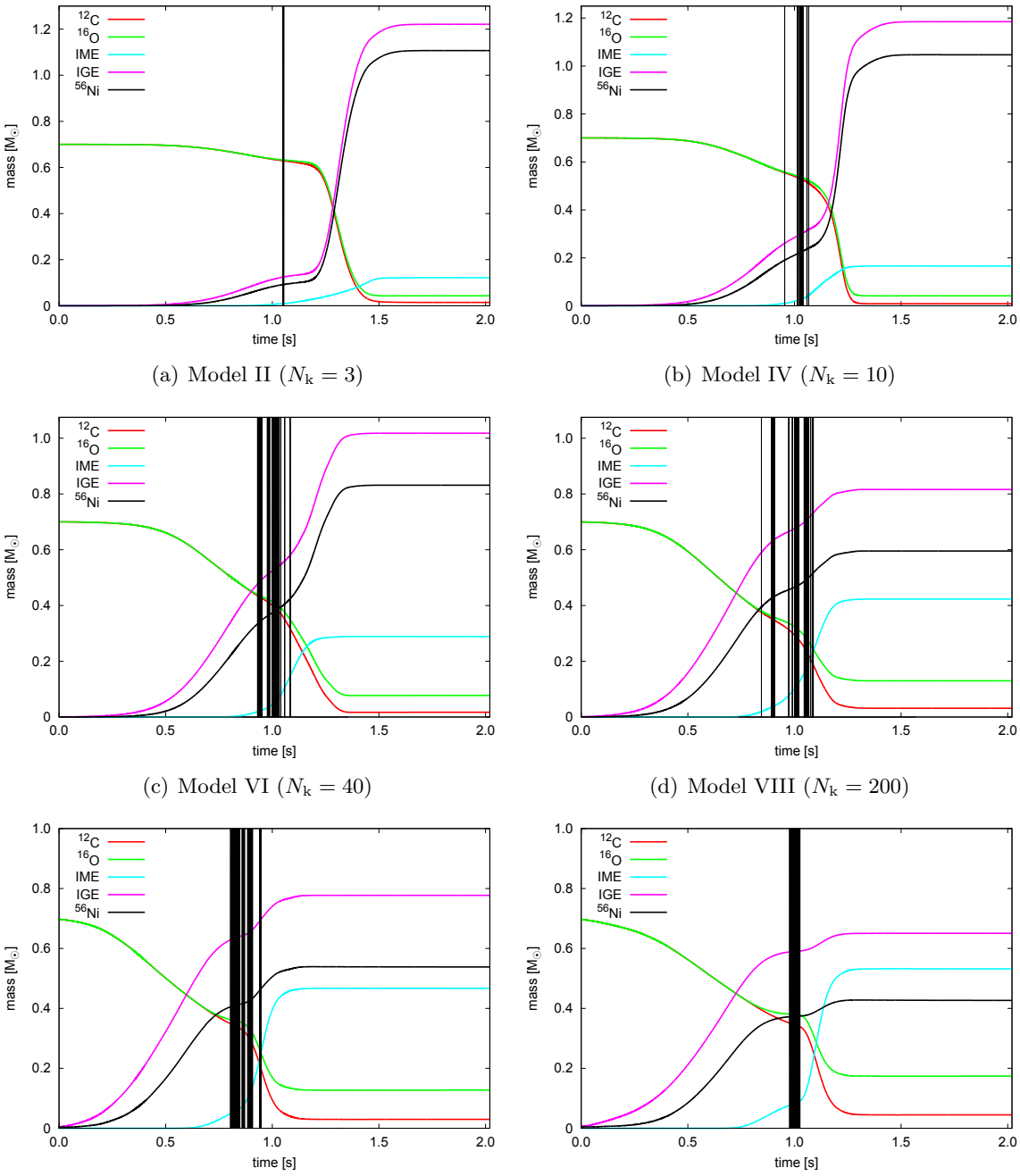

(a) Model II ($N_\mathrm{k} = 3$)

(b) Model IV ($N_\mathrm{k} = 10$)

(c) Model VI ($N_\mathrm{k} = 40$)

(d) Model VIII ($N_\mathrm{k} = 200$)

(e) Model IX ($N_\mathrm{k} = 1600$)

(f) Model X ($N_\mathrm{k} = 1600$)

Fig. 6.13: Obtained yields of chemical species as function of time in simulations of delayed detonations for six models of Study I. Initialized detonations are marked with vertical lines.

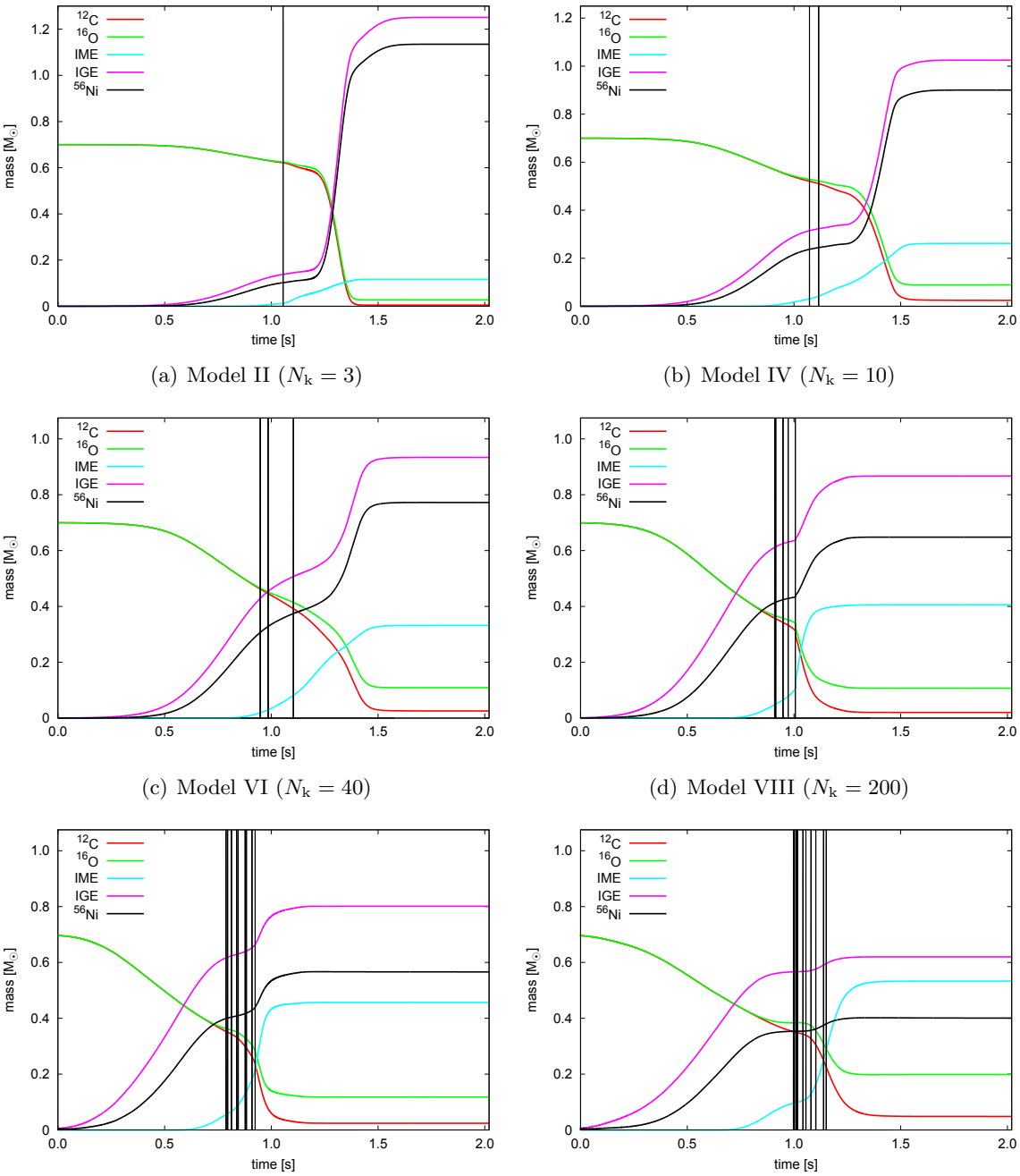

(a) Model II ($N_\mathrm{k} = 3$)

(b) Model IV ($N_\mathrm{k} = 10$)

(c) Model VI ($N_\mathrm{k} = 40$)

(d) Model VIII ($N_\mathrm{k} = 200$)

(e) Model IX ($N_\mathrm{k} = 1600$)

(f) Model X ($N_\mathrm{k} = 1600$)

Fig. 6.14: Obtained yields of chemical species as function of time in simulations of delayed detonations for six models of Study II. Initialized detonations are marked with vertical lines.

Study	Model	$t_{\mathrm{DDT}}^{\mathrm{1st}}$ [s]	$E_{\mathrm{nuc}}^{(t_{\mathrm{DDT}}^{\mathrm{1st}})}$ [ergs]	$F_{\mathrm{DDT}}^{(t_{\mathrm{DDT}}^{\mathrm{1st}})}$	$\sum F_{\mathrm{DDT}}$	$N_{\mathrm{t_{DDT}}}$	$^{56}\mathrm{Ni}^{(t_{\mathrm{DDT}}^{\mathrm{1st}})}$ $[M_\odot]$	IGE $[M_\odot]$	^{56}Ni $[M_\odot]$	IME $[M_\odot]$	^{12}C $[M_\odot]$	^{16}O $[M_\odot]$	^{56}Ni/IGE
I	I	1.109	1.25e50	6 (2)	35	6	0.063	1.291	1.168	0.083	0.005	0.023	0.905
I	II	1.049	2.01e50	1 (1)	6	2	0.092	1.221	1.102	0.121	0.017	0.046	0.903
I	III	1.017	3.49e50	6 (2)	17	3	0.170	1.192	1.062	0.148	0.014	0.049	0.891
I	IV	0.954	3.97e50	30 (3)	94	8	0.198	1.185	1.042	0.165	0.009	0.042	0.879
I	V	1.012	6.02e50	4 (2)	88	12	0.276	1.082	0.918	0.230	0.018	0.072	0.848
I	VI	0.931	7.30e50	3 (1)	64	18	0.334	1.018	0.827	0.288	0.018	0.078	0.812
I	VII	0.928	8.07e50	7 (2)	99	20	0.362	0.990	0.785	0.312	0.017	0.082	0.793
I	VIII	0.845	9.00e50	1 (1)	71	20	0.395	0.816	0.592	0.423	0.032	0.131	0.725
I	IX	0.805	1.03e51	4 (2)	72	19	0.405	0.777	0.534	0.466	0.031	0.128	0.687
I	X	0.978	1.02e51	3 (1)	63	10	0.372	0.650	0.423	0.531	0.046	0.175	0.651
II	II	1.055	2.28e50	257 (14)	257	1	0.102	1.251	1.130	0.116	0.005	0.028	0.903
II	III	1.081	4.21e50	109 (9)	109	1	0.195	1.088	0.966	0.217	0.021	0.075	0.888
II	IV	1.073	5.27e50	36 (2)	52	2	0.237	1.025	0.896	0.262	0.025	0.089	0.874
II	V	1.050	6.43e50	468 (13)	2177	2	0.287	1.098	0.938	0.234	0.011	0.058	0.854
II	VI	0.948	6.62e50	18 (2)	202	3	0.307	0.934	0.768	0.332	0.026	0.110	0.822
II	VII	0.969	8.52e50	413 (7)	2918	2	0.368	1.001	0.799	0.323	0.010	0.067	0.798
II	VIII	0.910	9.99e50	8 (8)	10127	5	0.413	0.867	0.645	0.406	0.021	0.107	0.744
II	IX	0.789	1.02e51	10 (2)	4531	9	0.399	0.801	0.563	0.457	0.025	0.118	0.703
II	X	0.998	1.01e51	5 (3)	282	10	0.353	0.620	0.397	0.533	0.049	0.199	0.640

Table 6.3: Obtained yields of total iron group elements (IGE), ^{56}Ni, intermediate mass elements (IME), ^{12}C and ^{16}O after 100 seconds in the simulations of delayed detonations for the ten ignition models of Table 4.1 for both studies. In addition, the time of the first DDT $t_{\mathrm{DDT}}^{\mathrm{1st}}$, the nuclear energy release $E_{\mathrm{nuc}}^{(t_{\mathrm{DDT}}^{\mathrm{1st}})}$, the number of DDTs $F_{\mathrm{DDT}}^{(t_{\mathrm{DDT}}^{\mathrm{1st}})}$ and the yield of $^{56}\mathrm{Ni}^{(t_{\mathrm{DDT}}^{\mathrm{1st}})}$ at $t_{\mathrm{DDT}}^{\mathrm{1st}}$, as well as the total number of grid cells $\sum F_{\mathrm{DDT}}$ and time steps $N_{\mathrm{t_{DDT}}}$ where DDTs occur are shown. For $F_{\mathrm{DDT}}^{(t_{\mathrm{DDT}}^{\mathrm{1st}})}$ the number of connected grid cells that constitutes the largest DDT region at $t_{\mathrm{DDT}}^{\mathrm{1st}}$ is indicated in brackets.

6.3 Results and Discussion

6.3.1 Delayed detonations and explosion brightnesses

In the performed analysis we find a number of different characteristics that determine the dynamics and brightness of the explosion. The most dominant effect is the degree of expansion of the white dwarf prior to the first DDT. Strong deflagrations that evolve from models with large $N_{\rm k}$ burn out a significant part of the central region of the white dwarf that leads in the early explosion phase to an enhanced production of IGE, and hence ^{56}Ni. In very strong deflagrations, however, the associated early large expansion of the star leads to the effect that the flame soon encounters densities that are not sufficiently high to burn the fuel to IGE anymore. This explains why the ^{56}Ni yield is maximum in Model VIII and lower for Model IX and Model X in pure deflagrations. The described behavior can also be inferred from Figure 6.1, where Model IX and Model X show a higher initial growth rate of the nuclear energy release $E_{\rm nuc}$, but become outrun by Model VIII in the late explosion phase.

In simulations of delayed detonations we see in strong deflagrations only a slight additional burning of the fuel to ^{56}Ni after the onset of detonations (see Table 6.3). The reason is again the large expansion of the star, so that detonations encounter the fuel mainly at low densities that cannot be burned to IGE. In contrast, the expansion in weak deflagrations is much smaller and the white dwarf stays more compact and denser at $t_{\rm DDT}^{\rm 1st}$. Therefore, the detonation fronts propagate through the fuel at higher densities, leading to an enhanced production of IGE.

Compared to pure deflagrations, however, in the simulated delayed detonations the ^{56}Ni yield decreases continuously with increasing $N_{\rm k}$ without exception. We have to keep in mind, however, that Model IX and Model X have the same number of ignition kernels, but Model X has a far more compact initial flame configuration (compare Figure 4.2(h) and (i)). In the right panels of Figure 6.1 we see that the overall nuclear energy release saturates for strong deflagrations. In particular we find in Study II that the value of $E_{\rm nuc}$ at $t_{\rm DDT}^{\rm 1st}$ for Model VIII, Model IX and Model X is approximately equal, hence we expect that the degree of pre-expansion of the white dwarf prior to the first DDT in these models is very similar. Therefore, it is questionable whether the continuous decrease of the ^{56}Ni yield can be easily explained by a single parameter, like $E_{\rm nuc}$ at $t_{\rm DDT}^{\rm 1st}$.

To investigate this, we first consider again that a deflagration flame which evolves from large $N_{\rm k}$ propagates more spherically symmetric outward (see Figure 6.11 and 6.12), which may hinder ensuing detonations to move toward the center of the white dwarf.[6] Therefore, these detonations burn even less of the remaining fuel to IGE, since the burning due to detonations occurs predominantly at low densities ahead and along the deflagration flame. On the other hand, we mentioned above that strong deflagrations already burn a significant part of the stellar material in the central area of the white dwarf to IGE, so that the amount of fuel which is left behind the deflagration flame is smaller than for weak deflagrations. However, due to the symmetric and compact deflagration front, this fuel can commonly not

[6] The spherical symmetry of the ignition region and the deflagration front are not directly related to $N_{\rm k}$ but to the fact that in our ten ignition models we find with increasing $N_{\rm k}$ a larger number of *small spheres* of radius $r_{\rm k}$ that are randomly placed within a single *large sphere* of radius R (see Table 4.1 and Figure 4.2). Hence, with increasing $N_{\rm k}$ the entire ignition geometry becomes more compact and spherical symmetric which is most evident in Model X (see Figure 4.2(i)). In this context, the entire initial flame configuration of Model X may be replaced by a single large disturbed sphere of radius R.

be reached by the ensuing detonations.[7]

In contrast, a deflagration flame which evolves from far less ignition kernels propagates in a more aspherical way and leaves a larger amount of unburned material in the central region of the white dwarf. Here initialized detonations at the deflagration flame are able to move between the larger number of crevices between the mushroom cap like structures, eventually reaching the remaining *fuel pockets* deep inside the exploding star. Due to the high densities in these regions the fuel is converted to IGE.

Because of the compact initial flame configuration of Model X, the deflagration burns out a larger part of the central area of the white dwarf than any other of our models. In addition, we see in Table 6.3 that particularly for this model the ^{56}Ni mass at $t_{\mathrm{DDT}}^{\mathrm{1st}}$ is already a significant fraction of the overall produced ^{56}Ni in the simulated delayed detonation. Therefore, the deflagration already provides the major fraction of ^{56}Ni. We can conclude that the stronger the deflagration burns out the central area and the more fuel is already burned to heavier elements by the deflagration flame, the less material can be burned by detonations at high densities to IGE (see also Röpke & Niemeyer, 2007; Mazzali et al., 2007; Kasen et al., 2009). This behavior can also be inferred from Figure 6.5. We see that $A_{\mathrm{flame}}(t)$ at $t_{\mathrm{DDT}}^{\mathrm{1st}}$ has the tendency to be larger for stronger deflagrations. A larger flame surface area in turn implies that more fuel has been consumed by the deflagration flame up to this time that is not further available for occurring detonations which may burn the fuel with more efficiency to IGE. This effect is most pronounced in Model X. However, we note that the described behavior is in general a side effect in such strong deflagrations, whereas the pre-expansion of the white dwarf prior to the first DDT has usually a far higher impact on the explosion brightness.

There is a further secondary geometrical effect that may have an impact on the brightness of the explosion that is particularly relevant for strong deflagrations. This effect is related to the number and distribution of DDT regions at the deflagration flame. For DDTs that occur predominantly only at one side of the star where turbulence at the flame is most intense, it may become difficult for the detonations to propagate to the opposite side of the exploding and rapidly expanding white dwarf. This characteristic depends on the degree of expansion prior to the first DDT, the geometrical structure of the deflagration front and the amount of burned material that is left behind the deflagration flame that may affect or even block the propagation of the detonations (see Maier & Niemeyer, 2006). Since models with large N_{k} have a more compact structure of the deflagration front, the propagation of the detonation through the center to the opposite side of the star is usually completely prevented. Due to the large expansion of the white dwarf in strong deflagrations, despite their supersonic propagation it is also hardly possible for a detonation to move around the deflagration front to the other side of the star which may expand significantly further, while the detonation fronts are propagating onwards.

As seen, for instance, in Figure 6.12(b) in Model VIII of Study II there are eight DDTs at $t_{\mathrm{DDT}}^{\mathrm{1st}}$ in a single solitary region that is far away from the other side of the star. In contrast, in Model X there are only five DDTs but they are partially located at different positions at the deflagration flame (see Figure 6.12(c)). Hence in contrast to Model VIII where only a single detonation front exists, there are two spatially widely separated sources in Model X where

[7] There is further a low probability that a DDT is triggered right in one of the remaining fuel regions in the interior of the star. However, the propagation of a detonation in an isolated fuel region that is surrounded by ashes from the deflagration flame may be blocked (see Maier & Niemeyer, 2006) and the detonation will probably soon cease without propagating toward the surface of the white dwarf where further fuel is available (see also Section 7.2.1).

detonations can consume the surrounding fuel. In Figure 6.11(b) we see a similar behavior in Model VII and Model X of Study I. Here DDTs occur in Model VII predominantly in a specific region at the flame and the ensuing detonation fronts will join together within a very short time. In Model X in this study there are three DDTs in single cells that are located at completely different positions (see Figure 6.11(c)). However, in both studies additional DDTs occur several time steps later on the other side of the star in Model VII resp. Model VIII, so that the described geometrical effect becomes less important. But in the context of the brightness of an explosion, one should generally take this effect into account, since particularly in strong deflagrations it may affect the ^{56}Ni production in the detonation phase to a certain degree. In contrast, in weak deflagrations which show a small expansion of the white dwarf at $t_{\mathrm{DDT}}^{\mathrm{1st}}$ and an increased porosity of the deflagration flame, a single or a few detonation(s) that follow(s) from the first DDT may be able to burn most of the remaining fuel at a high rate to heavier elements.

The only explanation why DDTs occur frequently in regions that are composed of more connected grid cells or why they occur predominantly in a specific region that is located at one side of the star is that there are resolved turbulent structures at the flame that show strong velocity fluctuations. This is illustrated in Figure 6.15 for Model X of Study II where velocity fluctuations with $v'(\ell_{\mathrm{crit}}) \geq 2.5 \times 10^7\,\mathrm{cm\ s^{-1}}$ are shown as highlighted areas at the flame at $t_{\mathrm{DDT}}^{\mathrm{1st}}$. Here we also see clearly that these high velocity fluctuations do not occur on top of the mushroom cap like structures but in the crevices between them (see also Röpke, 2007). Obviously the regions with high velocity fluctuations are resolved in the simulation. In the case shown here, the strongest turbulent structure is found at the right edge at the flame which is encircled. If we compare Figure 6.15 with Figure 6.12(c) we find that this region just corresponds to one DDT region that is composed of three grid cells. This result originates from our chosen modeling approach, to initialize detonations at the locations where the strongest velocity fluctuations are found.

The described effects in this section lead to the conclusion that mainly the strength of the deflagration and the associated degree of expansion of the star prior to the first DDT which can be estimated with E_{nuc} at $t_{\mathrm{DDT}}^{\mathrm{1st}}$ determine the brightness of the explosions. However, for strong deflagrations that evolve from many ignition kernels, the enhanced production of ^{56}Ni in the early explosion phase, the compactness of the deflagration front, as well as the geometrical distribution of DDT regions may additionally affect the ^{56}Ni production in the detonation phase. This behavior will be further investigated in Section 7.2.

6.3.2 Turbulence and the flame surface area in deflagrations

In Figure 6.7 we see that the probability $P(v'(\ell_{\mathrm{crit}}) \geq 10^8\,\mathrm{cm\ s^{-1}})(t)$ of finding velocity fluctuations $v'(\ell_{\mathrm{crit}})$ on the scale ℓ_{crit} of at least $10^8\,\mathrm{cm\ s^{-1}}(t)$ at the deflagration flame is significantly higher for models with small N_{k} (e.g. Model I and Model II). In contrast, in the left panels of Figure 6.4 we find that E_{turb} is significantly lower for these models. Here we have to take into account that the quantity E_{turb} represents the overall generated turbulent energy on unresolved scales. Due to the co-moving grid technique $\Delta(t)$ increases faster in stronger deflagrations that show a rapid expansion of the star. Consequently, the amount of turbulent energy that is not resolved increases also faster in stronger deflagrations. However, far more crucially is that E_{turb} also includes the turbulence in ash regions. The sum of all ash regions inside the white dwarf is far larger than the area in the vicinity of the flame. In addition, turbulence seems to be more intense in ash regions (see Figures 5.7 and 5.10). All these effects contribute to the fact that the results concerning $P(v'(\ell_{\mathrm{crit}}) \geq 10^8\,\mathrm{cm\ s^{-1}})(t)$

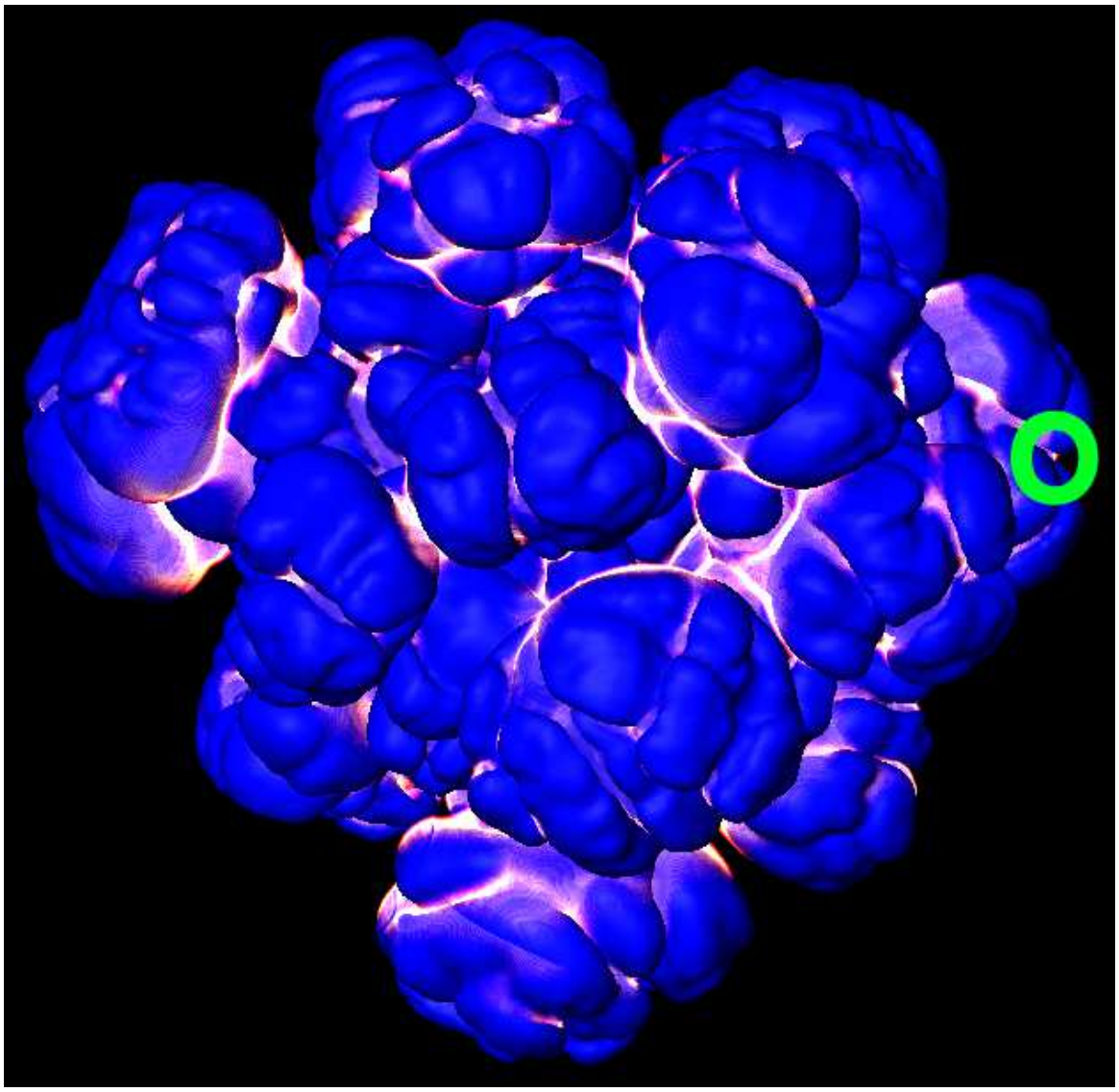

Fig. 6.15: Velocity fluctuations of $v'(\ell_{\mathrm{crit}}) \geq 2.5 \times 10^7$ cm s^{-1} (highlighted areas) at the deflagration flame (purple) in Model X of Study II. The strong turbulent velocity fluctuations are found in trailing edges and in crevices between the mushroom cap like structures that occur due to the influence of the RT instability, but not on top of them. The regions with high turbulent velocity fluctuations exceed mostly several grid cells, hence they are resolved in the simulation. The most intense turbulent structure is encircled.

and E_{turb} appear different at first glance.

The low values of $P(v'(\ell_{\mathrm{crit}}) \geq 10^8\,\mathrm{cm\ s^{-1}})(t)$ (Figure 6.7) at the flame in strong deflagrations at times where DDTs are expected can be understood with the following argument. For weak deflagrations there is one or a few isolated burning and fast rising bubble(s), where the action of local shear instabilities triggers strong turbulence. This is why we see in Figure 5.10 higher velocity fluctuations in the vicinity of the flame in weak deflagrations. Within the ten ignition models of Table 4.1, the time it takes for the merger of all ignition kernels becomes shorter for models with larger N_{k}. In this way, in stronger deflagrations an impenetrable compact flame front emerges and grows faster (see Figure 6.5), whereas the evolution of

locally intense turbulence (due to individual hot rising bubbles) is suppressed. For very strong deflagrations the merger of the kernels becomes so fast that soon after the ignition of the deflagration a single large burning front of high spherical symmetry propagates outward. Similar to the argument of Section 6.2.2 we can imagine that turbulence become partially suppressed in this case, because a slightly disturbed deflagration front which propagates in a spherical symmetric way is more robust against instabilities, even if there will be a larger number of kinks and bends at the flame where instabilities can arise (see Section 4.2.2). Therefore, we see on average lower velocity fluctuations at the flame in Figure 5.10 for stronger deflagrations. In addition, we find in strong deflagrations an earlier freeze out of turbulent motions (see also Khokhlov, 1995). This can also be inferred from Figure 5.10 where we see that the maximum of the velocity fluctuations are found at earlier times for stronger deflagrations. Hence, at later times when DDTs are expected, turbulence may be even weaker which eventually explains why the probability $P(v'(\ell_{\mathrm{crit}}) \geq 10^8\,\mathrm{cm\ s^{-1}})(t)$ is on average much lower in strong deflagrations. However, we also often find for a given model that the quantity $P(v'(\ell_{\mathrm{crit}}) \geq 10^8\,\mathrm{cm\ s^{-1}})(t)$ may rise even for times beyond $t_{\mathrm{DDT}}^{\mathrm{1st}}$ (see Figure 6.7). Since the fuel density at the flame declines during the deflagration, we assume that this behavior may be explained with the results in Section 5.2.6. Here we found stronger turbulence at higher densities, but a higher probability of the occurrence of particularly high velocity fluctuations at lower densities.

The growth rate of $A_{\mathrm{flame}}(t)$ depends mainly on the symmetry of the initial flame configuration of the deflagration. In asymmetric off-center ignitions the deflagration flame also propagates in an asymmetric way (predominantly within a certain solid angle or within a specific sector) toward the surface of the white dwarf (e.g. Röpke et al., 2007b), where the entire flame surface area remains small. In contrast, in Model IX and Model X for instance, the flame spreads spherically in all directions through the stellar material and $A_{\mathrm{flame}}(t)$ becomes very large. However, we argue that the growth rate of $A_{\mathrm{flame}}(t)$ further depends to a certain extent on the interaction of turbulence with the flame. This may explain the behavior of Model X in which turbulence is relatively weak in the late explosion phase and $A_{\mathrm{flame}}(t)$ is much smaller than in Model IX (see Figure 6.5). On the other hand, we find in Model IX some ignition kernels of the deflagration that are located at larger distances from the center of the white dwarf than in Model X (see Figure 4.2 (h/i)). Hence, the entire ignition region of the deflagration is larger in Model IX, which may also contribute to a larger growth rate of $A_{\mathrm{flame}}(t)$ in Model IX than in Model X. The weak turbulence and the associated low values of $P(v'(\ell_{\mathrm{crit}}) \geq 10^8\,\mathrm{cm\ s^{-1}})(t)$ in Model X further lead to the effect that $A^*_{\mathrm{flame}}(t)$ has to grow very large in order to meet the DDT criterion (see right panels of Figure 6.6).

6.3.3 The number of DDTs

Due to the less restrictive DDT criterion, the number of all DDTs $\sum F_{\mathrm{DDT}}$ in the simulations of the models in Study II is significantly larger compared to Study I. However, we find that the total number of time steps $N_{\mathrm{t_{DDT}}}$ where DDTs occur is smaller in Study II. In addition, we find here a clear trend that $N_{\mathrm{t_{DDT}}}$ increases continuously for models with larger N_{k}. In Study I this tendency is less pronounced. Here there is rather some kind of a saturation of $N_{\mathrm{t_{DDT}}}$ that occurs at Model VII, where $N_{\mathrm{t_{DDT}}}$ begins to decrease again for Model IX and Model X.

These effects occur due to different reasons that are outlined in the following. First we see in Figure 6.6 that for most models the quantity $A^*_{\mathrm{flame}}(t)$ at $t_{\mathrm{DDT}}^{\mathrm{1st}}$ is far away from its global maximum. Hence, there will be a larger flame surface area for times $t > t_{\mathrm{DDT}}^{\mathrm{1st}}$ that

meet the DDT constraints. From the Figures 6.7 and 6.8 we can see that the probability $P(v'(\ell_{\mathrm{crit}}) \geq 10^8\,\mathrm{cm\ s^{-1}})(t)$ is in addition for a specific time frame sufficiently high to meet the DDT criterion for $t > t^{\mathrm{1st}}_{\mathrm{DDT}}$ in nearly all simulations so that further detonations follow and $N_{\mathrm{t_{DDT}}}$ increases.

Apart from the fact that the probability $P(v'(\ell_{\mathrm{crit}}) \geq 10^8\,\mathrm{cm\ s^{-1}})(t)$ is higher in weaker deflagrations, there are further differences between weak and strong deflagrations in the context of this quantity. We see in Figure 6.7 that $P(v'(\ell_{\mathrm{crit}}) \geq 10^8\,\mathrm{cm\ s^{-1}})(t)$ varies faster with time for weak deflagrations. Therefore, these deflagrations become an enhanced chance that the condition $A_{\mathrm{det}}(t) < A_{\mathrm{crit}}$ occurs before $\tau_{\mathrm{eddy}_{1/2}}(\ell_{\mathrm{crit}})$ is reached. This behavior can be seen clearly in Study I when comparing Figure 6.10(a) with Figure 6.10(b). We conclude that the unpredictable behavior of the occurrence of high turbulent velocity fluctuations in weak deflagrations that is attributed to strong intermittency in turbulence may prevent DDTs, leading smaller of $N_{\mathrm{t_{DDT}}}$.

A further effect is that the overall time interval where $P(v'(\ell_{\mathrm{crit}}) \geq 10^8\,\mathrm{cm\ s^{-1}})(t)$ has noticeable values, shows the tendency to be narrower for weak deflagrations. For instance, in Study I in Model I this time interval ranges approximately from 1.10 to 1.22 seconds, while in Model VIII this interval spans a range from 0.82 to 1.11 seconds (see upper panels of Figure 6.7). This further reduces $N_{\mathrm{t_{DDT}}}$ in weak deflagrations. The origin of this effect lies mainly in the evolution of the detonation fronts and the number of grid cells $N^*_{\mathrm{flame}}(t)$ that meet the DDT constraints concerning X_{fuel} and ρ_{fuel}. As described in Section 6.2.4 the detonations in weak deflagrations evolve faster in the explosion due to the smaller expansion of the white dwarf. This means that already shortly after the first DDT commences, detonations may propagate through a significant fraction of the small number of grid cells $N^*_{\mathrm{flame}}(t)$ that originally were (or would have been later) a contribution to $A^*_{\mathrm{flame}}(t)$. We already indicated that $A^*_{\mathrm{flame}}(t)$ may rise for a certain time beyond $t^{\mathrm{1st}}_{\mathrm{DDT}}$, indicating that detonations have not yet led to a significant decrease in the quantity $N^*_{\mathrm{flame}}(t)$. Here, the growth rate of $A^*_{\mathrm{flame}}(t)$ is mainly given by the further expansion of the grid, where this behavior is more pronounced for strong deflagrations (see Figure 6.6).

In the less restrictive DDT criterion of Study II, the ratio of initialized detonations F_{DDT} to $N^*_{\mathrm{flame}}(t = t^{\mathrm{1st}}_{\mathrm{DDT}})$ at the time $t^{\mathrm{1st}}_{\mathrm{DDT}}$ of the first DDT is relatively high for the Model II, Model III and Model V. This leads to a short but very steep decline of the quantity $A^*_{\mathrm{flame}}(t)$ that can be identified in Figure 6.6(c). In general, a high ratio of F_{DDT} to $N^*_{\mathrm{flame}}(t = t_{\mathrm{DDT}})$ at times t_{DDT} where DDTs occur will lead to a certain reduction of $A^*_{\mathrm{flame}}(t)$ and consequently of $A_{\mathrm{det}}(t)$. This makes it difficult for the corresponding models to meet the DDT criterion for later times that eventually leads on average to smaller $N_{\mathrm{t_{DDT}}}$. Due to the lower resolution we find in Study II much lower values of $N^*_{\mathrm{flame}}(t)$. In contrast, the DDT criterion is less restrictive in Study II, so we find higher values of F_{DDT}. In summary, we find in Study II higher ratios of F_{DDT} to $N^*_{\mathrm{flame}}(t = t_{\mathrm{DDT}})$ in the models, explaining the lower values of $N_{\mathrm{t_{DDT}}}$ compared to Study I. In this context, there is a remarkable event in Study II that occurs in Model VIII and happens at about one second in the explosion. The final DDT occurs here in several thousand grid cells (see Figure 6.8(d)), leading to an abrupt decline of $A^*_{\mathrm{flame}}(t)$ that can be seen in Figure 6.6(d). However, it should be clear that even if further DDTs occur in such simulations, the additional detonations have no more effect on the explosion dynamics.

Finally, we see in Study I that for very strong deflagrations that have weak turbulence, $A_{\mathrm{det}}(t)$ is sometimes not large enough to exceed the high threshold value of A_{crit} (see Figure 6.8), so that we find in this study that $N_{\mathrm{t_{DDT}}}$ decreases again for Model IX and Model X. We note that this behavior will also occur in Study II, if we increase the threshold value

of $A_{\rm crit}$ to a certain extent.

From the described effects we conclude that strong turbulent intensity in weak deflagrations may trigger DDTs, but the potential detonation area $A_{\rm det}(t)$ may often not exceed the required critical flame surface area $A_{\rm crit}$ for a DDT long enough for the initialization of the detonation. The main reason is the unpredictable behavior of the strong intermittency in weak deflagrations that becomes apparent in fast variations of the quantity $P(v'(\ell_{\rm crit}) \geq 10^8\,{\rm cm\ s^{-1}})(t)$ with time that eventually prevents several DDTs. In contrast, the weaker turbulence in stronger deflagrations leads to lower values of the probability $P(v'(\ell_{\rm crit}) \geq 10^8\,{\rm cm\ s^{-1}})(t)$ which, however, shows far less temporal variations in this case. Together with the larger flame surface area $A^*_{\rm flame}(t)$ in strong deflagrations we find steady values of $A_{\rm det}(t)$ that can frequently exceed $A_{\rm crit}$ long enough to trigger DDTs. Hence we find in strong deflagrations more time steps where DDTs occur. In models that have a very small flame surface area that meets the DDT constraints or models that show only very weak turbulence at the flame, the DDT criterion may sometimes not be met, leading to a decrease of $N_{\rm t_{DDT}}$ in both cases.

6.3.4 Remarks on the eddy turnover time

In general, it is important to keep in mind that a significant part of the described results is based on the inclusion of $\tau_{\rm eddy_{1/2}}(\ell_{\rm crit})$ that prevents direct detonations if $A_{\rm det}(t) \geq A_{\rm crit}$ (or equivalently $F_{\rm DDT} \approx 1$). We outline here that the application of $\tau_{\rm eddy_{1/2}}(\ell_{\rm crit})$ has an additional physical effect. One can imagine that for a given value of $A^*_{\rm flame}(t)$ in our DDT model, the probability of the occurrence of DDTs becomes higher with stronger turbulence. If, however, turbulence becomes too intense, the flame is in reality so heavily disturbed and disrupted that potential DDT regions can be practically destroyed before they either grow large enough or before fuel and ash within these regions are sufficiently mixed for a DDT. In the simulated models, the most intense turbulence is found in local structures in weak deflagrations, where the quantity $A_{\rm det}(t)$ (or equivalently $P(v'(\ell_{\rm crit}) \geq 10^8\,{\rm cm\ s^{-1}})(t)$) shows faster variations in successive time steps. If $\tau_{\rm eddy_{1/2}}(\ell_{\rm crit})$ is not included, these models will experience a much larger number of DDTs, but here $\tau_{\rm eddy_{1/2}}(\ell_{\rm crit})$ acts as a quantity which ensures that very intense turbulence leads to fewer DDTs. In addition, we note that very high velocity fluctuations cause also very high fluctuations in the temperature and in the chemical composition (and hence in the fuel fraction) at the flame. Since a DDT that is based on the Zeldovich gradient mechanism requires a sufficiently shallow gradient of induction times (see Section 3.3.1), too intense turbulence may lead to the effect that DDTs cannot occur (see Niemeyer, 1999).

6.3.5 Unsuccessful DDTs

According to our DDT model, we argue that DDTs in sufficiently weak and strong deflagrations may be in principle completely prevented. For the latter case, we note that there are a few indications that pure strong deflagrations may be capable of explaining some of the observed rare peculiar SN Ia events (see Section 2.3.3). For the former case, we showed in Section 6.2.1 that for models with $N_{\rm k} \leq 100$ a pure deflagration cannot gravitationally unbind the whole star anymore, leading to a lower mass of the ejecta and a compact bound remnant in the central region. Whether these *failed deflagrations* may explain some of the faint peculiar SN Ia events is uncertain (see also discussion in Plewa, 2007). In Model I which constitutes a single off-center ignition of the deflagration, the flame burns only a marginal

fraction of the fuel. If in this very weak deflagration no DDT occurs, the event is particularly faint. However, this model may also transition into the GCD scenario (see Section 2.3.6) in which a detonation occurs by a mechanism which is fundamentally different compared to the classical delayed detonation scenario described in the Sections 2.3.4 and 3.3. Since in this case the outer layers of the star may have expanded further prior to the initialization of the detonation than in Study I, this model will most likely produce less ^{56}Ni that would be more consistent with the observed bright events of normal SNe Ia or the 1991T-like objects.[8] Apart from the GCD scenario, the weak deflagrations may also evolve toward the pulsational delayed detonation or pulsational reverse detonation model (see Section 2.3.7).

6.3.6 Dynamics of deflagrations and detonations

We see in Table 6.2 that in all pure deflagrations, a significant amount of fuel is left. In simulations of delayed detonations we find that a major part of the remaining fuel is burned to heavier elements (see Table 6.3). For weak deflagrations we see that most of this fuel is burned in detonations to IGE, in particular to ^{56}Ni. This confirms our expectations that detonations in weak deflagrations burn the remaining unburned material at high densities. In contrast, we see in strong deflagrations that detonations lead to an increase of the ^{56}Ni yield as well, but most of the fuel is burned to IME and ^{16}O. Obviously the burning due to detonations occurs predominantly ahead of the deflagration flame at relatively low densities. Model II - Model IX follow this trend.

We further see in Table 6.2 the trend that the ratio of ^{56}Ni to IGE decreases for stronger deflagrations. This behavior is related to an enhanced neutronization in the early deflagration phase where the fuel is consumed at a high rate at high densities. Also simulations of delayed detonations show a higher neutronization for a stronger deflagration phase (see Table 6.3). The reason is that due to the expansion of the star, the fuel densities at $t_{\mathrm{DDT}}^{\mathrm{1st}}$ have declined so far that an additional strong neutronization in the detonation phase is unlikely. Therefore, the deflagration already provides the major contribution to the neutronization, which also holds to a certain extent for weak deflagration phases. In Section 7.3 we will further investigate the effects of neutronization in exploding white dwarfs which have different initial central densities.

Interestingly, we can infer from the time evolution of the produced amounts of different chemical species in the Figures 6.13 and 6.14 a behavior that is related to the dynamics of the deflagration flame in the different models. We see in Model X that the deflagration has almost ceased at $t_{\mathrm{DDT}}^{\mathrm{1st}}$, since the slope of the curve of IGE is ≈ 0 at this time. Here we can infer from Figure 4.1 that the entire burning occurs predominantly at relatively low densities. In Study I for instance, a significant part of the deflagration flame is in the range of fuel densities of $0.6 \times 10^7\,\mathrm{g\ cm^{-3}} \leq \rho_{\mathrm{fuel}} \leq 0.7 \times 10^7\,\mathrm{g\ cm^{-3}}$ at the same time, which is also confirmed by the curve shape and the large values of $A^*_{\mathrm{flame}}(t)$ seen in Figure 6.6(b). We can conclude that the deflagration flame has a high spherical symmetry in this model. In contrast, the burning in the deflagration phase for weak deflagrations is far more incomplete at $t_{\mathrm{DDT}}^{\mathrm{1st}}$. Here the slope of the curve of IGE is still high and the burning of the fuel to IME has just begun. This means that only a small part of the deflagration flame is in the range of fuel densities of $0.6 \times 10^7\,\mathrm{g\ cm^{-3}} \leq \rho_{\mathrm{fuel}} \leq 0.7 \times 10^7\,\mathrm{g\ cm^{-3}}$, whereas the rest of the flame resides at higher densities. Obviously the flame has propagated asymmetrically.

[8] The detonation in the GCD model occurs most certainly later than $t_{\mathrm{DDT}}^{\mathrm{1st}}$.

6.3.7 Comparison with the resolution study

The comparison of $A^*_{\text{flame}}(t)$ in Model X of Study II in Figure 6.6(d) with Model X* in Figure 5.11(c) from the resolution study in Section 5.4 shows that the values of $A^*_{\text{flame}}(t)$ are in both cases of the same order of magnitude. However, in the latter case the chosen range of allowed fuel densities for the DDT criterion is $1.5 \times 10^7\,\text{g cm}^{-3} \leq \rho_{\text{fuel}} \leq 0.5 \times 10^7\,\text{g cm}^{-3}$ and hence significantly higher than in the criterion used in Study II. Therefore, it seems that the higher values of the parameters r_{k} and d_{k} of the ignition geometry of Model X that constitutes a more compact and denser initial flame configuration than the setup of Model X* have a significant effect on the flame propagation. There is obviously a relatively large number of grid cells $N^*_{\text{flame}}(t)$ that meet the constraints concerning ρ_{fuel} in Model X at the same time. With the described effect of the spherical symmetry of the flame propagation in the context of the obtained values of $A^*_{\text{flame}}(t)$ we conclude that the compact ignition geometry of Model X leads to a flame propagation with a high spherical symmetry.

In contrast to $A^*_{\text{flame}}(t)$, there is a difference in the quantity $P(v'(\ell_{\text{crit}}) \geq 10^8\,\text{cm s}^{-1})(t)$ in Model X of Study II in Figure 6.7(d) compared to Model X* in Figure 5.13(a) from the resolution study in Section 5.4, where in the latter case $P(v'(\ell_{\text{crit}}) \geq 10^8\,\text{cm s}^{-1})(t)$ is partially about one order of magnitude lower. Since the initial flame configuration is more compact in Model X we would expect weaker turbulence in this model, but the opposite is the case. Therefore, we can conclude that the probability $P(v'(\ell_{\text{crit}}) \geq 10^8\,\text{cm s}^{-1})(t)$ is significantly higher for a range of lower fuel densities (see also the histograms in Figure 5.9(b) in Section 5.2.6). A similar behavior can be found when comparing $P(v'(\ell_{\text{crit}}) \geq 10^8\,\text{cm s}^{-1})(t)$ in the simulations of Study I and Study II, where for Study I, fuel densities not higher than $0.7 \times 10^7\,\text{g cm}^{-3}$ are taken into account. In Figure 6.7 we see that the probability $P(v'(\ell_{\text{crit}}) \geq 10^8\,\text{cm s}^{-1})(t)$ is on average higher for the simulations of Study I. We note that we also placed different constraints on the quantity X_{fuel} in both studies but we see in Figure 5.9(a) that the histogram of $v'(\ell_{\text{crit}})$ (and hence the probability $P(v'(\ell_{\text{crit}}) \geq 10^8\,\text{cm s}^{-1})(t)$) seems to be largely independent of these constraints.

6.4 Conclusions

In this chapter the new SGS model for DDTs for simulations of delayed detonations in SN Ia explosions has been applied with two different DDT criteria to ten ignition models that give rise to different strengths of the deflagration. The decisive parameter of these ignition models is the number of ignition kernels N_{k} from which the deflagration flame evolves. Apart from one model which could not be analyzed due to insufficient data for the application of the DDT model, the two DDT criteria were met in all simulations of delayed detonations. We obtained a range of ^{56}Ni yields in both studies that is consistent with the expectations from observations of normal SNe Ia (e.g. Contardo et al., 2000; Stritzinger et al., 2006; Mazzali et al., 2007).

We showed that in the performed simulations there are locally resolved large-scale structures of strong turbulence at the deflagration flame that becomes apparent in high velocity fluctuations in more connected grid cells. Since the DDT model is designed to initialize detonations in the grid cells where the values of $v'(\ell_{\text{crit}})$ are highest, it follows that also DDTs frequently occur in regions that exceed more than one grid cell. For weak deflagrations, a single DDT may be capable of burning most of the remaining fuel. In contrast, in strong deflagrations, the large expansion of the white dwarf and the compact structure of the deflagration front may affect the propagation of the detonations, so that the number and times

where DDTs occur may become important for the further ^{56}Ni production.

The mechanism that causes DDTs is fundamentally different for weak and strong deflagrations. In weak deflagrations the high velocity fluctuations at the flame that are induced by strong shear instabilities trigger the DDT. In contrast, in strong deflagrations turbulence is weaker, but the larger flame surface area that meets the DDT constraints and the lesser temporal variations of the probability $P(v'(\ell_{\mathrm{crit}}) \geq 10^8\,\mathrm{cm\ s^{-1}})(t)$ of finding velocity fluctuations $v'(\ell_{\mathrm{crit}})$ on the scale ℓ_{crit} of at least $10^8\,\mathrm{cm\ s^{-1}}$ at this flame surface area causes DDTs. In both cases, DDTs may be completely prevented, leading either to a failed deflagration (that may further transition into a scenario where a detonation is triggered in a different way or a pure strong deflagration. These scenarios, however, cannot explain the whole observed variations in the brightness and/or some of the main characteristic features of normal SNe Ia.

One problem that occurs in our analysis is that one model could not be analyzed. The reason is that the available number of grid cells $N^*_{\mathrm{flame}}(t)$ that meet the DDT constraints is too small to construct and fit the histogram of $v'(\ell_{\mathrm{crit}})$ in the entire simulation. Therefore, we are unable to determine a single value for the quantity $P(v'(\ell_{\mathrm{crit}}) \geq 10^8\,\mathrm{cm\ s^{-1}})(t)$. This problem may occur generally for very weak deflagrations in combination with too restrictive DDT criteria (see Section 5.3.3).

As in the resolution test of the SGS model in Section 5.4, the threshold values of the individual DDT quantities in this chapter were chosen arbitrary, even if all threshold values in the used two parameter sets are selected within in a physically sensible range. It is clear that the uncertainties of the threshold values of the DDT quantities raise some questions. Since we obtain in our analysis with two different DDT criteria a very similar result concerning the ^{56}Ni yields one question is to what extent a change of the threshold values of one or several DDT quantities has generally an effect on the brightness of an explosion. This problem will be tackled within a detailed parameter study in the next chapter.

7

Parameter studies of delayed detonations

From the results of the last chapter it becomes obvious that the interplay between several quantities of the DDT model plays an important role in the question of whether or not the necessary conditions for delayed detonations are met in SN Ia explosions. These quantities are partially afflicted with large uncertainties and there will be a variety of possible combinations of their threshold values where the same variation of the ^{56}Ni yields can be obtained as in the used parameter sets in Chapter 6. For this reason even a detailed parameter study provides only some hints and cannot fully answer the question of whether there are certain parameter sets for the DDT criterion that explain in simulations of delayed detonations the observed properties of SNe Ia best.

On the other hand, a parameter study can retroactively provide valuable information about individual DDT quantities by using a process of elimination. If, for instance, in all simulations within a parameter study the initialized DDTs at a given fuel density lead to no faint events with less than $0.4\,M_\odot$ of ^{56}Ni, we can conclude that delayed detonations at these high densities cannot account for the whole observed variations in the brightness of normal SNe Ia. In addition, a parameter study can reveal which of the quantities have the highest impact on the degree of restrictiveness of the DDT criterion and the obtained brightness of the explosion. We can further underpin the indicated correlation in Chapter 6.3.1 between the strength of the deflagration and the obtained ^{56}Ni yield, by applying the DDT model with additional criteria to other various ignition models. Moreover, we will investigate the influence of the secondary parameters of the ignition geometry (σ, r_k and d_k) of the deflagration on the results of simulations of pure deflagrations and delayed detonations. An open question that is particularly related to strong deflagrations was also whether the degree of the expansion of the white dwarf prior to the first DDT is a good proxy to estimate the explosion brightness, and to what extent this estimation is affected by the distribution of DDT regions (see Section 6.3.1). With the following parameter study we can analyze which effect dominates.

We first describe in Section 7.1 the setup of the DDT criteria and how the parameter study is organized. The results of this study are discussed in Section 7.2. In Section 7.3 we vary the central density of the initial white dwarf model and investigate to what extent this variation affects the ^{56}Ni production in simulations of delayed detonations. Since we

showed in Section 5.4 that the DDT model is largely resolution-independent we perform all simulations in this chapter with a resolution of 256^3 grid cells only, so that a relatively large number of models and criteria can be analyzed. An exception are the higher resolved simulations in Section 7.3 that are not directly connected to the parameter study.

7.1 Setups of the main DDT criteria and organization of the parameter study

The initial white dwarf model is described in Section 4.2. Since there are too many quantities within the DDT criterion to vary each of them to a large extent, we first perform a preselection of threshold values of the individual DDT quantities. In the following list, the physical range of each DDT quantity (see also Section 3.3.2) and the selected threshold value(s) for the main study, in the following referred to as *Study A*, are summarized:

1. The range of fuel densities ρ_{fuel} in the grid cells is given by $\rho_{\text{fuel}}^{\text{min}} \leq \rho_{\text{fuel}} \leq \rho_{\text{fuel}}^{\text{max}}$. Following Woosley (2007) we can choose $\rho_{\text{fuel}}^{\text{min}} = 0.5 \times 10^7\,\text{g cm}^{-3}$ and $\rho_{\text{fuel}}^{\text{max}} = 1.5 \times 10^7\,\text{g cm}^{-3}$ for the DDT criterion. In this case, however, the obtained range of allowed fuel densities is quite large and we use the following four smaller intervals for ρ_{fuel}, where for all of them $\rho_{\text{fuel}} \leq 10^7\,\text{g cm}^{-3}$ holds:
   a) $0.8 \times 10^7\,\text{g cm}^{-3} \leq \rho_{\text{fuel}} \leq 1.0 \times 10^7\,\text{g cm}^{-3}$
   b) $0.6 \times 10^7\,\text{g cm}^{-3} \leq \rho_{\text{fuel}} \leq 1.0 \times 10^7\,\text{g cm}^{-3}$
   c) $0.6 \times 10^7\,\text{g cm}^{-3} \leq \rho_{\text{fuel}} \leq 0.8 \times 10^7\,\text{g cm}^{-3}$
   d) $0.5 \times 10^7\,\text{g cm}^{-3} \leq \rho_{\text{fuel}} \leq 0.8 \times 10^7\,\text{g cm}^{-3}$

   We will investigate the impact of higher fuel densities with $\rho_{\text{fuel}} \geq 10^7\,\text{g cm}^{-3}$ in a separate study.

2. The range of fuel fractions X_{fuel} in the grid cells is given by $X_{\text{fuel}}^{\text{min}} \leq X_{\text{fuel}} \leq X_{\text{fuel}}^{\text{max}}$. Here we choose three intervals:
   a) $0.1 \leq X_{\text{fuel}} \leq 0.9$
   b) $0.2 \leq X_{\text{fuel}} \leq 0.8$
   c) $0.3 \leq X_{\text{fuel}} \leq 0.7$

3. For the minimum required velocity fluctuations v'_{crit} for a DDT we choose the following two values:
   a) $v'_{\text{crit}} = 0.5 \times 10^8\,\text{cm s}^{-1}$ (Woosley et al., 2009)
   b) $v'_{\text{crit}} = 1.0 \times 10^8\,\text{cm s}^{-1}$ (Lisewski et al., 2000)

   We will vary v'_{crit} between both values in an additional analysis.

4. The half eddy turnover time $\tau_{\text{eddy}_{1/2}}(\ell_{\text{crit}})$ is estimated by $0.5 \cdot \ell_{\text{crit}}/v'_{\text{crit}}$ (equation (3.48)). With $\ell_{\text{crit}} = 10^6\,\text{cm}$ and the above values for v'_{crit} we find:
   a) $\tau_{\text{eddy}_{1/2}}(\ell_{\text{crit}}) = 0.5 \times 10^{-2}\,\text{s}$
   b) $\tau_{\text{eddy}_{1/2}}(\ell_{\text{crit}}) = 1.0 \times 10^{-2}\,\text{s}$

   As described in Section 3.3.2 the eddy turnover time is afflicted with some uncertainties and we will investigate the influence of a different value of $\tau_{\text{eddy}_{1/2}}(\ell_{\text{crit}})$ separately.

5. For the critical flame surface area A_{crit} for a DDT we use the following two values (see also Section 6.1):
   a) $A_{\mathrm{crit}} = \ell_{\mathrm{crit}}^2$ (DDT region has a smooth surface area.)
   b) $A_{\mathrm{crit}} = \ell_{\mathrm{crit}}^D$ (DDT region has a fractal dimension of $D = 2.36$.)

The different DDT criteria of Study A are given by all possible combinations of the chosen threshold values of the DDT quantities, hence there is a total of $4 \cdot 3 \cdot 2 \cdot 2 \cdot 2 = 96$ different DDT criteria that are summarized in the Tables 7.1 and 7.2. We note that we estimated $\tau_{\mathrm{eddy}_{1/2}}(\ell_{\mathrm{crit}})$ by $0.5 \cdot \ell_{\mathrm{crit}}/v'_{\mathrm{crit}}$ (see Section 3.3.2). Since ℓ_{crit} is a fixed quantity, we could in principle determine $\tau_{\mathrm{eddy}_{1/2}}(\ell_{\mathrm{crit}})$ with respect to v'_{crit} and use the obtained value for $\tau_{\mathrm{eddy}_{1/2}}(\ell_{\mathrm{crit}})$ in the corresponding criterion. However, due to the described uncertainties of the eddy turnover time in Section 3.3.2, we treat here $\tau_{\mathrm{eddy}_{1/2}}(\ell_{\mathrm{crit}})$ as an independent and free parameter (like the other DDT quantities).[1]

All 96 DDT criteria are applied to Model III, Model VIII and Model X of Table 4.1 that give rise to different strengths of the deflagration. From this study we can estimate the range of ^{56}Ni yields that can be obtained for each criterion. In *Study B* we construct additional, partly more restrictive DDT criteria and apply them to six ignition models that consist of the three models of Study A and Model VI and Model IX of Table 4.1 and Model 5 of Table 4.2. Here we vary some of the individual DDT parameters to a larger extent than in Study A, while keeping the other parameters constant in a way that favors the occurrence of faint explosions. If at some point the variation of an individual parameter the simulations yield no event with approximately $0.4\,M_\odot$ of ^{56}Ni anymore, we can place some constraints on this parameter. In addition, we investigate in this study under what circumstances the DDT criterion cannot be met anymore. Here we can derive additional necessary constraints for a DDT to occur in deflagrations of white dwarfs generally. In *Study C* we finally choose four DDT criteria in which the obtained ^{56}Ni yields cover a broad range within the simulated ignition models used in Study A and Study B. These criteria are applied to all remaining ignition models shown in the Tables 4.1 and 4.2, hence a total of 46 different ignition setups are taken into account. With this study we can find out whether the correlation between the strength of the deflagration and the obtained ^{56}Ni yield in simulations of delayed detonations of the different models and within the chosen DDT criteria is maintained. We further investigate here the influence of the secondary parameters of the ignition geometry σ, r_{k} and d_{k} (see Section 4.2.2) on the simulation results of both pure deflagrations and delayed detonations. Finally, the number of all simulated delayed detonations is sufficient to evaluate to what extent the expansion of the white dwarf prior to the first DDT and the distribution of the DDT regions determine the brightness of the explosion.

[1] One of the uncertainties mentioned in Section 3.3.2 concerns the isotropy of turbulence. However, we assumed isotropic turbulence at the flame on the relevant scales, such as ℓ_{crit} (see Section 5.2.3), so that this uncertainty may be ignored. However, it remains an open question of whether and to what extent different turbulent intensities in combination with a certain intermittency affect $\tau_{\mathrm{eddy}_{1/2}}(\ell_{\mathrm{crit}})$ (see also discussion in Section 3.3.2).

Crit	ρ_{fuel} $[10^7\,\text{g cm}^{-3}]$	X_{fuel}	v'_{crit} $[10^8\,\text{cm s}^{-1}]$	$\tau_{\text{eddy}_{1/2}}$ $[10^{-2}\,\text{s}]$	A_{crit}	**Crit**	ρ_{fuel} $[10^7\,\text{g cm}^{-3}]$	X_{fuel}	v'_{crit} $[10^8\,\text{cm s}^{-1}]$	$\tau_{\text{eddy}_{1/2}}$ $[10^{-2}\,\text{s}]$	A_{crit}
1	0.8 ... 1.0	0.1 ... 0.9	0.5	0.5	ℓ^2_{crit}	**25**	0.8 ... 1.0	0.1 ... 0.9	0.5	1.0	ℓ^2_{crit}
2	0.6 ... 1.0	0.1 ... 0.9	0.5	0.5	ℓ^2_{crit}	**26**	0.6 ... 1.0	0.1 ... 0.9	0.5	1.0	ℓ^2_{crit}
3	0.6 ... 0.8	0.1 ... 0.9	0.5	0.5	ℓ^2_{crit}	**27**	0.6 ... 0.8	0.1 ... 0.9	0.5	1.0	ℓ^2_{crit}
4	0.5 ... 0.8	0.1 ... 0.9	0.5	0.5	ℓ^2_{crit}	**28**	0.5 ... 0.8	0.1 ... 0.9	0.5	1.0	ℓ^2_{crit}
5	0.8 ... 1.0	0.2 ... 0.8	0.5	0.5	ℓ^2_{crit}	**29**	0.8 ... 1.0	0.2 ... 0.8	0.5	1.0	ℓ^2_{crit}
6	0.6 ... 1.0	0.2 ... 0.8	0.5	0.5	ℓ^2_{crit}	**30**	0.6 ... 1.0	0.2 ... 0.8	0.5	1.0	ℓ^2_{crit}
7	0.6 ... 0.8	0.2 ... 0.8	0.5	0.5	ℓ^2_{crit}	**31**	0.6 ... 0.8	0.2 ... 0.8	0.5	1.0	ℓ^2_{crit}
8	0.5 ... 0.8	0.2 ... 0.8	0.5	0.5	ℓ^2_{crit}	**32**	0.5 ... 0.8	0.2 ... 0.8	0.5	1.0	ℓ^2_{crit}
9	0.8 ... 1.0	0.3 ... 0.7	0.5	0.5	ℓ^2_{crit}	**33**	0.8 ... 1.0	0.3 ... 0.7	0.5	1.0	ℓ^2_{crit}
10	0.6 ... 1.0	0.3 ... 0.7	0.5	0.5	ℓ^2_{crit}	**34**	0.6 ... 1.0	0.3 ... 0.7	0.5	1.0	ℓ^2_{crit}
11	0.6 ... 0.8	0.3 ... 0.7	0.5	0.5	ℓ^2_{crit}	**35**	0.6 ... 0.8	0.3 ... 0.7	0.5	1.0	ℓ^2_{crit}
12	0.5 ... 0.8	0.3 ... 0.7	0.5	0.5	ℓ^2_{crit}	**36**	0.5 ... 0.8	0.3 ... 0.7	0.5	1.0	ℓ^2_{crit}
13	0.8 ... 1.0	0.1 ... 0.9	1.0	0.5	ℓ^2_{crit}	**37**	0.8 ... 1.0	0.1 ... 0.9	1.0	1.0	ℓ^2_{crit}
14	0.6 ... 1.0	0.1 ... 0.9	1.0	0.5	ℓ^2_{crit}	**38**	0.6 ... 1.0	0.1 ... 0.9	1.0	1.0	ℓ^2_{crit}
15	0.6 ... 0.8	0.1 ... 0.9	1.0	0.5	ℓ^2_{crit}	**39**	0.6 ... 0.8	0.1 ... 0.9	1.0	1.0	ℓ^2_{crit}
16	0.5 ... 0.8	0.1 ... 0.9	1.0	0.5	ℓ^2_{crit}	**40**	0.5 ... 0.8	0.1 ... 0.9	1.0	1.0	ℓ^2_{crit}
17	0.8 ... 1.0	0.2 ... 0.8	1.0	0.5	ℓ^2_{crit}	**41**	0.8 ... 1.0	0.2 ... 0.8	1.0	1.0	ℓ^2_{crit}
18	0.6 ... 1.0	0.2 ... 0.8	1.0	0.5	ℓ^2_{crit}	**42**	0.6 ... 1.0	0.2 ... 0.8	1.0	1.0	ℓ^2_{crit}
19	0.6 ... 0.8	0.2 ... 0.8	1.0	0.5	ℓ^2_{crit}	**43**	0.6 ... 0.8	0.2 ... 0.8	1.0	1.0	ℓ^2_{crit}
20	0.5 ... 0.8	0.2 ... 0.8	1.0	0.5	ℓ^2_{crit}	**44**	0.5 ... 0.8	0.2 ... 0.8	1.0	1.0	ℓ^2_{crit}
21	0.8 ... 1.0	0.3 ... 0.7	1.0	0.5	ℓ^2_{crit}	**45**	0.8 ... 1.0	0.3 ... 0.7	1.0	1.0	ℓ^2_{crit}
22	0.6 ... 1.0	0.3 ... 0.7	1.0	0.5	ℓ^2_{crit}	**46**	0.6 ... 1.0	0.3 ... 0.7	1.0	1.0	ℓ^2_{crit}
23	0.6 ... 0.8	0.3 ... 0.7	1.0	0.5	ℓ^2_{crit}	**47**	0.6 ... 0.8	0.3 ... 0.7	1.0	1.0	ℓ^2_{crit}
24	0.5 ... 0.8	0.3 ... 0.7	1.0	0.5	ℓ^2_{crit}	**48**	0.5 ... 0.8	0.3 ... 0.7	1.0	1.0	ℓ^2_{crit}

Table 7.1: Setups of the DDT criteria for Study A - Part I. Shown are the allowed ranges of fuel densities ρ_{fuel} ($\rho^{\text{min}}_{\text{fuel}} \dots \rho^{\text{max}}_{\text{fuel}}$) and fuel fractions X_{fuel} ($X^{\text{min}}_{\text{fuel}} \dots X^{\text{max}}_{\text{fuel}}$) in the grid cells, as well as the threshold values of the quantities v'_{crit}, $\tau_{\text{eddy}_{1/2}}(\ell_{\text{crit}})$ and A_{crit}.

Crit	ρ_{fuel} $[10^7\,\text{g cm}^{-3}]$	X_{fuel}	v'_{crit} $[10^8\,\text{cm s}^{-1}]$	$\tau_{\text{eddy}_{1/2}}$ $[10^{-2}\,\text{s}]$	A_{crit}	**Crit**	ρ_{fuel} $[10^7\,\text{g cm}^{-3}]$	X_{fuel}	v'_{crit} $[10^8\,\text{cm s}^{-1}]$	$\tau_{\text{eddy}_{1/2}}$ $[10^{-2}\,\text{s}]$	A_{crit}
49	0.8 ... 1.0	0.1 ... 0.9	0.5	0.5	ℓ^D_{crit}	**73**	0.8 ... 1.0	0.1 ... 0.9	0.5	1.0	ℓ^D_{crit}
50	0.6 ... 1.0	0.1 ... 0.9	0.5	0.5	ℓ^D_{crit}	**74**	0.6 ... 1.0	0.1 ... 0.9	0.5	1.0	ℓ^D_{crit}
51	0.6 ... 0.8	0.1 ... 0.9	0.5	0.5	ℓ^D_{crit}	**75**	0.6 ... 0.8	0.1 ... 0.9	0.5	1.0	ℓ^D_{crit}
52	0.5 ... 0.8	0.1 ... 0.9	0.5	0.5	ℓ^D_{crit}	**76**	0.5 ... 0.8	0.1 ... 0.9	0.5	1.0	ℓ^D_{crit}
53	0.8 ... 1.0	0.2 ... 0.8	0.5	0.5	ℓ^D_{crit}	**77**	0.8 ... 1.0	0.2 ... 0.8	0.5	1.0	ℓ^D_{crit}
54	0.6 ... 1.0	0.2 ... 0.8	0.5	0.5	ℓ^D_{crit}	**78**	0.6 ... 1.0	0.2 ... 0.8	0.5	1.0	ℓ^D_{crit}
55	0.6 ... 0.8	0.2 ... 0.8	0.5	0.5	ℓ^D_{crit}	**79**	0.6 ... 0.8	0.2 ... 0.8	0.5	1.0	ℓ^D_{crit}
56	0.5 ... 0.8	0.2 ... 0.8	0.5	0.5	ℓ^D_{crit}	**80**	0.5 ... 0.8	0.2 ... 0.8	0.5	1.0	ℓ^D_{crit}
57	0.8 ... 1.0	0.3 ... 0.7	0.5	0.5	ℓ^D_{crit}	**81**	0.8 ... 1.0	0.3 ... 0.7	0.5	1.0	ℓ^D_{crit}
58	0.6 ... 1.0	0.3 ... 0.7	0.5	0.5	ℓ^D_{crit}	**82**	0.6 ... 1.0	0.3 ... 0.7	0.5	1.0	ℓ^D_{crit}
59	0.6 ... 0.8	0.3 ... 0.7	0.5	0.5	ℓ^D_{crit}	**83**	0.6 ... 0.8	0.3 ... 0.7	0.5	1.0	ℓ^D_{crit}
60	0.5 ... 0.8	0.3 ... 0.7	0.5	0.5	ℓ^D_{crit}	**84**	0.5 ... 0.8	0.3 ... 0.7	0.5	1.0	ℓ^D_{crit}
61	0.8 ... 1.0	0.1 ... 0.9	1.0	0.5	ℓ^D_{crit}	**85**	0.8 ... 1.0	0.1 ... 0.9	1.0	1.0	ℓ^D_{crit}
62	0.6 ... 1.0	0.1 ... 0.9	1.0	0.5	ℓ^D_{crit}	**86**	0.6 ... 1.0	0.1 ... 0.9	1.0	1.0	ℓ^D_{crit}
63	0.6 ... 0.8	0.1 ... 0.9	1.0	0.5	ℓ^D_{crit}	**87**	0.6 ... 0.8	0.1 ... 0.9	1.0	1.0	ℓ^D_{crit}
64	0.5 ... 0.8	0.1 ... 0.9	1.0	0.5	ℓ^D_{crit}	**88**	0.5 ... 0.8	0.1 ... 0.9	1.0	1.0	ℓ^D_{crit}
65	0.8 ... 1.0	0.2 ... 0.8	1.0	0.5	ℓ^D_{crit}	**89**	0.8 ... 1.0	0.2 ... 0.8	1.0	1.0	ℓ^D_{crit}
66	0.6 ... 1.0	0.2 ... 0.8	1.0	0.5	ℓ^D_{crit}	**90**	0.6 ... 1.0	0.2 ... 0.8	1.0	1.0	ℓ^D_{crit}
67	0.6 ... 0.8	0.2 ... 0.8	1.0	0.5	ℓ^D_{crit}	**91**	0.6 ... 0.8	0.2 ... 0.8	1.0	1.0	ℓ^D_{crit}
68	0.5 ... 0.8	0.2 ... 0.8	1.0	0.5	ℓ^D_{crit}	**92**	0.5 ... 0.8	0.2 ... 0.8	1.0	1.0	ℓ^D_{crit}
69	0.8 ... 1.0	0.3 ... 0.7	1.0	0.5	ℓ^D_{crit}	**93**	0.8 ... 1.0	0.3 ... 0.7	1.0	1.0	ℓ^D_{crit}
70	0.6 ... 1.0	0.3 ... 0.7	1.0	0.5	ℓ^D_{crit}	**94**	0.6 ... 1.0	0.3 ... 0.7	1.0	1.0	ℓ^D_{crit}
71	0.6 ... 0.8	0.3 ... 0.7	1.0	0.5	ℓ^D_{crit}	**95**	0.6 ... 0.8	0.3 ... 0.7	1.0	1.0	ℓ^D_{crit}
72	0.5 ... 0.8	0.3 ... 0.7	1.0	0.5	ℓ^D_{crit}	**96**	0.5 ... 0.8	0.3 ... 0.7	1.0	1.0	ℓ^D_{crit}

Table 7.2: Setups of the DDT criteria for Study A - Part II. Shown are the allowed ranges of fuel densities ρ_{fuel} $(\rho^{\text{min}}_{\text{fuel}} \dots \rho^{\text{max}}_{\text{fuel}})$ and fuel fractions X_{fuel} $(X^{\text{min}}_{\text{fuel}} \dots X^{\text{max}}_{\text{fuel}})$ in the grid cells, as well as the threshold values of the quantities v'_{crit}, $\tau_{\text{eddy}_{1/2}}(\ell_{\text{crit}})$ and A_{crit}.

7.2 Results of the parameter study

7.2.1 Study A

The ^{56}Ni yields obtained in Study A are summarized in Table 7.3. For each DDT criterion we find the expected behavior that strong deflagrations (Model X) lead to faint events, while bright explosions follow from weak deflagrations (Model III). However, we see clearly that there are only a few criteria in which we obtain faint events from Model X with approximately $0.4\,M_\odot$ of ^{56}Ni (see Table 7.3). In contrast, simulations of Model III produce in most cases bright explosions with a ^{56}Ni yield of $\gtrsim 1.0\,M_\odot$ which is slightly higher than the expected ^{56}Ni yields of normal SNe Ia. Therefore, compared to observations, our ranges of ^{56}Ni yields are on average slightly shifted toward brighter explosions. But due to the uncertainties of the ignition process, the question arises of whether and to what extent our modeled ignition scenarios (like the setup of Model III or models with even less ignition kernels that lead to bright explosions) are realized in white dwarfs generally. However, from the different DDT criteria and the obtained ^{56}Ni yields we can draw the following conclusions:

1. DDTs in regions that have a higher value of ρ_{fuel} lead to brighter explosions. This behavior is obvious because the denser the material ahead of the detonation the more material can be burned to IGE. In addition, detonations may occur significantly earlier, where the pre-expansion of the white dwarf is smaller and the burning in the deflagration phase is far more incomplete at some places, leading to a larger amount of fuel that can be burned by ensuing detonations more efficiently to IGE than deflagrations. For the density ranges $0.6 \times 10^7\,\text{g cm}^{-3} \leq \rho_{\text{fuel}} \leq 0.8 \times 10^7\,\text{g cm}^{-3}$ and $0.5 \times 10^7\,\text{g cm}^{-3} \leq \rho_{\text{fuel}} \leq 0.8 \times 10^7\,\text{g cm}^{-3}$ no significant differences and trends of the obtained ^{56}Ni yields can be found.

2. For a larger range of allowed values for X_{fuel}, the explosions become on average brighter. The main reason is that $N^*_{\text{flame}}(t)$ is larger, since more grid cells meet the less stringent constraints on X_{fuel}. This implies that $A^*_{\text{flame}}(t)$ is also larger, so that the DDT criterion can be met easier. However, we note that the larger the allowed range of X_{fuel} the more grid cells are taken into account that may not or only marginally be crossed by the flame (see Section 5.1.1). Hence, for larger ranges of allowed values for X_{fuel}, the number of grid cells in which the physical quantities represent mainly the conditions in fuel and ash regions becomes larger. We emphasize that the restrictions on X_{fuel} have a direct effect on the quantity $A^*_{\text{flame}}(t)$ but not on the quantity $P(v'(\ell_{\text{crit}}) \geq v'_{\text{crit}})(t)$ (see also Section 5.2.6 and Figure 5.9)(a)).

3. With the lower threshold value of $v_{\text{crit}} = 0.5 \times 10^8\,\text{cm s}^{-1}$ the explosions become brighter. The reason lies in a much higher probability $P(v'(\ell_{\text{crit}}) \geq v'_{\text{crit}})(t)$, so that the criterion can be met easier.

4. For $\tau_{\text{eddy}_{1/2}}(\ell_{\text{crit}})$ there is no evidence that a variation of the threshold value of this quantity affects the explosion brightness. We will investigate in a following study whether this is a general behavior by increasing the threshold value of $\tau_{\text{eddy}_{1/2}}(\ell_{\text{crit}})$.[2]

[2] We have not considered threshold values for $\tau_{\text{eddy}_{1/2}}(\ell_{\text{crit}})$ lower than $0.5 \times 10^{-2}\,\text{s}$, because in that case $\tau_{\text{eddy}_{1/2}}(\ell_{\text{crit}})$ would become comparable to the simulation time step (see Section 5.3.3). However, since the obtained ^{56}Ni yields are similar for the cases $\tau_{\text{eddy}_{1/2}}(\ell_{\text{crit}}) = 0.5 \times 10^{-2}\,\text{s}$ and $\tau_{\text{eddy}_{1/2}}(\ell_{\text{crit}}) = 1.0 \times 10^{-2}\,\text{s}$, we do not expect that even faster eddy turnover times lead to very different results.

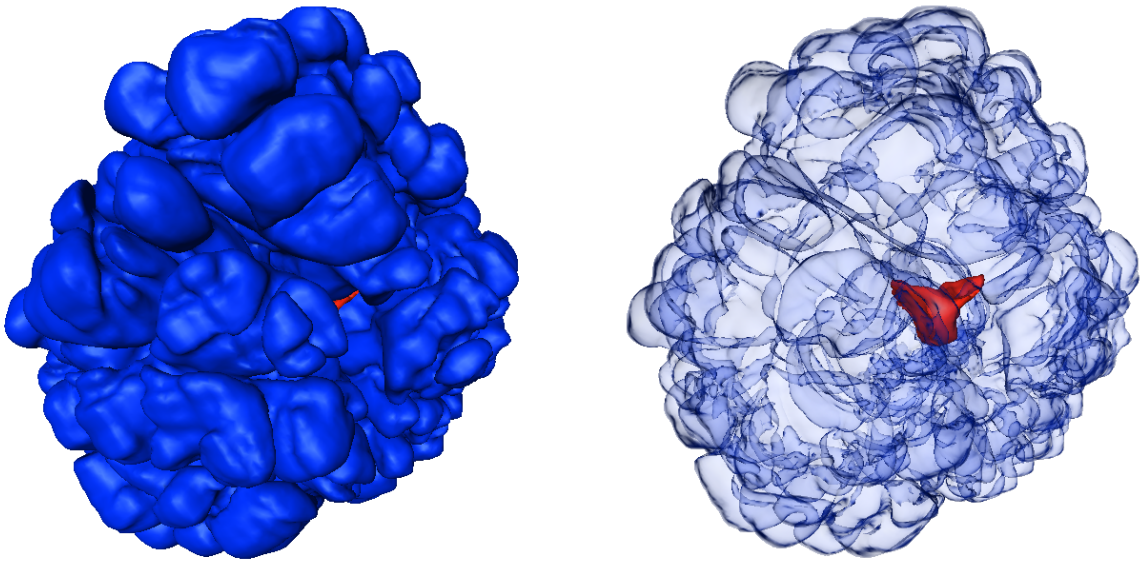

Fig. 7.1: Deflagration (blue) and detonation level set (red) in the simulation of Model III using DDT criterion 95, 0.05 seconds after $t_{\mathrm{DDT}}^{\mathrm{1st}}$. The DDT occurs in a region that becomes enclosed by the deflagration front which hinders the detonation to propagate further outward through the unburned material. A small fraction of the fuel is burned by the detonation in the interior of the star that can be seen in the transparent view in the right figure.

5. For a lower threshold value of A_{crit} the explosions become brighter, since $A_{\mathrm{det}}(t) \geq A_{\mathrm{crit}}$ can be met easier and earlier.

We note that the found influences of the individual quantities on the explosion brightness are more pronounced for Model VIII and Model X. This behavior can be explained with the assumptions discussed in Section 6.3.1 where we argued that for stronger deflagrations the number of DDTs may become important for the ^{56}Ni production, since a single or a few detonation front(s) may be incapable of propagating through a significant part of the remaining fuel. In the context of this study, we can conclude that the more restrictive the DDT criterion the fewer DDTs occur and the less detonation fronts evolve leading to fainter explosions in the case of strong deflagrations. Moreover, the different distributions of the few DDT regions lead to a certain variation of the ^{56}Ni yield (and hence of the explosion brightness) for strong deflagrations. This effect is analyzed in more detail in Section 7.2.3.

However, we also find a remarkable event in criterion 95 in the weak deflagration of Model III, where a DDT occurs but almost no additional burning happens. The obtained ^{56}Ni yield is slightly higher than the amount of ^{56}Ni produced in the simulated pure deflagration of this model, which was approximately $0.2\,M_{\odot}$ (see Table 6.2). The reason is a geometrical effect which is visualized in Figure 7.1. Here a snapshot of the simulation is shown, 0.05 seconds after $t_{\mathrm{DDT}}^{\mathrm{1st}}$. A DDT (the only one in the entire simulation) occurs at a specific place at the deflagration front, where the latter blocks the propagation of the detonation soon after the DDT is initialized. Therefore, the detonation becomes trapped inside the exploding star where it can only burn a minor part of the remaining fuel to ^{56}Ni.

Finally, we find that Model III fails to meet the DDT criterion 93 in the entire simulation. The reason is that the maximal time interval $t_{(A_{\mathrm{det}}(t) \geq A_{\mathrm{crit}})}$ where $A_{\mathrm{det}}(t) \geq A_{\mathrm{crit}}$ is approximately 0.9×10^{-2} s. Hence, the constraint $\tau_{\mathrm{eddy}_{1/2}}(\ell_{\mathrm{crit}}) = 1.0 \times 10^{-2}$ s is never reached in

this simulation. Except for a lower threshold value of $\tau_{\mathrm{eddy}_{1/2}}(\ell_{\mathrm{crit}}) = 0.5 \times 10^{-2}\,\mathrm{s}$, criterion 69 and 93 have the same parameter set. As expected, a DDT is successfully initialized in Model III using criterion 69, since $\tau_{\mathrm{eddy}_{1/2}}(\ell_{\mathrm{crit}}) < 0.9 \times 10^{-2}\,\mathrm{s}$. Apart from Model III using criterion 93, we find in Study A that the DDT criteria are all met at least once in the corresponding simulations.

Crit	^{56}Ni III $[M_\odot]$	^{56}Ni VIII $[M_\odot]$	^{56}Ni X $[M_\odot]$	**Crit**	^{56}Ni III $[M_\odot]$	^{56}Ni VIII $[M_\odot]$	^{56}Ni X $[M_\odot]$	**Crit**	^{56}Ni III $[M_\odot]$	^{56}Ni VIII $[M_\odot]$	^{56}Ni X $[M_\odot]$	**Crit**	^{56}Ni III $[M_\odot]$	^{56}Ni VIII $[M_\odot]$	^{56}Ni X $[M_\odot]$
1	1.138	0.826	0.690	**25**	1.138	0.802	0.679	**49**	1.106	0.734	0.568	**73**	1.115	0.731	0.574
2	1.140	0.819	0.648	**26**	1.138	0.819	0.681	**50**	1.137	0.727	0.572	**74**	1.126	0.701	0.565
3	1.119	0.756	0.593	**27**	1.119	0.760	0.612	**51**	1.095	0.668	0.493	**75**	1.090	0.664	0.507
4	1.122	0.766	0.626	**28**	1.122	0.762	0.624	**52**	1.109	0.671	0.492	**76**	1.107	0.654	0.475
5	1.136	0.814	0.656	**29**	1.133	0.816	0.638	**53**	1.104	0.709	0.555	**77**	1.098	0.712	0.559
6	1.138	0.810	0.665	**30**	1.138	0.769	0.677	**54**	1.123	0.701	0.558	**78**	1.109	0.692	0.545
7	1.119	0.738	0.605	**31**	1.120	0.735	0.601	**55**	1.075	0.647	0.474	**79**	1.067	0.636	0.473
8	1.119	0.756	0.609	**32**	1.119	0.743	0.602	**56**	1.087	0.653	0.485	**80**	1.061	0.628	0.465
9	1.109	0.792	0.616	**33**	1.107	0.739	0.621	**57**	1.065	0.673	0.555	**81**	1.075	0.696	0.561
10	1.132	0.804	0.612	**34**	1.130	0.778	0.660	**58**	1.057	0.678	0.534	**82**	1.077	0.668	0.498
11	1.113	0.686	0.596	**35**	1.109	0.707	0.569	**59**	1.039	0.636	0.454	**83**	1.026	0.630	0.433
12	1.114	0.746	0.599	**36**	1.113	0.682	0.599	**60**	1.041	0.599	0.459	**84**	1.031	0.618	0.459
13	1.130	0.770	0.593	**37**	1.136	0.796	0.587	**61**	1.080	0.673	0.496	**85**	1.078	0.666	0.452
14	1.140	0.781	0.575	**38**	1.139	0.728	0.551	**62**	1.105	0.646	0.493	**86**	1.096	0.625	0.483
15	1.121	0.718	0.535	**39**	1.113	0.697	0.554	**63**	1.058	0.589	0.449	**87**	1.056	0.592	0.427
16	1.123	0.660	0.502	**40**	1.121	0.649	0.499	**64**	1.073	0.585	0.429	**88**	1.062	0.583	0.426
17	1.131	0.766	0.571	**41**	1.111	0.735	0.565	**65**	1.064	0.668	0.489	**89**	1.069	0.629	0.482
18	1.138	0.734	0.563	**42**	1.137	0.700	0.559	**66**	1.092	0.637	0.480	**90**	1.073	0.625	0.471
19	1.089	0.681	0.491	**43**	1.086	0.662	0.510	**67**	1.049	0.572	0.434	**91**	1.042	0.569	0.426
20	1.105	0.678	0.462	**44**	1.077	0.679	0.484	**68**	1.071	0.576	0.429	**92**	1.062	0.542	0.423
21	1.105	0.661	0.561	**45**	1.107	0.740	0.583	**69**	1.015	0.618	0.467	**93**	No DDT	0.614	0.455
22	1.060	0.716	0.549	**46**	1.074	0.694	0.569	**70**	1.011	0.617	0.461	**94**	0.972	0.595	0.456
23	1.035	0.650	0.494	**47**	1.055	0.678	0.511	**71**	0.828	0.538	0.413	**95**	0.298	0.518	0.398
24	1.035	0.662	0.484	**48**	1.042	0.671	0.475	**72**	0.973	0.532	0.408	**96**	0.916	0.530	0.392

Table 7.3: Obtained ^{56}Ni yields of Model III, Model VIII and Model X in Study A.

7.2.2 Study B

For Study B we construct new DDT criteria and try to obtain faint explosions with ^{56}Ni yields of $\lesssim 0.4\,M_\odot$ which were hardly found in Study A. At first we vary a single parameter, while we keep the other parameters constant. For the latter we can infer from the results of Study A which threshold values should be assigned to these parameters in order that preferentially faint explosion are obtained. Afterwards we construct very restrictive DDT criteria, where it is our intention to let some models fail to meet the DDT constraints in the simulations. Here we can draw some further conclusions on the necessary constraints for the occurrence of DDTs in deflagrations in white dwarfs. All DDT criteria of this study are summarized in Table 7.4.

A. Necessary constraints for faint explosions

For the quantity X_{fuel} we face the problem that a much further reduction of the allowed interval of this quantity than the most restrictive one used in Study A is not possible, since we perform lowly resolved simulations where $N^*_{\mathrm{flame}}(t)$ is generally small. Therefore, we do not vary X_{fuel} further, but use in the following exclusively $1/3 \leq X_{\mathrm{fuel}} \leq 2/3$. This is the most restrictive range for X_{fuel} where in all simulations of Study B enough data was available for the application of the DDT model (see also Section 5.3.3). We found in Study A that a different threshold value for $\tau_{\mathrm{eddy}_{1/2}}(\ell_{\mathrm{crit}})$ seems to have no effect on the produced ^{56}Ni yields, so we use only $\tau_{\mathrm{eddy}_{1/2}}(\ell_{\mathrm{crit}}) = 0.5 \times 10^{-2}\,\mathrm{s}$. A variation of A_{crit} is related to a variation of the fractal dimension D, where we always assume $\ell_{\mathrm{crit}} = 10^6\,\mathrm{cm}$. Since we use a constant value for D we do not vary A_{crit} to a larger extent and use (except for one criterion) $A_{\mathrm{crit}} = \ell_{\mathrm{crit}}^D$. Using these fixed threshold values for X_{fuel}, $\tau_{\mathrm{eddy}_{1/2}}(\ell_{\mathrm{crit}})$ and A_{crit} that favor the occurrence of faint explosions, only ρ_{fuel} and v'_{crit} are varied in the following.

Variation of the fuel density threshold

In Study A we found that DDTs in higher fuel densities produce brighter explosions. Here we analyze whether DDTs in fuel densities of $\rho_{\mathrm{fuel}} \geq 10^7\,\mathrm{g\,cm^{-3}}$ that have not been considered so far can still lead to faint events. Since very strong deflagrations produce the faintest explosions, we will only perform simulations with Model X. We further use $v'_{\mathrm{crit}} = 10^8\,\mathrm{cm\,s^{-1}}$ where fainter explosions were obtained in Study A. We use four different density ranges which correspond to criteria 97 - 100 in Table 7.4. The criterion 100 in which the full density range according to Woosley (2007) is covered, equals the criterion used in Section 5.4 for the resolution study where a similar ignition geometry (Model X*) was used.

Variation of the threshold value of the minimum required velocity fluctuations

For $v'_{\mathrm{crit}} = 0.5 \times 10^8\,\mathrm{cm\,s^{-1}}$ it was hardly possible to obtain faint explosions in Study A. Here we vary now v'_{crit} from $0.5 \times 10^8\,\mathrm{cm\,s^{-1}}$ to $1.0 \times 10^8\,\mathrm{cm\,s^{-1}}$ in steps of $0.1 \times 10^8\,\mathrm{cm\,s^{-1}}$ which constitute the six criteria 101 - 106 in Table 7.4.[3] We use for the range of allowed fuel densities exclusively $0.5 \times 10^7\,\mathrm{g\,cm^{-3}} \leq \rho_{\mathrm{fuel}} \leq 0.8 \times 10^7\,\mathrm{g\,cm^{-3}}$. We found in Section 6.2.3 that the behavior of the quantity $P(v'(\ell_{\mathrm{crit}}) \geq v'_{\mathrm{crit}})(t)$ depends strongly on the evolution of the turbulent deflagration. For this reason we cautiously apply the six DDT criteria to the six ignition models described in Section 7.1.

[3] Due to the uncertainties of the eddy turnover time (see Section 3.3.2) we do not vary $\tau_{\mathrm{eddy}_{1/2}}(\ell_{\mathrm{crit}})$ for each different threshold value of v'_{crit}.

Crit	ρ_{fuel} $[10^7\ \text{g cm}^{-3}]$	v'_{crit} $[10^8\ \text{cm s}^{-1}]$	$\tau_{\text{eddy}_{1/2}}$ $[10^{-2}\ \text{s}]$	A_{crit}	^{56}Ni Model III $N_{\text{k}} = 5$ $[M_\odot]$	^{56}Ni Model VI $N_{\text{k}} = 40$ $[M_\odot]$	^{56}Ni Model 5 $N_{\text{k}} = 60$ $[M_\odot]$	^{56}Ni Model VIII $N_{\text{k}} = 200$ $[M_\odot]$	^{56}Ni Model IX $N_{\text{k}} = 1600$ $[M_\odot]$	^{56}Ni Model X $N_{\text{k}} = 1600$ $[M_\odot]$
97	1.0 . . . 1.5	1.0	0.5	ℓ^D_{crit}	-	-	-	-	-	0.582
98	1.0 . . . 1.2	1.0	0.5	ℓ^D_{crit}	-	-	-	-	-	0.518
99	0.8 . . . 1.2	1.0	0.5	ℓ^D_{crit}	-	-	-	-	-	0.543
100	0.5 . . . 1.5	1.0	0.5	ℓ^2_{crit}	-	-	-	-	-	0.659
101	0.5 . . . 0.8	1.0	0.5	ℓ^D_{crit}	0.868	0.812	0.808	0.502	0.420	0.387
102	0.5 . . . 0.8	0.9	0.5	ℓ^D_{crit}	1.027	0.821	0.869	0.647	0.609	0.411
103	0.5 . . . 0.8	0.8	0.5	ℓ^D_{crit}	1.061	0.846	0.891	0.660	0.643	0.419
104	0.5 . . . 0.8	0.7	0.5	ℓ^D_{crit}	1.069	0.840	0.902	0.628	0.652	0.431
105	0.5 . . . 0.8	0.6	0.5	ℓ^D_{crit}	1.082	0.873	0.924	0.646	0.630	0.448
106	0.5 . . . 0.8	0.5	0.5	ℓ^D_{crit}	1.088	0.911	0.924	0.687	0.640	0.468
107	0.6 . . . 0.8	1.0	0.5	ℓ^2_{crit}	0.966	0.768	0.860	0.645	0.563	0.397
108	0.5 . . . 0.8	1.0	0.5	ℓ^2_{crit}	1.021	0.870	0.926	0.682	0.518	0.459
109	0.6 . . . 0.8	1.0	1.0	ℓ^2_{crit}	No DDT	0.822	0.832	0.623	0.530	0.362
110	0.5 . . . 0.8	1.0	1.0	ℓ^2_{crit}	1.012	0.915	0.892	0.655	0.500	0.459
111	0.6 . . . 0.8	1.0	5.0	ℓ^2_{crit}	No DDT	0.879	0.748	0.646	0.456	0.364
112	0.5 . . . 0.8	1.0	5.0	ℓ^2_{crit}	No DDT	0.929	0.873	0.611	0.450	0.476
113	0.6 . . . 0.8	1.0	0.5	ℓ^D_{crit}	No DDT	0.723	0.759	0.520	0.430	No DDT
114	0.6 . . . 0.8	1.0	1.0	ℓ^D_{crit}	No DDT	0.652	0.693	0.499	0.412	No DDT
115	0.5 . . . 0.8	1.0	1.0	ℓ^D_{crit}	0.932	0.793	0.808	0.536	0.411	0.388
116	0.6 . . . 0.8	1.0	5.0	ℓ^D_{crit}	No DDT	0.700	No DDT	0.486	No DDT	No DDT
117	0.5 . . . 0.8	1.0	5.0	ℓ^D_{crit}	No DDT	0.710	0.752	0.461	No DDT	0.370

Table 7.4: Setups of the DDT criteria for Study B and the obtained ^{56}Ni yields.

Conclusions for ρ_{fuel} and v'_{crit} from the simulation results

The obtained ^{56}Ni yields are shown in the upper part of Table 7.4. We see that with the criteria 97 - 100 no faint explosions with the very strong deflagration in Model X are obtained. Therefore, according to our DDT model, we exclude that DDTs which occur in regions with $\rho_{\mathrm{fuel}} \geq 10^7\,\mathrm{g\,cm^{-3}}$ can account for the whole observed variations in the brightness of normal SNe Ia. As expected we find with the criteria 101 - 106 an increase of the ^{56}Ni yield with decreasing v'_{crit}. But for Model X we can still find faint events with a ^{56}Ni mass of approximately $0.4\,M_\odot$ for threshold values of $v'_{\mathrm{crit}} < 10^8\,\mathrm{cm\,s^{-1}}$. However, for $v'_{\mathrm{crit}} = 0.5 \times 10^8\,\mathrm{cm\,s^{-1}}$ the explosion in Model X becomes principally too bright to be consistent with the faintest observed explosions of normal SNe Ia. Therefore, according to our DDT model, we find that if velocity fluctuations of $0.5 \times 10^8\,\mathrm{cm\,s^{-1}}$ are already sufficient for a DDT to occur, the observed faintest events of normal SNe Ia cannot be reproduced by delayed detonations. This agrees also with study A where for $v'_{\mathrm{crit}} = 0.5 \times 10^8\,\mathrm{cm\,s^{-1}}$ the lowest ^{56}Ni mass is found to be $0.433\,M_\odot$ (criterion 83 in Table 7.3).

B. Necessary constraints for a successful DDT

In the lower part of Table 7.4 the very restrictive DDT criteria 107 - 117 are shown which are applied to the six ignition models described in Section 7.1. In the following analysis and discussion the criterion 101 is included to complete the study consistently. We use exclusively $1/3 \leq X_{\mathrm{fuel}} \leq 2/3$ and $v'_{\mathrm{crit}} = 10^8\,\mathrm{cm\,s^{-1}}$ and vary the threshold values for ρ_{fuel}, A_{crit} and $\tau_{\mathrm{eddy}_{1/2}}(\ell_{\mathrm{crit}})$. For ρ_{fuel} only the two ranges with the lower densities of $0.6 \times 10^7\,\mathrm{g\,cm^{-3}} \leq \rho_{\mathrm{fuel}} \leq 0.8 \times 10^7\,\mathrm{g\,cm^{-3}}$ and $0.5 \times 10^7\,\mathrm{g\,cm^{-3}} \leq \rho_{\mathrm{fuel}} \leq 0.8 \times 10^7\,\mathrm{g\,cm^{-3}}$ are taken into account where fainter events are obtained. We use $A_{\mathrm{crit}} = \ell^2_{\mathrm{crit}}$ and $A_{\mathrm{crit}} = \ell^D_{\mathrm{crit}}$ for the critical flame surface area. Since we found for $\tau_{\mathrm{eddy}_{1/2}}(\ell_{\mathrm{crit}})$ no evidence that this quantity has an effect on the ^{56}Ni yield we use here a high value of $\tau_{\mathrm{eddy}_{1/2}}(\ell_{\mathrm{crit}}) = 5 \times 10^{-2}\,\mathrm{s}$ and analyze whether this behavior still holds. The criterion 107 equals the criterion of Study II in Chapter 6.

Results

The ^{56}Ni yields of these simulations are shown in the lower part of Table 7.4. We find that even for $A_{\mathrm{crit}} = \ell^2_{\mathrm{crit}}$ some faint explosions with ^{56}Ni yields of less than $0.4\,M_\odot$ can be obtained. In most simulations Model III fails to meet the DDT constraints. Here in the criteria where $A_{\mathrm{crit}} = \ell^2_{\mathrm{crit}}$, the condition $A_{\mathrm{det}}(t) \geq A_{\mathrm{crit}}$ cannot hold for high threshold values of $\tau_{\mathrm{eddy}_{1/2}}(\ell_{\mathrm{crit}})$. For $A_{\mathrm{crit}} = \ell^D_{\mathrm{crit}}$ even A_{crit} could frequently not be exceeded by $A_{\mathrm{det}}(t)$. In Model IX which shows weak turbulence (see discussion in Section 6.3.2), the condition $A_{\mathrm{det}}(t) \geq A_{\mathrm{crit}}$ can hold longer than $5 \times 10^{-2}\,\mathrm{s}$ only in the case of $A_{\mathrm{crit}} = \ell^2_{\mathrm{crit}}$. In Model X in which turbulence is even weaker than in Model IX the DDT criterion is met in all cases where $0.5 \times 10^7\,\mathrm{g\,cm^{-3}} \leq \rho_{\mathrm{fuel}} \leq 0.8 \times 10^7\,\mathrm{g\,cm^{-3}}$. For $A_{\mathrm{crit}} = \ell^D_{\mathrm{crit}}$, however, the DDT criterion is never met for $0.6 \times 10^7\,\mathrm{g\,cm^{-3}} \leq \rho_{\mathrm{fuel}} \leq 0.8 \times 10^7\,\mathrm{g\,cm^{-3}}$ in this model, regardless of the value of $\tau_{\mathrm{eddy}_{1/2}}(\ell_{\mathrm{crit}})$. We may expect here that since for a larger allowed interval for ρ_{fuel} there are more grid cells $N^*_{\mathrm{flame}}(t)$ which meet the DDT constraints, also $A^*_{\mathrm{flame}}(t)$ is larger and the DDT criterion can be met easier. However, a wider impact has the probability $P(v'(\ell_{\mathrm{crit}}) \geq v'_{\mathrm{crit}})(t)$ which is much higher for $0.5 \times 10^7\,\mathrm{g\,cm^{-3}} \leq \rho_{\mathrm{fuel}} \leq 0.8 \times 10^7\,\mathrm{g\,cm^{-3}}$ than for $0.6 \times 10^7\,\mathrm{g\,cm^{-3}} \leq \rho_{\mathrm{fuel}} \leq 0.8 \times 10^7\,\mathrm{g\,cm^{-3}}$ (see also discussion in Section 6.3.7), so that in the former case $A_{\mathrm{det}}(t) \geq A_{\mathrm{crit}}$ also holds for the higher threshold value of $A_{\mathrm{crit}} = \ell^D_{\mathrm{crit}}$. The fact that both values of $A^*_{\mathrm{flame}}(t)$ and $P(v'(\ell_{\mathrm{crit}}) \geq v'_{\mathrm{crit}})(t)$ are lower for an allowed

density range of 0.6×10^7 g cm$^{-3} \leq \rho_{\text{fuel}} \leq 0.8 \times 10^7$ g cm^{-3} (which makes it more difficult for the models to meet the DDT criterion) leads to the effect that the produced ^{56}Ni yields are on average lower than for simulations with the same DDT constraints except for an allowed density range of 0.5×10^7 g cm$^{-3} \leq \rho_{\text{fuel}} \leq 0.8 \times 10^7$ g cm^{-3}. The most restrictive DDT criterion is obviously criterion 116 where 2/3 of the models fail to meet the DDT constraints.

We find in Table 7.4 that the ^{56}Ni yield of Model 5 which has $N_{\text{k}} = 60$ is often slightly higher than Model VI which has only $N_{\text{k}} = 40$. When comparing both ignition setups in the Tables 4.1 and 4.2 we see that the values of d_{k} and σ (and hence R) are smaller for Model 5, leading to a smaller and more compact region in the interior of the white dwarf in which the deflagration commences. This probably leads to a slightly weaker deflagration phase prior to the first DDT than in Model VI, which may explain why Model 5 produces in simulations of delayed detonations on average slightly more ^{56}Ni. We will investigate this behavior in more detail in Study C by analyzing the impact of a variation of all parameters but N_{k} of the ignition geometry on the simulation results.

C. Summary and remarks

With the performed simulations we can now place some further constraints on individual DDT quantities. According to our DDT model, we find that if we allow DDTs to occur in regions with fuel densities of $\rho_{\text{fuel}} \geq 10^7$ g cm^{-3} no faint explosions are obtained. Moreover, if velocity fluctuations v'_{crit} of 0.5×10^8 cm s^{-1} are already sufficient for a DDT, than the probability $P(v'(\ell_{\text{crit}}) \geq v'_{\text{crit}})(t)$ is so high that DDTs are triggered frequently, leading to no faint events. We further find that the narrower the range of allowed values for X_{fuel} the fainter the explosions. The reason is that the DDT criterion becomes more stringent, since there are less grid cells $N^*_{\text{flame}}(t)$ and hence a smaller flame surface area $A^*_{\text{flame}}(t)$ that meet the DDT constraints. We note that the most restrictive range for X_{fuel} ensures that we capture mainly the grid cells that are clearly traversed by the flame.

In the case of a successful DDT in simulations in which the DDT criteria vary only in the threshold value of $\tau_{\text{eddy}_{1/2}}(\ell_{\text{crit}})$, there is no evidence whether this quantity affects the explosion brightness. There are, however, two other closely related side effects that occur if the chosen threshold value for $\tau_{\text{eddy}_{1/2}}(\ell_{\text{crit}})$ is high. First, it can happen that no DDTs occur in weak deflagrations, since due to the fast variations of the quantity $P(v'(\ell_{\text{crit}}) \geq v'_{\text{crit}})(t)$, $A_{\text{det}}(t)$ cannot exceed A_{crit} for a long time (see Section 6.2.3). The other effect appears frequently in strong deflagrations, where we find that if the DDT criterion is met, DDTs occur in a particularly large number of grid cells. The reason is that when the condition $A_{\text{det}}(t) \geq A_{\text{crit}}$ is reached, the lesser variations of the quantity $P(v'(\ell_{\text{crit}}) \geq v'_{\text{crit}})(t)$ and the growing flame surface area $A^*_{\text{flame}}(t)$ that meets the DDT constraints may lead to a continuous and uninterrupted increase of the quantity $A_{\text{det}}(t)$ for $\tau_{\text{eddy}_{1/2}}(\ell_{\text{crit}})$. At $t^{\text{1st}}_{\text{DDT}}$ eventually, $A_{\text{det}}(t) \gg A_{\text{crit}}$, hence F_{DDT} is very large and detonations are now initialized in various regions at the deflagration flame.

A higher threshold value of $\tau_{\text{eddy}_{1/2}}(\ell_{\text{crit}})$ leads further to the expected result that the number of time steps $N_{\text{t}_{\text{DDT}}}$ where DDTs occur becomes smaller. This, however, seems to have no significant effect on the obtained explosion brightness that probably results from the following compensating effect. For large $\tau_{\text{eddy}_{1/2}}(\ell_{\text{crit}})$, a large number of DDTs occur in many places in one or a few time steps. In contrast, for small $\tau_{\text{eddy}_{1/2}}(\ell_{\text{crit}})$ detonations are mostly initialized at a few locations only, but here the larger number of time steps where DDTs occur leads to the effect that detonations are also found in a large number of different

places in the end. In both cases, the burning due to detonations results in approximately the same ^{56}Ni mass. However, we find in the case of $\tau_{\mathrm{eddy}_{1/2}}(\ell_{\mathrm{crit}}) = 5 \times 10^{-2}\,\mathrm{s}$ that DDTs in weak deflagrations are prevented (consider Model III in Table 7.4). Hence, the required time for mixing the fuel and ash in potential DDT regions in weak deflagrations must be shorter than $5 \times 10^{-2}\,\mathrm{s}$ in order to trigger a DDT. If this is not the case, we cannot obtain bright explosions with approximately $0.9 \ldots 1.0\,M_{\odot}$ of ^{56}Ni anymore, so that delayed detonations cannot account for the whole observed variations in the brightness of normal SNe Ia.

Apart from some very restrictive DDT criteria in Table 7.4 we obtain only faint events for $A_{\mathrm{crit}} = \ell^{D}_{\mathrm{crit}}$, since $A_{\mathrm{det}}(t) \geq A_{\mathrm{crit}}$ is harder to meet (compare the results in Table 7.3). However, the uncertainty of the geometrical structure of the DDT regions prevents us to draw any strict conclusions here, even if the parameter study indicates that the assignment of a fractal dimension to DDT regions leads to results that explain the observed variations in the brightness of normal SNe Ia better. But we can also see in Table 7.4 that for $A_{\mathrm{crit}} = \ell^{D}_{\mathrm{crit}}$ in combination with very restrictive threshold values of the other parameters (e.g. criterion 116), no DDTs occur in most models. Here, either $A^{*}_{\mathrm{flame}}(t)$ is too small in weak deflagrations or turbulence is too weak in strong deflagrations to meet the DDT criterion.

From the parameter study we can further derive a feature of the DDT model, which concerns the degree of restrictiveness of the DDT criterion. For the quantities X_{fuel} and ρ_{fuel} we always use specific allowed intervals instead of one fixed threshold value. We already indicated that for too narrow allowed ranges for these quantities the DDT criterion may not be met in the entire simulation. This may have either a physical cause (for instance $A_{\mathrm{det}}(t)$ may not exceed A_{crit} due to the stringent DDT constraints) or a lack of sufficient data to construct and fit the histogram of $v'(\ell_{\mathrm{crit}})$. While both situations may appear for a too narrow allowed range of X_{fuel}, the quantity ρ_{fuel} behaves here differently. The reason is that the occurrence of high turbulent velocity fluctuations depends strongly on ρ_{fuel} (see also Section 5.2.6). If we extend the interval of allowed values of ρ_{fuel} to lower fuel densities, the DDT criteria become indeed easier to meet (compare for instance the results of Model X in Table 7.4 obtained for different criteria). In contrast, if we extend this range to higher fuel densities this effect is far less pronounced or the criterion becomes even more restrictive. We find that an extension of the intervals will definitely always lead to an increase of $A^{*}_{\mathrm{flame}}(t)$, but in the latter case the probability $P(v'(\ell_{\mathrm{crit}}) \geq v'_{\mathrm{crit}})(t)$ can be significantly lower. A similar behavior was found by the comparison of Model X in the analysis of Study II in Section 6.2 and the resolution study in Section 5.4. Here, the probability $P(v'(\ell_{\mathrm{crit}}) \geq v'_{\mathrm{crit}})(t)$ was higher in a narrower range of significantly lower densities (see discussion in Section 6.3.7). In terms of the restrictiveness of the DDT criterion we can summarize that if the range of allowed values for ρ_{fuel} is extended toward higher fuel densities, the occurring lower values of $P(v'(\ell_{\mathrm{crit}}) \geq v'_{\mathrm{crit}})(t)$ cannot be compensated by the larger flame surface area $A^{*}_{\mathrm{flame}}(t)$ that meet the DDT constraints, leading to a decrease of the potential detonation area $A_{\mathrm{det}}(t)$ and eventually to a more restrictive DDT criterion.

Apart from lower values of $P(v'(\ell_{\mathrm{crit}}) \geq v'_{\mathrm{crit}})(t)$ in regions with higher fuel densities[4], we showed in Study B that successful DDTs in regions with too high fuel densities are mostly incapable of producing faint explosions. However, although we are able to place a constraint on ρ_{fuel} for the occurrence of faint events in simulations of delayed detonations, we unfortunately cannot place strict constraints on this quantity for a DDT to occur generally.

In our study we were hardly able to reproduce the observed faint explosions of normal SNe Ia that yield approximately $0.4\,M_{\odot}$ of ^{56}Ni. Here we need very restrictive constraints

[4]That is also why model III in criterion 93 fails to meet the DDT criterion.

for DDTs to occur where too restrictive DDT criteria cannot be met particularly by models that have a weak deflagration phase. Therefore, the guarantee for a successful DDT in all our different ignition models and the capability of obtaining faint events are contrary effects.

7.2.3 Study C

For Study C we choose the criteria 68, 85, 107 and 115 for the following reasons. The corresponding simulations show a broad range of ^{56}Ni yields in Study A and Study B. Criterion 107 has already been applied to some different models in Chapter 6. Within the chosen four criteria we find some of the faint events that are difficult to obtain and in which detonations do not burn much fuel to ^{56}Ni. Apart from two simulations of Model I, all models meet the DDT criteria. Finally, the used parameter sets in the criteria are relatively diverse. All four criteria are applied to all ignition models shown in the Tables 4.1 and 4.2.

A. Correlation between the strength of the deflagration and the explosion brightness

The obtained ^{56}Ni yields of Study C are shown in Table 7.5. For comparison these tables partially include the results of Study A and Study B and Chapter 6. The simulations of the models which yield the highest and lowest amount of ^{56}Ni for a given criterion are marked in boldface. All models were also simulated as pure deflagrations, of which the ^{56}Ni yields are listed in the table as well. In Figure 7.2 we show the obtained ^{56}Ni yields as function of the number of ignition kernels N_k that set mainly the strength of the deflagration. For the simulated pure deflagrations, a saturation of the ^{56}Ni yield occurs at $N_\mathrm{k} \approx 200$, where for stronger deflagrations the ^{56}Ni yield begins to decrease again. This result is consistent with those found in Chapter 6, even if we obtain marginally different ^{56}Ni yields for equal models (compare Table 6.2 with Table 7.5) where the reason is a slight resolution dependence. In the simulated delayed detonations we see a clear trend that for a given DDT criterion the events become fainter with increasing N_k. Again, we observe a saturation that occurs at the compact Model X (where $N_\mathrm{k} = 1600$). The explosion in the models with larger N_k produce more ^{56}Ni (where this behavior can be seen better in Table 7.5 than in Figure 7.2 since there are more models with $N_\mathrm{k} = 1600$, of which the data points are vertically scattered in the figure). The reason is probably the less compact structure of the initial flame configuration for models with $N_\mathrm{k} \geq 3000$. Therefore, Model X which was already used in Study A and Study B provides the lowest ^{56}Ni yield in simulations of delayed detonations in all four DDT criteria. This means that for the criteria 68 and 85, where Model X produces more than $0.4\,M_\odot$ of ^{56}Ni, no event is obtained that may reproduce the faint explosions of normal SNe Ia. We see that the ^{56}Ni yields obtained from the criteria 85 and 107 are on average higher compared to the other two criteria. For each criterion the highest ^{56}Ni yield is not obtained in Model I but in Model II, because for the criteria 107 and 115 the DDT model could not be applied due to insufficient data, while for the other two criteria we obtain a slightly higher ^{56}Ni yield in Model II. Due to statistical uncertainties such incidents are expected.[5] However, particularly for the criteria 107 and 115 we obtain a range of ^{56}Ni yields that is fairly consistent with the observed variations in the brightness of normal SNe Ia (e.g. Contardo et al., 2000; Stritzinger et al., 2006; Mazzali et al., 2007).

[5] We can for instance vary the distance of the single ignition kernel to the center of the white dwarf in Model I or the distribution of the three ignition kernels in Model II several times and apply these new ignition geometries to the four criteria. Then we would expect that Model I produces on average more ^{56}Ni (provided the DDT criterion can be met), as in Study I in Chapter 6 (see Table 6.3).

Model	I	II	III	IV	V	VI	VII	VIII	IX	X
N_k	1	3	5	10	20	40	100	200	1600	1600
$^{56}Ni_{DEF}$	0.079	0.109	0.211	0.249	0.322	0.376	0.404	0.432	0.408	0.349
$^{56}Ni_{068}$	1.120	**1.135**	1.071	0.984	0.885	0.847	0.700	0.576	0.514	**0.429**
$^{56}Ni_{085}$	1.127	**1.145**	1.078	1.016	0.928	0.883	0.800	0.666	0.651	**0.452**
$^{56}Ni_{107}$	-	**1.130**	0.966	0.896	0.938	0.768	0.799	0.645	0.563	**0.397**
$^{56}Ni_{115}$	-	**1.124**	0.932	0.946	0.844	0.793	0.635	0.536	0.411	**0.388**
Model	1	2	3	4	5	6	7	8	9	10
N_k	5	30	40	50	60	60	80	125	150	175
$^{56}Ni_{DEF}$	0.216	0.380	0.385	0.474	0.376	0.376	0.422	0.415	0.441	0.435
$^{56}Ni_{068}$	1.087	0.828	0.801	0.693	0.811	0.844	0.737	0.680	0.644	0.642
$^{56}Ni_{085}$	1.099	0.871	0.856	0.755	0.886	0.889	0.824	0.761	0.766	0.743
$^{56}Ni_{107}$	1.086	0.905	0.882	0.778	0.860	0.842	0.854	0.631	0.693	0.778
$^{56}Ni_{115}$	1.062	0.794	0.784	0.521	0.808	0.719	0.717	0.618	0.562	0.617
Model	11	12	13	14	15	16	17	18	19	20
N_k	200	200	200	200	200	200	200	200	200	200
$^{56}Ni_{DEF}$	0.462	0.440	0.485	0.527	0.537	0.556	0.447	0.445	0.432	0.444
$^{56}Ni_{068}$	0.631	0.622	0.748	0.638	0.579	0.823	0.648	0.598	0.644	0.610
$^{56}Ni_{085}$	0.703	0.676	0.803	0.692	0.642	0.875	0.736	0.731	0.720	0.692
$^{56}Ni_{107}$	0.733	0.702	0.798	0.734	0.680	0.714	0.749	0.700	0.737	0.754
$^{56}Ni_{115}$	0.614	0.545	0.674	0.593	0.594	0.662	0.642	0.589	0.622	0.504
Model	21	22	23	24	25	26	27	28	29	30
N_k	200	250	300	350	400	500	600	700	800	900
$^{56}Ni_{DEF}$	0.550	0.455	0.418	0.416	0.444	0.450	0.419	0.414	0.423	0.404
$^{56}Ni_{068}$	0.618	0.596	0.615	0.623	0.595	0.570	0.566	0.541	0.601	0.548
$^{56}Ni_{085}$	0.643	0.694	0.620	0.655	0.700	0.662	0.649	0.627	0.679	0.621
$^{56}Ni_{107}$	0.651	0.681	0.550	0.709	0.752	0.660	0.682	0.702	0.525	0.600
$^{56}Ni_{115}$	0.595	0.551	0.442	0.583	0.558	0.529	0.513	0.490	0.511	0.484
Model	31	32	33	34	35	36				
N_k	1000	1200	1400	1600	3000	5000				
$^{56}Ni_{DEF}$	0.420	0.410	0.419	0.415	0.417	0.379				
$^{56}Ni_{068}$	0.542	0.546	0.463	0.487	0.471	0.657				
$^{56}Ni_{085}$	0.621	0.608	0.623	0.551	0.520	0.753				
$^{56}Ni_{107}$	0.537	0.573	0.558	0.576	0.517	0.648				
$^{56}Ni_{115}$	0.453	0.475	0.461	0.477	0.454	0.661				

Table 7.5: Obtained ^{56}Ni yields of Study C. Shown are the results of simulations of pure deflagrations ($^{56}Ni_{DEF}$) and delayed detonations ($^{56}Ni_{068}$, $^{56}Ni_{085}$, $^{56}Ni_{107}$, $^{56}Ni_{115}$) using the DDT criteria 68, 85, 107 and 115 after 100 seconds.

B. The influence of the secondary parameters of the ignition geometry of the deflagration on the explosion brightness

With a fixed number of $N_k = 200$ we vary the other parameters of the ignition geometry, where these setups correspond to the standard Model VIII in Table 4.1 and Model 11 - Model 21 in Table 4.2. The vertical scatter in the ^{56}Ni yield at $N_k = 200$ seen in Figure 7.2 results

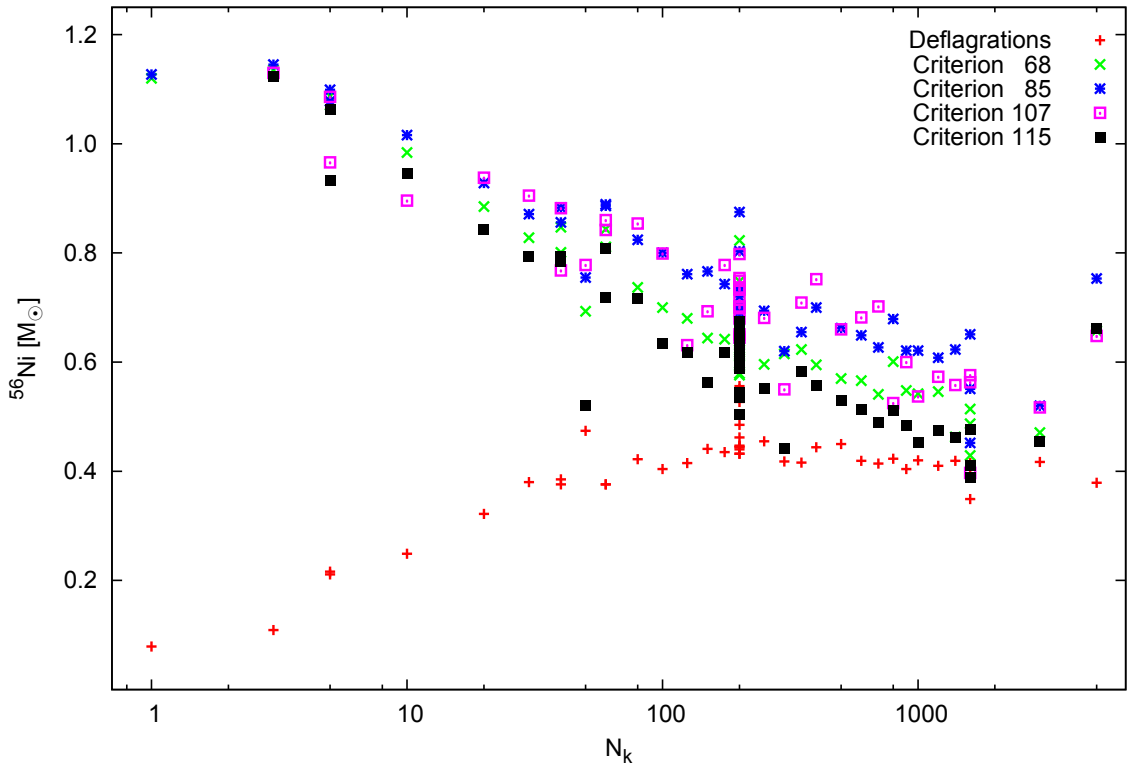

Fig. 7.2: Obtained ^{56}Ni yields after 100 seconds as function of N_k in simulations of pure deflagrations and delayed detonations using four different DDT criteria.

from these different ignition models. Obviously the secondary parameters of the ignition geometry affect the explosion brightness to a certain degree.

From the obtained ^{56}Ni yields in Table 7.5 we can draw the following conclusions. With increasing σ and hence a larger allowed distance from the center of the white dwarf for the placement of the ignition kernels that is given by $R = 2.5 \cdot \sigma$ (see Chapter 4.2.2), pure deflagrations become brighter. In particular for large σ, we obtain ^{56}Ni yields higher than $0.5\,M_\odot$ (e.g. Model 14 - Model 16). This behavior can be expected, since for higher σ the ignition occurs in a larger area in the interior of the white dwarf. There are also some isolated sources which are composed of a few merged ignition kernels in which thermonuclear burning occurs decoupled from other sources for some time. However, from a physical point of view we argue that the larger σ the more inappropriate are the thermodynamic conditions for the ignition of the deflagration at R (e.g. Wunsch & Woosley, 2004; Zingale et al., 2009; Nonaka et al., 2012). The behavior that the ^{56}Ni yield rises with increasing σ does not hold for simulations of delayed detonations.

We found no clear conclusion of how the parameters r_k and d_k affect the explosion brightnesses but we see that a variation of them leads to different ^{56}Ni yields in the simulations of pure deflagrations and delayed detonations. As indicated in Section 4.2.2 a variation of both quantities lead to different initial perturbations at the deflagration flame, since these quantities affect the time of the merger of the ignition kernels and the occurrence of different kinks and bends at the flame from which instabilities may arise. This results in slightly other evolutions of the deflagrations in which different masses of the fuel are burned to heavier

elements. In simulations of delayed detonations this effect leads further to a different distribution of DDT regions, where these distributions may vary strongly even for only slightly different initial flame configurations of the deflagration like those considered here. This also explains why in contrast to pure deflagrations no clear conclusion can be drawn of how the parameter σ affects the produced amount of ^{56}Ni in simulations of delayed detonations.

However, this behavior may change to a certain extent in a study of weaker deflagrations with smaller N_k. For instance, we see in Table 7.5 that the ^{56}Ni yields after 100 seconds of the simulated pure deflagrations of Model 5 which has $N_\mathrm{k} = 60$ and $\sigma = 0.4$ and Model VI which has only $N_\mathrm{k} = 40$ but $\sigma = 0.6$ are equal. In Study B it was found that Model 5 often produces slightly more ^{56}Ni than Model VI so that we may expect that at the time $t_\mathrm{DDT}^\mathrm{1st}$ where the first DDT occurs, Model VI had a stronger deflagration phase than Model 5. In addition, we may assume that the distribution of DDT regions has only a low influence on the dynamics of subsequent detonations and on the explosion brightness in these relatively weak deflagrations (see also Section 6.3.1). Therefore, we expect that the smaller N_k the higher is the impact of the secondary parameters σ, d_k and r_k of the ignition geometry on the deflagration strength and hence on the brightness of the explosion of both pure deflagrations and delayed detonations. The different evolution of deflagrations for different distributions of the ignition kernels within a given parameter set for the ignition geometry (e.g. Model VI in Table 4.1 and Model 3 in Table 4.2) leads also to a variation of the ^{56}Ni yields in simulations of both pure deflagrations and delayed detonations.

C. The impacts of the expansion of the white dwarf at $t_\mathrm{DDT}^\mathrm{1st}$ and the distribution of the DDT regions on the explosion brightness

In Section 6.3.1 we discussed two characteristics that determine the ^{56}Ni production in the detonation phase in simulations of delayed detonations. These characteristics are the degree of the pre-expansion of the white dwarf prior to the first DDT and the distribution of the DDT regions. With the performed parameter study we can investigate both effects in more detail. As indicated in Section 6.3.1 the degree of expansion of the white dwarf in the late deflagration phase can be estimated with the nuclear energy release E_nuc. In a similar way, we assume now that E_nuc at $t_\mathrm{DDT}^\mathrm{1st}$ can also be considered as a proxy of how occurring detonations affect the further ^{56}Ni production. We show in Figure 7.3 the ^{56}Ni yield after 100 seconds as function of E_nuc at $t_\mathrm{DDT}^\mathrm{1st}$ for all performed simulations of delayed detonations of the entire parameter study, where only simulations with successful DDTs are taken into account.

We see the tendency that the obtained ^{56}Ni yields decrease with higher values of E_nuc at $t_\mathrm{DDT}^\mathrm{1st}$. Except for a few outliers this trend is more pronounced for weaker deflagrations, where E_nuc at $t_\mathrm{DDT}^\mathrm{1st}$ is low. Hence for weak deflagrations, E_nuc at $t_\mathrm{DDT}^\mathrm{1st}$ can be used to estimate the explosion brightness. For strong deflagrations where E_nuc at $t_\mathrm{DDT}^\mathrm{1st}$ is high we see that the corresponding data points in Figure 7.3 are significantly more vertically scattered, indicating that for a given degree of expansion a large variation of the ^{56}Ni yield can be obtained. This confirms our assumption that the distribution of DDT regions at the deflagration flame becomes more important for strong deflagrations. In this context, we described in Study A a simulation in which a single DDT occurs but nearly no further burning happens after the onset of the detonation (Model III using criterion 95). Here (even if this event occurs in a weak deflagration) solely the location of the DDT region determines (or prevents) the further ^{56}Ni production, whereas E_nuc at $t_\mathrm{DDT}^\mathrm{1st}$ cannot be used to estimate the explosion brightness anymore. This event becomes apparent in the isolated data point in the lower

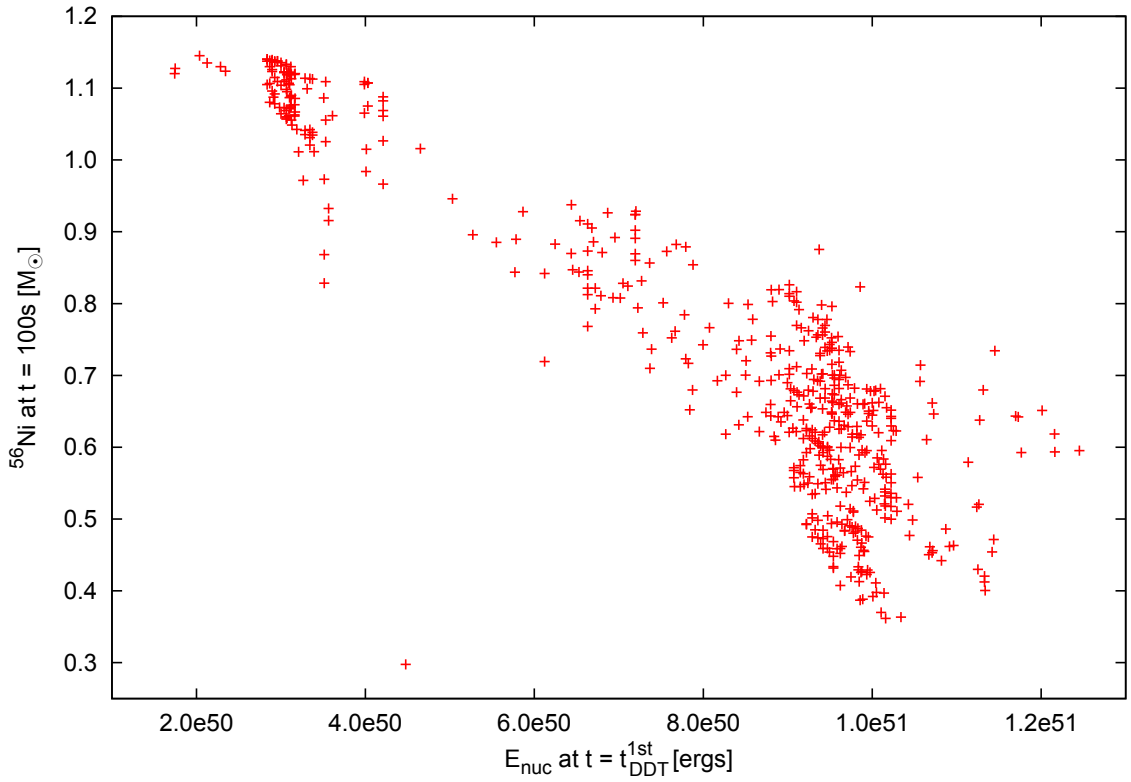

Fig. 7.3: The obtained ^{56}Ni yields after 100 seconds as function of the nuclear energy release E_{nuc} at $t^{1\mathrm{st}}_{\mathrm{DDT}}$ for all simulations of delayed detonations with successful DDTs.

left part in Figure 7.3. However, we also find for instance in several simulations of Model IX which has a strong deflagration phase, that for very restrictive DDT criteria the few initialized detonations burn only a very small part of the remaining fuel to ^{56}Ni (compare the ^{56}Ni yields of Model IX of the simulated deflagration and delayed detonations in the Tables 7.4 and 7.5).

7.2.4 Conclusions from the parameter study

In this section we described a parameter study of delayed detonations in which the newly implemented DDT model of Chapter 5 was used. With a wide range of simulations with different ignition models of the deflagration we showed that the DDT model leads to broad variations of the ^{56}Ni yields in several DDT criteria. From the result, whether for a given DDT criterion predominantly bright or faint events can be obtained and whether specific ignition models fail to meet some of our proposed DDT criteria we were further able to place some constraints on certain DDT quantities. In particular, we found no faint explosions if detonations occur at fuel densities higher than 10^7 g cm^{-3} and for the case that the minimum required velocity fluctuations for DDTs are far lower than 10^8 cm s^{-1}. For the occurrence of DDTs in weak deflagrations that produce the bright explosions of normal SNe Ia, the mixing time $\tau_{\mathrm{eddy}_{1/2}}$ of fuel and ash has to be faster than 5×10^{-2} s. In the case of a critical flame surface area of $A_{\mathrm{crit}} = \ell^2_{\mathrm{crit}}$, we hardly found faint explosions that are far more frequently obtained for $A_{\mathrm{crit}} = \ell^D_{\mathrm{crit}}$. However, for $A_{\mathrm{crit}} = \ell^D_{\mathrm{crit}}$ in combination with too restrictive

threshold values of the other DDT quantities, detonations will not occur in both weak and strong deflagrations, because for the former A^*_{flame} is too small and for the latter turbulence is too weak to meet the DDT criterion.

We underpinned the correlation between the strength of the deflagration and the brightness of the explosion in simulations of delayed detonations, where strong deflagrations lead to faint events and vice versa. Within the modeled ignition scenario, the number of ignition kernels N_{k} is the main parameter that sets the strength of the deflagration. In pure deflagrations, however, we find that the larger the allowed radius $R = 2.5 \cdot \sigma$ of the spherical region in which a given number of ignition kernels is distributed the more ^{56}Ni is produced. We find that the stronger the deflagration (and hence the larger the pre-expansion of the white dwarf prior to the first DDT) the higher is the impact of different distributions of the DDT ignition spots on the dynamics of subsequent detonations. This behavior leads to an additional variation of the ^{56}Ni yields, and hence of the explosion brightnesses.

7.3 The role of the white dwarfs initial central density in simulations of delayed detonations

The study described in this section is based on an analysis of highly resolved simulations of delayed detonations that has been published by Seitenzahl et al. (2011). We described in Section 2.3.1 that details of the final state in the simmering phase where the ignition of the deflagration occurs at the end of the convection stage in the center of the white dwarf are unknown. Therefore, the ignition scenario is generally parameterized. So far we investigated the impact of different ignition models of the deflagration on the explosion brightnesses, where only the distribution of ignition kernels was varied. This, however, is basically only one of several parameters of the initial model of the white dwarf (see Section 4.2.1).

In this section we closely follow the arguments described in the paper of Seitenzahl et al. (2011) and investigate the role of different central densities ρ_{c} of the white dwarfs at the time of deflagration ignition on the explosion brightness in simulations of delayed detonations. Using the new DDT model we perform 12 simulations with a resolution of 512^3 grid cells. To obtain different strengths of the deflagration phase we use the three ignition models of Study A for the initial flame configuration. We carry out six simulations of Model VIII and three simulations of Model III and Model X. Within each of these three simulation sets, the white dwarf models vary only in the initial central density ρ_{c}. For the DDT model we choose criterion 23 that is met in all simulations.

7.3.1 Introduction

Krueger et al. (2010) propose a connection between the age of the host stellar population and the explosion brightness of SNe Ia. By considering the effect of a longer cooling time on the central density of the white dwarf the authors investigated the impact of different central densities at the time of deflagration ignition on the explosion brightness. Using 150 two-dimensional simulations of delayed detonations within the statistical framework presented in Townsley et al. (2009), it was found that the total IGE yield seems to be largely independent of ρ_{c}. However, the thermonuclear burning at higher densities leads to a stronger neutronization that results from a higher rate of electron captures. Therefore, with increasing ρ_{c} an enhanced production of stable isotopes of the iron group occurs, while the fraction of ^{56}Ni to the total IGE yield decreases. The stronger neutronization at higher

densities, however, is only one of three partly opposed effects that have an impact on the ^{56}Ni production in the delayed detonation scenario. These effects are summarized in the following:

1. Under electron-degenerate conditions, electron capture rates on protons and iron group isotopes increase strongly with density (Langanke & Martínez-Pinedo, 2001). Hence, at higher densities a distribution of nuclei in nuclear statistical equilibrium neutronizes much faster (e.g. Seitenzahl et al., 2009b), leading to a lower ^{56}Ni yield.

2. With increasing ρ_c Chandrasekhar-mass white dwarfs in hydrostatic equilibrium have a smaller radius and a slightly higher mass, thus they are more compact and tightly bound. Therefore, at the time when DDTs occur, the white dwarf may also be more compact, leading to the burning of a larger part of the white dwarf to IGE in the detonation phase, which raises the ^{56}Ni yield.

3. White dwarfs that are more tightly bound have a higher gravitational acceleration. The growth rate of the RT instability scales with $\sqrt{g_{\mathrm{eff}}}$ (see equation (3.8)). Consequently, the evolution of turbulent deflagrations depends on g_{eff} (Khokhlov, 1995; Zhang et al., 2007), and hence on the initial central density ρ_c. Different deflagrations in turn affect the occurrence of detonations. Depending on the pre-expansion of the white dwarf prior to the first DDT and the distribution of the DDT spots, the total produced ^{56}Ni mass in the detonation phase may either be lower or higher.

7.3.2 Remarks on the analysis

The simulations in the study of Krueger et al. (2010) were carried out in two dimensions, where a large number of models could be analyzed. But in two-dimensional simulations the question arises whether all physical effects, such as the propagation of turbulent flames are treated properly. This is why we carry out three-dimensional full-star simulations. However, the high computational demand to perform highly resolved three-dimensional simulations prevents us to carry out a detailed statistic approach that would be comparable with those of Townsley et al. (2009), Krueger et al. (2010) and Jackson et al. (2010). For ρ_c we choose some specific values, so that the initial central densities cover the expected range due to different cooling ages and differences in the accretion history (Lesaffre et al., 2006) (see also Section 2.3.1). The DDT criterion in combination with the used ignition models is selected in a way to obtain a range of ^{56}Ni yields between $\sim 0.5\,M_\odot$ and slightly more than $1.0\,M_\odot$ for a constant central density of $\rho_c = 2.9 \times 10^9\,\mathrm{g\,cm^{-3}}$ (see Table 7.3). Following Krueger et al. (2010) we may expect that for $\rho_c > 2.9 \times 10^9\,\mathrm{g\,cm^{-3}}$, the ^{56}Ni yields will be shifted toward fainter explosions that would be more consistent with the observed variations in the brightness of normal SNe Ia. We have to take into account, however, that the above-mentioned ^{56}Ni yields were obtained from lower resolved simulations of the parameter study. Since the deflagration phase and particularly the distribution of DDT regions are resolution-dependent (see Section 5.3.3) we expect a certain deviation of the obtained ^{56}Ni yields for the same initial central density of $\rho_c = 2.9 \times 10^9\,\mathrm{g\,cm^{-3}}$. The white dwarf model meets the model described in Section 4.2.1 with the only difference that the initial central density ρ_c is varied between $1.0 \times 10^9\,\mathrm{g\,cm^{-3}}$ and $5.5 \times 10^9\,\mathrm{g\,cm^{-3}}$ (see Table 7.6).

Model	ρ_c [10^9 g cm^{-3}]	t_{DDT}^{1st} [s]	$E_{nuc}^{(t_{DDT}^{1st})}$ [10^{51} ergs]	$\rho_c^{(t_{DDT}^{1st})}$ [10^8 g cm^{-3}]	$\bar{\rho}^{(t_{DDT}^{1st})}$ [10^7 g cm^{-3}]
III	1.5	1.253	0.334	4.911	0.773
III	3.5	0.890	0.246	11.610	0.758
III	5.5	0.911	0.488	6.183	0.716
VIII	1.0	1.135	0.587	1.450	0.700
VIII	1.5	0.993	0.667	1.706	0.746
VIII	2.9	0.802	0.803	2.270	0.756
VIII	3.5	0.756	0.838	2.533	0.749
VIII	4.0	0.755	0.936	2.193	0.759
VIII	5.5	0.679	0.930	2.711	0.761
X	1.5	1.077	0.813	0.718	0.705
X	3.5	0.848	0.990	0.827	0.779
X	5.5	0.757	1.087	0.875	0.755

Table 7.6: Performed simulations of delayed detonations of Model III, Model VIII and Model X with different initial central densities ρ_c at the time of deflagration ignition. Shown are the time t_{DDT}^{1st} of the first DDT and the corresponding nuclear energy release $E_{nuc}^{(t_{DDT}^{1st})}$, the central density $\rho_c^{(t_{DDT}^{1st})}$ and the average density of the first DDT region(s) $\bar{\rho}^{(t_{DDT}^{1st})}$ at this time (Seitenzahl et al., 2011).

7.3.3 Results

The lower expansion in weak deflagrations (Model III) leads to a higher central density at t_{DDT}^{1st}. Hence, a larger fraction of the total mass of the white dwarf is burned to IGE during the detonation phase (see Table 7.7). The opposite behavior holds for strong deflagrations. Therefore also for different initial central densities of the white dwarf, the strength of the deflagration acts as a primary parameter that determines the brightness of the explosion in simulations of delayed detonations (see Figure 7.4(a)).[6] The comparison of the simulations where ρ_c equals or is close to the value of our standard model with $\rho_c = 2.9 \times 10^9$ g cm^{-3} reveals that the higher resolved simulations in this study yield higher ^{56}Ni masses (compare the ^{56}Ni yields for criterion 23 in Table 7.3 with those in Table 7.7 for $\rho_c = 2.9 \times 10^9$ g cm^{-3} and $\rho_c = 3.5 \times 10^9$ g cm^{-3}). This results from the resolution-depending effects described in Section 5.3.3. For our standard setup with $\rho_c = 2.9 \times 10^9$ g cm^{-3} we see in Table 6.2 and 6.3 that stronger deflagrations show a higher neutronization. This trend is even more pronounced for models with higher initial central density (see Figure 7.4(b) and Table 7.7).

For a given initial flame configuration we find that models with higher initial central density show a significantly faster growth rate in the generation of turbulent energy E_{turb} (see Figure 7.5), which in turn leads to the effect that already at relatively early times, high turbulent velocity fluctuations occur.[7] This can be explained by the difference of the effective

[6] We emphasize that a stronger neutronization and the associated enhanced production of stable isotopes of the iron group affect the radiative transport processes, which in turn influences the explosion brightness (see Section 2.1.1). Therefore, particularly for models with higher initial central density the obtained ^{56}Ni yields do not correlate with the explosion brightness very well.

[7] As discussed in Section 6.3.2 the different values of E_{turb} may also result to some extent from different grid expansions. On the other hand, a faster grid expansion of models with a higher initial central density retroactively implies a faster evolution of the turbulent deflagration.

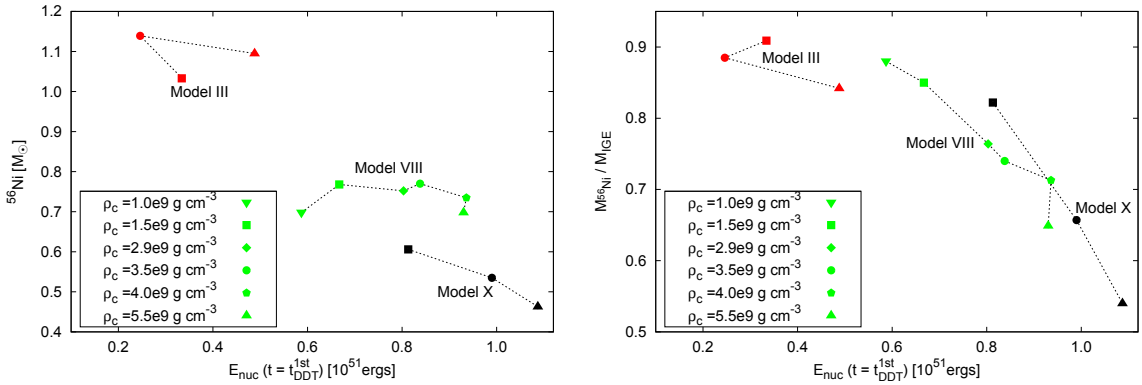

Fig. 7.4: Shown are the obtained ^{56}Ni yields (a) and the mass fractions of ^{56}Ni to the total synthesized IGE (b) as function of $E_{\rm nuc}$ at $t^{\rm 1st}_{\rm DDT}$ for the different simulated models. We see that the strength of the deflagration (estimated with $E_{\rm nuc}$ at $t^{\rm 1st}_{\rm DDT}$) is a good proxy for the ratio of ^{56}Ni to IGE (Seitenzahl et al., 2011).

gravitational acceleration $g_{\rm eff}$. For higher initial central densities there is a more compact mass distribution, hence $g_{\rm eff}$ is higher. For the Rayleigh-Taylor unstable deflagration front, the turbulent burning speed scales with $\sqrt{g_{\rm eff}}$ (see equation (3.27)). Therefore, for a given instant of time (e.g. 0.3 s) models with higher initial central density have burned a much larger amount of the stellar material than models with lower initial central density (compare Figures 7.6(b) and 7.6(c)). It further follows that the higher the initial central density the earlier the DDT criterion is met (see Table 7.6, but also note the outlier in Model III for 3.5×10^9 g cm^{-3}). We see the tendency that models with a higher initial central density also have a higher central density at $t = t^{\rm 1st}_{\rm DDT}$. The latter can be considered as a proxy of the fraction of fuel that can be burned at sufficiently high densities to IGE due to the ensuing detonations.

Within each of the ignition models we find that the total IGE yield increases with $\rho_{\rm c}$, while for Model III and Model VIII the ^{56}Ni yield appears constant, independent of $\rho_{\rm c}$ (see Figure 7.7 and Table 7.7). Only Model X shows the trend of a decreasing ^{56}Ni mass with increasing $\rho_{\rm c}$ (see Figure 7.7(b) and Table 7.7). In conclusion, our results are different from the results obtained by Krueger et al. (2010), where the authors found that with increasing $\rho_{\rm c}$, the total IGE yield remains constant while the ^{56}Ni mass decreases.

7.3.4 Discussion

A possible explanation of our obtained results concerning the ^{56}Ni yield, is a simultaneous or coincidental balance of opposing, partly suspending and competing effects that we indicated in Section 7.3.1. The stronger neutronization at higher central densities is compensated by the larger amount of produced IGE due to the compactness and higher gravitational acceleration of the white dwarf and the associated faster evolution of the flame toward DDT. The models with a higher initial central density show at early times a larger growth rate of turbulent energy, leading to a faster increase of the flame speed. The deflagration flame, still affected by strong turbulence approaches the low-density outer layers of the white dwarf earlier. Hence, the DDT criterion is also met earlier, when the central density of the

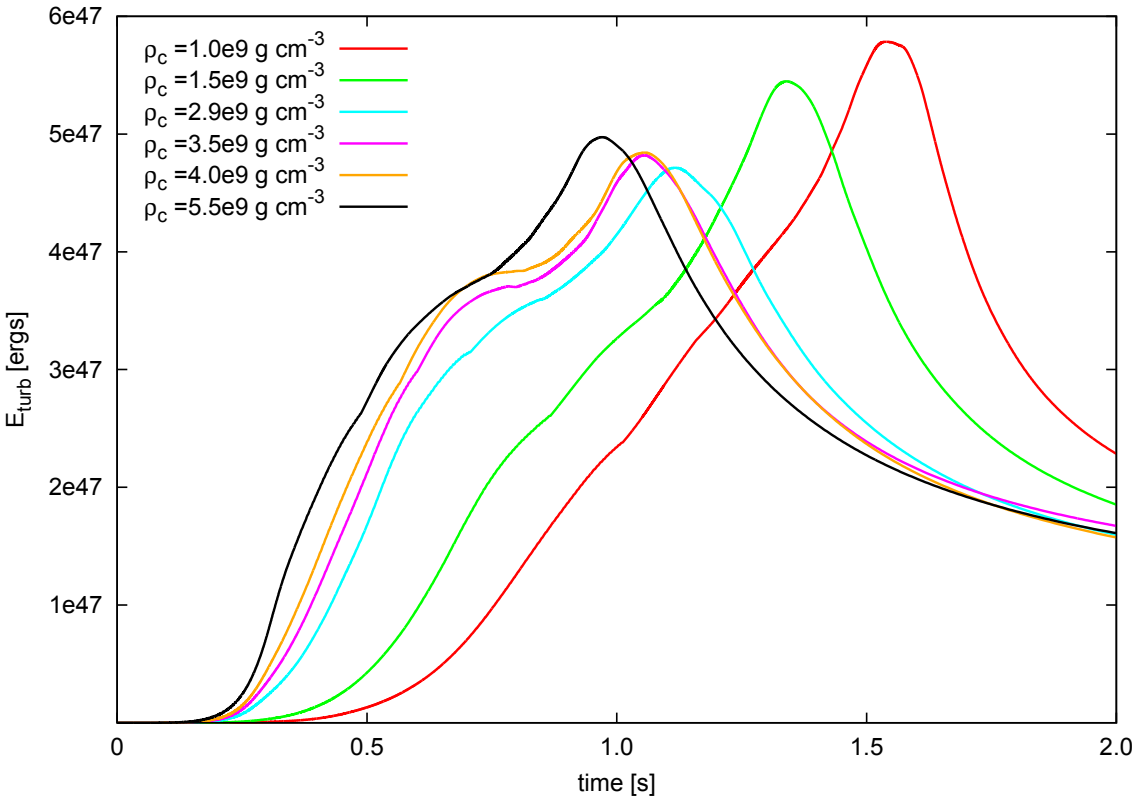

Fig. 7.5: Turbulent subgrid-scale energy E_{turb} as function of time for all six simulations of Model VIII. We see that the growth rate of E_{turb} is faster for models with higher initial central density ρ_{c} (Seitenzahl et al., 2011).

star is higher (see Table 7.6). In summary, we find that models with higher initial central density yield more IGE but due to the enhanced neutronization the fraction of ^{56}Ni to IGE decreases. As a result, the obtained ^{56}Ni mass appears to be approximately constant.

Model X with its compact dense initial flame configuration of the deflagration behaves differently. Here the major part of the central area of the white dwarf is burned out before the first DDT is triggered. The IGE that is synthesized in strong deflagrations provides already a significant fraction of the total IGE yield (see Tables 7.7 and 6.3). Moreover, these IGEs consist of a large fraction of neutron-rich stable iron group isotopes, since the electron captures occur extensively behind the deflagration flame at high densities. This effect is more pronounced in models with a higher initial central density. Therefore, the enhanced production of IGEs in cases where the deflagration already provides the major fraction of the total produced IGE mass does not result in a higher mass of ^{56}Ni. Finally the large expansion of the white dwarf in strong deflagrations lead to a very large decrease of the central density at $t_{\mathrm{DDT}}^{\mathrm{1st}}$. Therefore, occurring detonations are unable to burn sufficient fuel to ^{56}Ni to counteract to this trend. However, we note that explosions in which such large amounts of neutron-rich IGE material is synthesized cannot explain the majority of SN Ia explosions (e.g. Woosley, 1997).

Our study proposes a higher mass of IGE and a constant ^{56}Ni yield with increasing central density of the white dwarf at the time of deflagration ignition. This result is not in agreement with the study of Krueger et al. (2010) where a decrease of the ^{56}Ni yield and a constant

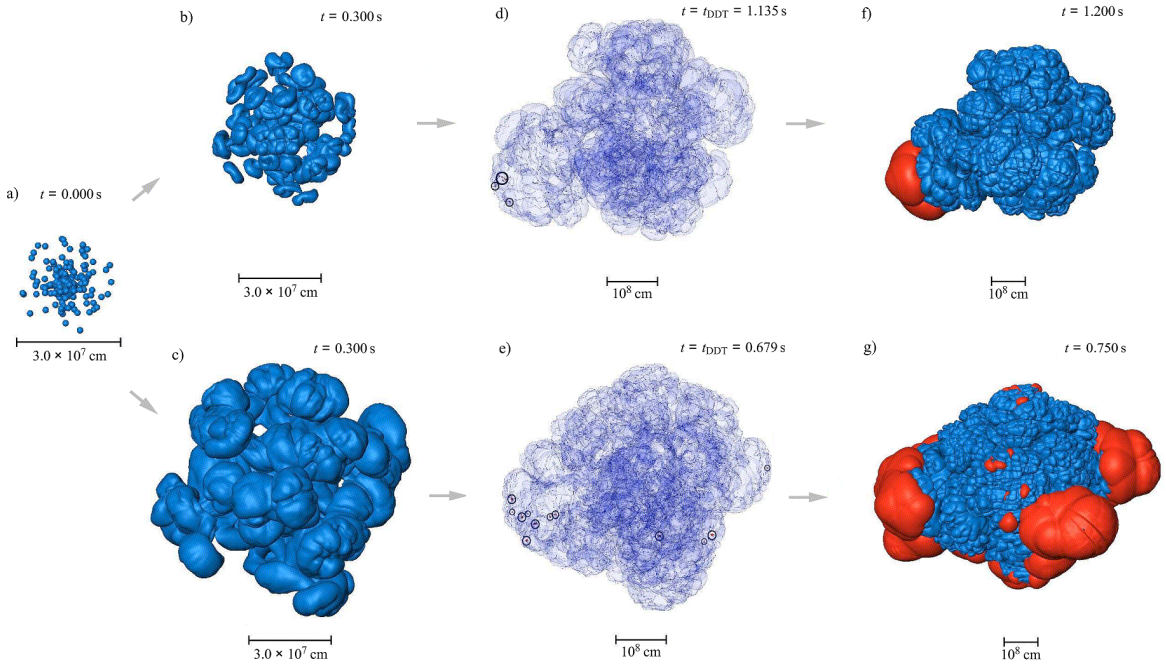

Fig. 7.6: Shown are the deflagration level set (blue) and the detonation level set (red) for Model VIII with the lowest (upper row, $\rho_c = 1.0 \times 10^9$ g cm^{-3}) and highest (lower row, $\rho_c = 5.5 \times 10^9$ g cm^{-3}) initial central density. (a) Both simulations have the same initial flame configuration. (b/c) At $t = 0.3$ s the deflagration of the model with the higher initial central density has burned significantly more of the stellar material. (d/e) The time $t_{\mathrm{DDT}}^{\mathrm{1st}}$ of the first DDT. Regions where DDTs occur are encircled. The first DDT happens much earlier in the model with the higher initial central density. (f/g) The detonations evolve from the DDT sources and propagate through the unburned material. Further detonations occur as long as the DDT criterion stays fulfilled. Despite the differences in the temporal evolution and the morphology of the explosion, both models yield approximately the same ^{56}Ni mass (Seitenzahl et al., 2011).

IGE mass was found with increasing ρ_c. A possible explanation for the disagreement of the trends between both studies is the difference of the method how the DDT is triggered. We mentioned in Section 3.3.1 that in most delayed detonation models, DDTs are triggered *per hand*, where commonly a certain density threshold is used at which the deflagration flame transitions into a detonation. In a recent study of Jackson et al. (2010) it was found that there is a quadratic dependence between the produced IGE and the logarithm of the transition density. In our study we used no transition density but the DDT model from Chapter 5 that takes into account the effect of different evolutions of the turbulent deflagration on the occurrence of DDTs. We emphasize again at this point that the decisive parameter for the DDT is not a transition density but the turbulence properties at the deflagration flame. In our simulations the DDT model begins to act at densities, just below 10^7 g cm^{-3}. Here Jackson et al. (2010) showed with a statistical set of simulations using such a transition density that the variation of the ^{56}Ni yields is relatively large (see Figure 3 in Jackson et al. (2010)), which is in agreement with our range of obtained ^{56}Ni yields.

In general, there are various other differences between our study and the one performed by Krueger et al. (2010). For instance, the treating of the propagation of the flame and

the nuclear energy release, the dimension (2D vs. 3D) as well as the numerical approach (adaptive mesh refinement vs. co-moving grid technique) may contribute to deviations and differences of the results.

Model	ρ_c $[10^9\ \mathrm{g\ cm^{-3}}]$	M_{tot} $[M_\odot]$	$\mathrm{IGE}(t^{\mathrm{1st}}_{\mathrm{DDT}})$ $[M_\odot]$	$^{56}\mathrm{Ni}(t^{\mathrm{1st}}_{\mathrm{DDT}})$ $[M_\odot]$	IGE $[M\odot]$	^{56}Ni $[M_\odot]$	IME $[M_\odot]$	^{12}C $[M_\odot]$	^{16}O $[M_\odot]$	$\frac{\mathrm{IGE}(t^{\mathrm{1st}}_{\mathrm{DDT}})}{\mathrm{IGE}}$	$\frac{^{56}\mathrm{Ni}(t^{\mathrm{1st}}_{\mathrm{DDT}})}{^{56}\mathrm{Ni}}$	$\frac{^{56}\mathrm{Ni}}{\mathrm{IGE}}$
III	1.5	1.378	0.221	0.182	1.136	1.033	0.205	0.004	0.033	0.195	0.176	0.909
III	3.5	1.406	0.168	0.125	1.287	1.139	0.100	0.002	0.017	0.131	0.110	0.885
III	5.5	1.416	0.288	0.172	1.301	1.095	0.098	0.002	0.015	0.221	0.157	0.842
VIII	1.0	1.361	0.385	0.321	0.793	0.698	0.447	0.017	0.104	0.485	0.460	0.880
VIII	1.5	1.378	0.447	0.348	0.904	0.768	0.390	0.012	0.073	0.494	0.453	0.850
VIII	2.9	1.400	0.547	0.359	0.984	0.752	0.346	0.008	0.063	0.556	0.477	0.764
VIII	3.5	1.406	0.573	0.354	1.040	0.770	0.307	0.006	0.053	0.551	0.460	0.740
VIII	4.0	1.409	0.622	0.375	1.031	0.735	0.314	0.007	0.057	0.603	0.510	0.713
VIII	5.5	1.416	0.626	0.325	1.076	0.698	0.280	0.007	0.053	0.582	0.466	0.649
X	1.5	1.378	0.478	0.366	0.737	0.606	0.523	0.014	0.104	0.649	0.604	0.822
X	3.5	1.406	0.600	0.346	0.814	0.535	0.479	0.015	0.098	0.737	0.647	0.657
X	5.5	1.416	0.665	0.310	0.858	0.463	0.449	0.015	0.094	0.775	0.670	0.540

Table 7.7: Shown are the total mass M_{tot} of the white dwarf and the obtained yields of total iron group elements (IGE), ^{56}Ni, intermediate mass elements (IME), ^{12}C and ^{16}O. In addition, the masses of IGE and ^{56}Ni at the time of the first DDT $t^{\mathrm{1st}}_{\mathrm{DDT}}$ and their relative fractions with respect to the total yields $\frac{\mathrm{IGE}(t^{\mathrm{1st}}_{\mathrm{DDT}})}{\mathrm{IGE}}$ and $\frac{^{56}\mathrm{Ni}(t^{\mathrm{1st}}_{\mathrm{DDT}})}{^{56}\mathrm{Ni}}$, as well as the fraction of ^{56}Ni to IGE are specified (Seitenzahl et al., 2011).

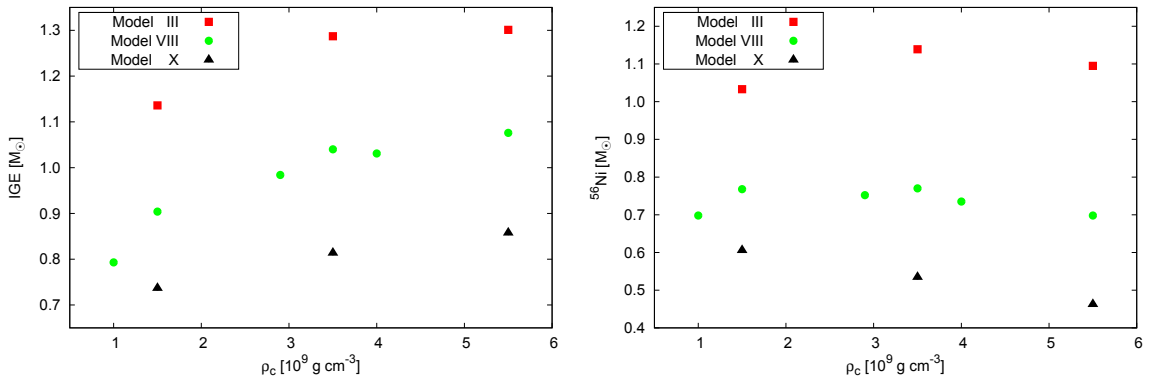

Fig. 7.7: Shown are the IGE yield (a) and the ^{56}Ni yield (b) as function of the initial central density ρ_c of the white dwarf. We see a trend that for each of the three ignition models the IGE yield rises with increasing ρ_c. In contrast, the ^{56}Ni yield seems to be independent of ρ_c for Model III and Model VIII. Only Model X shows a decrease of the ^{56}Ni yield with increasing ρ_c. Obviously the ignition model (which sets the strength of the deflagration) is the primary parameter that determines the ^{56}Ni yield, while ρ_c is only a secondary parameter (Seitenzahl et al., 2011).

7.3.5 Conclusions

In this section we described the analysis of 12 highly resolved three-dimensional simulations of delayed detonationss in which we varied the ignition geometry of the deflagration as well as the central density of the white dwarf at the time of deflagration ignition. In these simulations we find a clear trend that for a given ignition model the synthesized IGE rises with increasing initial central density. The reason is that the white dwarf with a higher initial central density is more compact and the flame evolves significantly faster due to the higher gravitational acceleration. In this case, DDTs occur earlier at a time when a relatively large amount of fuel still resides above a density threshold of 10^7 g cm^{-3} where detonations still burn the fuel to IGE (see Table 4.1). Despite the increase of the IGE yield, the stronger neutronization at high densities during the deflagration in the models with a higher initial central density leads to a smaller fraction of ^{56}Ni to the total produced IGE. As a consequence the ^{56}Ni mass appears approximately constant and is therefore largely independent of the initial central density. This result, however, does not hold for very strong deflagrations with an associated large expansion of the star prior to the first DDT which produce the fainter SN Ia events. Here, we find a trend that the ^{56}Ni yield decreases with increasing initial central density. This behavior is attributed to a strong neutronization in the deflagration phase that cannot be compensated by ensuing detonation(s), since the fuel densities have declined so far that detonations cannot burn much more fuel to ^{56}Ni anymore.

However, compared to the effect of a variation of the ignition geometry, this trend appears only of minor importance. Therefore, for a given ignition model the initial central density affects the explosion brightness only as a secondary parameter. It seems that a similar behavior also holds for the chemical composition (like metallicity and the C/O ratio) (Townsley et al., 2009; Bravo et al., 2010). Here, the analysis of high-quality V- and B-band light curves of SNe Ia from the Carnegie Supernova Project indicates that the chemical composition and the central density are indeed two independent secondary parameters for the SN Ia light

curves (Höflich et al., 2010).

In view of the significance of the ignition geometry of the deflagration for the explosion brightness, it is very important to establish how the central density at ignition time and the metallicity affect the statistical properties (such as the number, size and position) of the ignition kernels themselves, and not their individual direct effects on the result of an explosion, once a random initial flame configuration is chosen. For this reason it should be an aim to investigate the impact of the chemical composition, the cooling time and the accretion history on the ignition process, for instance by mapping them into an exponentiation parameter in a stochastic ignition prescription (see Schmidt & Niemeyer, 2006). However, as described in Section 2.3.1 there are still a number of uncertainties of the physics within the simmering phase (including details of the convection, the effects of electron captures and the mechanism of the URCA process) that eventually lead to the ignition of the deflagration.

8 Summary

As far as we know today, Type Ia supernovae originate from the explosions of white dwarfs. The details of the progenitor system and the explosion mechanism, however, remain highly uncertain. One promising scenario are delayed detonations of Chandrasekhar-mass carbon/oxygen white dwarfs (Khokhlov, 1991a). When approaching the Chandrasekhar-mass limit (for instance by mass accretion from a companion star) the carbon in the center of the white dwarf may ignite that eventually leads to a thermonuclear runaway which marks the birth of a flame. In the delayed detonation model it is assumed that the flame starts out as a subsonic deflagration and transitions into a supersonic detonation in the late explosion phase. Despite two decades of intensive research, the physics of the necessary deflagration to detonation transition (DDT) in white dwarfs is not well understood. However, from various studies in this field several necessary constraints on DDTs in SNe Ia can be derived. The main goal of this thesis was to implement these constraints in a hydrodynamic simulation code. Since the DDT quantities are not resolved in our studies we used a subgrid-scale (SGS) modeling approach. In the introduction section of this work we raised a number of issues and questions that will be summarized and sequentially answered in the following:

1. Are the properties of turbulence at the deflagration flame suitable for the occurrence of DDTs?

   According to Lisewski et al. (2000) and Woosley et al. (2009) high turbulent velocity fluctuations at the deflagration flame are required for a DDT. In agreement with the analysis of Röpke (2007), our study shows a non-vanishing probability of finding these high velocity fluctuations at the flame for different deflagration models. This result may indicate that there is a certain degree of intermittency in turbulence at the flame, which is sufficient to trigger a DDT. But we note that the origin of the found high velocity fluctuations remain somewhat uncertain, since there is yet no physical motivated model that may explain their occurrence. However, since these fluctuations can be reproduced with the resolved velocity field a significant turbulence- or flame modeling effect seems unlikely.

2. How can the necessary physical constraints on delayed detonations be treated in a numerical approach on unresolved scales properly? What are the requirements to keep the constructed DDT-SGS model robust and resolution-independent?

   Our DDT model is primarily based on the concept of the so-called *Zeldovich gradient mechanism* (Zel'dovich et al., 1970) where it is assumed that a spontaneous ignition of the fuel in a turbulently mixed region of hot burned material and cold fuel can lead to a supersonic reaction wave that eventually transitions into a detonation. The mixed regions have to exceed a critical length of approximately 10^6 cm (e.g. Khokhlov et al., 1997; Seitenzahl et al., 2009a) and they occur only when the deflagration flame and the burning dynamics are significantly affected by strong turbulent velocity fluctuations. This holds particularly in the late deflagration phase at low fuel densities at the flame.

   For the implementation, we first ensure that a sufficient number of grid cells at the flame have a specific fuel fraction and a certain fuel density. Then we determine a suitable flame surface area for DDTs from the number and size of these grid cells where we assume that the turbulent flame can be considered as a fractal object. Simultaneously, a histogram of the turbulent velocity fluctuations in these cells is constructed, where we rescale these fluctuations from the simulation grid scale to the critical length of a DDT region by assuming isotropic turbulence. The probability of finding high turbulent velocity fluctuations that are required for the DDT is determined by applying a fit to the histogram and integrating the obtained approximated probability density function. This probability multiplied with the suitable flame surface area for DDTs constitutes our potential detonation area which has to be compared with the critical flame surface area for a DDT. The latter is estimated with the critical length where we assume that the DDT region has either a smooth two-dimensional surface or a fractal structure. Finally the potential detonation area has to exceed the critical flame surface area for at least a half eddy turnover time to ensure that fuel and ash become sufficiently mixed. If this condition is met detonations are initialized in the grid cells at the suitable flame surface area for DDTs that contain the highest velocity fluctuations, until the number of initialized detonations equals the ratio of the potential detonation area to the critical flame surface area.

   Since the physics of DDTs and hence the values of the DDT quantities are not well known, we first applied a specific parameter set for the DDT criterion to the deflagration model of Röpke et al. (2007a). Here we find that the implemented SGS model for DDTs is robust and largely resolution-independent, when using a resolution of at least 256^3 grid cells. However, there is a low possibility for very weak deflagrations in combination with a very restrictive DDT criterion that the number of grid cells at the flame that meet the DDT constraints is insufficient to apply the DDT model.

3. Can three-dimensional simulations of delayed detonations that use the new DDT-SGS model reproduce the observed variations in the brightness of normal SNe Ia? What are the effects of different ignition scenarios of the deflagration and the associated different evolutions of the turbulent deflagration on the DDT model? What are the immediate consequences for the dynamics of the ensuing detonation phase?

   The explosion brightness of SNe Ia can be estimated with the produced amount of ^{56}Ni which is in the range of approximately $0.4 \ldots 0.9$ solar masses for normal SNe Ia (Contardo et al., 2000; Stritzinger et al., 2006; Mazzali et al., 2007). With two sets of different threshold values of the DDT quantities, applied to ten ignition models that

give rise to different strength of the deflagration, we obtain a range of ^{56}Ni yields that is fairly consistent with the observed variations in the brightness of normal SNe Ia.

According to our DDT model, we find that the mechanism which is responsible for DDTs is fundamentally different for weak and strong deflagrations. In weak deflagrations the high velocity fluctuations at the flame that are induced by strong shear instabilities trigger the DDT. In strong deflagrations that show weaker turbulence, the larger flame surface area that meets the DDT constraints and the lesser temporal variations of the probability of finding sufficiently high velocity fluctuations at this flame surface area causes DDTs. In all models we find resolved large-scale structures of strong turbulence at the flame, which becomes apparent in the occurrence of high velocity fluctuations in more connected grid cells. Therefore, it follows that also DDTs occur frequently in regions that exceed more than one grid cell.

Within the performed simulations we reproduced the generally expected behavior that the stronger the deflagration phase the weaker the additional burning due to detonations and the fainter the explosion. For weak deflagrations, a single DDT may set the brightness of the explosion, since most of the remaining fuel can be reached and burned by already one or a few detonations. In strong deflagrations, the large expansion of the white dwarf prior to the first DDT and the compact structure of the deflagration front may affect the dynamics of ensuing detonations, so that here the distribution of the DDT spots influences the further ^{56}Ni production and hence the explosion brightness.

4. How can the explosion brightness be controlled with the DDT model? To what extent is a variation of the values of the DDT quantities or a different evolution of the deflagration the decisive parameter that determines the explosion brightness? Can we place any constraints on DDT quantities, so that the obtained range of brightnesses in the simulations is largely consistent with the observed variations in the brightness of normal SNe Ia? Can we further derive any necessary constraints for DDTs to occur in deflagrations of white dwarfs generally?

   In general, we find for a given deflagration model that more restrictive DDT criteria tend to produce fainter explosions due to the less initialized detonations. This is far more pronounced for a strong deflagration in which a few initialized detonations may not reach a significant part of the remaining fuel. As indicated above, different distributions of the DDT regions lead further to an additional variation of the ^{56}Ni yield in strong deflagrations. However, compared to a change of the restrictiveness of the DDT criterion, we find that a variation of the strength of the deflagration has a far higher impact on the explosion brightness. To some extent, the nuclear energy release at the time when the deflagration is close to extinction and the first DDT occurs can be used to estimate the brightness of the explosion. But we note that this characteristic is partially affected by the distribution of DDT regions that determine the burning dynamics of detonations, particularly in strong deflagrations.

   We find that detonations in densities higher than 10^7 g cm^{-3} yield no events that can reproduce the faint explosions that are found within the observed variations in the brightness of normal SNe Ia. This holds also for the case that the minimum required velocity fluctuations for triggering a DDT are far lower than 10^8 cm s^{-1}. To reproduce the observed bright events with delayed detonations, a DDT in a sufficiently weak deflagration is required. Due to the higher temporal variations of the probability of finding sufficiently high velocity fluctuations at the flame in weak deflagrations, DDTs

occur here only when the mixing of fuel and ash occurs faster than 5×10^{-2} s. Based on our fractal description, it seems that compared to a two-dimensional geometry, the assignment of a fractal dimension for the DDT region explains the observed variations in the brightness of normal SNe Ia better. However, depending on the restrictiveness of the other DDT quantities we find in this case that the DDT criterion may often not be met. The reason is that the suitable flame surface area for DDTs may be too small in weak deflagrations, while turbulence may not be intense enough at the large flame surface area in strong deflagrations to meet the DDT criterion.

Finally, we find that different initial central densities of the white dwarf at the time of deflagration ignition have except for very strong deflagrations no effect on the ^{56}Ni yield. The reason is that a stronger neutronization at higher central densities that decreases the ^{56}Ni production is compensated by the larger amount of synthesized iron group elements due to the compactness of the white dwarf and the earlier onset of the DDT.

A weakness of the implemented DDT model is that it includes a global criterion, where all grid cells that meet the necessary DDT constraints are taken into account. Therefore, we have no information about the conditions in local areas and there are also no clues at which locations DDTs should be initialized. Due to the grid discretization in combination with the preselection of grid cells for the DDT model, a certain fraction of the deflagration flame that may meet the necessary DDT constraints is not taken into account. The resulting underestimate of the occurrence of DDTs depends primarily on the restriction on the fuel fraction in the grid cells, but not on the velocity threshold chosen for calculating the probability of finding sufficiently high velocity fluctuations for a DDT. A further problem occurs for very weak deflagrations, where insufficient data may prevent the application of the DDT model in lowly resolved simulations.

The proposed DDT model is based on the properties of turbulence in the vicinity of the deflagration flame. Details of the turbulent behavior in these regions, such as isotropy and intermittency, are not well known. Therefore, we followed the suggestion of Röpke (2007) and used an empirical approach to fit the histogram of the turbulent velocity fluctuations at the flame in order to obtain an estimate of the probability of finding high velocity fluctuations. However, since there exists no physically motivated model to explain intermittency in the turbulence at the deflagration flame in an exploding white dwarf, some uncertainties of this probability remain.

We further note that the properties of turbulence in the deflagration phase depend crucially on the ignition process of the deflagration flame. Therefore, further studies of the ignition properties of the deflagration can provide important information for the delayed detonation scenario.

The DDT model itself can also be further improved. So far, this model appears mostly static, since all threshold values of the DDT quantities are kept constant within a simulation. However, the properties of turbulence and the flame structure change during the explosion phase. Hence, we may take into account the temporal evolution of the turbulent quantities (such as the integral length scale, the transition length scale between Kolmogorov and Rayleigh-Taylor instability driven turbulence and the eddy turnover time) and the fractal dimension of the flame. Furthermore, the dependencies of these quantities among themselves have not been considered so far. It would also be desirable to improve the link between our DDT model to the microphysical nature of the DDT process. For a DDT which is based on the Zeldovich gradient mechanism, a sufficient flat gradient of induction times is required.

To investigate whether this prerequisite is fulfilled we need to find out how temperature and fuel composition change over a certain length scale. This length scale is not resolved in our study and both the fuel temperature and the fuel composition cannot be modeled on unresolved scales within our SGS modeling approach consistently.

The discontinuity approach of the flame prevents us to determine the physical properties of potential DDT regions precisely. Here the question arises, of whether the implemented flame model is appropriate to investigate DDTs in detail. Our study indicates that the obtained turbulent velocity fluctuations are not significantly affected by a flame modeling effect. However, since the latter cannot be ruled out completely an important next step would be to examine, whether and to what extent our results are based on the flame model in the simulation code. Alternatively, a detailed analysis of the intermittent behavior in turbulence at the flame can provide some clues, of whether the found high velocity fluctuations are of physical nature. Such an analysis would also help to verify the capability of the implemented DDT model to explain delayed detonations in SNe Ia properly.

Bibliography

Abdel-Gayed, R. G., Al-Khishali, K. J., & Bradley, D. 1984, Proc. R. Soc. Lond. A, 391, 393

Abdel-Gayed, R. G., Bradley, D., & Lawes, M. 1987, Proc. R. Soc. Lond. A, 414, 389

Almgren, A. S., Bell, J. B., Rendleman, C. A., & Zingale, M. 2006, *ApJ*, 637, 922

Anders, E., & Grevesse, N. 1989, *Geochim. Cosmochim. Acta*, 53, 197

Aparicio, J. M., & Isern, J. 1993, *A&A*, 272, 446

Arnett, D., & Livne, E. 1994a, *ApJ*, 427, 330

Arnett, D., & Livne, E. 1994b, *ApJ*, 427, 315

Arnett, W. D. 1969, *Ap&SS*, 5, 180

Arnett, W. D. 1971a, *ApJ*, 169, 113

Arnett, W. D. 1971b, *ApJ*, 166, 153

Arnett, W. D. 1982, *ApJ*, 253, 785

Arnett, W. D., Branch, D., & Wheeler, J. C. 1985, *Nature*, 314, 337

Aspden, A. J., Bell, J. B., Day, M. S., Woosley, S. E., & Zingale, M. 2008, *ApJ*, 689, 1173

Aspden, A. J., Bell, J. B., Dong, S., & Woosley, S. E. 2011, *ApJ*, 738, 94

Aspden, A. J., Bell, J. B., & Woosley, S. E. 2010, *ApJ*, 710, 1654

Asplund, M., Grevesse, N., & Sauval, A. J. 2005, in Astronomical Society of the Pacific Conference Series, Vol. 336, Cosmic Abundances as Records of Stellar Evolution and Nucleosynthesis, ed. T. G. Barnes III & F. N. Bash, 25

Axelrod, T. S. 1980, in Texas Workshop on Type I Supernovae, ed. J. C. Wheeler, 80–95

Baade, W., & Zwicky, F. 1934, Proceedings of the National Academy of Science, 20, 254

Barkat, Z., & Wheeler, J. C. 1990, *ApJ*, 355, 602

Baron, E., Jeffery, D. J., Branch, D., Bravo, E., García-Senz, D., & Hauschildt, P. H. 2008, *ApJ*, 672, 1038

Benetti, S., Meikle, P., Stehle, M., Altavilla, G., Desidera, S., Folatelli, G., Goobar, A., Mattila, S., Mendez, J., Navasardyan, H., Pastorello, A., Patat, F., Riello, M., Ruiz-Lapuente, P., Tsvetkov, D., Turatto, M., Mazzali, P., & Hillebrandt, W. 2004, *MNRAS*, 348, 261

Benz, W., Cameron, A. G. W., Press, W. H., & Bowers, R. L. 1990, *ApJ*, 348, 647

Blinnikov, S. I., & Khokhlov, A. M. 1986, Soviet Astronomy Letters, 12, 131

Blinnikov, S. I., & Khokhlov, A. M. 1987, Soviet Astronomy Letters, 13, 364

Blinnikov, S. I., & Sasorov, P. V. 1996, *Phys. Rev. E*, 53, 4827

Blondin, S., Kasen, D., Röpke, F. K., Kirshner, R. P., & Mandel, K. S. 2011, *MNRAS*, 417, 1280

Borghi, R. W. 1985, in Recent advances in the aerospace sciences, ed. C. Casci (New York: Plenum Publishing Corporation), 117–138

Branch, D., Fisher, A., & Nugent, P. 1993, *AJ*, 106, 2383

Bravo, E., Domínguez, I., Badenes, C., Piersanti, L., & Straniero, O. 2010, *ApJ*, 711, L66

Bravo, E., & García-Senz, D. 2005, in IAU Colloq. 192: Cosmic Explosions, On the 10th Anniversary of SN1993J, ed. J.-M. Marcaide & K. W. Weiler, 339–+

Bravo, E., & García-Senz, D. 2006, *ApJ*, 642, L157

Bravo, E., & García-Senz, D. 2008, *A&A*, 478, 843

Burbidge, E. M., Burbidge, G. R., Fowler, W. A., & Hoyle, F. 1957, Reviews of Modern Physics, 29, 547

Caldwell, R. R., Dave, R., & Steinhardt, P. J. 1998, Physical Review Letters, 80, 1582

Caldwell, R. R., Kamionkowski, M., & Weinberg, N. N. 2003, Physical Review Letters, 91, 071301

Cappellaro, E., Evans, R., & Turatto, M. 1999, *A&A*, 351, 459

Carroll, S. M. 2001, Living Reviews in Relativity, 4, 1

Cassisi, S., Iben, Jr., I., & Tornambe, A. 1998, *ApJ*, 496, 376

Chandrasekhar, S. 1931, *ApJ*, 74, 81

Chandrasekhar, S. 1961, Hydrodynamic and Hydromagnetic Stability (Oxford: Clarendon Press)

Chapman, D. L. 1899, Philosophical Magazine, 47, 90

Ciaraldi-Schoolmann, F., Schmidt, W., Niemeyer, J. C., Röpke, F. K., & Hillebrandt, W. 2009, *ApJ*, 696, 1491

Colella, P., & Woodward, P. R. 1984, Journal of Computational Physics, 54, 174

Colgate, S. A. 1979, *ApJ*, 232, 404

Colgate, S. A., & McKee, C. 1969, *ApJ*, 157, 623

Contardo, G., Leibundgut, B., & Vacca, W. D. 2000, *A&A*, 359, 876

Cooper, R. L., Steiner, A. W., & Brown, E. F. 2009, *ApJ*, 702, 660

Courant, R., & Friedrichs, K. O. 1948, Supersonic Flow and Shock Waves (New York: Springer Verlag)

Cox, J. P. 1968, Principles of stellar structure - Vol.1: Physical principles; Vol.2: Applications to stars (New York: Gordon and Breach, 1968)

Damköhler, G. 1940, Z. f. Elektroch., 46, 601

Darrieus, G. 1938, communication presented at *La Technique Moderne*, Unpublished.

Davies, R. M., & Taylor, G. 1950, Royal Society of London Proceedings Series A, 200, 375

Di Stefano, R., Voss, R., & Claeys, J. S. W. 2011, *ApJ*, 738, L1

Domínguez, I., Höflich, P., & Straniero, O. 2001, *ApJ*, 557, 279

Dunina-Barkovskaya, N. V., Imshennik, V. S., & Blinnikov, S. I. 2001, Astronomy Letters, 27, 353

Dursi, L. J., & Timmes, F. X. 2006, *ApJ*, 641, 1071

Feder, J. 1988, Fractals (New York: Plenum Press)

Filippenko, A. V. 1997, *ARA&A*, 35, 309

Filippenko, A. V., Richmond, M. W., Branch, D., Gaskell, M., Herbst, W., Ford, C. H., Treffers, R. R., Matheson, T., Ho, L. C., Dey, A., Sargent, W. L. W., Small, T. A., & van Breugel, W. J. M. 1992a, *AJ*, 104, 1543

Filippenko, A. V., Richmond, M. W., Matheson, T., Shields, J. C., Burbidge, E. M., Cohen, R. D., Dickinson, M., Malkan, M. A., Nelson, B., Pietz, J., Schlegel, D., Schmeer, P., Spinrad, H., Steidel, C. C., Tran, H. D., & Wren, W. 1992b, *ApJ*, 384, L15

Fink, M. 2010, Phd thesis, Technical University of Munich

Fink, M., Hillebrandt, W., & Röpke, F. K. 2007, *A&A*, 476, 1133

Fink, M., Röpke, F. K., Hillebrandt, W., Seitenzahl, I. R., Sim, S. A., & Kromer, M. 2010, *A&A*, 514, A53+

Förster, F., Lesaffre, P., & Podsiadlowski, P. 2010, *ApJS*, 190, 334

Frisch, U. 1995, Turbulence. The legacy of A.N. Kolmogorov (Cambridge: Cambridge University Press)

Frisch, U., Sulem, P.-L., & Nelkin, M. 1978, Journal of Fluid Mechanics, 87, 719

Fryxell, B. A., Müller, E., & Arnett, W. D. 1989, Hydrodynamics and nuclear burning, MPA Green Report 449, Max-Planck-Institut für Astrophysik, Garching

Gallagher, J. S., Garnavich, P. M., Caldwell, N., Kirshner, R. P., Jha, S. W., Li, W., Ganeshalingam, M., & Filippenko, A. V. 2008, *ApJ*, 685, 752

Gamezo, V. N., Khokhlov, A. M., & Oran, E. S. 2005, *ApJ*, 623, 337

Gamezo, V. N., Khokhlov, A. M., Oran, E. S., Chtchelkanova, A. Y., & Rosenberg, R. O. 2003, Science, 299, 77

Gamow, G., & Schoenberg, M. 1941, Physical Review, 59, 539

Garcia-Senz, D., & Woosley, S. E. 1995, *ApJ*, 454, 895

Garnavich, P. M., Bonanos, A. Z., Krisciunas, K., Jha, S., Kirshner, R. P., Schlegel, E. M., Challis, P., Macri, L. M., Hatano, K., Branch, D., Bothun, G. D., & Freedman, W. L. 2004, *ApJ*, 613, 1120

Gasques, L. R., Afanasjev, A. V., Aguilera, E. F., Beard, M., Chamon, L. C., Ring, P., Wiescher, M., & Yakovlev, D. G. 2005, *Phys. Rev. C*, 72, 025806

Gasques, L. R., Brown, E. F., Chieffi, A., Jiang, C. L., Limongi, M., Rolfs, C., Wiescher, M., & Yakovlev, D. G. 2007, *Phys. Rev. C*, 76, 035802

Gilfanov, M., & Bogdán, Á. 2010, *Nature*, 463, 924

Golombek, I., & Niemeyer, J. C. 2005, *A&A*, 438, 611

Gouldin, F. C. 1987, Combustion and flame, 68, 249

Guillochon, J., Dan, M., Ramirez-Ruiz, E., & Rosswog, S. 2010, *ApJ*, 709, L64

Gülder, O. L. 1991, Symposium (International) on Combustion, 23, 835

Gutierrez, J., Garcia-Berro, E., Iben, I. J., Isern, J., Labay, J., & Canal, R. 1996, *ApJ*, 459, 701

Haensel, P. 1995, *Space Sci. Rev.*, 74, 427

Halsey, T. C., Jensen, M. H., Kadanoff, L. P., Procaccia, I., & Shraiman, B. I. 1986, Phys. Rev. A, 33, 1141

Hamuy, M., Phillips, M. M., Suntzeff, N. B., Schommer, R. A., Maza, J., & Aviles, R. 1996, *AJ*, 112, 2391

Hicken, M., Challis, P., Jha, S., Kirshner, R. P., Matheson, T., Modjaz, M., Rest, A., Wood-Vasey, W. M., Bakos, G., Barton, E. J., Berlind, P., Bragg, A., Briceño, C., Brown, W. R., Caldwell, N., Calkins, M., Cho, R., Ciupik, L., Contreras, M., Dendy, K.-C., Dosaj, A., Durham, N., Eriksen, K., Esquerdo, G., Everett, M., Falco, E., Fernandez, J., Gaba, A., Garnavich, P., Graves, G., Green, P., Groner, T., Hergenrother, C., Holman, M. J., Hradecky, V., Huchra, J., Hutchison, B., Jerius, D., Jordan, A., Kilgard, R., Krauss, M., Luhman, K., Macri, L., Marrone, D., McDowell, J., McIntosh, D., McNamara, B., Megeath, T., Mochejska, B., Munoz, D., Muzerolle, J., Naranjo, O., Narayan, G., Pahre, M., Peters, W., Peterson, D., Rines, K., Ripman, B., Roussanova, A., Schild, R., Sicilia-Aguilar, A., Sokoloski, J., Smalley, K., Smith, A., Spahr, T., Stanek, K. Z., Barmby, P., Blondin, S., Stubbs, C. W., Szentgyorgyi, A., Torres, M. A. P., Vaz, A., Vikhlinin, A., Wang, Z., Westover, M., Woods, D., & Zhao, P. 2009, *ApJ*, 700, 331

Hicken, M., Garnavich, P. M., Prieto, J. L., Blondin, S., DePoy, D. L., Kirshner, R. P., & Parrent, J. 2007, *ApJ*, 669, L17

Hillebrandt, W., & Niemeyer, J. C. 2000, *ARA&A*, 38, 191

Hix, W. R., & Thielemann, F.-K. 1996, *ApJ*, 460, 869

Höflich, P. 1995, *ApJ*, 443, 89

Höflich, P., Khokhlov, A., Wheeler, J. C., Phillips, M. M., Suntzeff, N. B., & Hamuy, M. 1996, *ApJ*, 472, L81+

Höflich, P., Krisciunas, K., Khokhlov, A. M., Baron, E., Folatelli, G., Hamuy, M., Phillips, M. M., Suntzeff, N., Wang, L., & NSF07-SNIa Collaboration. 2010, *ApJ*, 710, 444

Höflich, P., & Stein, J. 2002, *ApJ*, 568, 779

Höflich, P., Wheeler, J. C., & Thielemann, F. K. 1998, *ApJ*, 495, 617

Howell, D. A., Sullivan, M., Nugent, P. E., Ellis, R. S., Conley, A. J., Le Borgne, D., Carlberg, R. G., Guy, J., Balam, D., Basa, S., Fouchez, D., Hook, I. M., Hsiao, E. Y., Neill, J. D., Pain, R., Perrett, K. M., & Pritchet, C. J. 2006, *Nature*, 443, 308

Hoyle, F., & Fowler, W. A. 1960, *ApJ*, 132, 565

Huterer, D., & Turner, M. S. 1999, *Phys. Rev. D*, 60, 081301

Iapichino, L., Brüggen, M., Hillebrandt, W., & Niemeyer, J. C. 2006, *A&A*, 450, 655

Iapichino, L., & Lesaffre, P. 2010, *A&A*, 512, A27+

Iben, Jr., I., & Tutukov, A. V. 1984, *ApJS*, 54, 335

Iben, Jr., I., & Tutukov, A. V. 1985, *ApJS*, 58, 661

Itoh, N., Tomizawa, N., Wanajo, S., & Nozawa, S. 2003, *ApJ*, 586, 1436

Ivanova, L. N., Imshennik, V. S., & Chechetkin, V. M. 1974, *Ap&SS*, 31, 497

Jackson, A. P., Calder, A. C., Townsley, D. M., Chamulak, D. A., Brown, E. F., & Timmes, F. X. 2010, *ApJ*, 720, 99

Jha, S., Branch, D., Chornock, R., Foley, R. J., Li, W., Swift, B. J., Casebeer, D., & Filippenko, A. V. 2006, *AJ*, 132, 189

Jiang, C. L., Rehm, K. E., Back, B. B., & Janssens, R. V. F. 2007, *Phys. Rev. C*, 75, 015803

Johnson, H. L., & Morgan, W. W. 1953, *ApJ*, 117, 313

Jordan, IV, G. C., Fisher, R. T., Townsley, D. M., Calder, A. C., Graziani, C., Asida, S., Lamb, D. Q., & Truran, J. W. 2008, *ApJ*, 681, 1448

Jouguet, C. E. 1905, Journal des Mathématiques Pures et Appliquées, Series 6, 1, 347

Justham, S. 2011, *ApJ*, 730, L34+

Kahabka, P., & van den Heuvel, E. P. J. 1997, *ARA&A*, 35, 69

Kasen, D. 2006, *ApJ*, 649, 939

Kasen, D., Röpke, F. K., & Woosley, S. E. 2009, *Nature*, 460, 869

Kerstein, A. R. 1988, Combust. Sci. Technol., 60, 441

Kerstein, A. R. 1991, *Phys. Rev. A*, 44, 3633

Kerstein, A. R. 2001, *Phys. Rev. E*, 64, 066306

Khokhlov, A., Müller, E., & Höflich, P. 1993, *A&A*, 270, 223

Khokhlov, A. M. 1991a, *A&A*, 245, 114

Khokhlov, A. M. 1991b, *A&A*, 246, 383

Khokhlov, A. M. 1995, *ApJ*, 449, 695

Khokhlov, A. M. 2000, arXiv:astro-ph/0008463

Khokhlov, A. M., Oran, E. S., & Wheeler, J. C. 1997, *ApJ*, 478, 678

Kolmogorov, A. 1941, Akademiia Nauk SSSR Doklady, 30, 301

Kolmogorov, A. N. 1962, Journal of Fluid Mechanics, 13, 82

Kolmogorov, A. N. 1991, Royal Society of London Proceedings Series A, 434, 9

Kowal, C. T. 1968, *AJ*, 73, 1021

Kozma, C., Fransson, C., Hillebrandt, W., Travaglio, C., Sollerman, J., Reinecke, M., Röpke, F. K., & Spyromilio, J. 2005, *A&A*, 437, 983

Kromer, M., Sim, S. A., Fink, M., Röpke, F. K., Seitenzahl, I. R., & Hillebrandt, W. 2010, *ApJ*, 719, 1067

Krueger, B. K., Jackson, A. P., Townsley, D. M., Calder, A. C., Brown, E. F., & Timmes, F. X. 2010, *ApJ*, 719, L5

Kuchner, M. J., Kirshner, R. P., Pinto, P. A., & Leibundgut, B. 1994, *ApJ*, 426, L89+

Kuhlen, M., Woosley, S. E., & Glatzmaier, G. A. 2006, *ApJ*, 640, 407

Landau, L. D. 1944, Acta Physicochim. URSS, 19, 77

Landau, L. D., & Lifschitz, E. M. 1991, Lehrbuch der theoretischen Physik, Vol. 6, Hydrodynamik (Berlin: Akademie Verlag)

Langanke, K., & Martínez-Pinedo, G. 2001, Atomic Data and Nuclear Data Tables, 79, 1

Leibundgut, B., Kirshner, R. P., Phillips, M. M., Wells, L. A., Suntzeff, N. B., Hamuy, M., Schommer, R. A., Walker, A. R., Gonzalez, L., Ugarte, P., Williams, R. E., Williger, G., Gomez, M., Marzke, R., Schmidt, B. P., Whitney, B., Coldwell, N., Peters, J., Chaffee, F. H., Foltz, C. B., Rehner, D., Siciliano, L., Barnes, T. G., Cheng, K.-P., Hintzen, P. M. N., Kim, Y.-C., Maza, J., Parker, J. W., Porter, A. C., Schmidtke, P. C., & Sonneborn, G. 1993, *AJ*, 105, 301

Lesaffre, P., Han, Z., Tout, C. A., Podsiadlowski, P., & Martin, R. G. 2006, *MNRAS*, 368, 187

Lesaffre, P., Podsiadlowski, P., & Tout, C. A. 2005, *MNRAS*, 356, 131

Li, W., Leaman, J., Chornock, R., Filippenko, A. V., Poznanski, D., Ganeshalingam, M., Wang, X., Modjaz, M., Jha, S., Foley, R. J., & Smith, N. 2011, *MNRAS*, 412, 1441

Lisewski, A. M., Hillebrandt, W., & Woosley, S. E. 2000, *ApJ*, 538, 831

Livio, M., & Truran, J. W. 1992, *ApJ*, 389, 695

Livne, E. 1999, *ApJ*, 527, L97

Livne, E., & Arnett, D. 1995, *ApJ*, 452, 62

Lorén-Aguilar, P., Isern, J., & García-Berro, E. 2009, in American Institute of Physics Conference Series, Vol. 1122, American Institute of Physics Conference Series, ed. K. E. Kunze, M. Mars, & M. A. Vázquez-Mozo, 320–323

Maier, A., & Niemeyer, J. C. 2006, *A&A*, 451, 207

Mandelbrot, B. B. 1983, The fractal geometry of nature (New York: W. H. Freeman)

Mannucci, F., Della Valle, M., Panagia, N., Cappellaro, E., Cresci, G., Maiolino, R., Petrosian, A., & Turatto, M. 2005, *A&A*, 433, 807

Marietta, E., Burrows, A., & Fryxell, B. 2000, *ApJS*, 128, 615

Mathieu, J., & Scott, J. 2000, An Introduction to Turbulent Flow (Cambridge: Cambridge University Press)

Mazzali, P. A., Chugai, N., Turatto, M., Lucy, L. B., Danziger, I. J., Cappellaro, E., della Valle, M., & Benetti, S. 1997, *MNRAS*, 284, 151

Mazzali, P. A., Danziger, I. J., & Turatto, M. 1995, *A&A*, 297, 509

Mazzali, P. A., Röpke, F. K., Benetti, S., & Hillebrandt, W. 2007, Science, 315, 825

Meakin, C. A., Seitenzahl, I., Townsley, D., Jordan, G. C., Truran, J., & Lamb, D. 2009, *ApJ*, 693, 1188

Mikhel'son, V. A. 1889, PhD thesis, Univ. Moscow, see *Collected works*, Vol. 1, Novyi Agronom Press, Moscow (1930)

Minkowski, R. 1941, *PASP*, 53, 224

Motl, P. M., Frank, J., Tohline, J. E., & D'Souza, M. C. R. 2007, *ApJ*, 670, 1314

Nadyozhin, D. K. 1995, *Space Sci. Rev.*, 74, 455

Nandkumar, R., & Pethick, C. J. 1984, *MNRAS*, 209, 511

Navier, C. L. M. H. 1823, Mem. Acad. Sci. Inst. Fr., 6, 389

Niemeyer, J. C. 1995, PhD thesis, Technical University of Munich, also available as MPA Green Report 911

Niemeyer, J. C. 1999, *ApJ*, 523, L57

Niemeyer, J. C., Bushe, W. K., & Ruetsch, G. R. 1999, *ApJ*, 524, 290

Niemeyer, J. C., & Kerstein, A. R. 1997, New Astronomy, 2, 239

Niemeyer, J. C., & Woosley, S. E. 1997, *ApJ*, 475, 740

Nomoto, K. 1982, *ApJ*, 253, 798

Nomoto, K., & Kondo, Y. 1991, *ApJ*, 367, L19

Nomoto, K., & Sugimoto, D. 1977, *PASJ*, 29, 765

Nomoto, K., Sugimoto, D., & Neo, S. 1976, *Ap&SS*, 39, L37

Nomoto, K., Thielemann, F.-K., & Yokoi, K. 1984, *ApJ*, 286, 644

Nonaka, A., Aspden, A. J., Zingale, M., Almgren, A. S., Bell, J. B., & Woosley, S. E. 2012, *ApJ*, 745, 73

North, G. L., & Santavicca, D. A. 1990, Combustion Science and Technology, 72, 215

Oboukhov, A. M. 1962, Journal of Fluid Mechanics, 13, 77

Osher, S., & Sethian, J. A. 1988, Journal of Computational Physics, 79, 12

Paczyński, B. 1972, *Astrophys. Lett.*, 11, 53

Pakmor, R. 2010, Phd thesis, Technical University of Munich

Pakmor, R., Hachinger, S., Röpke, F. K., & Hillebrandt, W. 2011, *A&A*, 528, A117+

Pakmor, R., Kromer, M., Röpke, F. K., Sim, S. A., Ruiter, A. J., & Hillebrandt, W. 2010, *Nature*, 463, 61

Pakmor, R., Kromer, M., Taubenberger, S., Sim, S. A., Röpke, F. K., & Hillebrandt, W. 2012, *ApJ*, 747, L10

Pan, L., Wheeler, J. C., & Scalo, J. 2008, *ApJ*, 681, 470

Perlmutter, S., Aldering, G., Goldhaber, G., Knop, R. A., Nugent, P., Castro, P. G., Deustua, S., Fabbro, S., Goobar, A., Groom, D. E., Hook, I. M., Kim, A. G., Kim, M. Y., Lee, J. C., Nunes, N. J., Pain, R., Pennypacker, C. R., Quimby, R., Lidman, C., Ellis, R. S., Irwin, M., McMahon, R. G., Ruiz-Lapuente, P., Walton, N., Schaefer, B., Boyle, B. J., Filippenko, A. V., Matheson, T., Fruchter, A. S., Panagia, N., Newberg, H. J. M., Couch, W. J., & The Supernova Cosmology Project. 1999, *ApJ*, 517, 565

Peters, N. 1986, in Twenty-First Symposium (International) on Combustion (Pittsburgh: The Combustion Institute), 1231–1250

Peters, N. 1999, Journal of Fluid Mechanics, 384, 107

Peters, N. 2000, Turbulent Combustion (Cambridge: Cambridge University Press)

Pfannes, J. M. M., Niemeyer, J. C., & Schmidt, W. 2010a, *A&A*, 509, A75+

Pfannes, J. M. M., Niemeyer, J. C., Schmidt, W., & Klingenberg, C. 2010b, *A&A*, 509, A74+

Phillips, M. M. 1993, *ApJ*, 413, L105

Phillips, M. M., Li, W., Frieman, J. A., Blinnikov, S. I., DePoy, D., Prieto, J. L., Milne, P., Contreras, C., Folatelli, G., Morrell, N., Hamuy, M., Suntzeff, N. B., Roth, M., González, S., Krzeminski, W., Filippenko, A. V., Freedman, W. L., Chornock, R., Jha, S., Madore, B. F., Persson, S. E., Burns, C. R., Wyatt, P., Murphy, D., Foley, R. J., Ganeshalingam, M., Serduke, F. J. D., Krisciunas, K., Bassett, B., Becker, A., Dilday, B., Eastman, J., Garnavich, P. M., Holtzman, J., Kessler, R., Lampeitl, H., Marriner, J., Frank, S., Marshall, J. L., Miknaitis, G., Sako, M., Schneider, D. P., van der Heyden, K., & Yasuda, N. 2007, *PASP*, 119, 360

Phillips, M. M., Lira, P., Suntzeff, N. B., Schommer, R. A., Hamuy, M., & Maza, J. 1999, *AJ*, 118, 1766

Phillips, M. M., Wells, L. A., Suntzeff, N. B., Hamuy, M., Leibundgut, B., Kirshner, R. P., & Foltz, C. B. 1992, *AJ*, 103, 1632

Piersanti, L., Cassisi, S., Iben, Jr., I., & Tornambé, A. 1999, *ApJ*, 521, L59

Piersanti, L., Cassisi, S., Iben, Jr., I., & Tornambé, A. 2000, *ApJ*, 535, 932

Piro, A. L., & Bildsten, L. 2008, *ApJ*, 673, 1009

Piro, A. L., & Chang, P. 2008, *ApJ*, 678, 1158

Plewa, T. 2007, *ApJ*, 657, 942

Plewa, T., Calder, A. C., & Lamb, D. Q. 2004, *ApJ*, 612, L37

Pocheau, A. 1994, *Phys. Rev. E*, 49, 1109

Podsiadlowski, P., Mazzali, P., Lesaffre, P., Han, Z., & Förster, F. 2008, New Astronomy Reviews, 52, 381

Poludnenko, A. Y., Gardiner, T. A., & Oran, E. S. 2011, Physical Review Letters, 107, 054501

Pope, S. B. 2000, Turbulent Flows (Cambridge: Cambridge University Press)

Preibisch, T., & Zinnecker, H. 1999, *AJ*, 117, 2381

Preibisch, T., & Zinnecker, H. 2001, in Astronomical Society of the Pacific Conference Series, Vol. 243, From Darkness to Light: Origin and Evolution of Young Stellar Clusters, ed. T. Montmerle & P. André, 791–+

Prialnik, D. 2000, An Introduction to the Theory of Stellar Structure and Evolution (Cambridge: Cambridge University Press)

Reinecke, M., Hillebrandt, W., & Niemeyer, J. C. 2002, *A&A*, 391, 1167

Reinecke, M., Hillebrandt, W., Niemeyer, J. C., Klein, R., & Gröbl, A. 1999, *A&A*, 347, 724

Reinecke, M. A. 2001, PhD thesis, Technical University of Munich, available at http://tumb1.biblio.tu-muenchen.de/publ/diss/allgemein.html

Reynolds, O. 1883, Royal Society of London Philosophical Transactions Series I, 174, 935

Richardson, L. F. 1922, Quarterly Journal of the Royal Meteorological Society, 48, 282

Riess, A. G., Filippenko, A. V., Challis, P., Clocchiatti, A., Diercks, A., Garnavich, P. M., Gilliland, R. L., Hogan, C. J., Jha, S., Kirshner, R. P., Leibundgut, B., Phillips, M. M., Reiss, D., Schmidt, B. P., Schommer, R. A., Smith, R. C., Spyromilio, J., Stubbs, C., Suntzeff, N. B., & Tonry, J. 1998, *AJ*, 116, 1009

Riess, A. G., Filippenko, A. V., Li, W., Treffers, R. R., Schmidt, B. P., Qiu, Y., Hu, J., Armstrong, M., Faranda, C., Thouvenot, E., & Buil, C. 1999, *AJ*, 118, 2675

Riess, A. G., Strolger, L.-G., Tonry, J., Casertano, S., Ferguson, H. C., Mobasher, B., Challis, P., Filippenko, A. V., Jha, S., Li, W., Chornock, R., Kirshner, R. P., Leibundgut, B., Dickinson, M., Livio, M., Giavalisco, M., Steidel, C. C., Benítez, T., & Tsvetanov, Z. 2004, *ApJ*, 607, 665

Röpke, F. K. 2003, PhD thesis, Technical University of Munich

Röpke, F. K. 2005, *A&A*, 432, 969

Röpke, F. K. 2007, *ApJ*, 668, 1103

Röpke, F. K., Hillebrandt, W., Niemeyer, J. C., & Woosley, S. E. 2006, *A&A*, 448, 1

Röpke, F. K., Hillebrandt, W., Schmidt, W., Niemeyer, J. C., Blinnikov, S. I., & Mazzali, P. A. 2007a, *ApJ*, 668, 1132

Röpke, F. K., & Niemeyer, J. C. 2007, *A&A*, 464, 683

Röpke, F. K., & Schmidt, W. 2009, in Lecture Notes in Physics, Berlin Springer Verlag, Vol. 756, Interdisciplinary Aspects of Turbulence, ed. W. Hillebrandt & F. Kupka, 255–+

Röpke, F. K., Woosley, S. E., & Hillebrandt, W. 2007b, *ApJ*, 660, 1344

Ruiter, A. J., Belczynski, K., & Fryer, C. 2009, *ApJ*, 699, 2026

Saio, H., & Nomoto, K. 1985, *A&A*, 150, L21

Saio, H., & Nomoto, K. 1998, *ApJ*, 500, 388

Schmidt, W. 2004, PhD thesis, Technical University of Munich

Schmidt, W., Ciaraldi-Schoolmann, F., Niemeyer, J. C., Röpke, F. K., & Hillebrandt, W. 2010, *ApJ*, 710, 1683

Schmidt, W., & Niemeyer, J. C. 2006, *A&A*, 446, 627

Schmidt, W., Niemeyer, J. C., & Hillebrandt, W. 2006a, *A&A*, 450, 265

Schmidt, W., Niemeyer, J. C., Hillebrandt, W., & Röpke, F. K. 2006b, *A&A*, 450, 283

Schroeder, M. 1991, Fractals, Chaos, Power Laws: Minutes from an Infinite Paradise (New York: W.H. Freeman and Company)

Seeger, P. A., Fowler, W. A., & Clayton, D. D. 1965, *ApJS*, 11, 121

Seitenzahl, I., Röpke, F., Pakmor, R., & Fink, M. 2010a, in Nuclei in the Cosmos.

Seitenzahl, I. R. 2012, Private communication

Seitenzahl, I. R., Ciaraldi-Schoolmann, F., & Röpke, F. K. 2011, *MNRAS*, 563

Seitenzahl, I. R., Meakin, C. A., Townsley, D. M., Lamb, D. Q., & Truran, J. W. 2009a, *ApJ*, 696, 515

Seitenzahl, I. R., Röpke, F. K., Fink, M., & Pakmor, R. 2010b, *MNRAS*, 407, 2297

Seitenzahl, I. R., Townsley, D. M., Peng, F., & Truran, J. W. 2009b, Atomic Data and Nuclear Data Tables, 95, 96

Shapiro, S. L., & Teukolsky, S. A. 1983, Black holes, white dwarfs, and neutron stars: The physics of compact objects (New York: Wiley-Interscience)

Sharp, D. H. 1984, Physica D Nonlinear Phenomena, 12, 3

Silverman, J. M., Ganeshalingam, M., Li, W., Filippenko, A. V., Miller, A. A., & Poznanski, D. 2011, *MNRAS*, 410, 585

Sim, S. A., Röpke, F. K., Hillebrandt, W., Kromer, M., Pakmor, R., Fink, M., Ruiter, A. J., & Seitenzahl, I. R. 2010, *ApJ*, 714, L52

Smiljanovski, V., Moser, V., & Klein, R. 1997, Combustion Theory Modelling, 1, 183

Spyromilio, J., Meikle, W. P. S., Allen, D. A., & Graham, J. R. 1992, *MNRAS*, 258, 53P

Sreenivasan, K. R. 1991, Annual Review of Fluid Mechanics, 23, 539

Stokes, G. G. 1851, Transactions of the Cambridge Philosophical Society, 9, 8

Stritzinger, M., Leibundgut, B., Walch, S., & Contardo, G. 2006, *A&A*, 450, 241

Sullivan, M., Le Borgne, D., Pritchet, C. J., Hodsman, A., Neill, J. D., Howell, D. A., Carlberg, R. G., Astier, P., Aubourg, E., Balam, D., Basa, S., Conley, A., Fabbro, S., Fouchez, D., Guy, J., Hook, I., Pain, R., Palanque-Delabrouille, N., Perrett, K., Regnault, N., Rich, J., Taillet, R., Baumont, S., Bronder, J., Ellis, R. S., Filiol, M., Lusset, V., Perlmutter, S., Ripoche, P., & Tao, C. 2006, *ApJ*, 648, 868

Suntzeff, N. B. 2003, in From Twilight to Highlight: The Physics of Supernovae, ed. W. Hillebrandt & B. Leibundgut, 183–+

Taubenberger, S., Benetti, S., Childress, M., Pakmor, R., Hachinger, S., Mazzali, P. A., Stanishev, V., Elias-Rosa, N., Agnoletto, I., Bufano, F., Ergon, M., Harutyunyan, A., Inserra, C., Kankare, E., Kromer, M., Navasardyan, H., Nicolas, J., Pastorello, A., Prosperi, E., Salgado, F., Sollerman, J., Stritzinger, M., Turatto, M., Valenti, S., & Hillebrandt, W. 2011, *MNRAS*, 412, 2735

Taubenberger, S., Hachinger, S., Pignata, G., Mazzali, P. A., Contreras, C., Valenti, S., Pastorello, A., Elias-Rosa, N., Bärnbantner, O., Barwig, H., Benetti, S., Dolci, M., Fliri, J., Folatelli, G., Freedman, W. L., Gonzalez, S., Hamuy, M., Krzeminski, W., Morrell, N., Navasardyan, H., Persson, S. E., Phillips, M. M., Ries, C., Roth, M., Suntzeff, N. B., Turatto, M., & Hillebrandt, W. 2008, *MNRAS*, 385, 75

Timmes, F. X., Brown, E. F., & Truran, J. W. 2003, *ApJ*, 590, L83

Timmes, F. X., & Woosley, S. E. 1992, *ApJ*, 396, 649

Townsley, D. M., Calder, A. C., Asida, S. M., Seitenzahl, I. R., Peng, F., Vladimirova, N., Lamb, D. Q., & Truran, J. W. 2007, *ApJ*, 668, 1118

Townsley, D. M., Jackson, A. P., Calder, A. C., Chamulak, D. A., Brown, E. F., & Timmes, F. X. 2009, *ApJ*, 701, 1582

Travaglio, C., Hillebrandt, W., & Reinecke, M. 2005, *A&A*, 443, 1007

Travaglio, C., Hillebrandt, W., Reinecke, M., & Thielemann, F.-K. 2004, *A&A*, 425, 1029

Truran, J. W., Arnett, W. D., & Cameron, A. G. W. 1967, Canadian Journal of Physics, 45, 2315

Webbink, R. F. 1984, *ApJ*, 277, 355

Whelan, J., & Iben, Jr., I. 1973, *ApJ*, 186, 1007

Winget, D. E., Sullivan, D. J., Metcalfe, T. S., Kawaler, S. D., & Montgomery, M. H. 2004, *ApJ*, 602, L109

Woosley, S. E. 1990, in Supernovae, ed. A. G. Petschek (New York: Springer-Verlag), 182–212

Woosley, S. E. 1997, in NATO ASIC Proc. 486: Thermonuclear Supernovae, ed. P. Ruiz-Lapuente, R. Canal, & J. Isern, 313

Woosley, S. E. 2007, *ApJ*, 668, 1109

Woosley, S. E., Arnett, W. D., & Clayton, D. D. 1973, *ApJS*, 26, 231

Woosley, S. E., Kerstein, A. R., Sankaran, V., Aspden, A. J., & Röpke, F. K. 2009, *ApJ*, 704, 255

Woosley, S. E., Taam, R. E., & Weaver, T. A. 1986, *ApJ*, 301, 601

Woosley, S. E., & Weaver, T. A. 1986, *ARA&A*, 24, 205

Woosley, S. E., & Weaver, T. A. 1994, *ApJ*, 423, 371

Woosley, S. E., Wunsch, S., & Kuhlen, M. 2004, *ApJ*, 607, 921

Wunsch, S., & Woosley, S. E. 2004, *ApJ*, 616, 1102

Yamanaka, M., Kawabata, K. S., Kinugasa, K., Tanaka, M., Imada, A., Maeda, K., Nomoto, K., Arai, A., Chiyonobu, S., Fukazawa, Y., Hashimoto, O., Honda, S., Ikejiri, Y., Itoh, R., Kamata, Y., Kawai, N., Komatsu, T., Konishi, K., Kuroda, D., Miyamoto, H., Miyazaki, S., Nagae, O., Nakaya, H., Ohsugi, T., Omodaka, T., Sakai, N., Sasada, M., Suzuki, M., Taguchi, H., Takahashi, H., Tanaka, H., Uemura, M., Yamashita, T., Yanagisawa, K., & Yoshida, M. 2009, *ApJ*, 707, L118

Yoon, S.-C., & Langer, N. 2004, *A&A*, 419, 623

Yoon, S.-C., & Langer, N. 2005, *A&A*, 435, 967

Yoon, S.-C., Podsiadlowski, P., & Rosswog, S. 2007, *MNRAS*, 380, 933

Zel'Dovich, Y. B. 1966, Journal of Applied Mechanics and Technical Physics, 7, 68

Zel'dovich, Y. B., Librovich, V. B., Makhviladze, G. M., & Sivashinskii, G. I. 1970, Journal of Applied Mechanics and Technical Physics, 11, 264

Zhang, J., Messer, O. E. B., Khokhlov, A. M., & Plewa, T. 2007, *ApJ*, 656, 347

Zhao, F.-Y., Strom, R. G., & Jiang, S.-Y. 2006, Chinese Journal of Astronomy and Astrophysics, 6, 635

Zingale, M., Almgren, A. S., Bell, J. B., Nonaka, A., & Woosley, S. E. 2009, *ApJ*, 704, 196

Zingale, M., Woosley, S. E., Rendleman, C. A., Day, M. S., & Bell, J. B. 2005, *ApJ*, 632, 1021

Zwicky, F. 1938, *ApJ*, 88, 522

Zwicky, F. 1940, Reviews of Modern Physics, 12, 66

Acknowledgements

First of all I want to thank my supervisor Prof. Dr. Friedrich K. Röpke who supported me continuously throughout the work on this interesting project. I thank my office mates F. Miczek, R. Pakmor, P. Edelmann, S. Hachinger, J. von Groote, U. Noebauer, I. Seitenzahl, A. Ruiter and all other members of the hydro group for the numerous physical (and non-physical) discussions.

I would like to mention that there has been always a great atmosphere at the MPA. The people had always an open ear for all different kinds of problems. Furthermore, the various performed activities outside the institute, such as the Ostfriesian Bosseln (a sport in East Frisia which is similar to road bowling) were a great pleasure.

Finally my parents and my girlfriend Anamarija deserve my greatest thanks for their unsurpassed patience, while I was working on this project.